Laser site-selective spectroscopy, Zeeman spectroscopy and crystal-field analysis of yttrium orthosilicate doped with Sm^{3+} and Er^{3+} ions

---

Nicholas Lester Jobbitt

School of Physical and Chemical Sciences

University of Canterbury

Submitted in partial fulfilment of the requirements for the degree of Doctor of Philosophy in Physics

Under the supervision of M. F. Reid, J.-P. R. Wells and J. J. Longdell

November, 2021

Declaration

This thesis is based on work conducted by the author, in the School of Physical and Chemical Sciences at the University of Canterbury, New Zealand, during the period January 2018 to July 2021. All the work described in this thesis is original, unless otherwise acknowledged in the text or in the references. None of this work has been submitted for any another degree in this or any other University.

Abstract

Lanthanide-doped crystals are excellent candidates in the realisation of quantum information processing and communication devices. The ZEro First Order Zeeman (ZEFOZ) technique, which involves determining external magnetic fields at which the hyperfine structure is insensitive to magnetic field fluctuations in any direction, is the primary techniques used in the development of such devices. However, ZEFOZ points are notoriously difficult to find experimentally and are therefore required to be predicted through the use of, for example, a crystal-field Hamiltonian.

This thesis focuses on crystal-field modelling the $4f^5$ configuration of Sm^{3+}:Y_2SiO_5, and refining the crystal-field model for the $4f^{11}$ configuration of Er^{3+}:Y_2SiO_5. Temperature-dependent, Zeeman, Raman heterodyne and fluorescence spectroscopy was performed in order to determine the electronic and magnetic structure of both systems. The parameterised crystal-field models not only accurately reproduces the electronic, magnetic and low-field hyperfine structure of these systems, but is also able to predict polarisation and high-field hyperfine structure that was not fitted to in determining the crystal-field parameters. The parameter set for Sm^{3+}:Y_2SiO_5 was scaled to fit to the electronic structure of Eu^{3+}:Y_2SiO_5 and was able to predict the location of the ZEFOZ point of Eu^{3+}:Y_2SiO_5 that was utilised in obtaining a six hour coherence time.

An understanding of the underlying dynamics of energy transfer is essential in the creation of efficient phosphors, white light emitting diodes and solar cells. Therefore, the energy transfer dynamics of Sm^{3+}:Y_2SiO_5 was investigated through the use of site-selective laser spectroscopy. Intra-site energy transfer was found to proceed via a dipole-dipole mechanism for both sites. While the radiative decay rates were found to be insensitive to temperature for both sites, the energy transfer parameters were found to increase with temperature. Inter-site energy transfer from site 2 to site 1 was observed and became much stronger as the temperature increased. However, the reverse process, from site 1 to site 2, remained very weak at all temperatures.

Acknowledgements

I would like to thank my supervisors, Professors Mike Reid and Jon-Paul Wells and Associate Professor Jevon Longdell for the continual guidance and support throughout my thesis. I appreciate always having a door open for my incessant questions. I am also grateful to the Dodd-Walls centre for the finical support in the form of a PhD scholarship, without which this PhD would not be possible.

Particular thanks goes to the technical assistance of Stephen Hemmingsen, Rob Thirkettle and Graeme MacDonald and to the IT support of Dr. Orlon Petterson. The help in keeping the labs running, despite the many hiccups along the way, is greatly appreciated.

Thanks to Ruchita, Alejandra, Nathan and Claudio for the great hang outs. The distractions from my thesis definitely kept me sane throughout the last three years.

I am grateful to the fellow members, past and present, of the lanthanide spectroscopy and ring-laser group; Jamin, Yashar, Kieran, Dian, Caroline, Pratik, Sagar and Sangeetha. The discussions, ideas and chats were of great help throughout my PhD.

Additionally, I would like to thank the members of Jevon's group; Jono, Gavin, Maddie, Li and Finn, for making my research trip to the University of Otago productive and enjoyable.

And finally, my greatest thanks goes to mum for her continual love and support and for always being there when I needed it. You have always allowed me to pursue my interests and nurtured my curiosity of the world.

Contents

List of Figures

List of Tables

Chapter 1

Introduction and motivation

The last two decades has seen a global interest in the development of quantum computers and long distance quantum communications in order to enhance the current classical computation and communication infrastructure [1]. This interest has been spurred by the development of quantum algorithms throughout the 1990s and 2000s, such as the Deutsch-Jozsa and Bernstein-Vazirani algorithms, which promise to be exponentially more efficient than their classical counterparts [2, 3]. Quantum algorithms, the related information theory and their physical implementations will henceforward be collectively known as quantum information processing (QIP).

Despite this global interest, large scale development and implementation of QIP has remained elusive [4]. The key difficulty being faced in the realisation of these devices is the inability in maintaining an ensemble of superposition states for a prolonged period of time, while maintaining the ability to manipulate this ensemble. The rate at which the ensemble of superposition states degrades, through any interaction, is known as the coherence time. In order to maximise the coherence time, the system has to be in what is known as a 'closed box' environment, in which interactions between the system and the surrounding universe is drastically limited, while simultaneously retaining the ability to be manipulated by the user.

Lanthanide-doped insulating crystals serve as excellent candidates for use in QIP applications. This is due to shielding of the $4f$ electrons by the $5s$ and $5p$ electrons [5]. This leads to exceptionally narrow homogeneous spectral linewidths, which results in the long coherence times of the $4f^N \longrightarrow 4f^N$ transitions required for QIP. Linewidths as narrow as 100 Hz has been observed in Eu^{3+}:Y_2SiO_5 and 50 Hz in Er^{3+}:Y_2SiO_5 [6, 7]. Many lanthanide isotopes also has non-zero nuclear spins, which allows for the exploitation of the ground nuclear spin states that possesses coherence times on the order of hours.

The remainder of this chapter summarises the previous work that has been performed on lanthanide-doped insulating crystals in terms of QIP and the related crystal-field analyses that were performed to achieve such applications. Work performed on applications of such systems other than those in QIP, including the development of efficient phosphors is also explored. Finally the layout of this document is outlined, with the key chapters summarised.

1.1 Applications of lanthanide-doped crystals in quantum information processing

The experimental groundwork for applications of lanthanide-doped insulating crystals in QIP was first developed by Mossberg in the context of classical information storage [8]. This lead to the development of many successful lanthanide based optical classical memories and optical signal processing systems through the 1980s and 1990s [9–14]. Early developments in lanthanide based QIP were modeled off of the classical optical memories mentioned above. However, these early attempts required the use of photon-echo based storage schemes which are inherently noisy as the optical pulse unitised in order to rephase the state vectors also resulted in amplified spontaneous emission [9, 15, 16]. The first attempt in achieving rephasing without the use of optical pulses was in 2001 and was applied to Doppler broadened atomic gases [17]. Later this same technique was applied to lanthanide-doped crystals [18]. This technique became known as Controlled Reversible Inhomogeneous Broadening (CRIB) and has allowed for rephasing of lanthanide-doped systems without the need of optical sources, while still leaving most parameters in photon echos unchanged [19]. CRIB has been applied to Eu^{3+}:Y_2SiO_5 using an electric field as the source of inhomogeneous broadening [20], while storage efficiencies of up to 69 % has been achieved in Pr^{3+}:Y_2SiO_5 using the same technique [21]. Additional to CRIB, Atomic Frequency Combs (AFC) have been developed over the last 15 years as another method used to control dephasing in echo-based optical quantum memories [22–24]. This method utilises an ensemble of atoms with an excited state connected to two lower hyperfine states. One of the lower states is pumped in order to selectively transfer some atoms to the other lower state. The resulting large frequency span of equally spaced narrow homogeneous linewidths between the excited state and one of the lower states resembles a comb, hence the namesake. The ensemble is then exposed to an optical field that is on resonance with the transition between the excited state and lower state of interest. The optical field must have a bandwidth that spans multiple homogeneous lines of the comb while remaining less than the entire comb. As a result of the time-energy Heisenberg uncertainty relation, the entire frequency spectrum of the field is uniformly absorbed, despite the comb having gaps. The field is then stored in a coherent superposition of optical excitations across all resonant atoms in the comb. When the ensemble begins to dephase, the collective state can be re-established, resulting in a coherent re-emission of a photon similar to photon-echos. As the spacing between homogeneous peaks can be controlled, so can the coherence time of the system. Once a comb is created, however, there is no control over the time between absorption and re-emission of the photon.

Both of the aforementioned techniques rely on hyperfine state storage and so the main limiting factor is the coherence time of the hyperfine states. The key source of dephasing within lanthanide-doped insulated crystals then becomes nuclear spin-flips of the host ions, which results in fluctuating magnetic fields at the lanthanide ion. The most widely used technique in minimising this source of dephasing is the ZEro First Order Zeeman (ZEFOZ) technique, which involves determining external magnetic fields at which the electronic structure of the system becomes insensitive to small magnetic field fluctuations in any direction. The field points at which this occurs are known as ZEFOZ points, which are avoided crossings of the hyperfine levels that exists in lanthanide-doped materials. The Zeeman interaction at these points is therefore eliminated to the first order, for the particular transition of interest. In the case of non-Kramers ions such as Pr^{3+} and Eu^{3+},

these systems are already insensitive to magnetic field variations, resulting from having zero unpaired electrons, and so are ideal candidates in ZEFOZ applications. Figure 1.1 depicts an example ZEFOZ point, located in the hyperfine structure of the ground state of Eu^{3+}:Y_2SiO_5.

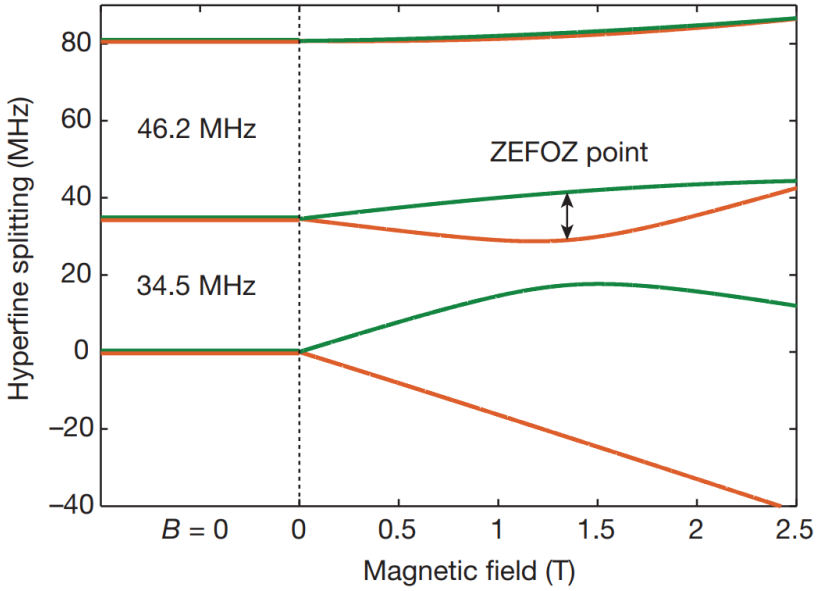

Figure 1.1: Example ZEFOZ point in Eu^{3+}:Y_2SiO_5. At a magnetic field of ∼1.3 T, applied down an appropriate direction, the gradient of the marked transition becomes very low, resulting in an insensitivity to magnetic field fluctuations. Figure is reused from [25].

Demonstrations utilising the ZEFOZ technique has resulted in observed coherence times exceeding 1 minute for Pr^{3+}:Y_2SiO_5 and 6 hours for Eu^{3+}:Y_2SiO_5 [25, 26]. These coherence times have only been observed when the systems are at or below liquid helium temperatures ($\leq$ 4.2 K), due to the negligible effect of phonon induced dephasing at these temperatures. However, a recent study has observed reasonably long coherence times for Eu^{3+}:Y_2SiO_5 above liquid helium temperatures, with the observed coherence times remaining stable between 2 K and 16 K at 25 ms, before dropping to 7 ms at 19 K and 3.3 ms at 21 K [27]. This paves the way for the possibly of QIP at higher temperatures. Although non-Kramers ions have been shown to result in the longest observed coherence times, Kramers ions, which have unpaired electrons, such as Yb^{3+}:Y_2SiO_5 and Er^{3+}:Y_2SiO_5 have shown coherence times of l ms and 1.3 ms respectively at high magnetic field strengths [28,29]. Furthermore, studies have obtained coherence times of 0.8 ms and 1.48 ms for Yb^{3+}:Y_2SiO_5 and Er^{3+}:Y_2SiO_5 respectively without the need of applying an external magnetic field [30, 31]. The ZEFOZ points used to obtain such coherence times are difficult to find experimentally but can be computationally predicted, for example, through the use of a spin Hamiltonian, which is used to model the electronic structure of a single state [32]. When a spin Hamiltonian is used in conjunction with a crystal-field Hamiltonian, the full $4f^N$ configuration, including the hyperfine, magnetic and electronic interactions can be modelled and the obtained parameter sets can be transferred between ions within the lanthanide series. The details of which are further explored in Section 1.2 and Chapter 2.

Through utilisation of the techniques outlined here, demonstrations of optical quantum memories [23,25,28,33–35], single photon sources [36], microwave-to-optical photon modulators [37,38], and quantum gate implementations [39,40] have been made. While all of these demonstration have been shown to work in a laboratory environment, the ability to transport information beyond a few hundred kilometers becomes impracticable as a result of losses due to diffraction and scattering, in both fibers and free-space [41,42]. In order to overcome this problem, a network of quantum repeaters is required to be developed, which involves performing entanglement swapping among pairs of photons at each repeater along the transmission channel [43,44]. As a pair of entangled photon are unlikely to arrive at the repeater simultaneously, the network also requires a quantum memory at be located at each repeater. These memories will store the first photon to arrive at the repeater until the second photon arrives for the entanglement swapping to take place [45].

1.2 Crystal-field analyses for low symmetry systems

Crystal-field theory is the key technique used in order to predict the full $4f^N$ electronic structure of lanthanide-doped materials and was first described by Bethe in 1929 [46]. Crystal-field theory reached maturity in the 1960s with the theoretical framework developed by Judd and Wybourne [5,47]. This framework allowed for the well known crystal-field analyses by Dieke on $LaCl_3$ [48], and Carnall on LaF_3 [49], with predictions of the energy level structure of lanthanides doped within these hosts accurate to $\sim$10 cm^{-1}. Since the 1980s, crystal-field theory has been applied to many lanthanide-doped materials including: Er^{3+}:$Y_3Al_5O_{12}$ [50], RE^{3+}:$LiYF_4$ [51], Ce^{3+}:$LuPO_4$ [52], RE^{3+}:REOCl [53] and Ho^{3+}:CaF_2 [54] among many others. Crystal field theory involves constructing an 'effective Hamiltonian' that characterises the energy levels of interest through the use of multiple sets of operators and their related parameters, with each set of operators defining a different interaction. The interactions defined are the; free-ion, crystal-field, Zeeman, and nuclear interactions, the details of which are described in Section 2.3. Through diagonalising this Hamiltonian, the energy levels of the system of interest can be obtained. Until recently, crystal-field analyses could only be performed on high symmetry systems as these systems require less parameters in order to be fully characterised, with the C_{4v} symmetry systems of REOCl and CaF_2 requiring five crystal-field parameters to fully describe, while the D_2 symmetry environment of $Y_3Al_5O_{12}$ requires nine independent crystal-field parameters [50,53,54]. Lower symmetry systems require increasingly large matrices to be diagonalised, which in turn requires an increasingly larger amount of computing power. Only in the last five years have we seen crystal-field analyses for C_1 symmetry systems, such as in the case of Er^{3+}:Y_2SiO_5. This system requires 27 independent parameters, three real and twelve of which are complex, that are required to be fitted in order to characterise the entire crystal-field interaction alone [55]. Crystal-field analyses also require a large amount of experimental data, such as electronic energy levels, in order to constrain these parameters.

In addition to the large amount of computational power required in order to perform crystal-field analysis on low symmetry system such as Y_2SiO_5, there is also a phase freedom that arises from the presence of complex crystal-field parameters. In order to constrain this phase freedom, directional data such as the magnetic response of electronic states, which varies depending on the direction of the applied magnetic field, is required

to be fitted in addition to electronic levels [56]. The key approach used to model the magnetic structure, in addition to the hyperfine structure, utilises a spin Hamiltonian. Here, the crystal-field energy levels, also known as Stark levels, are set as a constant offset and the hyperfine and magnetic structure of an individual state is then modelled. As many applications in QIP requires manipulation of the hyperfine states present in lanthanide-doped systems, which are well described by a spin Hamiltonian, this method has become the most used method in order to describe the magnetic and hyperfine interactions of such materials [32, 55, 57–62]. However, spin Hamiltonian parameters are unique to each state and therefore a different spin Hamiltonian is required to be experimentally determined for each state. When a spin Hamiltonian is used in conjunction with a crystal-field Hamiltonian, both the small scale hyperfine structure in addition to the larger scale Stark levels are able to be accurately determined.

Furthermore, not only does crystal-field theory provide an excellent prediction of the energy level structure of a particular lanthanide doped into a crystal, the determined parameters can also be used to form trends across the lanthanide series for a particular crystal. This proves to be useful in predicting the energy level structure of non-Kramers ions, as such ions often have a negligible response to applied magnetic fields, and so often lacks the directional data required to perform such an analysis. Trends have been established across the lanthanide series for systems including RE^{3+}:$Cs_2NaLnCl_6$ [43,63–66] and RE^{3+}:LaF_3 [49, 67]. The Slater parameters, related to the free-ion coulomb interaction between electrons increases across the lanthanide series. This is a result of an increasing nuclear charge across the lanthanide series, leading to a small ionic radius and greater coulomb repulsion between electrons. Likewise, the spin-orbit interaction increases across the lanthanide series, resulting from the smaller ionic radius. This can be interpreted in the classical sense as the electrons 'orbiting' around the nucleus faster as nuclear charge increases. The values for these parameters only vary by a few percent between ions in free space and their counterparts that are doped within crystals and so are largely invariant to which crystal the lanthanide is doped into [49,68]. Contrarily, the crystal-field parameters are very sensitive to the crystal-field environment that the lanthanide experiences. However, trends across the lanthanide series can still be established given a particular crystal. For RE^{3+}:$Cs_2NaLnCl_6$, it was found that both of the crystal-field parameters relevant to this system decreases linearly over the lanthanide series [43, 63–66]. For RE^{3+}:LaF_3, it was found that many of the parameters followed a different trend whether the lanthanide ion of interest is located in the first or second half of the lanthanide series [49]. A follow up study rectified these parameters trends by using the full C_2 symmetry of LaF_3 and not the approximation used by Carnall *et al.* assuming C_{2v} symmetry in order to reduce the computational power required [67].

In addition to the crystal-field model described here, a number of other models have been developed in order to determine the electronic energy levels of lanthanide-doped crystals. Of particular renown are the superposition [69,70] and exchange-charge models [71]. Both of these models calculate a number of parameters from the crystal structure of the system under investigation, with the number of parameters required to fully define a system being considerably less than their crystal-field theory counterparts. The superposition model employs as few as six parameters, while a system can be fully defined by as few as a single parameter using the exchange-charge model [72]. However, the key difficulty faced by both of these models are uncertainties in the crystal structure of the system under investigation, as substituting a lanthanide into the crystal introduces distortions

which can be difficult to accurately model [70]. Despite this, predictions of the electronic structure of Pr^{3+}:LaF_3 [73], R^{3+}:BaY_2F_8 (R = Er, Dy, Nd) [74], and Nd^{3+}:AWO_4 (A = Ca, Sr, Pb) [75], among others, have been made using the superposition model. Likewise, the exchange-charge model has been utilised in order to predict the electronic structure of, for example, Tm^{3+}:$LiYF_4$ [76], Pr^{3+}:$CsCdBr_3$ [77], and $Tb_2Ti_2O_7$ [78].

This thesis focuses on creating accurate crystal-field models for lanthanide-doped Y_2SiO_5 through the use of both crystal-field and spin Hamiltonian parameters by fitting to electronic, magnetic and hyperfine data simultaneously. This will allow for the prediction of ZEFOZ points across the lanthanide series, which then in turn could be probed in order to achieve the long coherence times required for QIP.

1.3 Additional applications of lanthanide-doped crystals

Lanthanide-doped crystals have many appealing applications besides those in QIP discussed above. In particular, such systems have been shown to be attractive materials in the development of efficient phosphors. This is a result of lanthanides possessing many optical transitions across a vast range of wavelengths from the infra-red through to the ultraviolet regions. For example, divalent europium is widely used as a blue phosphor while trivalent europium is used as a red phosphor [79, 80]. When used in conjunction with the green/yellow phosphor of trivalent terbium, trichromatic lighting is achieved, which forms the basis of much of our current display technologies. The past decade has also seen the development of white light emitting diode (WLED) technologies, which provides luminous, energy efficient, and environmentally friendly alternatives to traditional light sources such as incandescent, halogen and fluorescent lamps [81]. Commercially available WLEDs include the yellow-emitting Ce^{3+}:$Y_3Al_5O_{12}$, coupled with a blue GaN/InGaN LED chip [82–85]. However, as this system lacks emission in the red portion of the visible spectrum, the resulting light produced has a high correlated colour temperature (CCT) of >6000 K and poor colour rendering index (CRI) values of <80 [86]. This problem is overcome with the addition of red Mn^{4+} phosphors into the system, resulting in lower CCT and higher CRI values [87–89]. Additionally it has been shown that co-doping Ce^{3+} and Sm^{3+} into $CaSrSiO_4$ also produces a WLED when coupled with Eu^{2+}:Sr_2SiO_4 and an ultraviolet chip [90]. Sm^{3+} doped Y_2SiO_5 nanoparticles has also been shown to produce near white fluorescence when fluxes are introduced into the synthesis process which is applicable in the production of WLEDs [91].

The development of efficient solar cells is also an active area of research, motivated in order to provide environmentally friendly alternatives to conventional fossil-fuel electricity generation. The well established Shockley-Queisser limit states that the maximum possible single junction solar cell efficiency is limited to 33.7 % [92]. This limit arises from only a small proportion of the photons are efficiently absorbed by the solar cell. If the photon has an energy less than that of the band gap, it does not interact with the solar cell, while if the photon has an energy significantly greater than the band gap, then this surplus energy is lost as heat. In order to overcome this problem, many studies have been performed in order to use up-conversion and down-conversion possesses to further increase the efficiency of solar cells, converting either ultraviolet or infrared photons into visible photons which are more efficiently absorbed by solar cells. Up-conversion from

Yb^{3+},Er^{3+}-co-doped-Y_2SiO_5 has been observed, with 980 nm photons being up-converted into the visible, with fluorescence being observed at quantum efficiencies of 87 % and 55 % for red and green light respectively [93]. Tb^{3+}:Y_2SiO_5 has been demonstrated to down-convert from the ultraviolet at 248 nm to green light at 544 nm [94]. Down-converting Eu^{3+}:Sr_2CeO_4 also has been shown to increase the power conversion efficiency of perovskite solar cells by 14.15 % [95]. Additionally, work has been performed in increasing the efficiency of photochromic smart windows though the use of up-conversion. When a photochromic smart window is exposed to ultraviolet light, the window becomes opaque, and when the window is exposed to visible light, it becomes transparent once again. Such windows have applications in reducing building energy consumption through maintaining a homeostatic temperature within the building. Pr^{3+}:Y_2SiO_5 has been shown to increase the colouration rate of a photochromic $H_3PW_{12}O_{40}$ film by a factor of 7 through up-conversion of visible 505 nm light to ultraviolet light at 270 nm – 380 nm [96].

Central to improving the efficiency of the above applications is a detailed understanding of the underlying non-radiative energy transfer mechanisms between the lanthanide ions doped into these materials. For energy transfer to occur, the ions of interest typically have to be located close to each other spatially in addition to having energy levels that are close to each other, or close to integer multiples of each each in the case of up- and down-conversion. This allows for energy to be transferred non-radiatively from a so called 'donor' ion to an 'acceptor' ion, where the acceptor ion then relaxes radiatively and fluorescence can be monitored. The theory of energy transfer was first developed in the 1940s and 1950s by Förster and Dexter [97, 98]. Förster Resonant Energy Transfer (FRET) involves dipole-dipole coupling between the electronic states of the donor and acceptor. For FRET to proceed, the donor and acceptor energy states must have spectral overlap and the distance scales involved must be very small, $\mathcal{O}(10$ Å), due to such an interaction being inversely proportional to the sixth power of the donor-acceptor separation. If there is no spectral overlap between the electronic states, that is if the electronic states are well separated in terms of energy, then energy transfer can only take place with the assistance of phonons. Phonon-assisted energy transfer occurs if the difference in energy of the electronic states correspond to the energy distribution of the phonons, the so called phonon density of states, of the host material in question [99]. As phonons are lattice vibrations of the host material, the possible phonon energies and therefore the possible phonon-assisted energy transfer pathways are dependent on the crystal under investigation. Different interactions other than the dipole-dipole interaction can also be involved. Higher order interactions include the dipole-quadrupole and quadrupole-quadrupole interactions, which have higher order $\frac{1}{r^8}$ and $\frac{1}{r^{10}}$ separation dependencies respectively. This makes these higher order interactions more sensitive to donor-acceptor separation and so are only significant on separation scales <10 Å. Dexter electron transfer, which is also known as the exchange mechanism, involves transferring the excited electron from the donor to the acceptor. This interaction requires wavefunction overlap between the donor and acceptor making it another very short scale interaction on separation scales <10 Å.

Non-radiative energy transfer typically occurs on time scales of ns to a few μs. This is much less than the fluorescence lifetimes of most lanthanides, which often occurs on time scales of a few ms, resulting in a fast decay in the time evolution of the fluorescence, followed by another much longer decay. As lanthanide ions doped within a crystal are located at discrete distances from each other, early attempts at developing a model to fit to fluorescence transients, which assumes a continuous random distribution of acceptors

around a donor, proved to be unsuitable. A well known example is the model by Inokuti and Hirayama, developed in the 1960s, which fits to fluorescence transients utilising a multipole interaction in order to determine an average florescence lifetime [100]. This discrepancy was rectified in the 1990s by Vasquez and Flint with the development of a 'shell model' [101]. In this model acceptors are randomly placed around a donor at discrete distances in nearest neighbour, next nearest neighbours, and so on, shells. This model allows for the radiative rates of isolated ions and an average energy transfer rate of donor-acceptor pairs to be determined. While the shell model does an excellent job in modeling higher symmetry systems, it becomes increasingly difficult to apply to lower symmetry systems [102, 103]. This is a result of the models dependence on a so called 'occupancy factor', which is the statistical probability of having r_n electrons in the nth shell. For low symmetry systems, which has an increasingly large number of different possible acceptor distributions, the required computational requirements therefore becomes increasingly more intensive. In this thesis I will instead fit to the fluorescence transients using Monte-Carlo methods where a random distribution of acceptors around a single donor at a given concentration is simulated [104, 105]. The details of which will be further discussed in Section 2.6. The key advantage of such an approach is the unit cell is the only input needed to model the system and so greatly simplifies the computational requirements while still remaining physically accurate.

1.4 Thesis outline

Chapter 2 introduces the $4f^N$ electronic structure of lanthanide-doped Y_2SiO_5 and the formalisms used to accurately model this electronic structure, in addition to quantifying the energy transfer dynamics present within such materials. Furthermore, I will outline the algorithms and code used in order to fit to experimental data, required to provide an accurate crystal-field model of the C_1 point group symmetry sites of lanthanide-doped Y_2SiO_5. Chapter 3 details the lanthanide-doped Y_2SiO_5 samples analysed in this study in addition to the experimental setups used in order to perform various spectroscopic investigations. In particular I outline the components used in temperature dependent absorption, Zeeman, fluorescence and Raman heterodyne spectroscopy.

Using these spectroscopic techniques, Chapters 4 - 6 are largely experimental chapters focusing on crystal-field modelling and quantifying the energy transfer in lanthanide-doped Y_2SiO_5. The key results of this thesis are presented in Chapter 4 where I developed a comprehensive crystal-field model for the $4f^5$ configuration of Sm^{3+}:Y_2SiO_5 through the use of Zeeman, Raman-heterodyne, and fluorescence spectroscopy in addition to the theoretical work of fitting this experimental data using the outlined algorithms. Chapter 5 models the energy-transfer dynamics of our Sm^{3+}:Y_2SiO_5 sample through the use of Monte-Carlo methods and fitting to obtained fluorescence spectra. Chapter 6 aims to continue the work of Horvath to further develop his crystal-field model on the $4f^{11}$ configuration of Er^{3+}:Y_2SiO_5 through the addition of electronic data and g values, obtained by utilising temperature dependent absorption spectroscopy and Zeeman spectroscopy respectively [55, 106]. Finally Chapter 7 takes the crystal-field parameters found for Sm^{3+}:Y_2SiO_5, and through appropriate scaling, uses the crystal-field parameters to model the hyperfine structure of $4f^6$ configuration of Eu^{3+}:Y_2SiO_5.

Chapter 2

Modelling the $4f^N$ structure and dynamics of lanthanide-doped Y_2SiO_5

2.1 Crystal structure of Y_2SiO_5

Spin-flips of the host ions, which results in magnetic field fluctuations, is the major cause of dephasing within a lanthanide-doped material. Therefore, Y_2SiO_5 is an ideal host for lanthanide ions in the realisation of QIP devices, due to the host ions having near zero nuclear spins. Almost 100 % of naturally occurring oxygen and silicon have zero nuclear spin and the only naturally occurring isotope of yttrium, ^{89}Y, has a nuclear spin of $\frac{1}{2}$. The minimisation of spin-flips has allowed lanthanide-doped Y_2SiO_5 to be observed to have the narrowest linewidths, 50 Hz in $Er^{3+}Y_2SiO_5$, and the longest coherence times ever seen in any material, over 1 minute for $Pr^{3+}Y_2SiO_5$ and 6 hours for $Eu^{3+}Y_2SiO_5$ [7, 25, 26].

Y_2SiO_5 is a monoclinic silicate crystal with space group C_{2h}^6 [107]. The lattice constants of Y_2SiO_5 are: $a = 10.4103$ Å, $b = 6.7212$ Å, $c = 12.4905$ Å, and $\beta = 102°39'$. Here the crystallographic b axis corresponds to the C_2 rotation axis and the crystallographic a and c axes are located in the mirror plane which is perpendicular to the crystallographic b axis. Y_2SiO_5 contains two substitutional Y^{3+} sites, Y_1 and Y_2, which will henceforth be labelled as site 1 and site 2. Both of these sites have point group C_1, or no symmetry, and are distinguished by their co-ordination numbers of six and seven respectively. A schematic of the crystal structure of Y_2SiO_5 is given in Figure 2.1. Throughout this thesis I focus on the X_2 phase of Y_2SiO_5, which is described above.

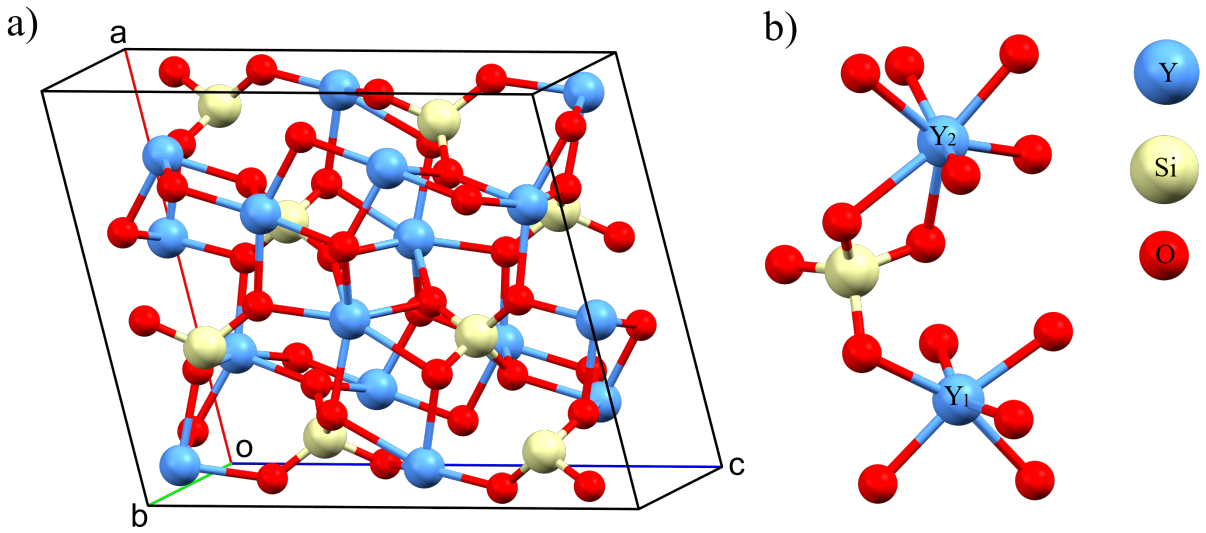

Figure 2.1: Crystal structure of Y_2SiO_5. a) Depicts the unit cell of Y_2SiO_5 with the crystallographic axes labeled. The origin is denoted with an 'o'. b) Depicts the six and seven co-ordinate sites of Y_2SiO_5, labeled as Y_1 and Y_2 respectively.

Following the convention of Li *et al.* we define the optical extinction axes as D_1 and D_2, which are located in the *a*-*c* mirror plane and are perpendicular to each other in addition to the crystallographic *b* axis [108]. The orientation of the crystallographic axes in relation to the extinction axes are given in Figure 2.2. Throughout this thesis we will refer to the extinction axes when interpreting orientational data.

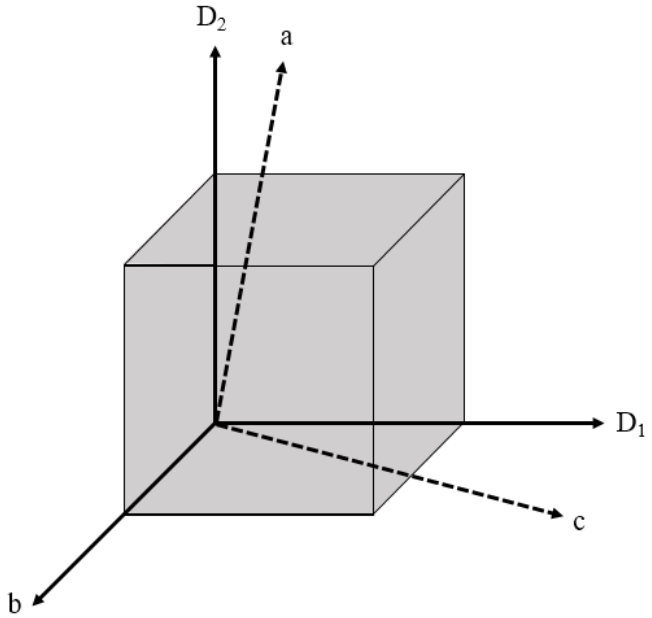

Figure 2.2: Crystallographic and extinction axes of Y_2SiO_5. The D_1 axis is 23.8° from the *c* axis and 78.7° from the *a* axis. The D_1, D_2 and C_2 (labeled as b) axes are perpendicular to each other.

In Y_2SiO_5, trivalent lanthanide ions substitute for the Y^{3+} cation without the need for additional charge compensation, due to both ions carrying the same charge. Ionic radii decreases across the lanthanide series, due to a larger nuclear charge. This results in ions near the end of the series substituting evenly between the two crystallographic sites, whereas ions near the beginning of the series prefer to substitute into site 2. Table 2.1 shows the ionic radii in the co-ordination sites of key ions investigated in this study. Lanthanides near to the start of the series tend to have higher populations in site 2, leading to more prominent spectral features for site 2 while lanthanides near to the end of the series tend to have more balanced populations and therefore balanced spectral features between the two sites.

Table 2.1: Ionic radii, in angstroms, of key ions investigated in this study [109].

Ion	6 co-ordinate (site 1)	7 co-ordinate (site 2)
Y^{3+}	1.04	1.10
Sm^{3+}	1.10	1.16
Er^{3+}	1.03	1.09

Additionally, each site of Y_2SiO_5 also contains two orientations, which arises from the C_{2h} symmetry of the unit cell. These two orientations are related by a 180° rotational symmetry and can be distinguished with the application of a magnetic field. This is particularly relevant in terms of Zeeman studies as lanthanides doped into the two orientations respond differently when a magnetic field is applied outside of the D_1-D_2 plane or the b axis [110].

2.2 Electronic structure of the lanthanide ions

The lanthanide series is comprised of the 15 elements ranging from lanthanum (atomic number $Z = 57$) to lutetium ($Z = 71$) which feature a progressive filling of the $4f$ orbital. As the nuclear charge, Ze, increases across the lanthanide series, so does the potential seen by $4f$ electrons. The resulting decrease in atomic radius as nuclear charge increases is known as lanthanide contraction [5]. The radial component of the valence $4f$ orbital wavefunctions are less than that of the closed $5s$ and $5p$ orbitals, resulting in the $4f$ electrons being shielded from the electric field of the environment of the host material [111]. This leads to the sharp $4f^N \longrightarrow 4f^N$ transitions frequently attributed to triply ionised lanthanide-doped materials. This study focuses on lanthanides which have had their outer $6s$ and $5d$ electrons, in addition to a maximum of one $4f$ electrons removed. The electronic configuration of triply ionised lanthanides is $[Xe]4f^N$ ($[Xe] = 1s^2 2s^2 2p^6 3s^2 3p^6 3d^{10} 4s^2 4p^6 4d^{10} 5s^2 5p^6$), where N increases from 1 (for cerium) up to 14 (for lutetium). Most spectroscopic studies of triply ionised lanthanide-doped systems tend to exclude lanthanum and lutetium as they have empty and full $4f$ orbitals respectively and therefore are optically inert.

The spectra of triply ionised lanthanide ions is dominated by the effects of the coulomb and spin-orbit interactions. Coulombic repulsion between $4f$ electrons splits the energies of the $4f^N$ configuration into multiple terms separated by approximately 10 000 cm^{-1}. Due to Ce^{3+} and Yb^{3+} having a single $4f$ electron and hole respectively, the coulomb interaction does not apply to either of these ions. The spin-orbit interaction is a relativistic coupling of the $4f$ electrons spin and orbital angular momenta. This splits these terms

into $2J+1$ levels separated on the order of 1000 cm^{-1}. These levels are called multiplets and following the conventions of Dieke *et al.* are labelled using the $^{2S+1}L_J$ notation [112]. Here S is the total spin angular momentum, L is the total orbital angular momentum and J is the total angular momentum. It should be noted that L follows the historic convention of using the spectroscopic letter notation; that is, $L = 0, 1, 2, 3, \ldots$ is denoted by S, P, D, F, ... respectively.

When a lanthanide ion is doped into a crystal it is subjected to the potential of the local crystal environment. This further splits up each multiplet into a number of Stark levels on the order of 100 cm^{-1}. The number of Stark levels each multiplet splits up into is dependent on the site symmetries of the crystal. To fully remove all degeneracy within the electronic energy level structure, the ions must be subjected to C_1 symmetry, within the crystal. If the ion of interest has an odd number of electrons, the crystal-field environment can only remove the degeneracy up to a maximum of a number of doubly degenerate Kramers sates. In order to remove all degeneracy, the ion must also be subjected to an external magnetic field.

Further interactions consist of; relativistic corrections, inter-configurational effects, magnetic effects, and the hyperfine interaction. The hyperfine interaction arises from the coupling of the electronic and nuclear angular momenta. This interaction splits each Stark level by an amount on the order of 0.1 cm^{-1} into $(2I+1)$ states, where I is the nuclear spin. The hyperfine interaction is therefore only present in isotopes that have a non-zero nuclear spin. To account for these interactions the following Hamiltonian is used to model the complete $4f^N$ configuration:

$$H = H_{FI} + H_{CF} + H_Z + H_{NZ} + H_{HF} + H_Q \tag{2.1}$$

Here H_{FI} is the free-ion Hamiltonian, which includes the coulomb and spin-orbit interactions among other higher order effects. H_{CF} is the crystal-field Hamiltonian. H_Z and H_{NZ} are the electronic and nuclear Zeeman Hamiltonians respectively. Lastly, H_{HF} and H_Q are the nuclear dipole hyperfine and nuclear quadrupole Hamiltonian's respectively. The exact mathematical details will be discussed later in Section 2.3. These splittings are represented schematically in Figure 2.3.

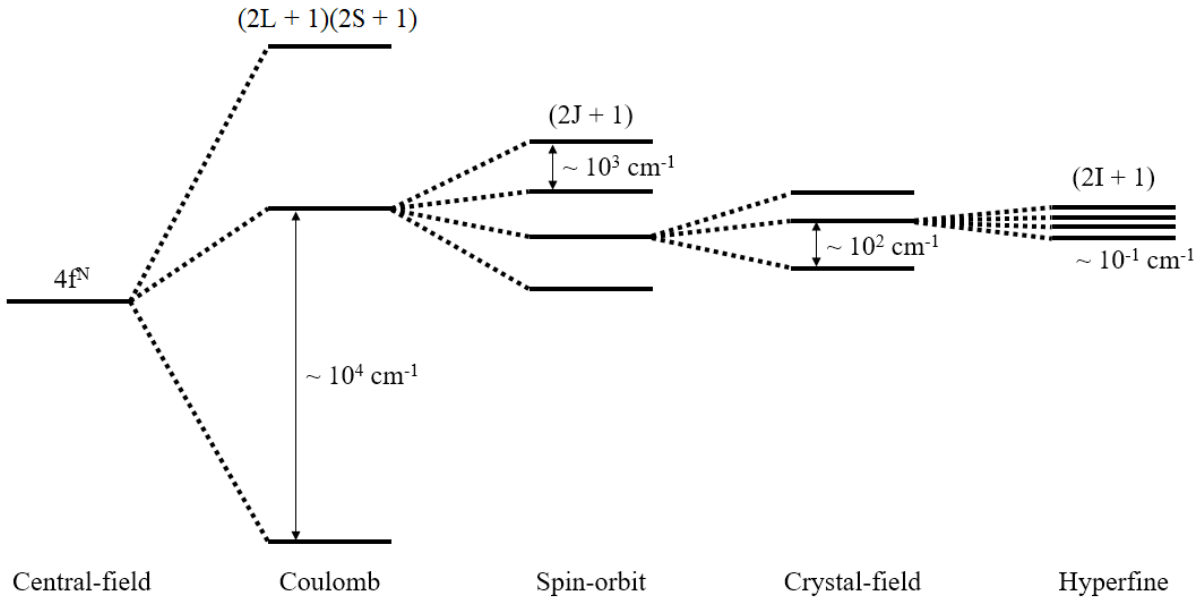

Figure 2.3: Energy splitting diagram of lanthanide ions due to the various interactions. The degeneracy of each interaction is labelled. The degeneracy of the crystal-field interaction is dependent on the point-group site symmetries and is therefore not shown.

Due to the shielding of the $4f$ electrons due the $5s$ and $5p$ electrons, the crystal-field interaction is small relative to the coulomb and spin-orbit interactions. This allows trends across the lanthanide series to be established. The splittings of the $^{2S+1}L_J$ multiplets across the lanthanide series is represented in what is known as a 'Dieke Diagram' [112]. The original diagram, created by Dieke in 1963 shows the energy level structure across the lanthanide series in $LaCl_3$ up to 40 000 cm^{-1}, with with notable exception of promethium owing to the nuclear instability of this element [112]. The work done by Dieke was extended by Carnall *et al.* in 1989 to include the energy level structure up to 50 000 cm^{-1} and to include promethium also in $LaCl_3$ [49]. Further work, performed by Wegh *et al.* in 2000, was undertaken to extend the observed energy level structure up to 70 000 cm^{-1} for many lanthanide-doped $LiYF_4$ systems [113]. An adaptation of this diagram is given in Figure 2.4. While both of these studies were performed using $LaCl_3$, the general trends hold true for any material and therefore the Dieke diagram is an invaluable tool in spectroscopic studies of triply ionised lanthanide-doped systems.

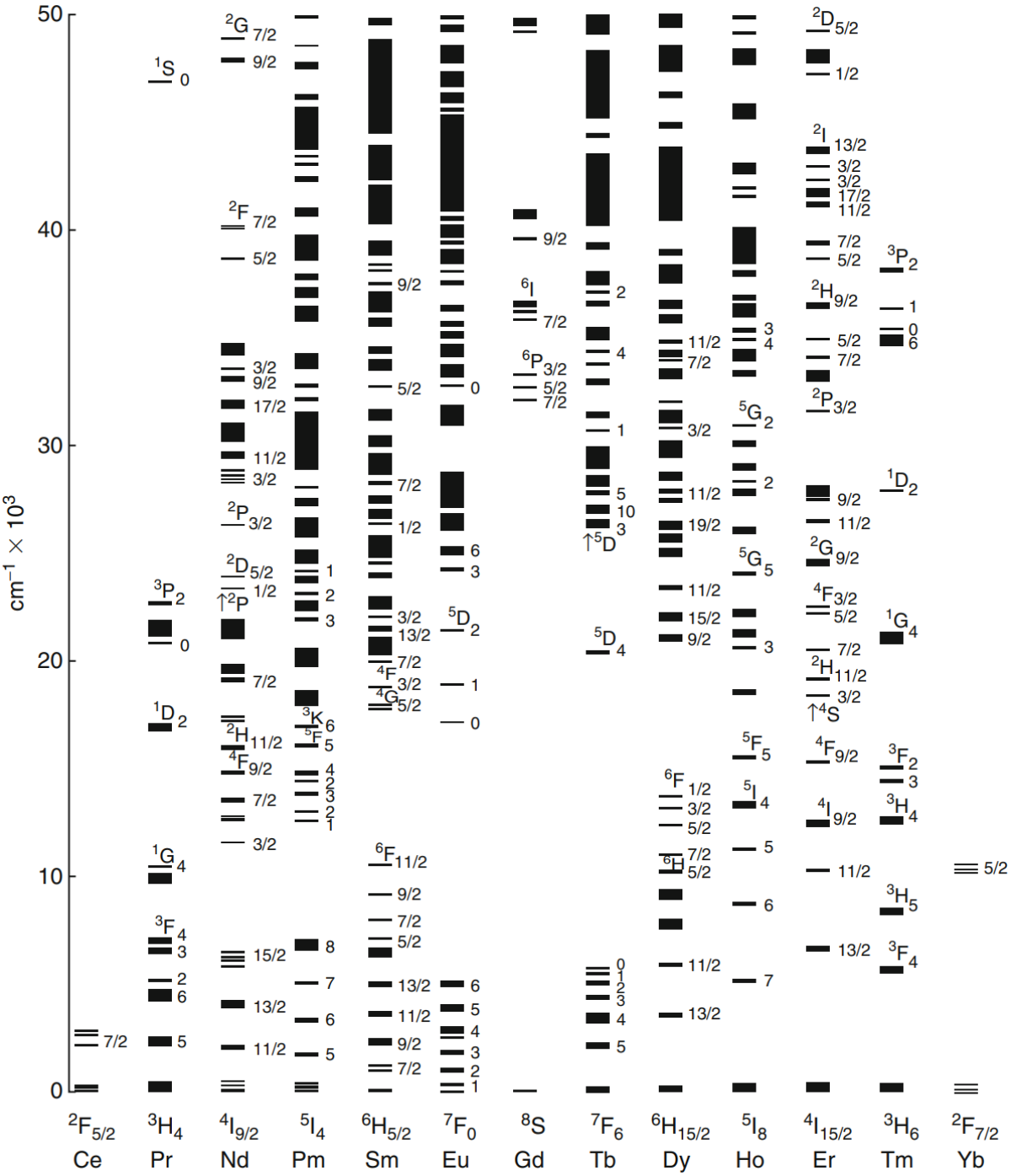

Figure 2.4: Energy level diagram of triply ionised lanthanides, up to 50 000 cm^{-1}. Figure is reused from [114].

2.3 Crystal-field theory

The aim of any crystal-field analysis is to accurately model the electronic structure of a given material through the use of a Hamiltonian operator. When the Hamiltonian operators acts upon the system, the energy eigenvalues of the entire system can be obtained. Consider the following full Hamiltonian equation:

$$H\left|a\right\rangle = E\left|a\right\rangle \tag{2.2}$$

H is the full Hamiltonian which when it acts on system, $|a\rangle$, it produces the eigenvalues, E, of the entire system. The key difficultly faced in the use of a full Hamiltonian that characterises the complete electronic structure of the entire system is the unachievable amount of computing power required to model the system. Instead an 'effective Hamiltonian' is employed that describes only a portion of the full electronic structure of a material, however, still gives identical eigenvalues for this portion. In the case of triply ionised lanthanide-doped materials, the effective Hamiltonian we are interested in is one that describes the $4f^N$ configuration intrinsic to these materials. Such a Hamiltonian is typically given as:

$$H_{\text{eff}}\left|\alpha SLJM\right\rangle = E_{4f}\left|\alpha SLJM\right\rangle \tag{2.3}$$

Here, an effective Hamiltonian, H_{eff}, acts on the $4f^N$ configuration of the system represented by the quantum numbers S, L, J and M (α represents the rest of the system not relating to the $4f^N$ configuration) and E_{4f} are the eigenvalues corresponding to the $4f^N$ configuration with $E_{4f} \subset E$.

We now will outline the formalisms applied in order to define the effective Hamiltonian used to accurately model the $4f^N$ configuration of lanthanide-doped crystalline systems. For a more rigorous derivation of the crystal-field and spin Hamiltonian formalisms, the reader is directed to the established literature in the field. For a general overview of the quantum mechanical operations and group theory representations, Wybourne, Weissbluth and Judd provide excellent resources [47, 115, 116]. Liu is an invaluable modern resource to crystal field modelling while Macfarlane details how spin Hamiltonians can be applied to spectroscopy of lanthanides [111, 117].

2.3.1 Free-ion Hamiltonian

Following Liu, for an N electron atom in free space, the relativistic Hamiltonian that is used to model a point charge nucleus with atomic number Z is given as [117]:

$$H_0 = \sum_{i=1}^{N}\left[\frac{-\hbar^2}{2m}\nabla_i^2 - \frac{Ze^2}{r_i} + \xi(r_i)(s\cdot l)_i\right] + \sum_{i<j}^{N}\frac{e^2}{r_{ij}} \tag{2.4}$$

The first term represents the kinetic energy of the ith electron with mass m whilst the second term represents the coulomb potential energy seen by the electron due to the nucleus located at a radial distance, r_i, from the nucleus. The third term is the spin-orbit interaction, which depends on the electrons spin, s, and orbital, l, angular momenta, in

addition to the spin-orbit coupling constant, $\xi(r_i)$, which depends on r_i. The final term describes coulomb repulsion between pairs of electrons separated by a distance r_{ij}. An exact solution to the Schrödinger equation is not possible for systems with more than one electron as we can not use the traditional methods of separation of variables as the final term in Equation (2.4) depends on the co-ordinates of both the ith and jth electrons. To overcome this we assume that each electron can move independently of each other and that the potential seen by each electron due to the other electrons is composed of a spherically average potential field. The central-field approximation is defined as:

$$H_0' = \sum_{i=1}^{N} \left[\frac{-\hbar^2}{2m} \nabla_i^2 + U(r_i) \right] \tag{2.5}$$

Where

$$\sum_{i=1}^{N} U(r_i) = -\sum_{i=1}^{N} \frac{Ze^2}{r_i} + \left\langle \sum_{i<j}^{N} \frac{e^2}{r_{ij}} \right\rangle \tag{2.6}$$

The second term in Equation (2.6) is the spherically averaged repulsion due to the electrons. The solutions of such a central field approximation are analogous to hydrogen with a single electron within a central potential. The spherically symmetric contributions of coulomb electron repulsion are described by Equation (2.6) and any remaining coulomb electron repulsion is small enough such that it can be defined by the following coulomb perturbation Hamiltonian:

$$H_C = \sum_{i<j}^{N} \frac{e^2}{r_{ij}} - \left\langle \sum_{i<j}^{N} \frac{e^2}{r_{ij}} \right\rangle \tag{2.7}$$

Likewise the spin-orbit interaction is small enough to be considered as a perturbation of the central field Hamiltonian and therefore can be defined by the following spin-orbit perturbation Hamiltonian:

$$H_{SO} = \sum_{i=1}^{N} \xi(r_i)(s \cdot l)_i \tag{2.8}$$

We can now redefine Equation (2.4) in terms of Equations (2.5), (2.7) and (2.8) to obtain:

$$H_0 = H_0' + H_C + H_{SO} \tag{2.9}$$

With the main contributions of H_0 deriving from H_0' with H_C and H_{SO} acting as perturbations of H_0'. We can now proceed by solving the following eigenvalue equation for the central-field Hamiltonian:

$$H_0' \Psi_0 = E_0 \Psi_0 \tag{2.10}$$

Where Ψ_0 are now the separable eigenfunctions of the system and can be separated following:

$$\Psi_0 = \prod_{i=1}^{N} \psi_i(nlm_l m_s) \tag{2.11}$$

and

$$E_0 = \sum_{i=1}^{N} \epsilon_i(nlm_l m_s) \tag{2.12}$$

Here n, l, m_l and m_s are the four quantum numbers that define bound electrons. The quantum numbers for the $4f^N$ configuration of lanthanides, which is a direct result of the Pauli exclusion principle, are given in Table 2.2.

Table 2.2: Quantum numbers of the $4f^N$ configuration of lanthanides.

n	l	m_l	m_s
4	3	-3, -2, -1, 0, 1, 2, 3	-1/2, 1/2

Applying Equations (2.11) and (2.12) to Equation (2.10) leads to N separable equations which has the following form:

$$\left[\frac{-\hbar^2}{2m}\nabla^2 + U(r)\right]\psi(nlm_l m_s) = \epsilon(nlm_l m_s)\psi(nlm_l m_s) \tag{2.13}$$

Equation (2.13) is analogous to the Schrödinger equation for hydrogen and as such we can use separation of variables to express the wave functions given in as a product of the radial and angular functions of the spherical harmonics multiplied by a two-component spinor:

$$\psi_{\lambda_i}(r, \theta, \phi) = \frac{R_{nl}}{r} Y_{lml}(\theta, \phi)\xi(s, m_s) \tag{2.14}$$

Here λ_i is a particular set of the four quantum numbers for the ith electron chosen from Table 2.2. R_{nl} is the radial function which depends on the central field potential. $\xi(s, m_s)$ is the two-component spinor which account for the two m_s spin projections given in Table 2.2. Finally, $Y_{lm}(\theta, \phi)$ are the spherical harmonic functions which describes the angular dependence of the wave functions and are identical to that of hydrogen:

$$Y_{lm}(\theta, \phi) = (-1)^m \left[\frac{(2l+1)(l-m)!}{4\pi(l+m)!}\right]^{\frac{1}{2}} P_l^m[\cos(\theta)]e^{im\phi} \tag{2.15}$$

Where the Legendre polynomials, $P_l^m(x)$, are evaluated as following:

$$P_l^m(x) = \frac{(1-x^2)^{\frac{1}{2}m}}{2^l l!}\frac{d^{l+m}}{dx^{l+m}}(x^2-1)^l \tag{2.16}$$

Finally, the individual electron wave functions, ψ_i, can be assembled into the central field wave function for N-electrons and are expressed as a Slater determinant:

$$\Psi(\lambda_1, \lambda_2, \ldots, \lambda_N) = \frac{1}{\sqrt{N!}} \begin{vmatrix} \psi_1(\lambda_1) & \psi_2(\lambda_1) & \cdots & \psi_N(\lambda_1) \\ \psi_1(\lambda_2) & \psi_2(\lambda_2) & \cdots & \psi_N(\lambda_2) \\ \vdots & \vdots & \ddots & \vdots \\ \psi_1(\lambda_N) & \psi_2(\lambda_N) & \cdots & \psi_N(\lambda_N) \end{vmatrix} \tag{2.17}$$

Thus we have solved the zero-order central potential of the $4f^N$ configuration. Next we turn to solving the perturbations on the central potential due to the coulomb interaction between electron pairs in addition to the spin orbit interaction.

In order to construct wave functions for the perturbation Hamiltonians, H_C and H_{SO}, we are required to define a coupling scheme of momentum summation. The two most common coupling schemes are the Russell-Saunders, or LS coupling scheme and the $j-j$ coupling scheme. The LS coupling scheme is used for lighter atoms as the spin-orbit interaction tends to be much smaller than the electrostatic interaction between electrons. This makes L and S good quantum numbers. As Z increases, the electrostatic repulsion between electrons decreases and the spin-orbit interactions becomes increasingly more important. Thus in heavier atoms the $j-j$ coupling scheme is preferred. In the case of lanthanide ions, the coulomb and spin orbit interactions have a similar order of magnitude, so neither coupling schemes are appropriate. Therefore, to calculate the matrix elements of the H_C and H_{SO} Hamiltonians we must develop a new coupling scheme. This new scheme, known as the intermediate coupling scheme, we will develop from the LS scheme.

For LS coupling, the orbital and spin angular momenta of the individual electrons are summed separately such that:

$$\mathbf{L} = \sum_{i=1}^{N} \mathbf{l}_i, \qquad \mathbf{S} = \sum_{i=1}^{N} \mathbf{s}_i \tag{2.18}$$

Here, $\mathbf{L}$ and $\mathbf{S}$ are the orbital and spin angular momenta operators respectively and are further summed to give the total angular momentum operator:

$$\mathbf{J} = \mathbf{L} + \mathbf{S} \tag{2.19}$$

As shown by Weissbluth we see that the angular momenta operators form the following commutation relations with the coulomb interaction Hamiltonian [116]:

$$[H_C, \mathbf{L}] = 0, \qquad [H_C, \mathbf{S}] = 0, \qquad \text{and} \qquad [H_C, \mathbf{J}] = 0 \tag{2.20}$$

Whereas the spin-orbit Hamiltonian forms the following commutation relations with the angular momenta operators:

$$[H_{SO}, \mathbf{L}] \neq 0, \qquad [H_{SO}, \mathbf{S}] \neq 0, \qquad \text{and} \qquad [H_{SO}, \mathbf{J}] = 0 \tag{2.21}$$

We see that the spin-orbit interaction breaks the symmetry of the LS coupling scheme. This means the L and S are not good quantum numbers while J and M still are. Thus thorough diagonalising the H_C and H_{SO} Hamiltonians in the LS coupling basis one obtains new eigenvectors which are linear combinations of the LS basis sets. These eigenvectors are known as the free-ion wave functions in the intermediate coupling scheme and are expressed as:

$$\mathbf{\Psi}(nlJ) = \sum_{\tau LS} a_{\tau LSJ} \left| nl\tau LSJ \right\rangle \tag{2.22}$$

Where the coefficients $a_{\tau LSJ}$ are determined by the matrix elements:

$$a_{\tau LSJ} = \sum_{\tau' L' S'} \left\langle nl\tau LSJ \right| H_C + H_{SO} \left| nl\tau' L' S' J' \right\rangle \delta_{JJ'} \tag{2.23}$$

Here we have introduced an additional quantum number, τ, which is called the seniority number and is used to distinguish states that have the same L and S quantum numbers.

Now that we have developed a basis for H_C and H_{SO}, we can set about determining the matrix elements of these Hamiltonians. First we will consider the coulomb Hamiltonian, H_C. Using the central field approximation, the orbital electronic wave functions can be separated into a products of radial and angular parts as shown in Equation (2.14). As such, the $\frac{1}{r_{ij}}$ term in Equation (2.7) can also be expressed in this form:

$$\frac{1}{r_{ij}} = \sum_{k=0}^{\infty} \frac{r_<^k}{r_>^{k+l}} \left(\mathbf{C}_i^{(k)} \cdot \mathbf{C}_j^{(k)} \right) \tag{2.24}$$

Where $r_<$ is the distance from the nucleus to a near electron and $r_>$ the distance from the nucleus to a further electron. $C_i^{(k)}$ are the spherical tensor operators, with the subscript i indicating that it is a function of the ith electron. The spherical tensor operators are related to the spherical harmonics, defined in Equation (2.15), following:

$$C_q^{(k)} = \sqrt{\frac{4\pi}{2k+1}} Y_{kq}(\theta, \phi) \tag{2.25}$$

From this, for N equivalent electrons in orbital nl, the matrix elements of the coulomb interaction Hamiltonian can be calculated as:

$$\left\langle l^N \tau LS \right| H_C \left| l^N \tau LS \right\rangle = \sum_k f_k(l,l) F^k(nl,nl) \tag{2.26}$$

Here $F^k(nl,nl)$ is the radial part of the electrostatic interaction and for $k = 0, 2, 4, 6$, are the Slater radial integrals defined as:

$$F^k(nl,nl) = e^2 \int_0^\infty \int_0^\infty \frac{r_<^k}{r_>^{k+l}} [R_{nl}(r_i)]^2 [R_{nl}(r_j)]^2 dr_i dr_j \tag{2.27}$$

The values of F^k may be determined using the Hartree-Fock method, however, in practice they are determined experimentally. The angular part of Equation (2.26) is defined as:

$$\begin{aligned} f_k(l,l) = \frac{1}{2}(2l+1)^2 \begin{pmatrix} l & k & l \\ 0 & 0 & 0 \end{pmatrix}^2 \\ \times \left[\frac{1}{2L+1} \sum_{\tau' L'} \left| \left\langle l^N \tau L S \right| \left| \mathbf{U}^{(k)} \right| \left| l^N \tau' L' S' \right\rangle \right|^2 - \frac{N}{2l+1} \right] \end{aligned} \tag{2.28}$$

Where $(\cdots)$ are the 3-j symbols which were determined by Edmonds [118]. $\mathbf{U}^{(k)}$ is the unit tensor operator and the reduced matrix elements of such have been compiled by Nielson and Koster [119].

We have now determined the matrix elements of the coulomb Hamiltonian, we will now do the same for the spin-orbit Hamiltonian. Following the same methods as Equation (2.26) the matrix elements of H_{SO} can also be split into radial and angular components:

$$\left\langle nl^N \tau L S J M \right| H_{SO} \left| nl^N \tau' L' S' J' M' \right\rangle = \zeta_{nl} A_{SO}(nl) \tag{2.29}$$

The radial component, ζ_{nl}, is known as the spin-orbit interaction parameter and is defined as:

$$\zeta_{nl} = \int_0^\infty [R_{nl}(r)]^2 \xi(r) dr \tag{2.30}$$

Like the Slater radial integrals, the spin-orbit interaction parameter can be determined using the Hartree-Fock method but instead is also determined experimentally. The matrix elements in Equation (2.29) can be expressed as:

$$\begin{aligned} A_{SO}(nl) = (-1)^{L+S'+J} \sqrt{(2l+1)(l+1)} \delta_{JJ'} \delta_{MM'} \begin{Bmatrix} L & S & J \\ S' & L' & 1 \end{Bmatrix} \\ \times \left\langle \tau L S \right| \left| \mathbf{V}^{(11)} \right| \left| \tau' L' S' \right\rangle \end{aligned} \tag{2.31}$$

Here $\{\cdots\}$ are the 6-j symbols, determined by Edmonds [118]. We have successfully derived expressions for the eigenvectors of the free-ion Hamiltonian expressed in Equation (2.9), however, there are higher order perturbations that have been neglected. The full free-ion Hamiltonian can therefore be expressed as:

$$\begin{aligned} H_{FI} = E_0 + \sum_{k=0,2,4,6} F^k f_k + \zeta_{nl} A_{SO}(nl) + \alpha L(L+1) + \beta G(G_2) + \gamma G(R_7) \\ + \sum_{i=2,3,4,6,7,8} T^i t_i + \sum_{i=0,2,4} M^i m_i + \sum_{i=2,4,6} P^i p_i \end{aligned} \tag{2.32}$$

Here α, β and γ are the two-body parameters (Trees parameters) associated with $G(G_2)$ and $G(R_7)$, which themselves are the Casimir operators for the groups G_2 and R_7. For

lanthanides with $N \geq 3$, a three body interaction term is introduced with T^i as the parameters (Judd parameters) pertaining to the three-particle operators t_i. Higher order spin effects such as the spin-spin and spin-other-orbit interactions are described by the Marvin integrals, M^i, and the related operators m_i. Finally two-body operators are introduced to account for electrostatically correlated magnetic interactions. This effect is represented by the effective operators p_i and the related parameters P^i.

2.3.2 Crystal-field Hamiltonian

While the free-ion Hamiltonian is spherically symmetric, this symmetry is reduced with the introduction of the lanthanide ion into a crystalline lattice, resulting in some if not all of the remaining $2J + 1$ electronic degeneracy being removed. The potential of the host material causes the splitting of the free-ion levels and the symmetry dictates the degree to which the remaining degeneracy is removed.

This section will mathematically describe the effect of a crystalline host, such as Y_2SiO_5, on the electronic structure of the $4f^N$ configuration of lanthanides. For lanthanides, the crystal-field is generally smaller than that of the coulomb or spin-orbit interactions, and as such can be treated as a perturbation of the free-ion states. Following Wybourne, the crystal-field potential may be defined as [115]:

$$H_{CF} = \sum_{k,q,i} B_q^k C_q^{(k)}(i) \tag{2.33}$$

Here i represents a summation over all $4f^N$ electrons. B_q^k are the crystal-field parameters and $C_q^{(k)}$ are the spherical tensor operators described in Equation (2.25). The allowed values for k and q depend on the site symmetry of the host and for the C_1 site symmetry of Y_2SiO_5, $k = 2, 4, 6$ and $|q| \leq k$ leading to a total of 27 separate parameters that are required to be determined experimentally. For higher symmetry sites in other crystals, many of the parameters can be omitted. Using the same methods as when determining the matrix elements of H_C and H_{SO}, we apply the Wigner-Eckart theorem to determine the matrix elements of the crystal field interaction in terms of the reduced matrix elements of the unit tensor, $\mathbf{U^{(k)}}$:

$$\langle l\tau SLJM | \, H_{CF} \, | l\tau' S'L'J'M' \rangle = \sum_{k,q} B_q^k (-1)^{J-M} \begin{pmatrix} J & k & J' \\ -M & q & M' \end{pmatrix} D_J^k \tag{2.34}$$

where:

$$\begin{aligned} D_J^k = (-1)^{S+L'+J+k} [(2J+1)(2J'+1)]^{1/2} \begin{Bmatrix} J & J' & k \\ L' & L & S \end{Bmatrix} \\ \times \langle l\tau SL | \, |\mathbf{U}^{(k)}| \, | l\tau' S'L' \rangle \, (-1)^l (2l+1) \begin{pmatrix} l & k & l \\ 0 & 0 & 0 \end{pmatrix} \end{aligned} \tag{2.35}$$

The corresponding 3-j and 6-j symbols were determined by Edmonds, while the reduced matrix elements can be retrieved from Nielson and Koster [118, 119]. It should be noted

that a 180° rotation about the b axis are equivalent. This results in a freedom of the crystal-field parameters where the odd-q B_q^k parameters are allowed swap signs while leaving the eigenvalue spectrum of the system unchanged.

Due to the large number of independent crystal-field parameters in the C_1 environment of Y_2SiO_5, it can prove useful to define three k rank parameters which can be used to compare different sets of crystal-field parameters. Such parameters are known as crystal-field strength parameters and are defined as [120]:

$$S^k = \left[\frac{1}{2k+1}\left((B_0^k)^2 + 2\sum_{q>0}\left|B_q^k\right|^2\right)\right]^{1/2} \tag{2.36}$$

2.3.3 Zeeman interactions

So far we have discussed the mathematical details of the large scale interactions from that of the crystal-field splitting (100 cm^{-1}) to the spin-orbit and coulomb interactions (1000 and 10 000 cm^{-1} respectively). We will now investigate the mathematical details of the magnetic Zeeman interaction. This interaction represents the splitting of each crystal-field level on the order of a few wavenumbers due to an external magnetic field through the lifting of the Kramers degeneracy.

Following Wybourne, the electronic Zeeman Hamiltonian, which describes the coupling of an electron's orbital and spin angular momenta to an external magnetic field is given as [115]:

$$H_Z = \mu_B \sum_i^N \mathbf{B}\cdot(l_i + 2s_i) \tag{2.37}$$

Here μ_B is the Bohr magneton, $\mathbf{B}$ is the applied magnetic field and l_i and s_i are the orbital and spin angular momenta of the ith electron respectively.

For a particular J multiplet, the matrix elements of the Zeeman interaction has the form:

$$\begin{aligned}\langle \alpha SLJM|\,\mathbf{L}+2\mathbf{S}\,|\alpha SLJ'M\rangle =& (-1)^{J-M}\begin{pmatrix} J & 1 & J' \\ -M & 0 & M\end{pmatrix} \\ &\times \langle \alpha SLJ|\,|\mathbf{L}+2\mathbf{S}|\,|\alpha SLJ'\rangle\end{aligned} \tag{2.38}$$

By writing the matrix elements of $\mathbf{L}+2\mathbf{S}$ in the tensor operator form given by Wybourne [115] and explicitly evaluating the 3-j and 6-j symbols, which are given by Edmonds [118], the diagonal matrix elements becomes:

$$\langle \alpha SLJM|\,\mathbf{L}+2\mathbf{S}\,|\alpha SLJM\rangle = gM \tag{2.39}$$

where g is the Lande g-factor and is given by:

$$g = 1 + \frac{J(J+1) - L(L+1) + S(S+1)}{2J(J+1)} \tag{2.40}$$

And the off-diagonal elements become:

$$\langle \alpha SLJM|\mathbf{L}+2\mathbf{S}\,|\alpha SLJ-1M\rangle = \sqrt{J^2-M^2} \times \sqrt{\frac{(S+L+J+1)(S+L+1-J)(L+J-S)(S+J-L)}{4J^2(2J+1)(2J-1)}} \tag{2.41}$$

In addition to the electronic Zeeman effect is the nuclear Zeeman effect, which describes the coupling of the nuclear spin to an external magnetic field and is given as:

$$H_{NZ} = -\frac{\mu_N \beta_N}{I}\mathbf{B}\cdot\mathbf{I} \tag{2.42}$$

Here μ_N is the nuclear magneton, β_N is the nuclear magnetic dipole moment and I is the nuclear spin. $\mathbf{B}$ is the applied magnetic field and $\mathbf{I}$ is the tensor representation of the nuclear spin. The nuclear Zeeman effect is of a much smaller magnitude than the electronic Zeeman effect and therefore can be neglected for cases which has unpaired electrons, such as Kramers ions. For non-Kramers ions, the electronic Zeeman effect does not apply and so the nuclear Zeeman effect becomes relevant.

It should be noted that, unlike any of the other interaction discussed here, the addition of the electronic and nuclear Zeeman Hamiltonians to a crystal-field analysis does not add any additional parameters that are required to be fitted. Rather the inclusion of experimental Zeeman data along multiple axes provides the orientational data required in order to determine a unique set of crystal-field parameters [56].

2.3.4 Nuclear interactions

We will now outline the smallest interactions that will be investigated in this study, the hyperfine and nuclear quadrupole interactions with splittings on the order of 0.1 cm^{-1}.

The hyperfine interaction arises from the coupling of an electron's orbital and spin angular momenta to the nucleus' spin angular momenta. This interaction therefore only occurs in isotopes with a non-zero nuclear spin. Each crystal-field level is split into $2I+1$ hyperfine levels, with I being the nuclear spin. Following Judd, the hyperfine Hamiltonian is given as [47]:

$$H_{HF} = \mu_B\left[\frac{\mu\cdot(l-s)}{r^3} + \frac{(\mu\cdot r)(s\cdot r)}{r^5} + \frac{8\pi}{3}\delta(r)\mu\cdot s\right] \tag{2.43}$$

Here r is the position vector of the electron and $\mu = \mu_N g_I i$ is the nuclear angular-momentum operator, with μ_N being the nuclear magneton. The matrix elements of the hyperfine Hamiltonian are given as:

$$\begin{aligned}
&\langle l\tau SLJMIM_I|\, H_{HF}\, |l\tau' S'L'J'M'IM_I\rangle \\
&= a_l\sqrt{[J][J'][I](I+1)}\delta_{SS'}\delta_{II'} \times \Bigg[(-1)^{L+S+M+I+M_I+1}\sqrt{[L](L+1)}\begin{Bmatrix} L & L' & 1 \\ J' & J & S\end{Bmatrix} \\
&- (-1)^{J+M+L+I+M_I}\sqrt{30[L][L'][S](S+1)} \times \begin{pmatrix} L' & 2 & L \\ 0 & 0 & 0\end{pmatrix}\begin{Bmatrix} S & S' & 1 \\ L & L' & 2 \\ J & J' & 1\end{Bmatrix}\Bigg] \\
&\times \sum_{q=-1}^{1}(-1)^q \begin{pmatrix} J & 1 & J' \\ -M & q & M'\end{pmatrix}\begin{pmatrix} I & 1 & I' \\ -M_I & q & M_I'\end{pmatrix}
\end{aligned} \tag{2.44}$$

With a_l being the magnetic-dipole hyperfine parameter which is another parameter that is usually allowed to vary within a crystal field fit and is defined as:

$$a_l = 2\mu_B\gamma\hbar\langle r_i^{-3}\rangle \tag{2.45}$$

Note that the square brackets denote a shorthand used in Equation (2.44) that follows:

$$[x] = 2x + 1 \tag{2.46}$$

The nuclear quadrupole interaction arises from unpaired nucleons which exhibits a quadrupolar charge distribution that then couples to the spin angular momentum of valence electrons in atoms with nuclear spin, $I \geq 1$. Following Wybourne, the nuclear quadrupole operator is given as [115]:

$$H_Q = -e^2\int_{\tau_e}\int_{\tau_n}\rho(r_e)\rho(r_n)\frac{r_n^2}{r_e^3}(C_e^{(2)}\cdot C_n^{(2)})d\tau_e d\tau_n \tag{2.47}$$

Where $e\rho(r_e)$ and $e\rho(r_r)$ are the electron and nuclear charge densities respectively and r_e and r_n are the radial distances of the electrons and nucleons from the centre of the nucleus. $C_e^{(2)}$ and $C_n^{(2)}$ are the 2$^{\text{nd}}$ rank spherical tensor operators as given in Equation (2.25).

Using the $JMIM_I$ coupling scheme, the matrix elements of the nuclear quadrupole interaction are given as:

$$\begin{aligned}
\langle \alpha JMIM_I|H_Q\,|\alpha' JM \pm qIM_I \mp q\rangle &= (-1)^{J-M}\begin{pmatrix} J & 2 & J \\ -M\mp q & 0 & M\pm q\end{pmatrix} \\
&\times (-1)^{I-M_I}\begin{pmatrix} I & 2 & I \\ -M_I\pm q & 0 & M_I\mp q\end{pmatrix} \\
&\times \frac{a_Q X_J}{4}\sqrt{\frac{(2I+1)(I+1)(2I+3)(2J+1)(J+1)(2J+3)}{I(2I-1)(2J-1)}}
\end{aligned} \tag{2.48}$$

Here X_J is a parameter which takes on a different value for different electronic states and a_Q is the electric-quadrupole coupling constant which is given as:

$$a_Q = e^2 Q \langle r^{-3} \rangle \tag{2.49}$$

a_Q is the second hyperfine parameter that will be fitted in order to create a crystal-field model. The nuclear quadrupole moment, Q, is the matrix element over the space of the nuclear co-ordinates, evaluated when I has its largest component in the z-direction:

$$\begin{aligned} Q &= \langle II | \, r_n^2 C_n^{(2)} \, | II \rangle \\ &= \begin{pmatrix} I & 2 & I \\ -I & 0 & I \end{pmatrix} \langle I | \, | r_n^2 C_n^{(2)} | \, | I \rangle \end{aligned} \tag{2.50}$$

With the reduced matrix elements given as:

$$\langle I | \, | r_n^2 C_n^{(2)} | \, | I \rangle = \frac{1}{2} \left(\frac{I(2I-1)}{(I+1)(2I+1)(2I+3)} \right)^{-\frac{1}{2}} \tag{2.51}$$

Finally, we will describe a second order effect which arises from coupling the crystal-field to the nuclear quadrupole interaction. The crystal-field produces an electric-field gradient at the nucleus which couples to the spin angular momentum of the electron. This effect is anti-shielded by the closed shell electrons. Following Guillot-Noël *et al.* we define the lattice contribution to the nuclear electric quadrupole as [121]:

$$H_Q^{\text{lat}} = - \sum_{q=-2}^{2} (-1)^q (r_n^2 (C_n)_q^{(2)}) \left(\frac{(1-\gamma_\infty)}{(1-\sigma_2)\langle r_e^2 \rangle} B_{-q}^2 \mathbf{1}_{-q}^2 \right) \tag{2.52}$$

Here the subscript n represents nucleus. r_n is the nuclear radius and $(C_n)_q^{(2)}$ are the spherical tensor operators given in Equation (2.25). γ_∞ is the quadrupole anti-shielding factor, which defines the total quadrupole moment induced in the closed shells of an ion by the nuclear quadrupole moment, while σ_2 is a parameter representing the shielding due to the more external $5s$ and $5p$ electrons. Finally, $\langle r_e^2 \rangle$ is the mean square radius of the $4f$ electron orbital, B_{-q}^2 are the 2^{nd} rank crystal-field parameters, while $\mathbf{1}^2$ is the 2^{nd} rank identity tensor. The matrix elements for this interaction are given in Equations (2.50) and (2.51).

We can parameterise the lattice contribution to the nuclear electric quadrupole as:

$$N_q^2 = - \frac{(1-\gamma_\infty)}{(1-\sigma_2)\langle r_e^2 \rangle} Q B_q^2 \tag{2.53}$$

The N_q^2 parameters are the final parameters that will be included in a crystal-field fit.

2.4 Spin Hamiltonian

While the effective Hamiltonian defined in Equation (2.1) and the formalisms defined thus far does an excellent job in predicting the energy level structure of lanthanide-doped materials, the typical approach used to predict the magnetic and hyperfine structure of such systems is to use a spin Hamiltonian. The benefit of using a spin Hamiltonian, defined in Equations (2.54) and (2.55), over the Hamiltonian defined in Equation (2.1) is that it much more accurately predicts the magnetic and hyperfine structure of the electronic state of focus. However, the obtained parameters only apply to a single electronic state and so in order to accurately predict the magnetic and hyperfine structure over the entire $4f^N$ configuration, a unique set of parameters is required to be determined for every electronic state. Following the formalism of Macfarlane, the spin Hamiltonian used for Kramers ions is expressed as [111]:

$$\mathscr{H} = \mu_B \mathbf{B} \cdot \mathbf{g} \cdot \mathbf{S} + \mathbf{I} \cdot \mathbf{A} \cdot \mathbf{S} + \mathbf{I} \cdot \mathbf{Q} \cdot \mathbf{I} - \mu_n g_n \mathbf{B} \cdot \mathbf{I} \tag{2.54}$$

Here μ_B corresponds to the Bohr magneton, $\mathbf{B}$ is the magnetic field vector, $\mathbf{g}$, $\mathbf{A}$ and $\mathbf{Q}$ are the magnetic g , hyperfine and electric-quadrupole tensors respectively. $\mathbf{S}$ and $\mathbf{I}$ are vector representations of the electronic and nuclear spin operators respectively. Finally, μ_n and g_n are the nuclear magneton and nuclear g factor respectively.

The spin Hamiltonian that will be used for non-Kramers ions is expressed as [61]:

$$\mathscr{H} = \mathbf{B} \cdot \mathbf{M} \cdot \mathbf{I} + \mathbf{I} \cdot \mathbf{Q} \cdot \mathbf{I} \tag{2.55}$$

Here $\mathbf{B} \cdot \mathbf{M} \cdot \mathbf{I}$ is analogous to the $\mu_B \mathbf{B} \cdot \mathbf{g} \cdot \mathbf{S}$ of Kramers ions. However, instead of the interaction between the magnetic field and the electronic spin, it is the interaction between the magnetic field and the nuclear spin.

Typically $\mathbf{g}$, $\mathbf{M}$, $\mathbf{A}$ and $\mathbf{Q}$ are fitted using experimental data which then can be used in a crystal field fit as an additional data set. The standard approach of projecting the crystal-field Hamiltonian to the spin Hamiltonian in order to perform a fit introduces ambiguities in the calculation in C_1 symmetry environments, such as those in Y_2SiO_5. This arises from a freedom in the phase of the matrix elements of $\mathbf{S}$ in Equation (2.54) resulting in asymmetric parameter matrices. This problem is overcome by using a "multi-Hamiltonian" approach and will be discussed further in Section 2.5.

Here we restrict to cases where $\mathbf{g}$, $\mathbf{M}$, $\mathbf{A}$ and $\mathbf{Q}$ are symmetric, additionally $\mathbf{Q}$ is also traceless. The tensors can therefore be diagonalised by an Euler rotation, $\mathbf{R}$, which aligns them to their principal axis orientation and has the following form:

$$\mathbf{g} = \mathbf{R}(\alpha_g, \beta_g, \gamma_g) \begin{pmatrix} g_x & 0 & 0 \\ 0 & g_y & 0 \\ 0 & 0 & g_z \end{pmatrix} \mathbf{R}^T(\alpha_g, \beta_g, \gamma_g) \tag{2.56}$$

Here g_x, g_y and g_z are the principle values of $\mathbf{g}$ which corresponds to the minimum, intermediate and maximum g values respectively. α_g, β_g and γ_g are the Euler angles that $\mathbf{g}$ is rotated by. Identical relationships can also be obtained for $\mathbf{M}$, $\mathbf{A}$ and $\mathbf{Q}$, aligning these tensors to their respective principal axis orientations.

As discussed in Section 2.1, Y_2SiO_5 contains two magnetically inequivalent orientations arising from the C_{2h} symmetry of the unit cell. The g tensors of both orientations, $\mathbf{g}$ and $\mathbf{g}'$, are related by the following relationship:

$$\mathbf{g}' = R\mathbf{g}R^T \tag{2.57}$$

Here R is a 180° rotation about the b axis which has the form:

$$R = R^T = \begin{pmatrix} -1 & 0 & 0 \\ 0 & -1 & 0 \\ 0 & 0 & 1 \end{pmatrix} \tag{2.58}$$

The relationship of the components of the $\mathbf{g}$ tensor between the two magnetically inequivalent orientations is as follows:

$$\begin{pmatrix} g_{xx} & g_{xy} & g_{xz} \\ g_{yx} & g_{yy} & g_{yz} \\ g_{zx} & g_{zy} & g_{zz} \end{pmatrix} \longrightarrow \begin{pmatrix} g_{xx} & g_{xy} & -g_{xz} \\ g_{yx} & g_{yy} & -g_{yz} \\ -g_{zx} & -g_{zy} & g_{zz} \end{pmatrix} \tag{2.59}$$

2.5 Crystal-field fitting

In order to accurately predict the energy level structure of any lanthanide-doped Y_2SiO_5 system, we are required to fit the free-ion parameters given by Equation (2.32), the crystal-field parameters given by Equation (2.33) in addition to the hyperfine parameters given in Equations (2.45), (2.49) and (2.53) to multiple sets of experimental data. In the case of the C_1 symmetry sites of Y_2SiO_5, there are a total of 27 $B_q^{(k)}$ crystal-field parameters that are required to be fitted. However, of the free-ion parameters, only the $4f^N$ barycenter, E_0, the 3 Slater parameters, F^k, and the spin-orbit parameter, ζ, were allowed to vary while performing a crystal-field fit, with the higher order effects being held constant at the values obtained by Carnall *et al.* for Ln^{3+}:LaF_3 [49]. With the addition of the hyperfine coupling strength and nuclear quadrupole strength parameters, a total of 34 independent parameters are required to be fitted simultaneously. Traditionally these parameters are determined using a least squares fit to the eigenvalues of the Hamiltonian and experimentally obtained energy levels. However, in this study I use the algorithms developed by Horvath to conduct a comprehensive crystal-field fit [122].

We will now briefly outline the function of the pycf program suite developed by Horvath in 2018 in order to perform crystal-field fitting which is based on the F-shell empirical program suite which was developed by Reid [106,122]. The pycf program suite consists of a python script that allows for the easy input of experimental data and initial parameters in addition to a c99 library, named *cfl*. This library contains the core of the packages and optimisation routines used in order to perform both the crystal-field and spin Hamiltonian calculations. *cfl* takes the experimental data sets and initial parameters as inputs and calculates the energy level structure at different magnetic field orientations using matrix elements contained within the F-shell empirical program suite. Truncated bases were used throughout this study as it greatly improves computing speed when compared to using the entire basis. For each set of experimental data and magnetic field orientation,

an independent Hamiltonian is formed. For example, a Hamiltonian could be formed in order to fit to Stark levels while another Hamiltonian could be formed to fit to the spin Hamiltonian parameters at a certain magnetic field orientation. This allows for quicker run times as each Hamiltonian could be diagonalised independently on separate threads, with only the final χ^2 (goodness of fit) values being required to be shared between Hamiltonians.

Due to the parameter space of such fits having many local minima, a fitting algorithm that could vary between these minimas to find the global minimum is required. A coarse fit was performed first using the free-ion parameters found by Carnall *et al.* for Ln^{3+}:LaF_3 and crystal-field parameters found by Horvath for Er^{3+}:Y_2SiO_5 [49, 55, 106]. The output parameters from the coarse fit was then used to create a more refined final fit. The algorithm that was used for the coarse fit was the basin-hopping algorithm [123, 124], which attempts a random step followed by a local minimisation. A visual representation of the basin-hopping algorithm is given in Figure 2.5. The metropolis criterion was then applied to check if the random step was accepted and the algorithm could then move to the newly found local minima [125]. The algorithm used for the local minimisation was the Bound Optimization BY Quadratic Approximation (BOBYQA) algorithm from the NonLinear optimisation (NLopt) package [126]. The advantage of this algorithm is that it is derivative free and so converges to local minima faster than their counterparts which requires the evaluation of derivatives. Note that the global minimum is not necessarily the final minimum found, the algorithm instead makes a fixed number of steps and returns the step that has the lowest χ^2 value.

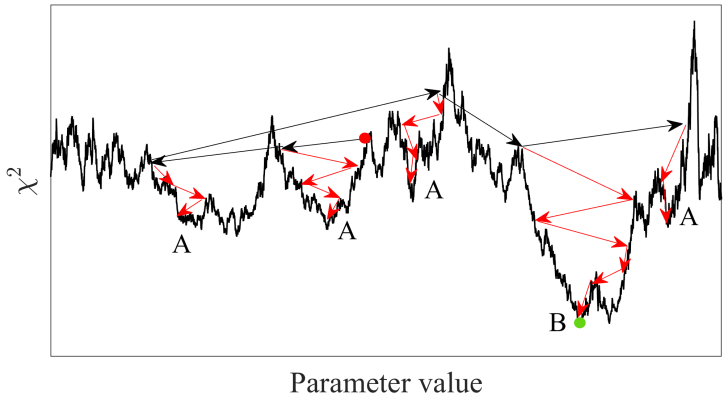

Figure 2.5: A single parameter representation of the basin-hopping algorithm. The black arrows represent an accepted step by the basin-hopping algorithm, followed by a local minimisation by the BOBYQA algorithm, represented by the red arrows. The staring position is given by the red circle, while the green circle represents the value the algorithm converges to. The regions labelled 'A' are the local minima discovered by the algorithm, while the global minimum is given by 'B'.

Once a coarse fit has been performed, a final fit was then conducted using simulated annealing [127]. Figure 2.6 depicts a two parameter visualisation of the simulated annealing algorithm. Like the basin-hopping algorithm, the metropolis criterion is applied once the algorithm attempts a step [125]. If successful, the algorithm takes this step. The step size of the algorithm was chosen so that it had a 10 % acceptance rate which is

recommended for this procedure [128]. The defining feature of such an algorithm is that as the fit progresses, the 'temperature' decreases exponentially. At high temperatures, the algorithm has enough 'energy' to overcome the barriers between local minima. Then as the temperature decreases, the algorithm becomes confined into the region of a single minima and slowly converges onto that minima. Simulated annealing has the advantage that the parameter uncertainties can be estimated using Markov Chain Monte-Carlo (MCMC) techniques through sampling the posterior probability distribution [128]. The algorithm is first allowed to 'burn in', which is represented the descent region of the χ^2 value in Figure 2.6, before 'orbiting' around the global minimum, represented by region B in Figure 2.6. Once the algorithm is allowed to 'burn in', the standard deviation of the remaining data is used as the parameter uncertainties.

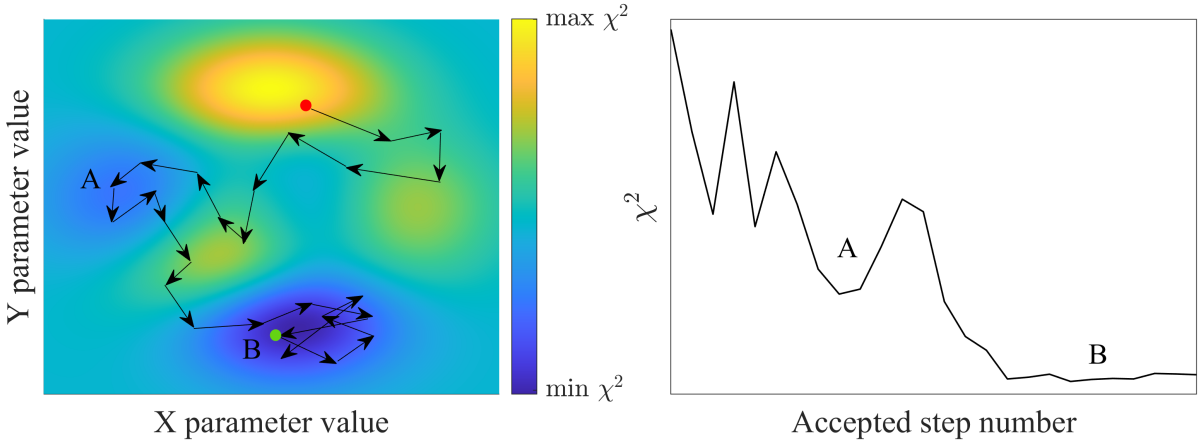

Figure 2.6: A two parameter representation of the simulated annealing algorithm. The left panel shows the parameter space, with the random walk undergone by the algorithm represented by the arrows. The staring position is given by the red circle, while the green circle represents the value the algorithm converges to. The right panel shows the decrease in the χ^2 value as the algorithm proceeds. As the algorithm traverses the parameter space, the algorithm encounters multiple local minima, represented by 'A' before finally converging on the global minimum, represented by 'B'.

2.6 Non-radiative energy transfer dynamics

Also investigated in this study is energy transfer between Sm^{3+} ions in Y_2SiO_5. We now will outline the theory used in this thesis to quantify the energy transfer processes present in such systems.

As discussed in Section 1.3, when an optically active ion is excited within a crystalline lattice it can decay radiatively through the emission of a photon, or non-radiatively by either releasing the energy into the lattice through phonons, or transferring some or all of its energy to neighbouring ions. When the latter occurs the first ion is called the donor and the ion that receives the energy from the donor is known as the acceptor. This form of energy transfer occur through either multipole interactions or the exchange mechanism (also known as Dexter electron transfer). The probability that these interactions proceeds is dependent on either an inverse power or negative exponential laws of the separation

between the donor and acceptor. The forms of these relationships are given in Equations (2.61) and (2.62). Resulting from this we can see that the probability of energy transfer between a donor and acceptor occurring falls off sharply as a function of separation, with a typical distance scale $\mathcal{O}(10\ \text{Å})$. In an extended material such as lanthanide-doped crystals, an ensemble of lanthanide ions are excited and each ion has the chance to non-radiatively decay through energy transfer mechanisms. As the probability of energy transfer is most significant on short separation scales, the higher the dopant concentration, the higher the probability of energy transfer. Following the methods of Wijngaarden and Vergeer, the fluorescence transient of a given configuration of acceptors around a single donor is given by a single exponential [104, 105]:

$$I(t) = \exp[-t(\gamma_r + \gamma_{tr})] \tag{2.60}$$

Where t is a time variable, γ_r is the radiative decay rate and γ_{tr} is the energy transfer rate from the donor to all surrounding acceptor ions. For a single step multipole-multipole interaction for acceptor ions at distances r_i from the donor ion, the energy transfer rate is given as:

$$\gamma_{tr} = C_{\text{nr}}^{(s)} \sum_i \left(\frac{r_0}{r_i}\right)^s \tag{2.61}$$

Here r_0 is the intra-site nearest neighbour distances (which for Y_2SiO_5 is 3.459 Å for site 1 and 3.621 Å for site 2). s is a parameter that depends on the type of interaction ($s = 6, 8, 10$ for dipole-dipole, dipole-quadrupole, and quadrupole-quadrupole interactions respectively). $C_{\text{nr}}^{(s)}$ is the non-radiative energy transfer rate of a single acceptor ion located at the nearest neighbour distance from a donor ion, and is also dependent on the type of multipole interaction.

In the case of an exchange interaction, the energy transfer rate is given as [98, 100]:

$$\gamma_{tr} = C_{\text{nr}}^{(\text{ex})} \sum_i \exp\left(-\frac{2r_i}{L}\right) \tag{2.62}$$

Where L is the 'effective average Bohr radius' which represents the average radius of the ion while in free space. $C_{\text{nr}}^{(\text{ex})}$ the non-radiative energy transfer rate of a single acceptor ion, located at a distance that approaches zero from the donor ion assuming an exchange interaction.

The experimental decay curve is considered as an ensemble average of different configurations. Therefore an ensemble average signal is calculated as:

$$\langle I(t)\rangle = \langle \exp[-t(\gamma_r + \gamma_{tr})]\rangle \tag{2.63}$$

Here $\langle \cdots \rangle$ denotes an ensemble average over a sufficiently large number of configurations so that the fitted rates converge. Monte-Carlo simulations were used to randomly generate each configuration of acceptors around a single donor.

Chapter 3

Experimental details

3.1 Crystal preparation

The Y_2SiO_5 crystals used in this study were both grown overseas in the X_2 phase via the Czochralski method. This method has been widely used for creating high quality, large, single crystal silicon boules for use in manufacturing silicon chips since the 1950s [129]. More recently this method has proven to be a robust technique in producing high quality Y_2SiO_5 crystals [130]. The Czochralski method of Y_2SiO_5 crystal growth involves melting equal parts of Y_2O_3 and SiO_2 in addition to an amount of Ln_2O_3 that corresponds to the desired dopant concentration in a crucible. The X_2 phase of Y_2SiO_5 requires high ($\sim$2000 °C) temperatures in order to form and crystallise. Once melted, a seed crystal is then lowered into the melt until contact occurs. The seed is then slowly raised and simultaneously rotated to create a single cylindrical crystal boule. Typical translation speeds are on the order of 1 mm/hr and typical rotation speeds are 20 rpm for Y_2SiO_5 [131]. The boule is then orientated through the use of X-ray diffraction, cut along the three excitation axes of Y_2SiO_5, and then polished to obtain crystals that can be used in spectroscopic studies.

3.1.1 Sm^{3+}:Y_2SiO_5

The Sm^{3+}:Y_2SiO_5 crystal was grown by and purchased from Scientific Materials Inc., Bozeman, Montana, with a Sm^{3+} dopant concentration of 0.5 molar %. This concentration was chosen in order to produce a large absorption depth, which is beneficial to the spectroscopic techniques undertaken in this study. The crystal has dimensions of (5.1 $\pm$ 0.1) mm along the D_1 axis, (4.9 $\pm$ 0.1) mm along the D_2 axis, and (6.0 $\pm$ 0.2) mm along the crystallographic b axis. All six faces were polished in order to perform spectroscopy along all three axes. Figure 3.1 a) shows the boule that the Sm^{3+}:Y_2SiO_5 sample was cut from and b) shows the Sm^{3+}:Y_2SiO_5 sample used in this study with the direction of the extinction axes labeled.

Figure 3.1: a) The boule from which the Sm^{3+}:Y_2SiO_5 sample was cut from. b) The Sm^{3+}:Y_2SiO_5 sample used in this study.

3.1.2 Er^{3+}:Y_2SiO_5

The Er^{3+}:Y_2SiO_5 crystal was grown by A. Ferrier, Chimie ParisTech, France, with a Er^{3+} dopant concentration of 0.005 molar %. The lower concentration of this crystal benefits the hyperfine and coherence time studies previously undertaken [55,106]. The crystal has dimensions of 6.27 mm along the D_1 axis, 6.18 mm along the D_2 axis, and 4.89 mm along the crystallographic b axis. Like the Sm^{3+}:Y_2SiO_5 crystal, all six faces were polished in order to perform spectroscopy along all three axes. Figure 3.2 shows the Er^{3+}:Y_2SiO_5 sample used in this study with the direction of the extinction axes labeled.

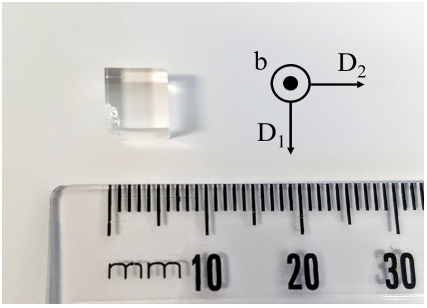

Figure 3.2: The Er^{3+}:Y_2SiO_5 sample used in this study.

3.2 Site-selective laser spectroscopy

Site-selective laser spectroscopy was performed on the Sm^{3+}:Y_2SiO_5 sample using a PTI GL-3300 pulsed nitrogen laser of wavelength 337.1 nm, which pumped a PTI GL-302 tunable dye laser that utilises various coumarin and rhodamine dyes as the lasing medium. Two dyes, coumarin 540A and coumarin 500 were used in this study. Coumarin 540A has a lasing range of 515 - 583 nm and was used to excite the $^4G_{5/2}$ multiplet of Sm^{3+}:Y_2SiO_5 while coumarin 500 lases in the range of 473 - 547 nm and was used to excite the $^4F_{3/2}$ and $^4G_{7/2}$ multiplets of Sm^{3+}:Y_2SiO_5. The beam path of the laser was directed onto the sample which was mounted onto a copper cold finger such that the laser beam passed through the b axis of the sample. This axis was chosen in order to maximise absorption as the b axis was cut to be the longest axis, see Section 3.1.1 for details. The sample was cooled to 10 K using a Janis CCS-150 closed-cycle cryostat and a Lakeshore 325 temperature controller which adjusted the current through a resistive heater attached to the back of the sample cold finger. The emission from the sample was then focused

into a Horiba iHR550 spectrometer and detected using either an air cooled Hamamatsu H10330C near infra-red photomultiplier tube or a water cooled Hamamatsu R2257 visible photomultiplier tube depending on the emission wavelength monitored. The voltages from these photomultiplier tubes was coupled with an optical laser trigger and were digitised using Hamamatsu photon counting units C9744 and C8855-01 before being supplied to a LabVIEW .vi on a computer where a spectrum could then be obtained. The experimental setup is schematically shown in Figure 3.3.

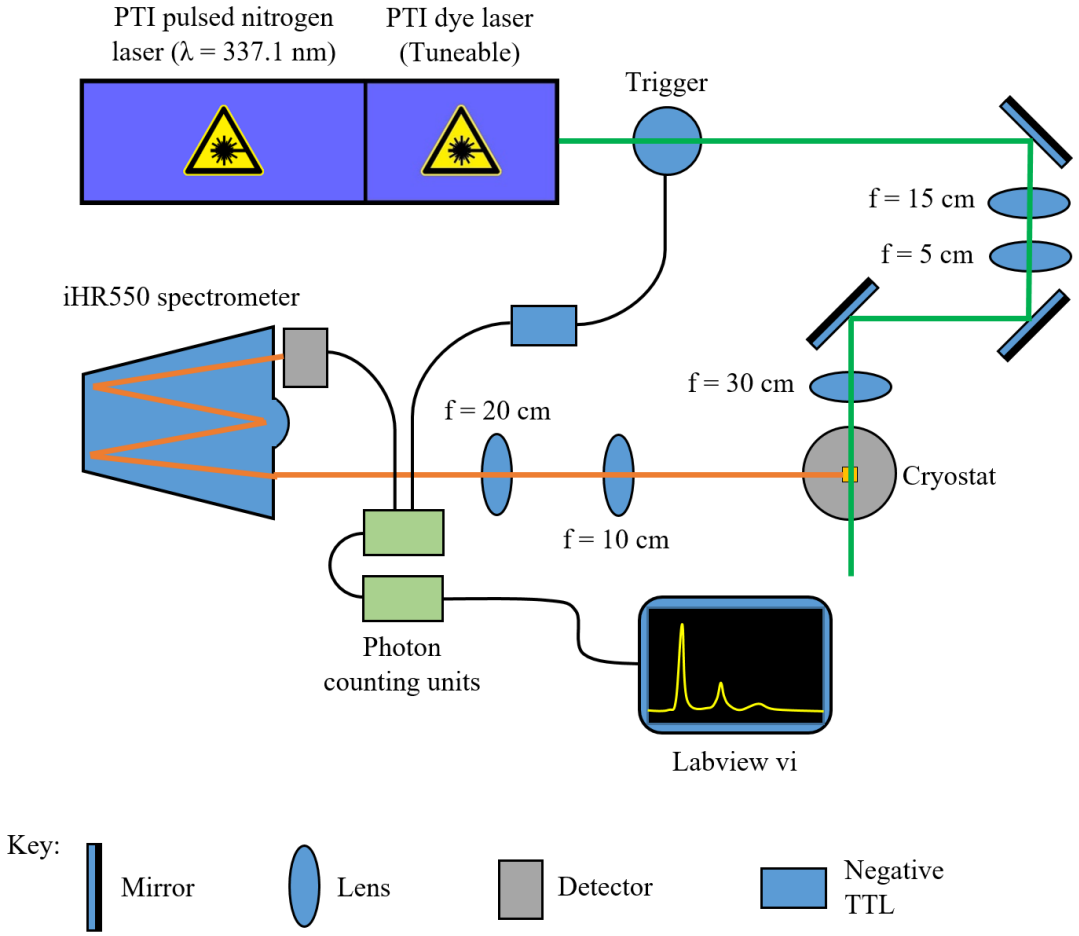

Figure 3.3: Key components of the site-selective laser spectroscopy experiment. Refer to the text for a detailed description of the key components. The beam path of the laser is depicted in green while the emission from the sample is given in orange.

The temporal dynamics of the Sm^{3+}:Y_2SiO_5 sample was investigated using the setup described above with key differences in the detection of the emission from the sample. Once the light passed through the Horiba iHR550 spectrometer it was instead detected using a Hamamatsu R3896 visible photomultiplier tube. The output voltage of the detector was then coupled with the optical laser trigger and digitised by a Tektronix DPO7104 digital oscilloscope such that the temporal transients could then be obtained.

3.3 Temperature dependent absorption spectroscopy

Temperature dependent absorption spectroscopy was performed on Er^{3+}:Y_2SiO_5 by mounting the sample on a copper holder which was cooled by thermal contact with a closed-cycle helium cryostat. The sample temperature was controlled by a home built temperature controller which adjusted the current through a resistive heater attached to the back of the sample cold finger. The cryostat was inserted into the main compartment of a Bruker Vertex-80 Fourier Transform InfraRed (FTIR) spectrometer so that it crosses the beam path of the FTIR and a spectrum could be obtained. The Bruker Vertex 80 FTIR is a high-resolution (0.075 cm^{-1}) spectrometer which is equipped with exchangeable sources, beamsplitters and detectors which are used in order to perform spectroscopy from the mid-infrared through to the ultraviolet (500 cm^{-1} – 30 000 cm^{-1}). A schematic of the FTIR with the XSA extension is shown in Figure 3.4. The exchangeable components and their corresponding spectral ranges are summarised in Table 3.1. The FTIR is nitrogen gas purged which protects the components, some of which are hydroscopic, in addition to minimising atmospheric absorption due to water vapour and carbon dioxide which is prevalent throughout the infrared region.

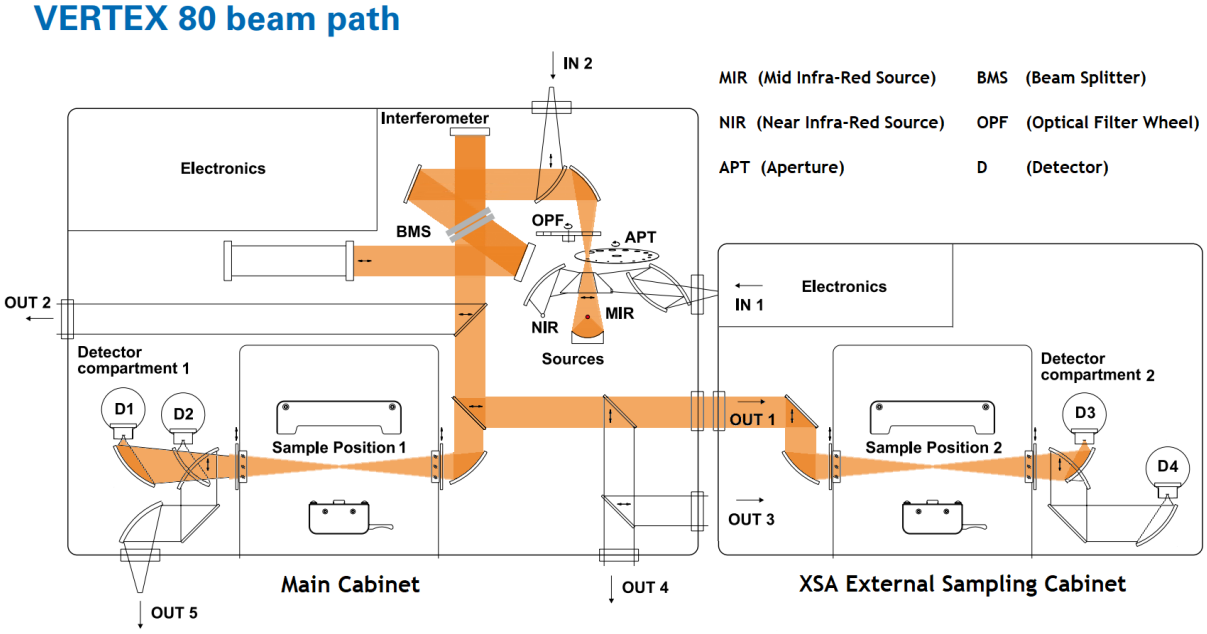

Figure 3.4: The beam path of the Bruker Vertex 80 FTIR. The cryostat sits in sample position 1 while the magnet sits in sample position 2. The orange denotes the beam path.

Table 3.1: The exchangeable components of the FTIR and their corresponding spectral ranges that a given combination of resources operates over. The spectral region marked with an asterisk also utilises a KG1 glass filter.

Spectral range (cm^{-1})	Source	Beamsplitter	Detector
1,500 - 4,000	Globar	KBr	MCT
4,000 - 9,000	Tungsten Halogen	CaF_2	InGaAs
9,000 - 13,000	Tungsten Halogen	CaF_2	SiDiode
13,000 - 19,000*	Tungsten Halogen	CaF_2 (UV-Vis-NIR)	SiDiode
19,000 - 30,000	Tungsten Halogen	CaF_2 (UV-Vis-NIR)	GaP

3.4 Zeeman absorption spectroscopy

Zeeman spectroscopy was performed on both samples using the Bruker Vertex-80 FTIR coupled with the XSA extension as depicted in Figure 3.4. The sample was thermally attached to a copper mount which was then screwed into the bore of a 4 T Oxford Instruments superconducting solenoid, of dimensions (10.16×2.34) cm, built into the can of a home built cryostat. The magnetic field direction is parallel to the light propagation direction of the FTIR and the sample was mounted such that a specific extinction axis was aligned with the magnetic field direction. A schematic of the magnet is given in Figure 3.5. The sample was cooled to 4.2 K by filling the vacuum evacuated cryostat with liquid nitrogen and helium. The magnet was lowered into the XSA compartment of the FTIR so that the bore of the solenoid and the sample crosses the beam path of the FTIR. The magnetic field strength was controlled by a British Oxygen Company PS60/72A power supply which provided the magnet with an operating current up to a maximum of 51.55 A which corresponds to a magnetic field strength of 4 T. Zeeman spectroscopy was performed in various spectral regions by interchanging the FTIR components given in Table 3.1.

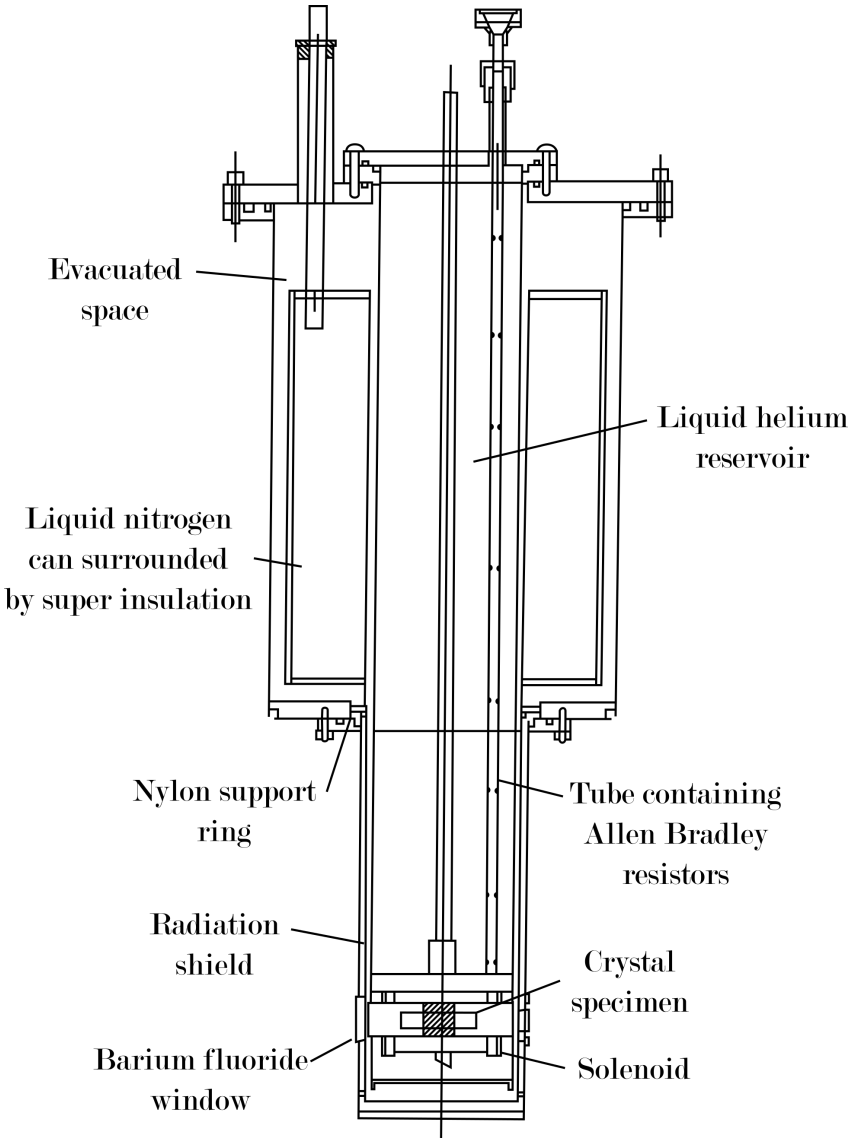

Figure 3.5: The 4 Tesla superconducting magnet used for Zeeman absorption spectroscopy.

When a magnetic field is applied to a Kramers ion doped into Y_2SiO_5, the Kramers degeneracy is lifted resulting in the splitting of each Stark level into two. This results in each electronic transition splitting into 4 transitions when the magnetic field is applied along the b axis or the D_1-D_2 plane as shown in Figure 3.6. As discussed in Section 2.1, when the magnetic field is applied down a general direction, each transition instead splits into eight transitions due to the two magnetically inequivalent orientations of Y_2SiO_5.

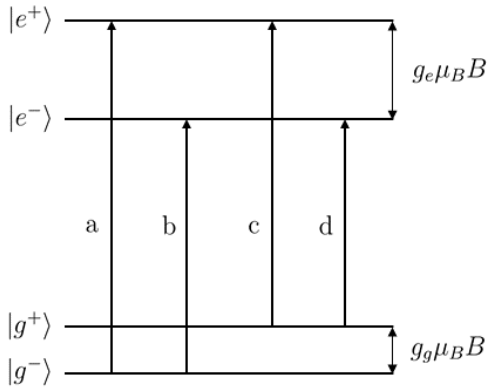

Figure 3.6: The four transitions seen for each spectral line when an external magnetic is applied along the b axis or the D_1-D_2 plane, lifting Kramers degeneracy.

From Figure 3.6 we see that the ground state g values can be expressed as:

$$g_g = \frac{E_a - E_c}{\mu_B B} = \frac{E_b - E_d}{\mu_B B} \tag{3.1}$$

And the excited state g values can be expressed as:

$$g_e = \frac{E_a - E_b}{\mu_B B} = \frac{E_c - E_d}{\mu_B B} \tag{3.2}$$

In both of the above equations, B is the applied magnetic field strength and μ_B is the Bohr Magneton.

3.5 Raman heterodyne spectroscopy

Raman heterodyne spectroscopy was performed during a visit to the University of Otago on the Sm^{3+}:Y_2SiO_5 sample, which involves coupling a radio frequency (R-F) excitation source to an optical source, typically supplied by a laser. This is a useful tool used in order to probe the low energy structure, such as hyperfine structure, that traditional means of spectroscopy are unable to probe due to the inhomogeneous broadening of spectral features present in lanthanide-doped crystals. Raman heterodyne spectroscopy was first used in the detection of nuclear magnetic resonance of Pr^{3+}:LaF_3 [132, 133]. Recent demonstrations have shown the ability to characterise many non-Kramers in addition to Kramers systems through the determination of spin Hamiltonian parameters [32,61,134]. In this study, Raman heterodyne spectroscopy was utilised in order to obtain the full magnetic g tensors of the $^6H_{5/2}Z_1$ and $^4G_{5/2}A_1$ states of Sm^{3+}:Y_2SiO_5 as traditional Zeeman studies described in Section 3.4 proved in be insufficient.

Figure 3.7 shows the Raman heterodyne process as a function of magnetic field strength. States $|1\rangle$ and $|2\rangle$ are the Zeeman levels of the ground state which become non-degenerate under the application of a magnetic field and states $|3\rangle$ and $|4\rangle$, the same for the excited state. The transition between the ground Zeeman states $|1\rangle$ and $|2\rangle$ is driven by the R-F field, ω_μ, whereas the transition between the ground Zeeman state, $|2\rangle$ and excited Zeeman state $|3\rangle$ is driven by the optical frequency field, ω_0. When both these frequencies

are resonant with a transition, an additional optical frequency field, ω_s, is generated whose frequency is the sum of the original optical field and the R-F field, $\omega_s = \omega_\mu + \omega_0$. The resulting laser beam will therefore be composed of the two optical frequencies, ω_s and ω_0. This creates a beat signal with frequency ω_μ. By filtering out for ω_μ at detection, the frequency of the Zeeman transition between states $|1\rangle$ and $|2\rangle$ can be determined.

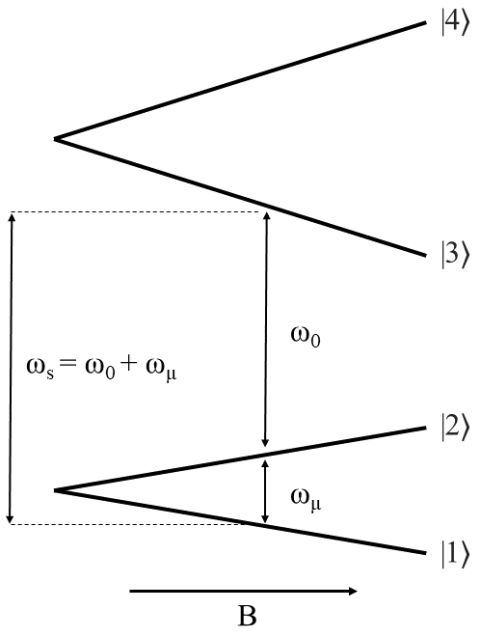

Figure 3.7: Energy level diagram relevant for Raman Heterodyne spectroscopy. $|1\rangle$ and $|2\rangle$ represents the Zeeman split levels of the ground state and $|3\rangle$ and $|4\rangle$, the same for the excited state. ω_μ represents the R-F driven transition, ω_0 represents the optical frequency driven transition and ω_s is the sum of the two.

The transitions that can be driven by the R-F and optical frequency excitations are not unique. The laser can be used to drive the transition between states $|1\rangle$ and $|3\rangle$ while the R-F excitation can drive the excited Zeeman states $|3\rangle$ and $|4\rangle$. This allows for the Zeeman structure of the excited state to be probed simultaneously to that of the ground state.

In order to perform Raman heterodyne spectroscopy, the sample was attached to an aluminium sample holder that included a 4 loop copper coil as depicted in Figure 3.8. The coil created the R-F field with frequencies that were experimentally determined to be up to 70 MHz before transmission drops off. In order to perform Raman heterodyne spectroscopy at frequencies higher than 100 - 200 MHz, a microwave cavity is required, with studies being able to achieve microwave frequencies of up to 5.3 GHz [31, 135, 136].

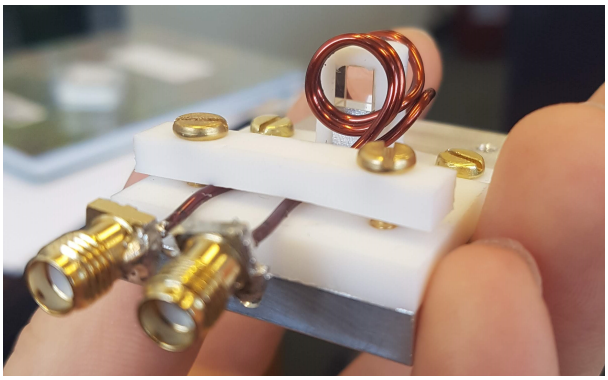

Figure 3.8: The R-F coil and sample holder used for Raman heterodyne spectroscopy.

The sample holder was screwed onto the cold finger of the cryostat, named the "Kraken-Xavostat" which is depicted in Figure 3.9, ensuring that the crystal was in thermal contact with the cryostat through the use of vacuum grease. The cryostat is described in detail in Ref. [134]. The cold finger was attached to a can of liquid helium allowing the sample to be cooled to 4.5 K and can be further cooled to 3.2 K while pumping on the liquid helium can. The temperature of the sample holder was monitored through a temperature sensor which was threaded through the top plate alongside the nitropool outer, to be attached to the sample holder. Within the cryostat, located around the sample holder is a HTS-110 Ltd. liquid nitrogen cooled superconducting vector magnet. The three coils, referred to as the x, y and z coils, can each provide a magnetic field along a particular perpendicular axis. The x and y coils provide fields of 0.343 mT/A, and the z coil provides a field of 10.4 mT/A, with up to 30 A being provided by individual power supplies each connected to the individual sets of coils. The magnetic coils $(x, y, z) = (D_2, b, D_1)$ axes of the crystal as shown in Figure 3.9.

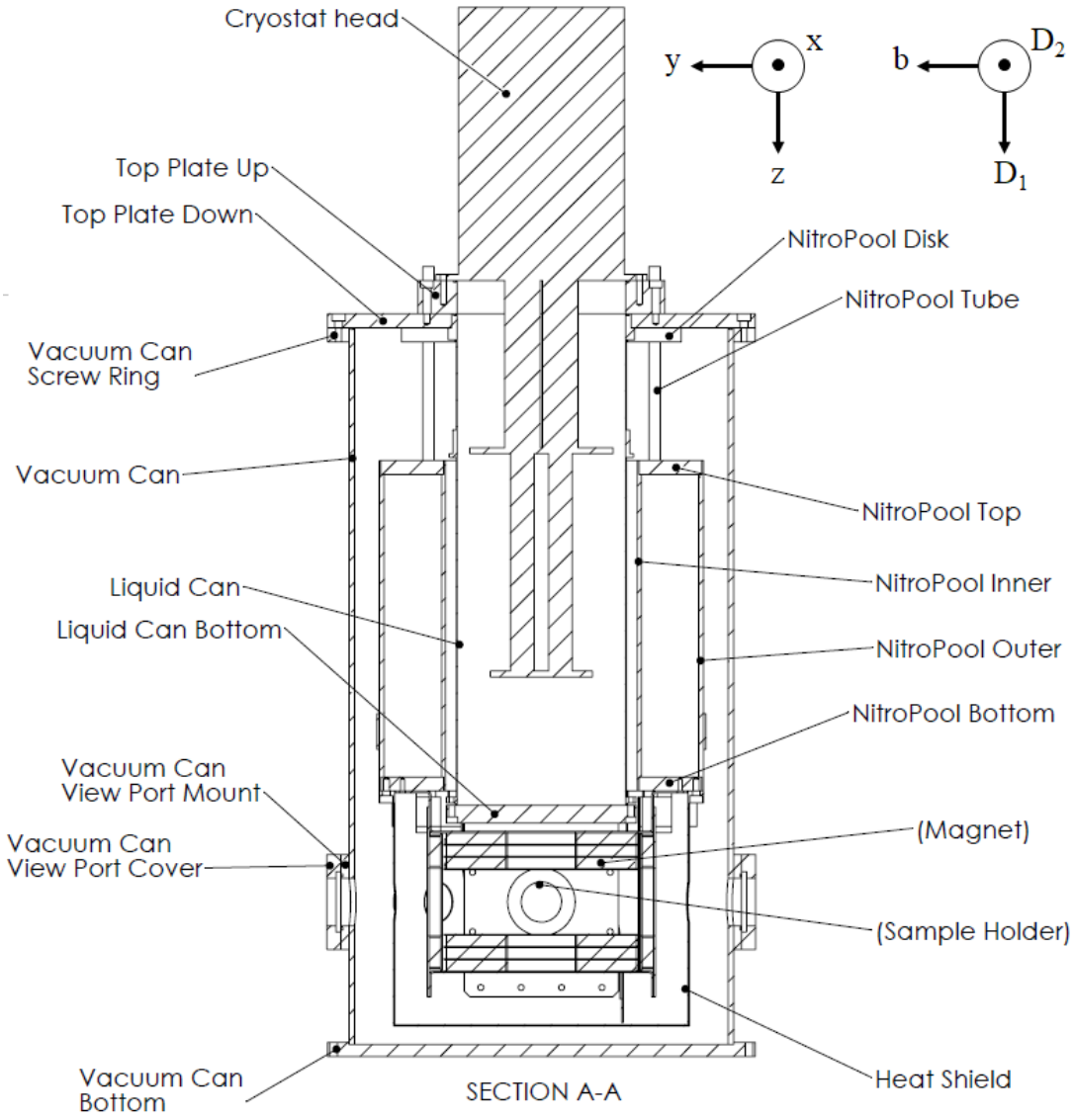

Figure 3.9: Schematic of the "Kraken-Xavostat" cryostat used to perform Raman heterodyne spectroscopy. The orientation of the magnetic coils relative to the crystallographic extinction axes of the sample are depicted.

The experimental setup of Raman heterodyne spectroscopy is depicted in Figure 3.10. The optical excitation was supplied by a Coherent Verdi-V10 diode pumped solid state laser ($\lambda = 532$ nm) which pumped a tunable Coherent CR-699-03 ring dye laser. Rhodamine 560 was the dye of choice for pumping the ${}^6H_{5/2}Z_1 \longrightarrow {}^4G_{5/2}A_1$ transition for both sites of Sm^{3+}:Y_2SiO_5 as this dye has a lasing rage of 533 – 600 nm. The dye was used via a home built dye jet system which reduces losses through the removal of optical surfaces. The output wavelength of the ring dye laser could be tuned coarsely via a scanning Brewster plate and finely through the use of a movable mirror, which altered the path length of the ring laser. The output wavelength of the ring dye laser was monitored by an Angstrom WS-7 wavelength meter. The output of the ring dye laser was coupled into a fibre optic in order to be directed into the cryostat located on another optical bench. The typical laser power incident on the cryostat windows was 25 mW.

The R-F field was supplied by a FieldFox network analyser after it has passed through an Amplifier Research 10W1000C R-F power amplifier, with a 50 Ω resistor to reduce reflections back into the amplifier. The resulting laser beam, which is composed of the two optical frequencies, ω_s and ω_0, was then directed to be incident on a New Focus 80 MHz balanced optical receiver after passing through a variable neutral density filter tuned to allow as much light as possible to be incident on the photodetector without causing the detector to saturate. The signal was then passed through a 50 nF DC block which filters out low frequency noise from the signal before being measured by the FieldFox. The FieldFox sweeps through a R-F field range while simultaneously measuring the beat signal of the resulting laser beam. A peak in the obtained spectrum occurs at frequencies where the R-F field is resonant to a Zeeman transition.

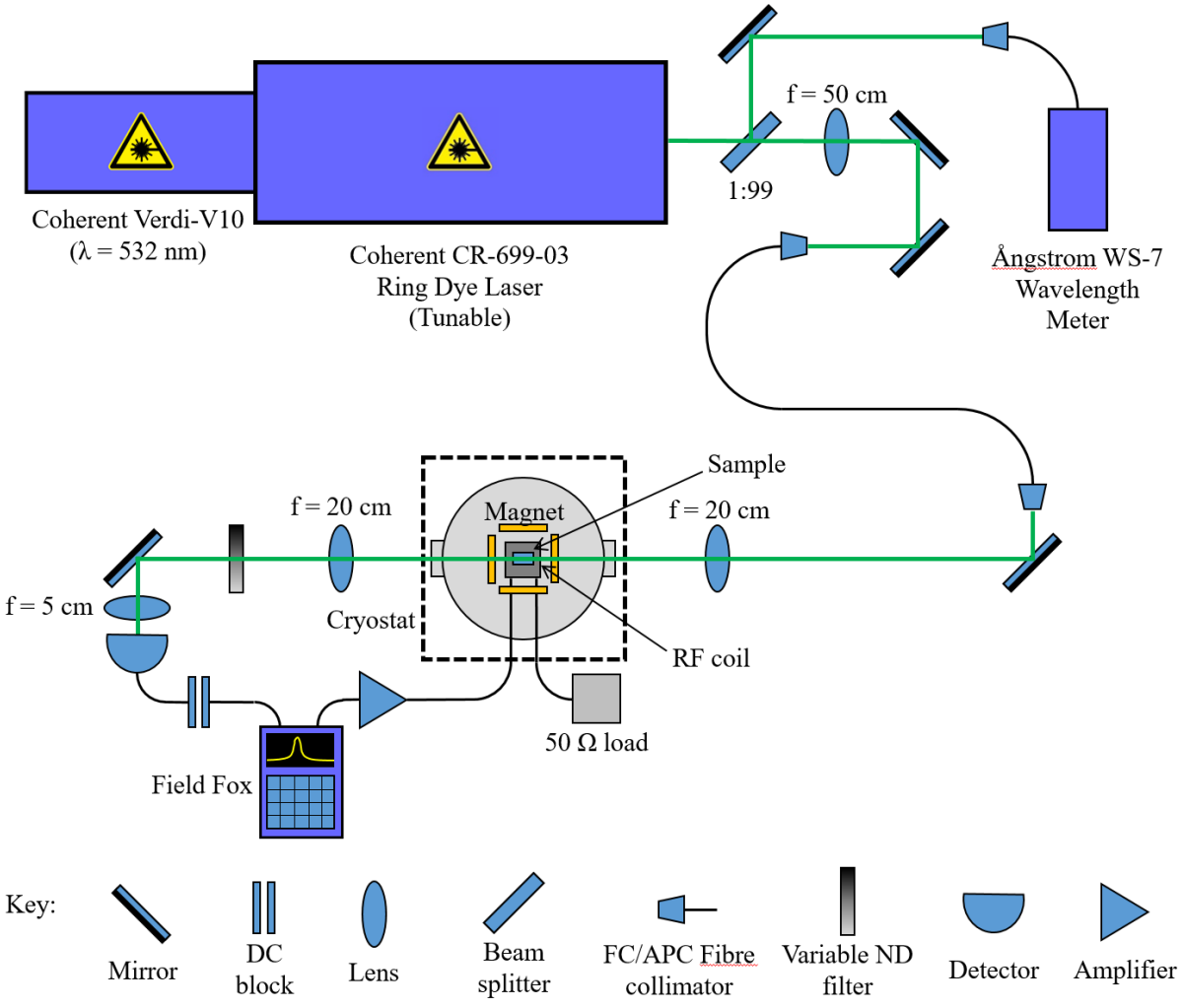

Figure 3.10: Key components of the Raman Heterodyne spectroscopy experiment. Refer to the text for a detailed description of the key components. The beam path of the laser is depicted in green.

Chapter 4

Spectroscopy and crystal-field analysis of Sm^{3+}:Y_2SiO_5

This chapter describes the crystal-field model developed for Sm^{3+}:Y_2SiO_5, fitted to data obtained through the use of various spectroscopic methods. Samarium is of particular interest due to its proximity in the lanthanide series to Europium, which itself is important in QIP studies. As discussed in Section 1.2, it is possible to transfer free-ion and crystal-field parameters between ions doped within Y_2SiO_5, which can then be refined to create an accurate crystal-field model with the available data for the ion in question [137]. This same method can be applied to Eu^{3+}:Y_2SiO_5 once a crystal-field model has been developed for Sm^{3+}:Y_2SiO_5. Parameterising a crystal-field model for the non-Kramers system of Eu^{3+}:Y_2SiO_5 directly is unfeasible, due to the lack of the necessary directional data, such as g values. This makes the transferability of parameters from neighbouring ions necessary. Furthermore, Sm^{3+}:Y_2SiO_5 is of possible interest in the development of QIP in its own right, due to Sm^{3+} possessing large hyperfine splittings, similar to Er^{3+}, while maintaining smaller ground state g values relative to Er^{3+}. This allows for the possibility of Sm^{3+}:Y_2SiO_5 being utilised for high-bandwidth QIP applications.

This study provides the first spectroscopic analyses of bulk crystal Sm^{3+}:Y_2SiO_5, with previous work focusing on low-resolution spectroscopy of Sm^{3+}:Y_2SiO_5 nanoparticles [91]. This chapter begins by introducing the spectroscopic properties of Sm^{3+}:Y_2SiO_5. Following this, results of site-selective laser and Zeeman absorption spectroscopy are presented. Finally, the crystal-field analysis performed by fitting the experimental data obtained in this study are presented.

4.1 Spectroscopic properties of Sm^{3+}:Y_2SiO_5

Samarium has atomic number 62 and so is located in the first half of the lanthanide series. The electronic structure of triply ionised Samarium, Sm^{3+}, is given as [Xe]$4f^5$. Sm^{3+} is a Kramers ion due to its five $4f$ valence electrons which leads to 1001 doubly-degenerate states, split into 198 multiplets. Under the influence of a magnetic field, the Kramers degeneracy is lifted and the total number of non-degenerate states doubles to 2002. Two isotopes of naturally occurring Samarium, ^{147}Sm and ^{149}Sm, which accounts for 15.0 % and 13.8 % of the natural abundances respectively, have a non-zero nuclear spin of $\frac{7}{2}$. Using the same $^{2S+1}\mathrm{L}_J$ and letter notation as [112], the energy level structure of

Sm^{3+}:Y_2SiO_5 up to 30 000 cm^{-1} is depicted in Figure 4.1. Due to the large crystal-field of Y_2SiO_5, significant J-mixing occurs, and multiplets with energies greater than that of the $^4G_{7/2}$ multiplet, in addition to the $^6F_{1/2}$, $^6F_{3/2}$, and $^6H_{15/2}$ multiplets can not be individually distinguished. Therefore, multiplets above $^4G_{7/2}$ multiplet are not labelled on Figure 4.1, while the $^6F_{1/2}$, $^6F_{3/2}$, and $^6H_{15/2}$ multiplets are all given the label 'S', as is the convention for Sm^{3+} [138]. The thickness of each line indicates the crystal-field splittings within each multiplet. The ionic radius of Sm^{3+} is larger than that of Y^{3+} which Sm^{3+} substitutes for, as shown in Table 2.1. This leads to the preferential substitution of Sm^{3+} ions into site 2 of Y_2SiO_5, resulting in a higher population and more prominent spectral features for site 2 at a ratio of 1.63:1.

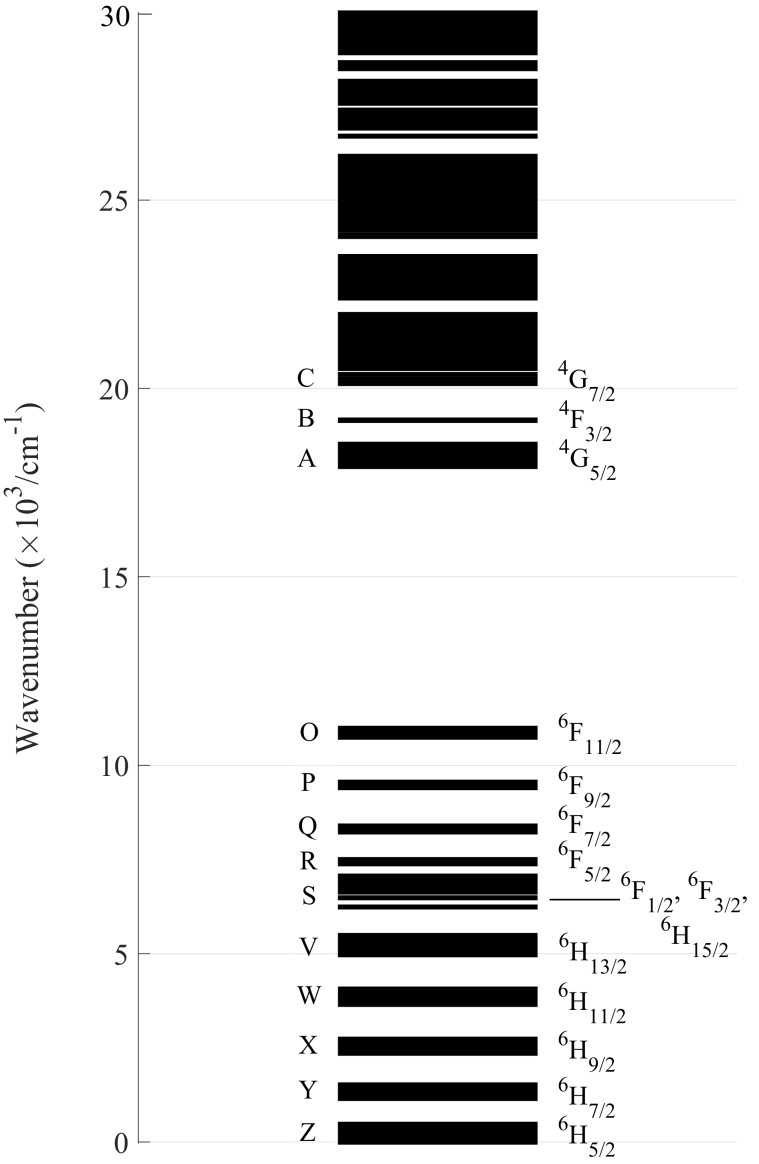

Figure 4.1: Energy level structure of Sm^{3+}:Y_2SiO_5 up to 30 000 cm^{-1} with the $^{2S+1}L_J$ multiplets labelled. The thickness of each line indicates the crystal-field splittings within each multiplet. Multiplets above the $^4G_{7/2}$ multiplet at 20 000 cm^{-1} are not labelled due to significant J-mixing preventing these multiplets from being distinguished.

4.2 Spectroscopy and assigning Stark levels to Sm^{3+}:Y_2SiO_5

Essential to creating an accurate crystal-field model for Sm^{3+}:Y_2SiO_5 was the assignment of each spectral line to their respective site. A narrowband tunable dye laser was used in order to perform site-selective fluorescence spectra that were used to assign each spectral line found in absorption. The experimental details are described in Section 3.2.

Fluorescence from the $^4G_{5/2}A_1$ state to all multiplets in the ^6H_J and ^6F_J manifolds was monitored with an excitation energy at or above the $^4G_{5/2}A_1$ state.

4.2.1 Fluorescence and absorption spectroscopy

As Y_2SiO_5 has large phonon energies, all energy gaps in the electronic structure of Sm^{3+}:Y_2SiO_5, which are 2000 cm^{-1} or less, are able to be bridged by these phonons, with the ∼7000 cm^{-1} energy gap below the $^4G_{5/2}A_1$ state the only gap not able to be bridged by phonons [139, 140]. Therefore any excitation at or above the $^4G_{5/2}A_1$ state will relax non-radiatively to the $^4G_{5/2}A_1$ state before radiatively fluorescing down to all multiplets below in the ^6H_J and ^6F_J manifolds. Fluorescence spectra were obtained by fixing the laser to be on resonance with a spectral line at or above the $^4G_{5/2}A_1$ state at ∼18 000 cm^{-1} and then monitoring the fluorescence from the $^4G_{5/2}A_1$ state to each multiplet in the ^6H_J and ^6F_J manifolds by scanning the spectrometer through each multiplet individually. The obtained fluorescence spectra were then compared to absorption spectra, where the absorption energy is equal to the energy of the $^4G_{5/2}A_1$ state (17 689 cm^{-1} for site 1 and 17 790 cm^{-1} for site 2) minus the energy of the spectral line found in fluorescence. Most of the $\frac{2J+1}{2}$ doubly degenerate Kramers states was observed for each multiplet and both sites.

Absorption spectra for the $^6H_{5/2}$ and $^6H_{7/2}$ multiplets could not be obtained due to these multiplets lying below the two-phonon absorption edge of Y_2SiO_5. Figure 4.2 shows an absorption spectrum of Sm^{3+}:Y_2SiO_5 up to 8000 cm^{-1} with the visible multiplets labelled. Clearly evident at 2000 cm^{-1} is the absorption edge of Y_2SiO_5. Also of note is partial absorption at ∼2600 cm^{-1} – 2800 cm^{-1} due to the two phonon mode, with phonon energies of ∼1300 cm^{-1}. The partial transmission visible at ∼1600 cm^{-1} is due to the lack of phonons with energies of ∼800 cm^{-1} [139, 140].

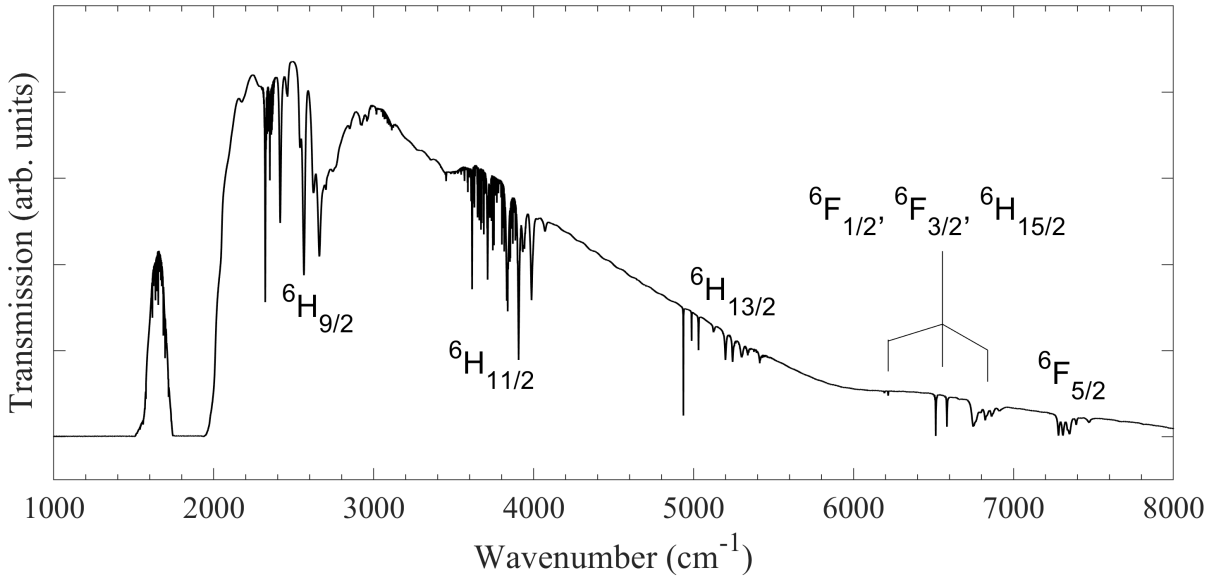

Figure 4.2: 4.2 K absorption spectrum of Y_2SiO_5:0.5%Sm^{3+} below 8000 cm^{-1} with all visible multiplets labeled. The absorption edge, which arises from the two phonon mode of Y_2SiO_5, is clearly evident at 2000 cm^{-1}.

Figures 4.3 and 4.4 depicts site-selective fluorescence spectra from the $^4G_{5/2}A_1$ state to the $^6H_{5/2}$ and $^6H_{7/2}$ multiplets respectively for both Sm^{3+} sites, measured at a sample temperature of 10 K. The excitation wavelength employed for the $^6H_{5/2}$ multiplet was the $^6H_{5/2}Z_1 \longrightarrow {}^4F_{3/2}B_1$ transition at 18 913 cm^{-1} for site 1 and 18 955 cm^{-1} for site 2. This transition was selected in order to keep the monitored fluorescence separated from the excitation given by the laser. The excitation employed for the $^6H_{7/2}$ multiplet was the $^6H_{5/2}Z_1 \longrightarrow {}^4G_{5/2}A_1$ transition at 17 689 cm^{-1} for site 1 and 17 790 cm^{-1} for site 2. In both cases the expected number of electronic levels can be observed with some phonon sideband structure, noticeably around the Z_2 and Z_3 lines for the $^6H_{5/2}$ multiplet and the Y_3 and Y_4 lines for the $^6H_{7/2}$ multiplet. Spectral features marked with an '*' is emission due to the other site, this will be further analysed in Section 5.2. The energies of all doubly degenerate Kramers states were determined for both sites in both multiplets, three for each site in the $^4H_{5/2}$ multiplet and four in the $^4H_{7/2}$ multiplet.

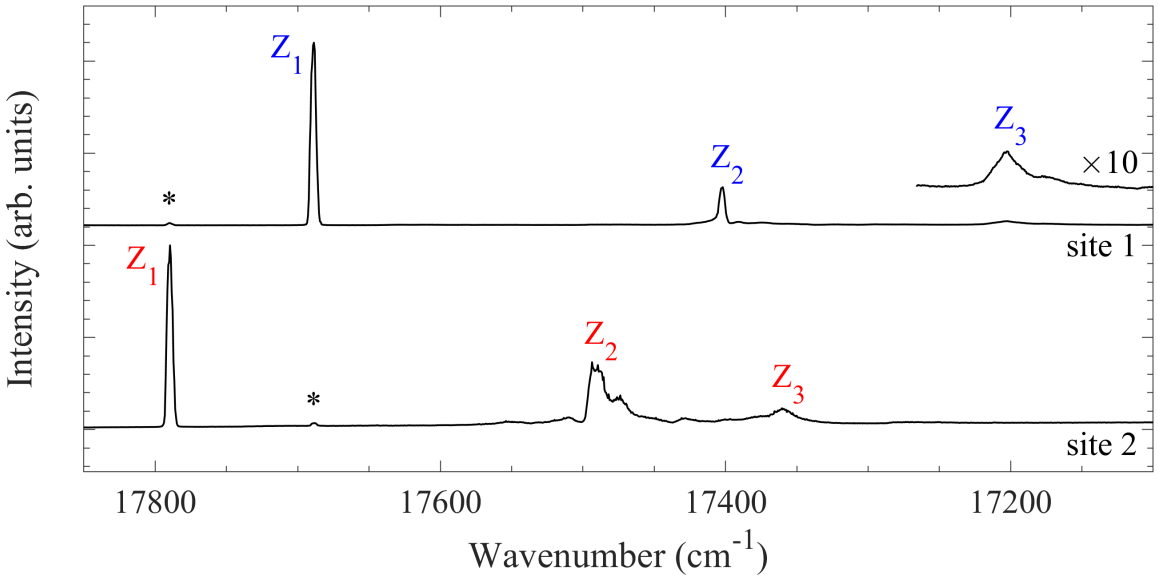

Figure 4.3: 10 K site-selective fluorescence spectra for site 1 (top, labelled in blue) and site 2 (bottom, labelled in red) of the $^6H_{5/2}$ multiplet in Y_2SiO_5:0.5%Sm^{3+} with the $^4G_{5/2}A_1 \longrightarrow {}^6H_{5/2}Z_i$ transitions labelled. The additional features seen around the Z_3 and Z_4 lines of both sites are due to vibronic transitions. The features labelled by an '*' is emission related to spectral features of the other site.

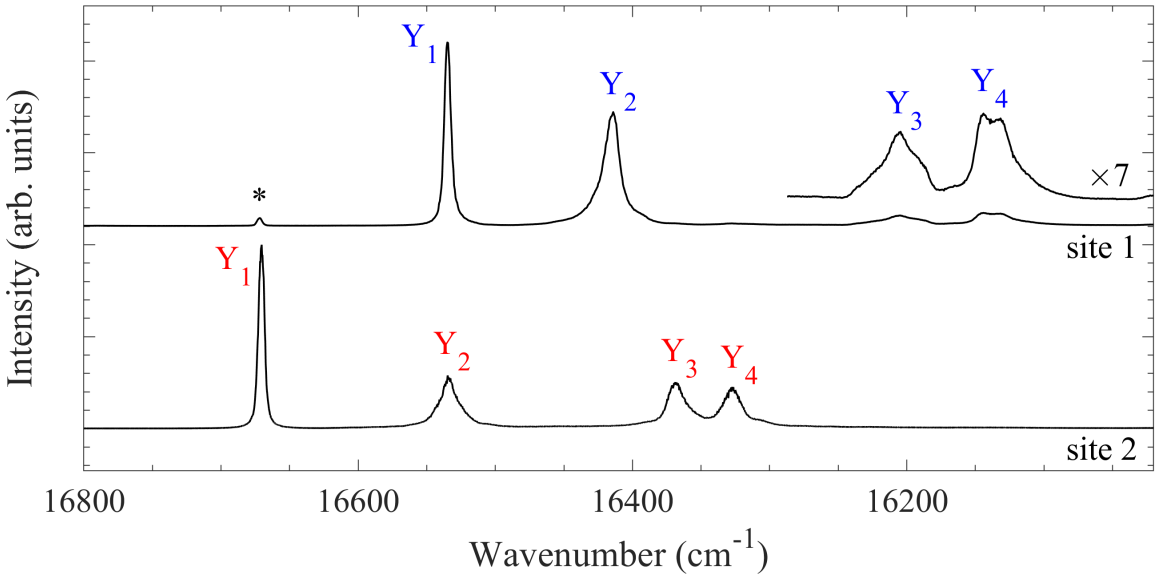

Figure 4.4: 10 K site-selective fluorescence spectra for site 1 (top, labelled in blue) and site 2 (bottom, labelled in red) of the $^6H_{7/2}$ multiplet in Y_2SiO_5:0.5%Sm^{3+} with the $^4G_{5/2}A_1 \longrightarrow {}^6H_{7/2}Y_i$ transitions labelled. The additional features seen around the Y_3 and Y_4 lines of both sites are due to vibronic transitions. The feature labelled by an '*' in the site 1 spectrum is emission related to site 2.

Figures 4.5 – 4.12 show site-selective fluorescence (top panels) and absorption spectra (bottom panels) of the $^6H_{9/2}$, $^6H_{11/2}$, $^6H_{13/2}$, $^6F_{1/2}$, $^6H_{15/2}$, $^6F_{3/2}$, $^6F_{5/2}$, $^6F_{7/2}$, $^6F_{9/2}$ and $^6F_{11/2}$ multiplets for both Sm^{3+} sites, measured at a sample temperature of 10 K. The excitation wavelength employed in order to obtain the fluorescence spectra for all multiplets was the $^6H_{5/2}Z_1 \longrightarrow {}^4G_{5/2}A_1$ transition at 17 689 cm^{-1} for site 1 and 17 790 cm^{-1} for site 2. All spectral features are labeled as either belonging to site 1 (blue) or site 2 (red). Spectral features marked with an '*' is emission due to the other site. Visible in most spectra in the mid infra-red region, up to the $^6F_{5/2}$ multiplet at $\sim$7000 cm^{-1} is absorption from atmospheric CO_2 and H_2O. Around many spectral lines in the $^6F_{7/2}$ – $^6F_{11/2}$ multiplets, as seen in Figures 4.10 – 4.12, are cluster sites which arises from the relatively high (0.5 %) concentration of our sample. All absorption spectra have been inverted and baseline corrected for clarity.

While all six expected spectral lines of the $^6F_{11/2}$ multiplet, as seen in Figure 4.12, was monitored for site 2, only five of the six spectral lines were observed for site 1. However, as all twelve spectral lines are visible in absorption, this allowed the remaining peak found in absorption, located at 10 920 cm^{-1}, to be inferred as belonging to site 1. This would put the fluorescence peak at 6774 cm^{-1}.

Site assignments for the $^6F_{1/2}$, $^6F_{3/2}$ and $^6H_{15/2}$ multiplets, as depicted in Figure 4.8, proved to be very difficult, as of the eleven spectral lines expected to be observed for either site, only three spectral lines for site 1, and seven spectral lines for site 2 could be observed in fluorescence for this spectral region. This is due to the photomultipler tubes used in this study being insensitive in this spectral range, in addition to the broad spectral line widths in this region (up to $\sim$20 cm^{-1}), reducing the ability to resolve individual spectral lines. A preliminary crystal-field fit was performed excluding data from this spectral region and then using the resulting theoretical values, the site assignments seen in Figure 4.8 could be made. A final crystal-field fit was then performed using these site assignments.

A total of 46 spectral lines for site 1 and 45 spectral lines for site 2 were assigned through the use of site-selective fluorescence spectroscopy. These values are summarised in Tables 4.5 and 4.6 for site 1 and 2 respectively.

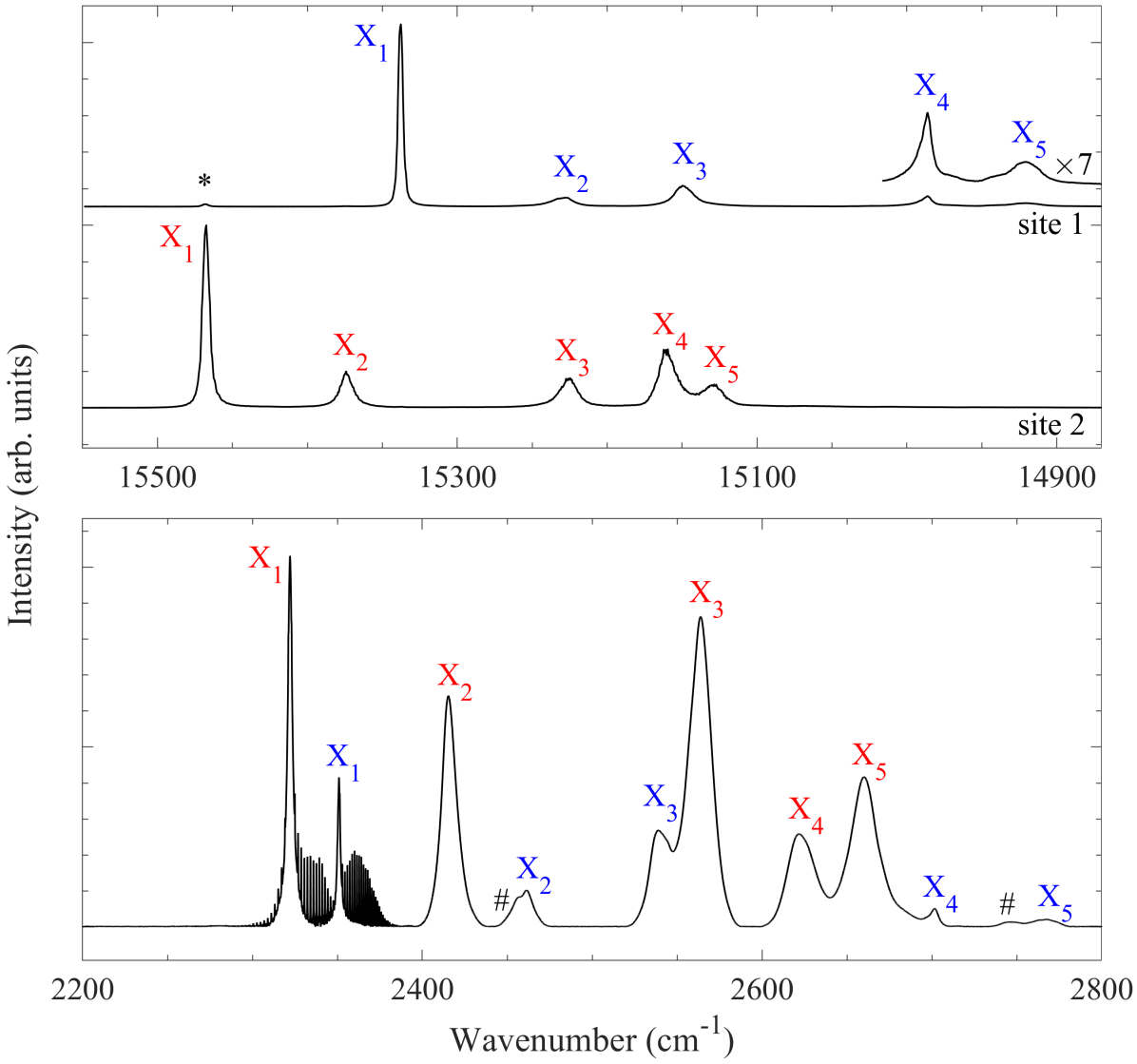

Figure 4.5: 10 K site-selective fluorescence (top) and absorption (bottom) spectra for site 1 (blue) and site 2 (red) of the $^6H_{9/2}$ multiplet in Y_2SiO_5:0.5%Sm^{3+} with the $^4G_{5/2}A_1 \longrightarrow {}^6H_{9/2}X_i$ transitions labelled. The feature labelled by an '*' in the site 1 spectrum is emission related to site 2. Spectral features labelled with a '#' are unrelated to Sm^{3+}:Y_2SiO_5. The extra structure found in absorption around the X_1 lines at 2300 – 2400 cm^{-1} is absorption due to atmospheric CO_2.

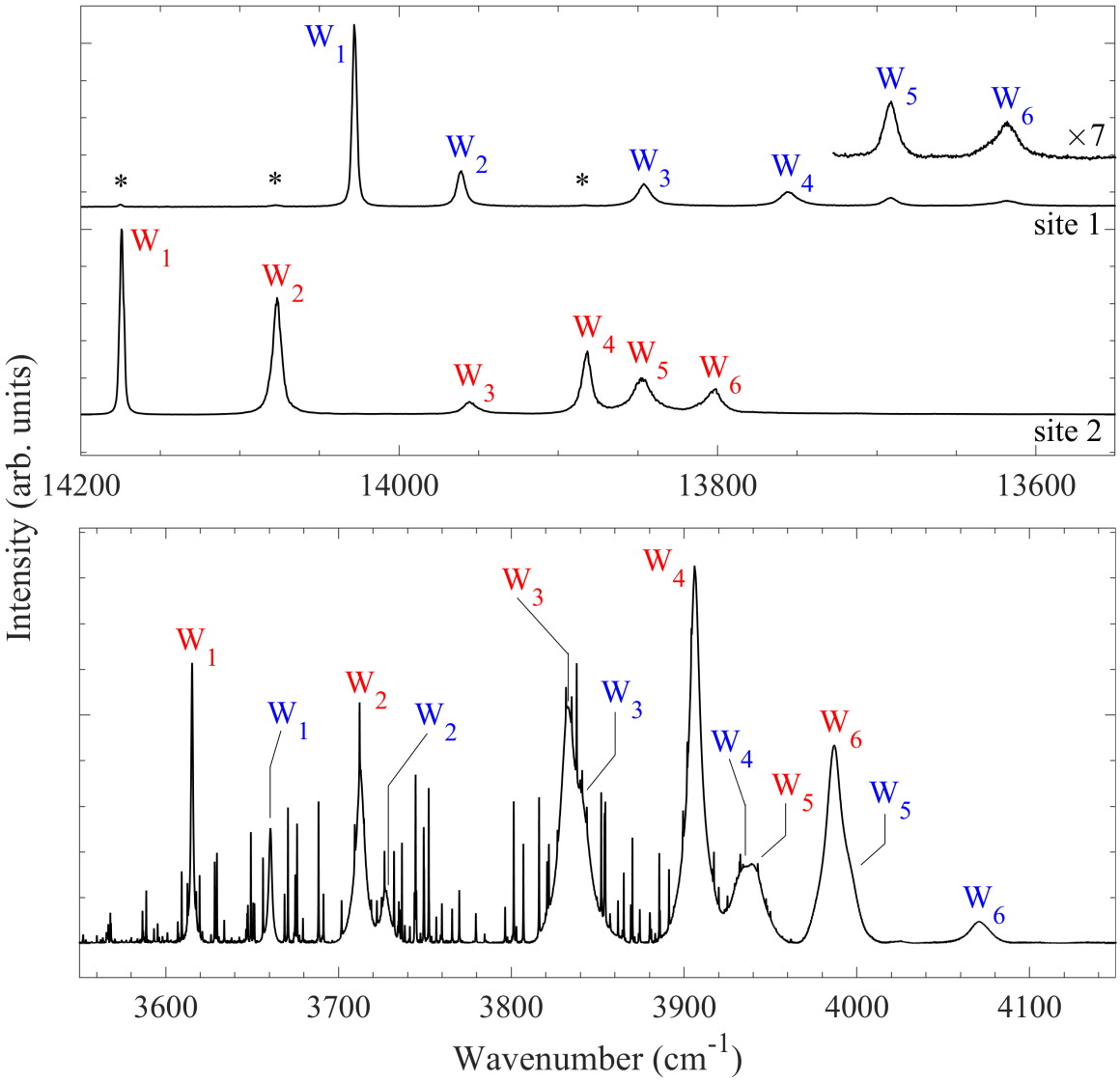

Figure 4.6: 10 K site-selective fluorescence (top) and absorption (bottom) spectra for site 1 (blue) and site 2 (red) of the $^6H_{11/2}$ multiplet in Y_2SiO_5:0.5%Sm^{3+} with the $^4G_{5/2}A_1 \longrightarrow {}^6H_{11/2}W_i$ transitions labelled. The features labelled by an '*' in the site 1 spectrum is emission related to site 2. The extra structure seen throughout the absorption spectrum is absorption due to atmospheric H_2O.

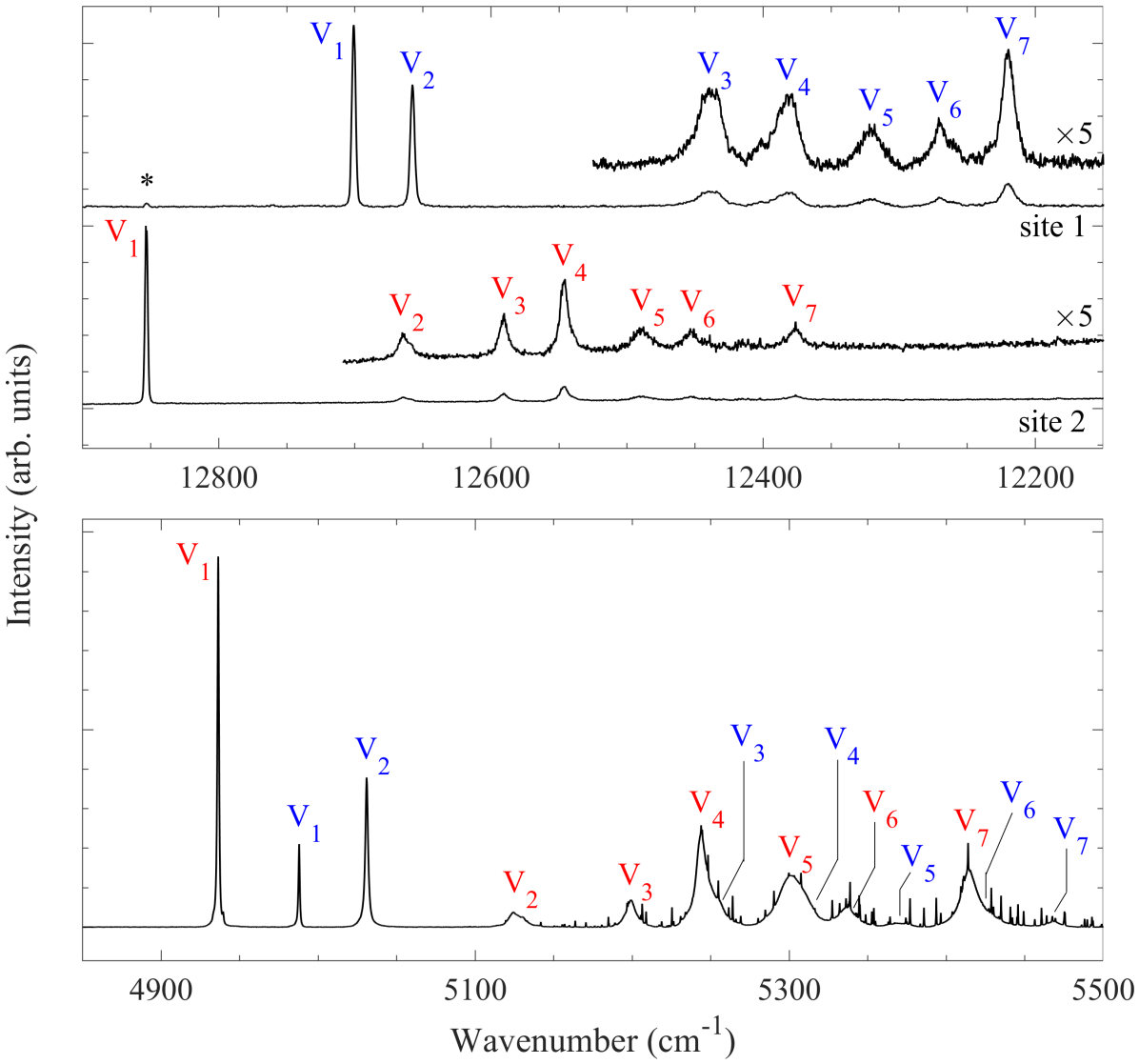

Figure 4.7: 10 K site-selective fluorescence (top) and absorption (bottom) spectra for site 1 (blue) and site 2 (red) of the $^6H_{13/2}$ multiplet in Y_2SiO_5:0.5%Sm^{3+} with the $^4G_{5/2}A_1 \longrightarrow {}^6H_{13/2}V_i$ transitions labelled. The features labelled by an '*' in the site 1 spectrum is emission related to site 2. The extra structure seen above 5100 cm^{-1} in the absorption spectrum is absorption due to atmospheric H_2O.

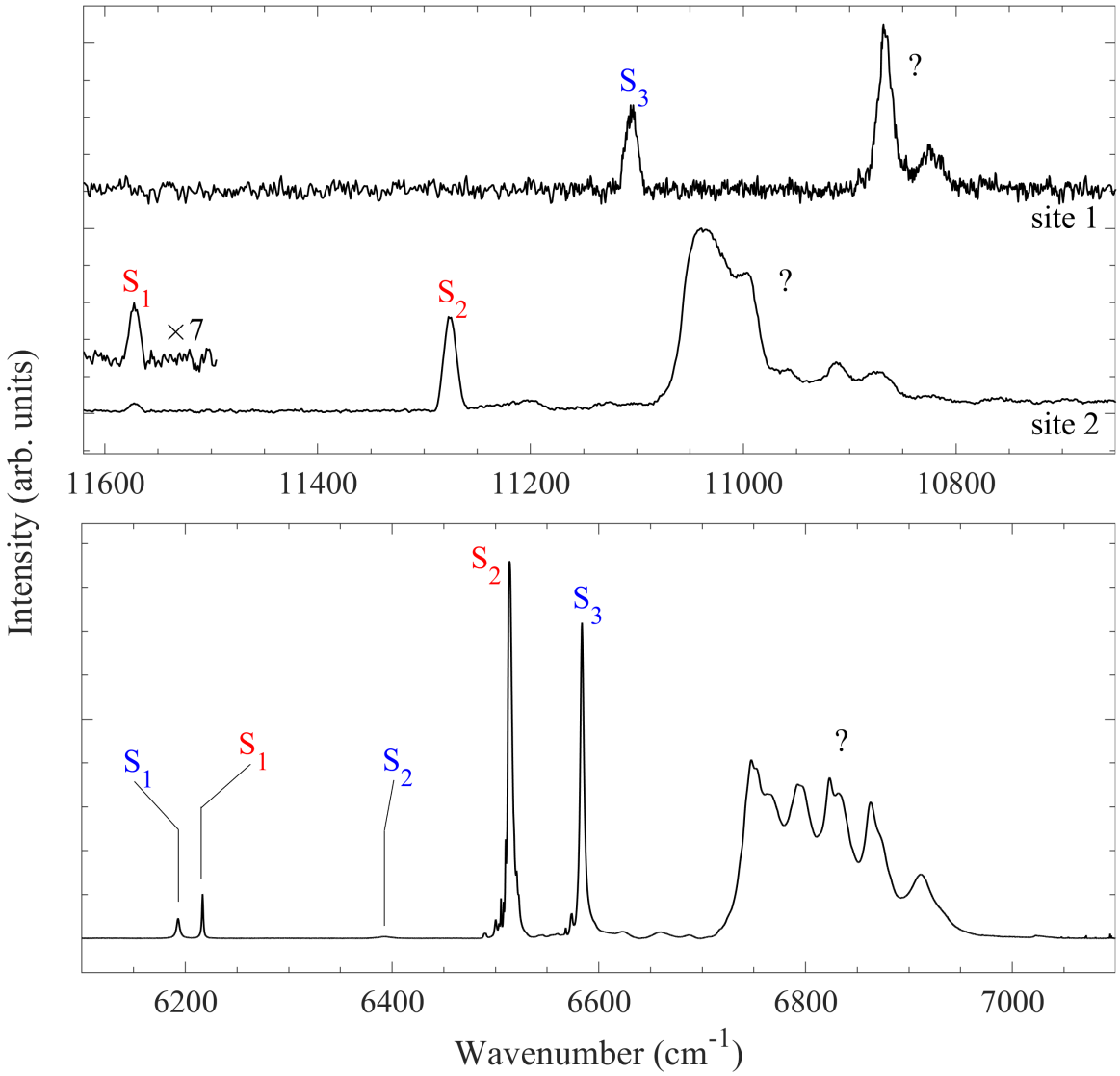

Figure 4.8: 10 K site-selective fluorescence (top) and absorption (bottom) spectra for site 1 (blue) and site 2 (red) of the $^6F_{1/2}$, $^6F_{3/2}$ and $^6H_{15/2}$ multiplets in Y_2SiO_5:0.5%Sm^{3+} with the assigned $^4G_{5/2}A_1 \longrightarrow {}^6F_{1/2}$, $^6F_{3/2}$ and $^6H_{15/2}S_i$ transitions labelled. The transitions marked with a '?' could not be assigned. The extra structure seen around the site 1 S_3 and site 2 S_2 lines are cluster sites which arises from the moderately high concentration of our sample.

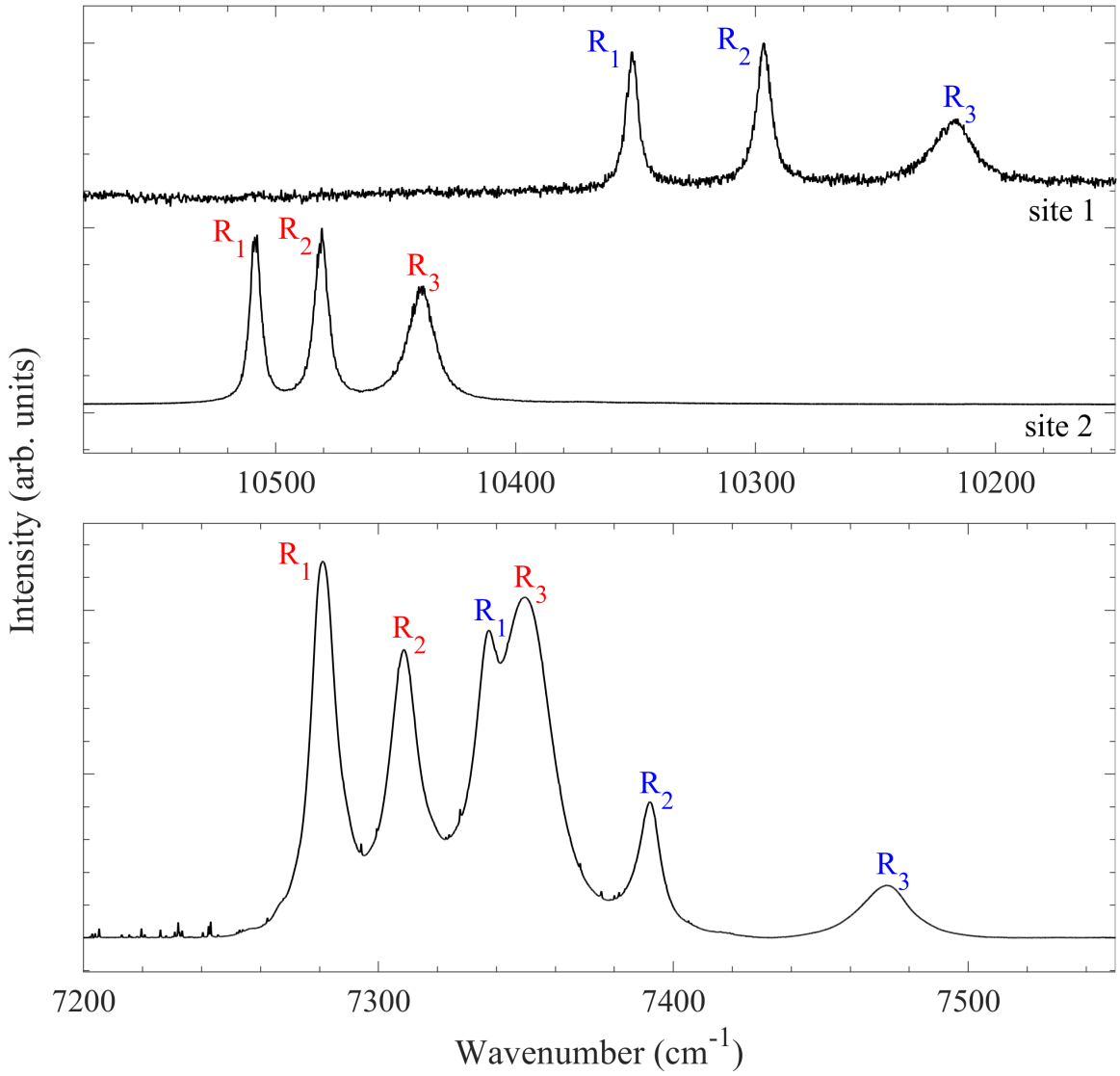

Figure 4.9: 10 K site-selective fluorescence (top) and absorption (bottom) spectra for site 1 (blue) and site 2 (red) of the $^6F_{5/2}$ multiplet in Y_2SiO_5:0.5%Sm^{3+} with the $^4G_{5/2}A_1 \longrightarrow {}^6F_{5/2}R_i$ transitions labelled. The extra structure found in absorption, seen below 7400 cm^{-1} in the bottom panel is absorption due to atmospheric H_2O.

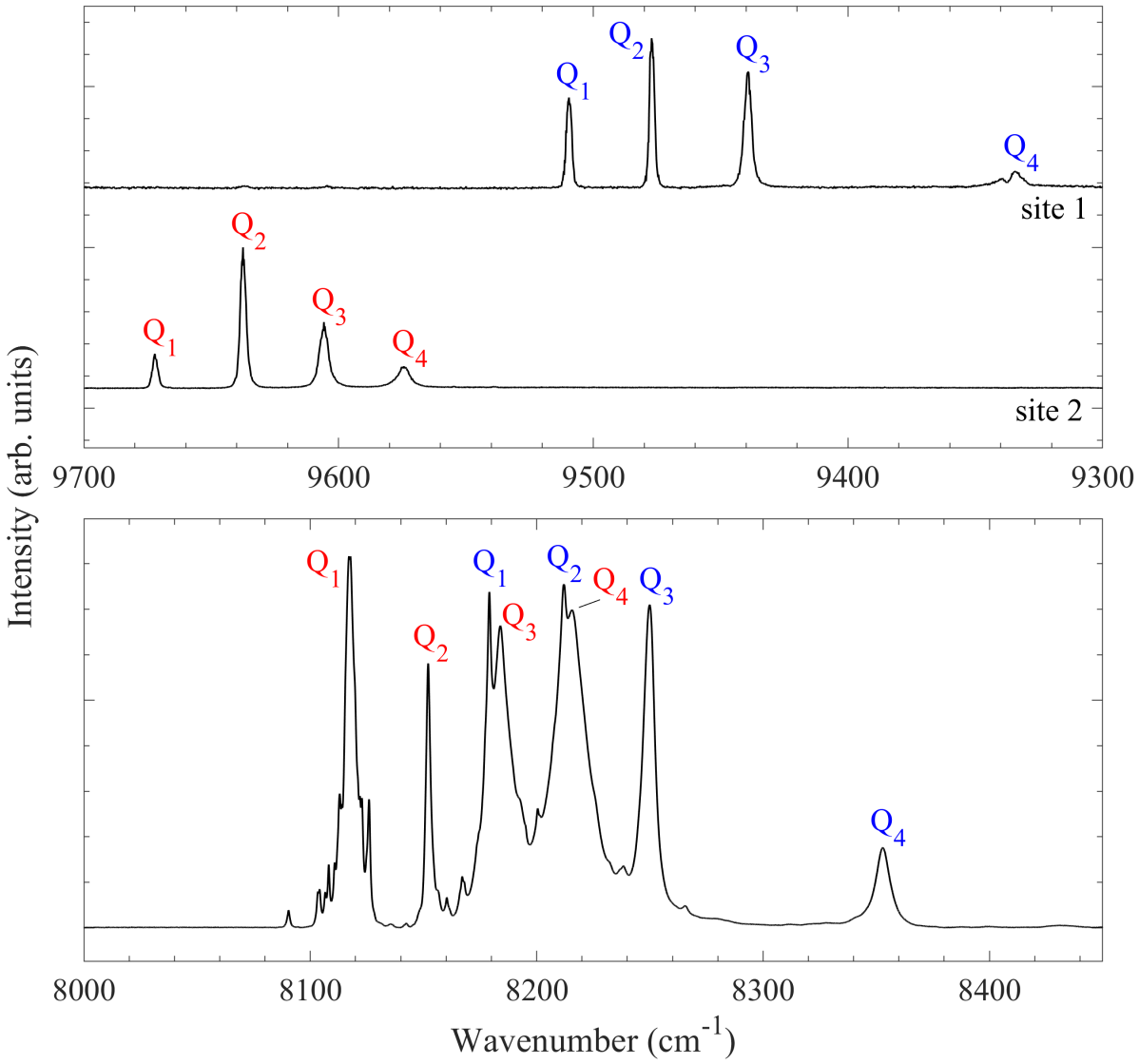

Figure 4.10: 10 K site-selective fluorescence (top) and absorption (bottom) spectra for site 1 (blue) and site 2 (red) of the $^6F_{7/2}$ multiplet in Y_2SiO_5:0.5%Sm^{3+} with the $^4G_{5/2}A_1 \longrightarrow {}^6F_{7/2}Q_i$ transitions labelled. The extra structure found in absorption are cluster sites which arises from the relatively high (0.5 %) concentration of our sample.

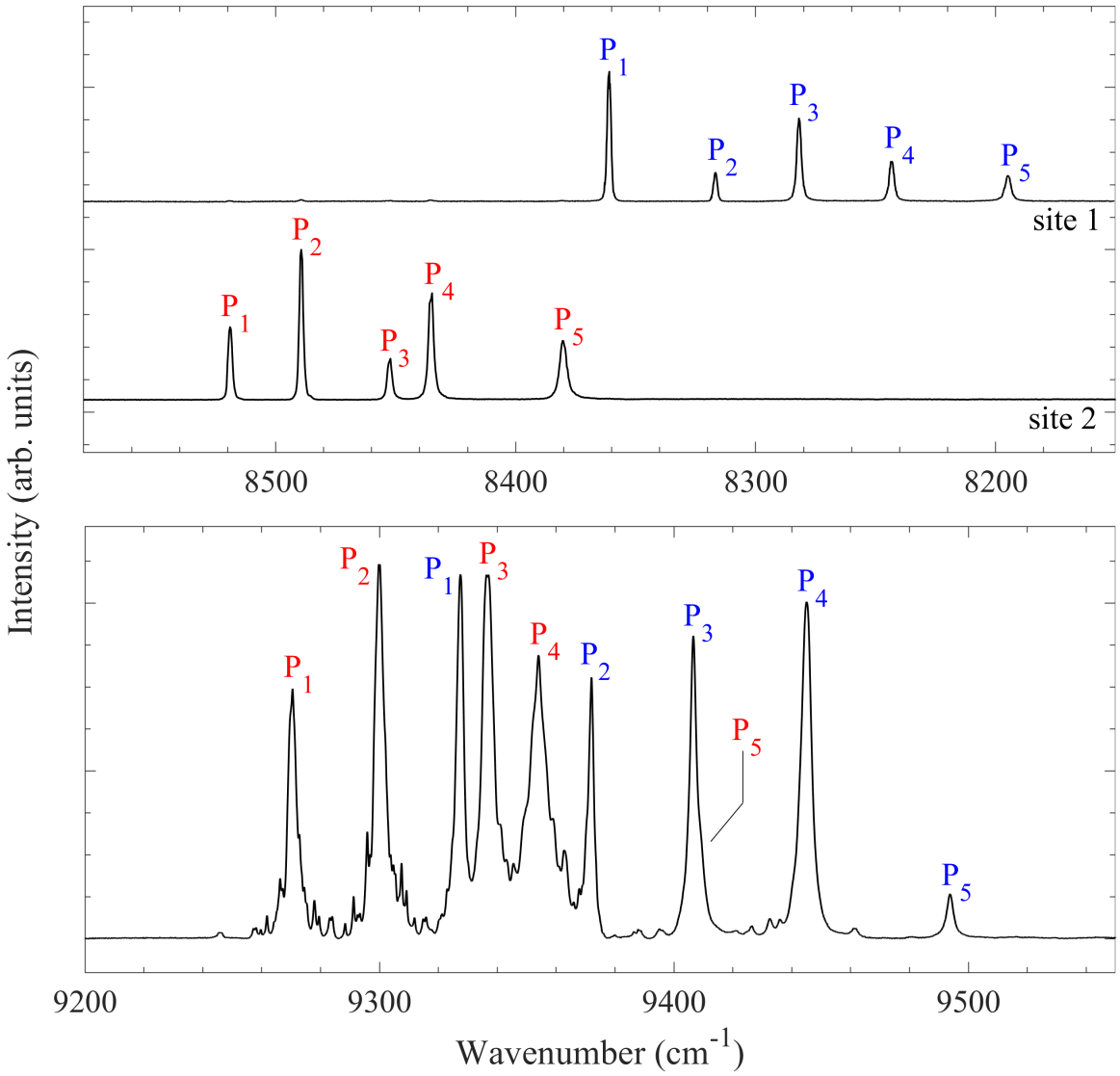

Figure 4.11: 10 K site-selective fluorescence (top) and absorption (bottom) spectra for site 1 (blue) and site 2 (red) of the $^6F_{9/2}$ multiplet in Y_2SiO_5:0.5%Sm^{3+} with the $^4G_{5/2}A_1 \longrightarrow {}^6F_{9/2}P_i$ transitions labelled. The extra structure found in absorption are cluster sites which arises from the relatively high (0.5 %) concentration of our sample.

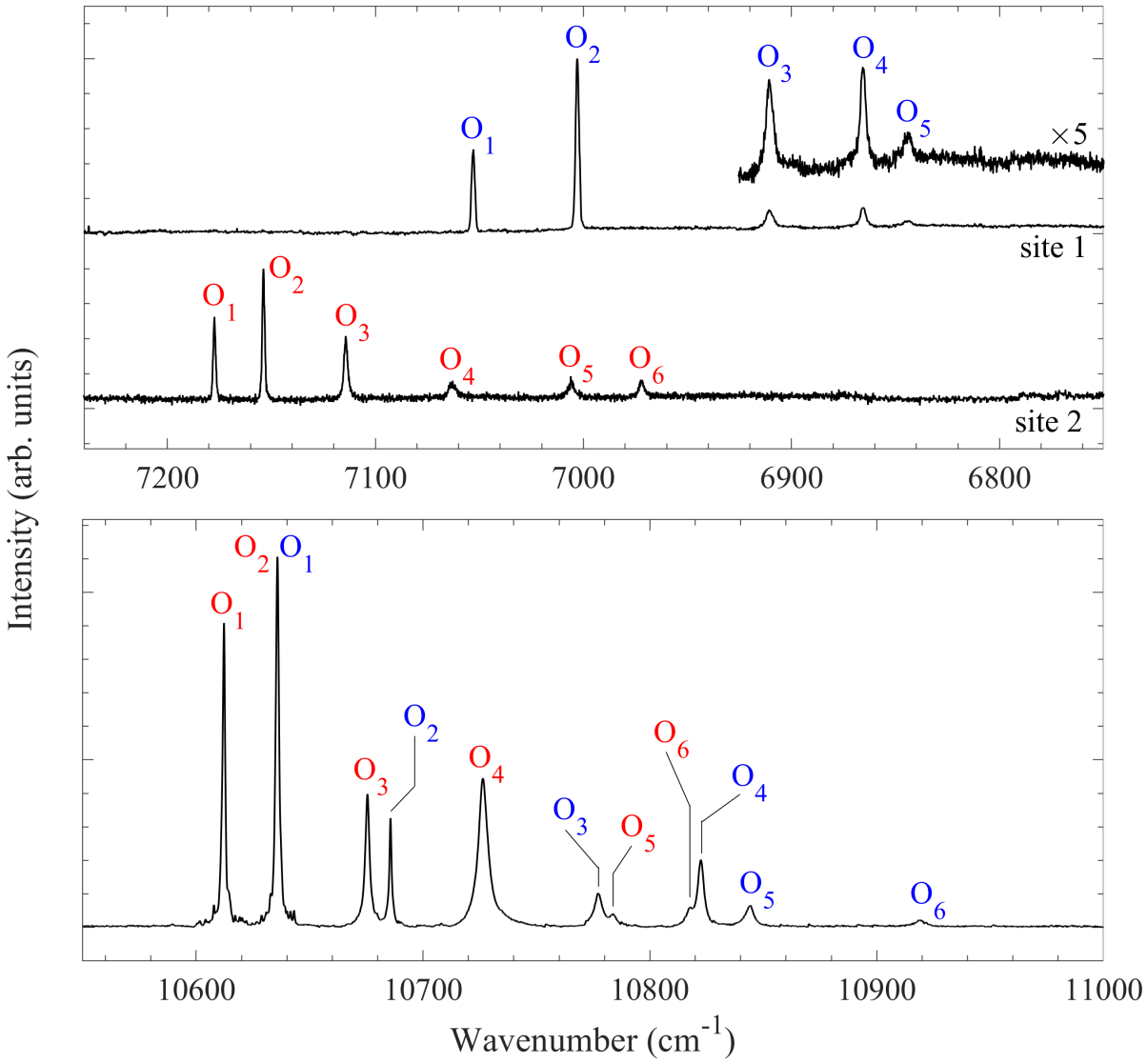

Figure 4.12: 10 K site-selective fluorescence (top) and absorption (bottom) spectra for site 1 (blue) and site 2 (red) of the $^6F_{11/2}$ multiplet in Y_2SiO_5:0.5%Sm^{3+} with the $^4G_{5/2}A_1 \longrightarrow {}^6F_{11/2}O_i$ transitions labelled. The extra structure found in absorption are cluster sites which arises from the relatively high (0.5 %) concentration of our sample.

4.2.2 Excitation and absorption spectroscopy

In addition to assigning spectral lines belonging to the ^6H_J and ^6F_J manifolds, it is possible to assign electronic states above this through the use of site-selective excitation spectroscopy. Here I stepped the laser through a multiplet, at an energy higher than the $^4G_{5/2}A_1$ state. The excitation then relaxed non-radiatively back to the $^4G_{5/2}A_1$ state before fluorescing to the ^6H_J and ^6F_J manifolds which were then monitored. This provided additional electronic energy levels, which was utilised in making a crystal-field model.

Site-selective excitation was able to be performed on the $^4G_{5/2}$, $^4F_{3/2}$, and $^4G_{7/2}$ multiplets, up to 20 000 cm^{-1}, and are shown in Figures 4.13, 4.14, and 4.15 respectively. Multiplets above 20 000 cm^{-1} could not be accurately measured due to inconsistent stepping of the laser, coupled with a high density of electronic states in this region. All absorption spectra have been inverted and baseline corrected for clarity.

Through performing excitation spectroscopy, an additional eight electronic energy levels were determined for both sites. With the levels found in fluorescence, a total of 54 levels for site 1 and 53 for site 2 were determined and employed in the the creation of a crystal-field model for Sm^{3+}:Y_2SiO_5. All experimentally determined energies are tabulated in Tables 4.5 and 4.6 for site 1 and 2 respectively.

Figure 4.13 depicts broadband excitation (top), site-selective excitation (middle) and absorption (bottom) spectra of the $^4G_{5/2}$ multiplet, all measured at 10 K. The broadband excitation spectrum was recorded by monitoring all $^4G_{5/2} \longrightarrow {}^6H_{9/2}$ transitions, centred at 15 300 cm^{-1}. Site-selective excitation of the $^4G_{5/2}$ multiplet was achieved by monitoring the $^4G_{5/2}A_1 \longrightarrow {}^6H_{9/2}X_1$ transition at 15 337 cm^{-1} for site 1 and the $^4G_{5/2}A_1 \longrightarrow {}^6H_{7/2}Y_1$ transition at 16 671 cm^{-1} for site 2. These transitions were chosen so there was no overlap with the laser or other spectral lines. The additional structure seen from 17 800 – 18 400 cm^{-1} in both the broadband excitation and site-selective excitation spectra are attributed to phonon sidebands.

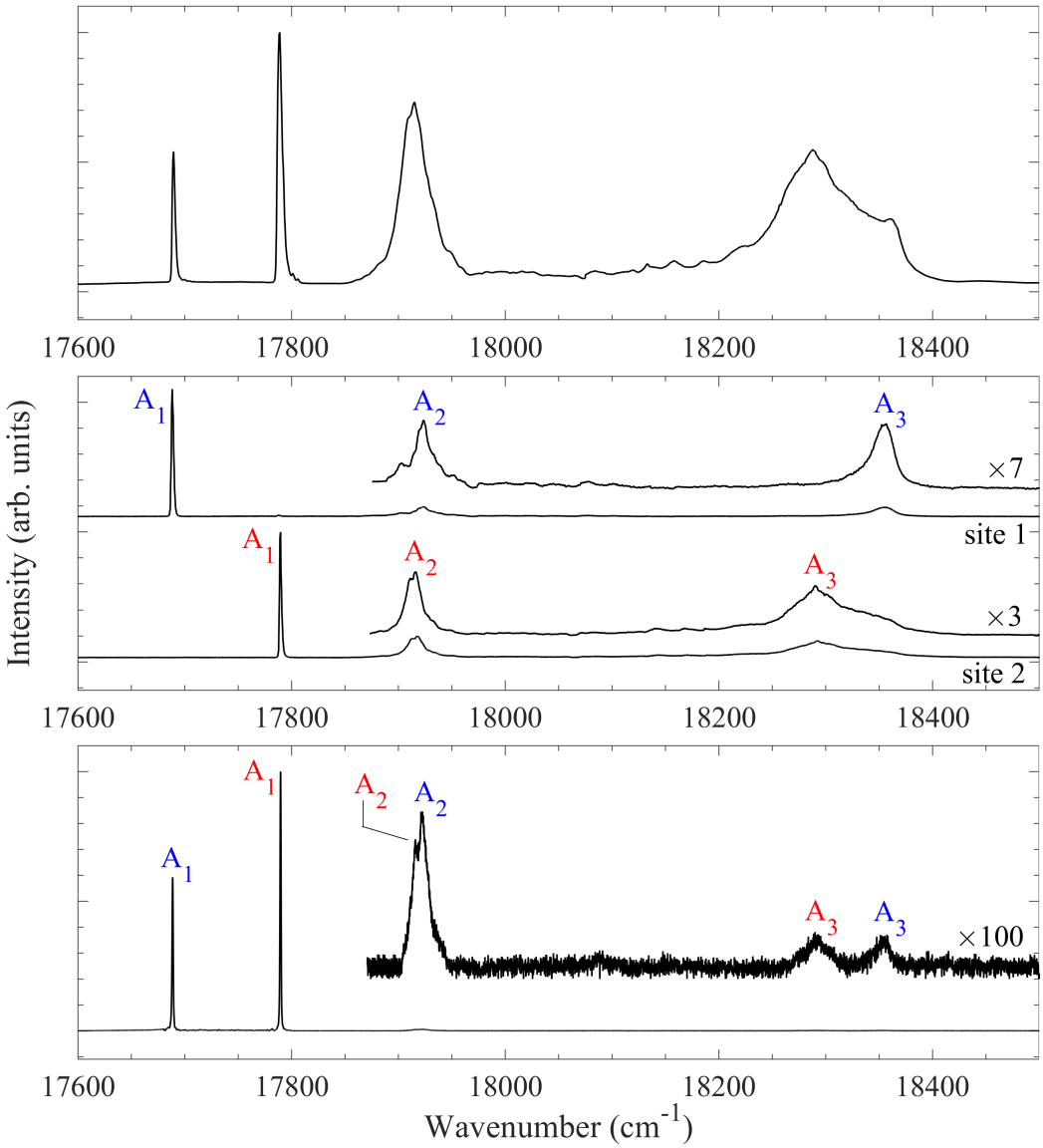

Figure 4.13: 10 K broadband excitation (top), site-selective excitation (middle) and absorption (bottom) spectra for the $^4G_{5/2}$ multiplet in Y_2SiO_5:0.5%Sm^{3+}. Transitions assigned to site 1 are in blue and those assigned to site 2 are in red.

Figure 4.14 depicts broadband excitation (top), site-selective excitation (middle) and absorption (bottom) spectra of the $^4F_{3/2}$ multiplet, all measured at 10 K. The broadband excitation spectrum was recorded by monitoring all $^4G_{5/2} \longrightarrow {}^6H_{9/2}$ transitions, centred around 15 300 cm^{-1}. The site-selective excitation spectra were recorded by monitoring fluorescence from the $^4G_{5/2}A_1 \longrightarrow {}^6H_{5/2}Z_1$ transitions at 17 689 cm^{-1} for site 1 and 17 790 cm^{-1} for site 2. The transitions marked with an '*' in the site 1 site-selective excitation spectrum is fluorescence related to site 2. This is indicative of inter-site energy transfer and will be further investigated in Section 5.2.

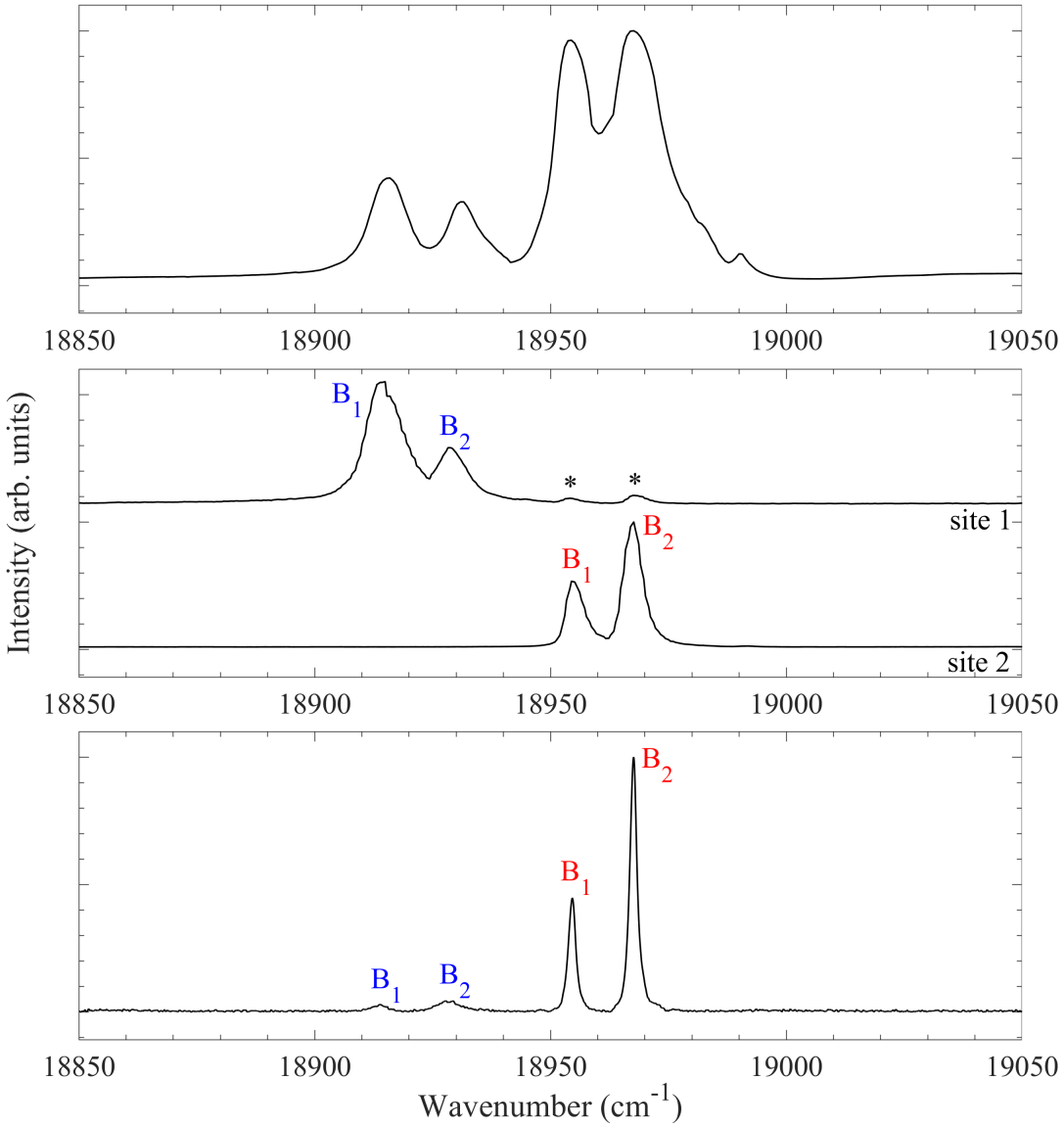

Figure 4.14: 10 K broadband excitation (top), site selective excitation (middle) and absorption (bottom) spectra for the $^4F_{3/2}$ multiplet in Y_2SiO_5:0.5%Sm^{3+}. Transitions assigned to site 1 are in blue and those assigned to site 2 are in red.

Figure 4.15 depicts broadband excitation (top), site-selective excitation (middle) and absorption (bottom) spectra of the $^4G_{7/2}$ multiplet, all measured at 10 K. Due to a non-linear scanning of the laser, coupled with a high density of electronic states above 20 000 cm^{-1}, only states up to the $^4G_{7/2}C_3$ state could be assigned for either site. The broadband excitation spectrum was recorded through monitoring all $^4G_{5/2} \longrightarrow {}^6H_{9/2}$ transitions, centred around 15 300 cm^{-1}. The site-selective excitation spectra were recorded by monitoring fluorescence from the $^4G_{5/2}A_1 \longrightarrow {}^6H_{5/2}Z_1$ transitions at 17 689 cm^{-1} for site 1 and 17 790 cm^{-1} for site 2.

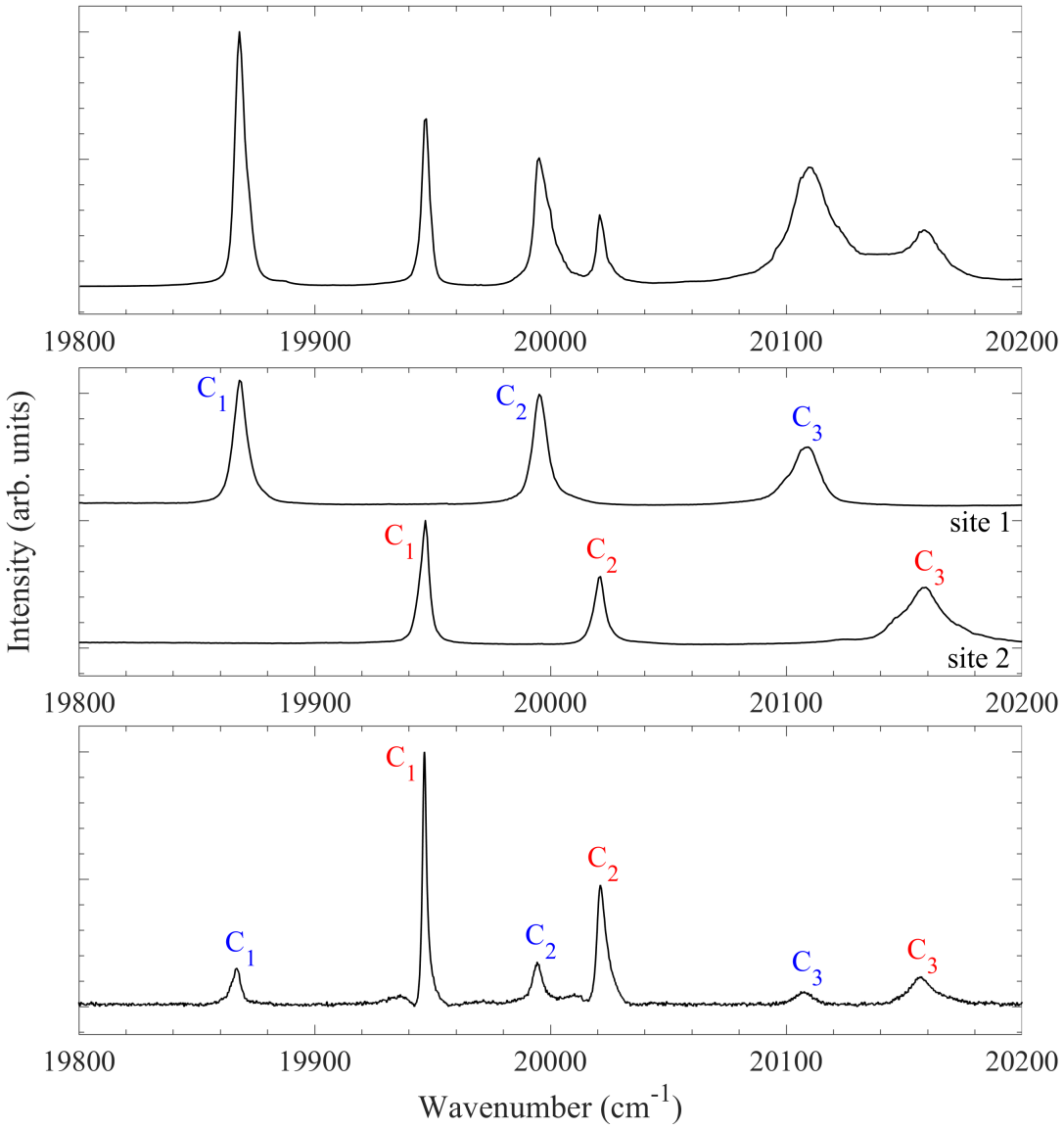

Figure 4.15: 10 K broadband excitation (top), site-selective excitation (middle) and absorption (bottom) spectra for the $^4G_{7/2}$ multiplet in Y_2SiO_5:0.5%Sm^{3+}. Transitions assigned to site 1 are in blue and those assigned to site 2 are in red.

4.3 Zeeman absorption spectroscopy

Zeeman spectroscopy was performed in order to complement the crystal-field fit, discussed in Section 4.5, with the addition of many magnetic g values, along all three crystallographic directions. This is required in order to determine the crystal-field orientation [138].

Zeeman absorption spectroscopy was performed along the D_1, D_2 and b axes using a Bruker Vertex-80 FTIR spectrometer and 4 Tesla superconducting magnet, see Section 3.4 for the experimental details. Spectra were obtained at 4.2 K for magnetic field strengths ranging from 0 T – 4 T in steps of 0.5 T for all multiplets from 2000 cm^{-1} to 20 000 cm^{-1}.

Figure 4.16 depicts a representative splitting diagram showing the magnetic field dependence of the $^6H_{5/2}Z_1 \longrightarrow {}^6H_{13/2}V_1$ transition for both sites along all three axes of Y_2SiO_5:0.5%Sm^{3+}. All spectra were measured at 4.2 K. The top, middle and bottom panels shows $B \parallel D_1$, $B \parallel D_2$ and $B \parallel b$ respectively. The left panels show the spectra while the right panels show the experimental splittings, represented by the circles, and the theoretical splittings (calculated from the crystal-field model developed in this study), represented by the red lines. The additional structure surrounding the site 2 line is attributed to cluster sites that formed within the crystal due to its relatively high Sm^{3+} concentration. The ground state magnetic g values along all three axes were found to be very small, with the largest magnetic g value being 0.52 for site 2 along the D_1 axis. When a magnetic field of 4 T is applied along the D_1 axis, the ground state for site 2 splits by $\sim$0.97 cm^{-1}. This is similar to the spectral line width of the narrowest line of Y_2SiO_5:0.5%Sm^{3+}, the site 2 V_1 line. Therefore, most spectral lines were observed to split into two transitions, instead of four, as the ground state splitting could not be resolved. In these cases, the observed splitting are purely attributed to the various excited states with ground state splitting being considered negligible. The excited states g values, g_e, were then calculated using:

$$g_e = \frac{\Delta E}{\mu_B B} \tag{4.1}$$

Where ΔE is the energy difference of the two spectral lines, μ_B is the Bohr magneton and B is the magnetic field strength.

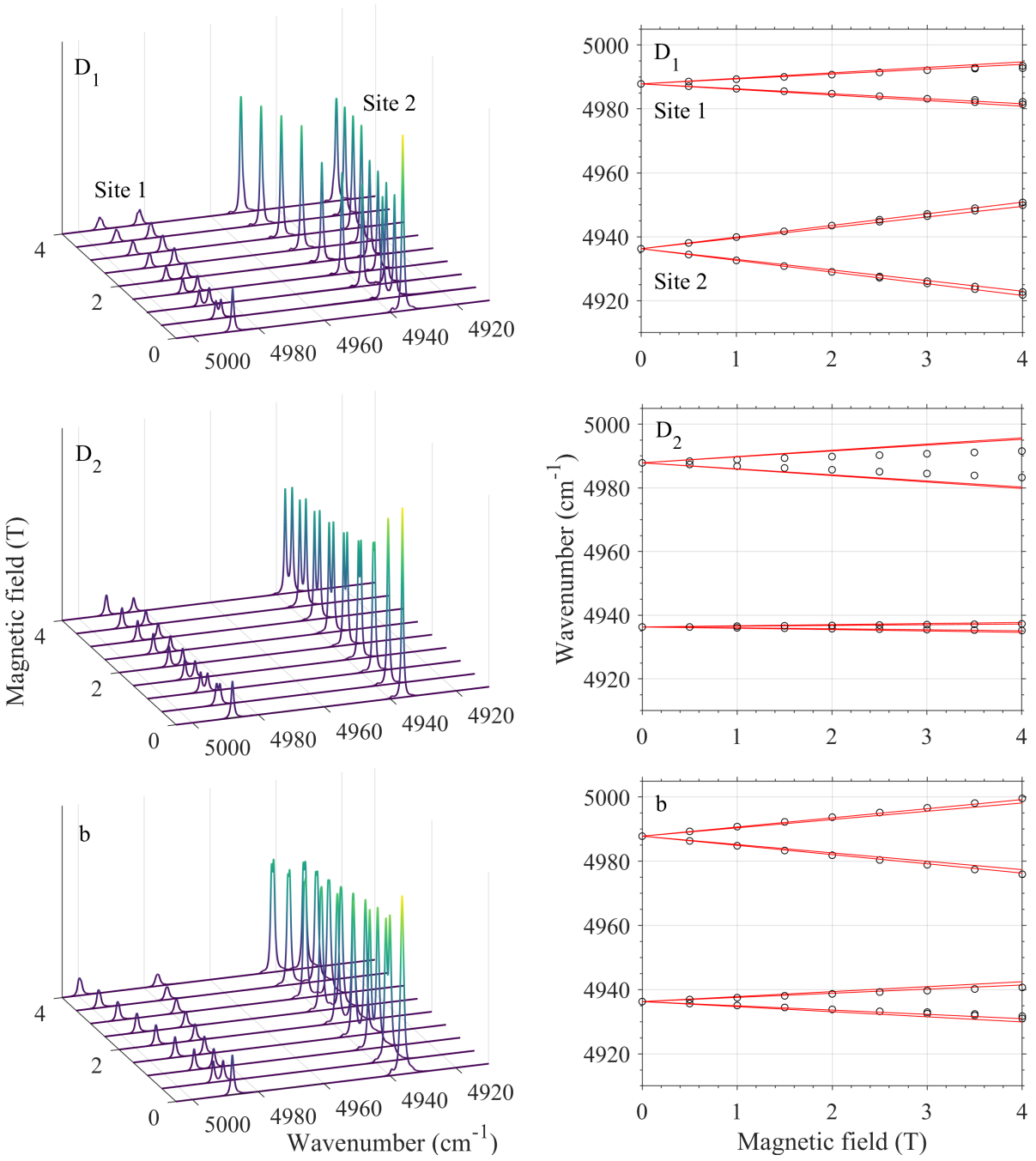

Figure 4.16: Magnetic splittings of the $^6H_{5/2}Z_1 \rightarrow {}^6H_{13/2}V_1$ transition of both sites in Y_2SiO_5:0.5%Sm^{3+} with a magnetic field applied along the three crystallographic axes of Y_2SiO_5. The top, middle and bottom panels shows $B \parallel D_1$, $B \parallel D_2$ and $B \parallel b$ respectively. The left panels show Zeeman absorption spectra at magnetic fields ranging from 0 T $\longrightarrow$ 4 T. The right panels show the experimental splittings, represented by the circles, and the theoretical splittings are represented by the red lines. All spectra were measured at 4.2 K.

Figures 4.17 - 4.38 depicts the magnetic splittings from the $^6H_{5/2}Z_1$ ground state to each assigned excited state from the $^6H_{9/2}$ to $^4G_{7/2}$ multiplet for both sites in Y_2SiO_5:0.005%Er^{3+}. Zeeman spectroscopy could not be performed on the $^6H_{5/2}$ or $^6H_{7/2}$ multiplets due to these multiplets being located below the two phonon absorption cutoff of Y_2SiO_5 at $\sim$2000 cm^{-1}. For each transition the top, middle and bottom panels shows the magnetic splittings with $B \parallel D_1$, $B \parallel D_2$ and $B \parallel b$ respectively. The left panels of each figure show the experimental splittings, represented by the circles, while the theoretical splittings, calculated from our crystal-field model (presented in Section 4.5), are represented by the red lines. The right panels of each transition show Zeeman absorption spectra at a magnetic field represented by the vertical line in the left panels.

A total of 72 g values (25 along the D_1 axis, 22 along the D_2 axis and 25 along the b axis) for site 1 and 92 g values (34 along the D_1 axis, 28 along the D_2 axis and 30 along the b axis) for site 2 were determined utilising Zeeman spectroscopy. These g values are summarised in Tables 4.5 and 4.6 for site 1 and site 2 respectively. The g values were determined by applying Equation (4.1) to spectra that are at sufficiently high magnetic field strengths where each state has resolved into two transitions, but not too high so that the transitions becomes noticeably non-linear due to interactions between Stark levels. g values could only be found for states that have a g value large enough for the splitting to be resolved relative to the states line width. In the cases where a g value could not be determined, the monitored splittings are, in general, well described by our crystal field model. Some transitions do not split as seen in, for example, the X_3 spectral lines of both sites, depicted in Figures 4.17 and 4.18.

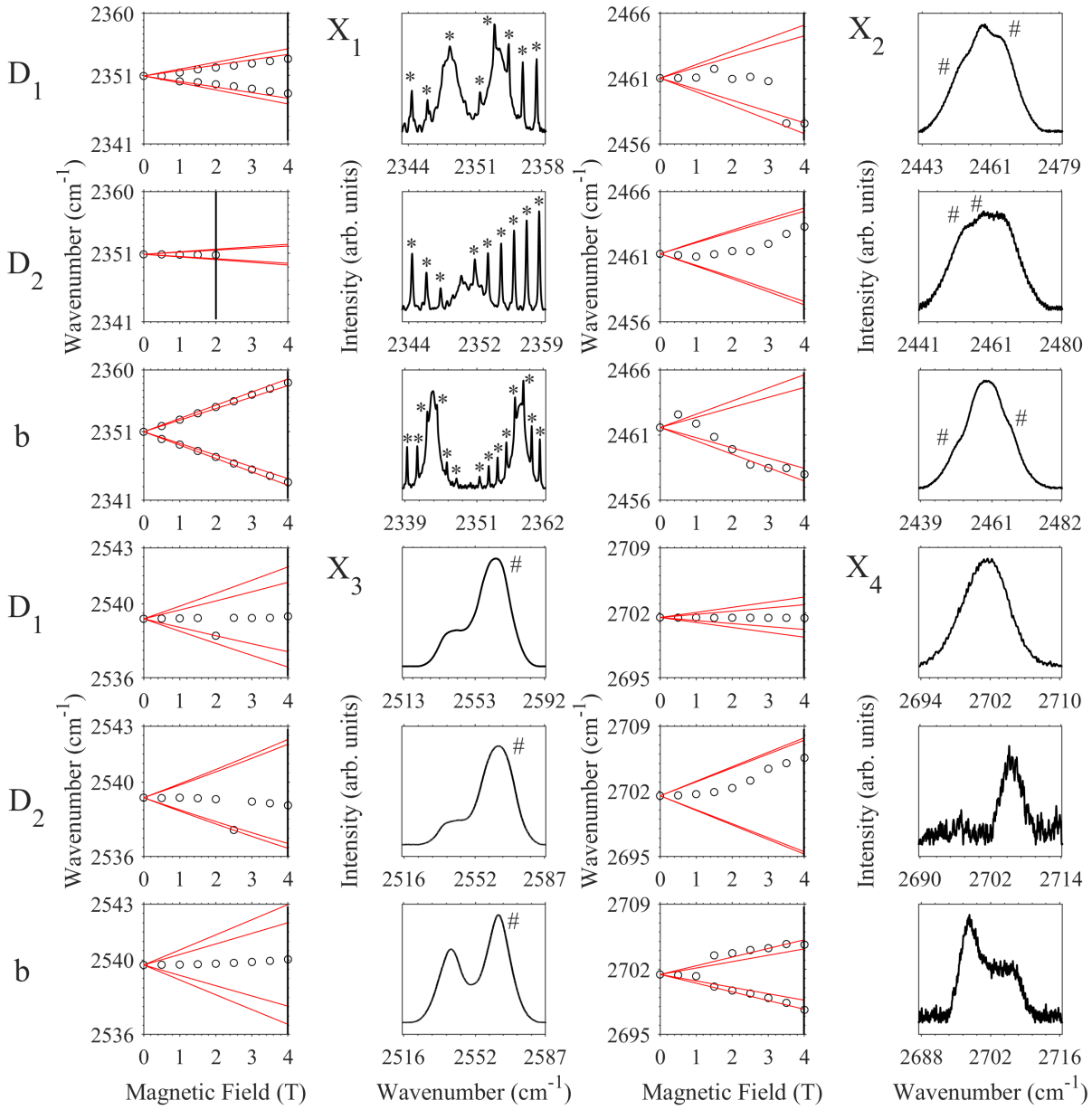

Figure 4.17: Magnetic splittings of the $^6H_{5/2}Z_1 \longrightarrow {}^6H_{9/2}X_i$ transitions for site 1 in Y_2SiO_5:0.5%Sm^{3+} with a magnetic field applied along the three crystallographic axes of Y_2SiO_5. The top, middle and bottom panels for each $Z_1 \longrightarrow X_i$ transition shows the magnetic splittings with $B \parallel D_1$, $B \parallel D_2$ and $B \parallel b$ respectively. The left panels depicts the experimental splittings, represented by the circles, and the theoretical splittings are represented by the red lines. The right panels shows Zeeman absorption spectra at a magnetic field represented by the vertical line in the left panels. All spectra were measured at 4.2 K. Spectral features labelled with a '#' are transitions not related to site 1 of Y_2SiO_5:0.5%Sm^{3+}. Spectral features labelled with an '*' is absorption due to carbon dioxide. Figure is continued over page.

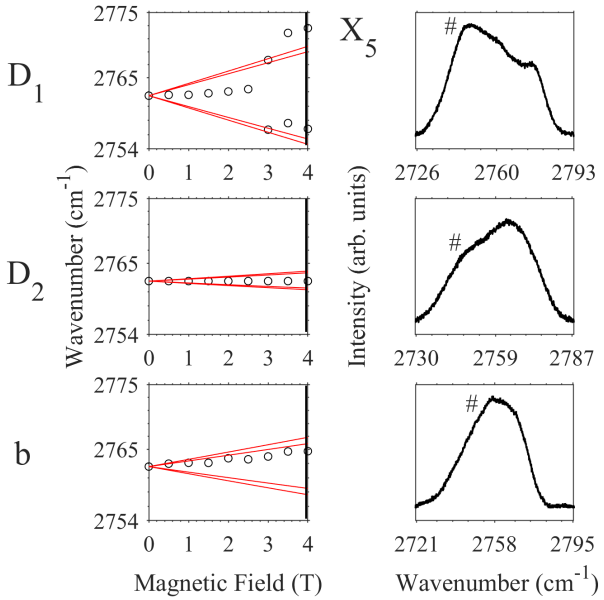

Figure 4.17: Magnetic splittings of the $^6H_{5/2}Z_1 \longrightarrow {}^6H_{9/2}X_i$ transitions for site 1 in Y_2SiO_5:0.5%Sm^{3+} with a magnetic field applied along the three crystallographic axes of Y_2SiO_5. The top, middle and bottom panels for each $Z_1 \longrightarrow X_i$ transition shows the magnetic splittings with $B \parallel D_1$, $B \parallel D_2$ and $B \parallel b$ respectively. The left panels depicts the experimental splittings, represented by the circles, and the theoretical splittings are represented by the red lines. The right panels shows Zeeman absorption spectra at a magnetic field represented by the vertical line in the left panels. All spectra were measured at 4.2 K. Spectral features labelled with a '#' are transitions not related to site 1 of Y_2SiO_5:0.5%Sm^{3+}.

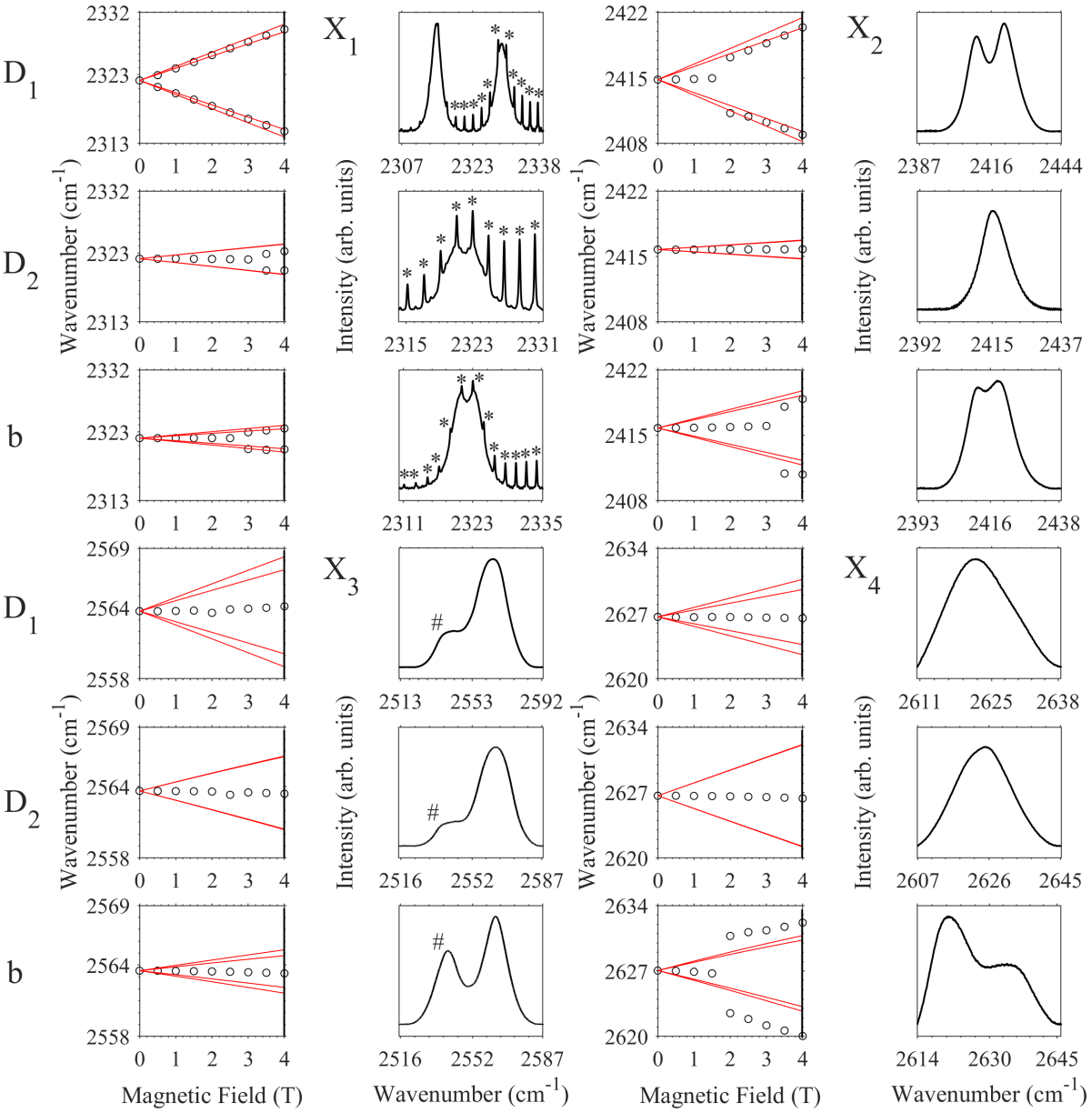

Figure 4.18: Magnetic splittings of the $^6H_{5/2}Z_1 \longrightarrow {}^6H_{9/2}X_i$ transitions for site 2 in Y_2SiO_5:0.5%Sm^{3+} with a magnetic field applied along the three crystallographic axes of Y_2SiO_5. The top, middle and bottom panels for each $Z_1 \longrightarrow X_i$ transition shows the magnetic splittings with $B \parallel D_1$, $B \parallel D_2$ and $B \parallel b$ respectively. The left panels depicts the experimental splittings, represented by the circles, and the theoretical splittings are represented by the red lines. The right panels shows Zeeman absorption spectra at a magnetic field represented by the vertical line in the left panels. All spectra were measured at 4.2 K. Spectral features labelled with a '#' are transitions not related to site 2 of Y_2SiO_5:0.5%Sm^{3+}. Spectral features labelled with an '*' is absorption due to carbon dioxide. Figure is continued over page.

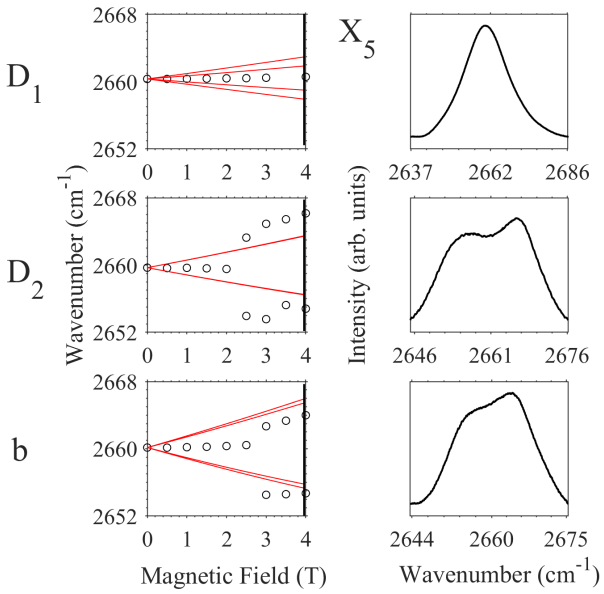

Figure 4.18: Magnetic splittings of the $^6H_{5/2}Z_1 \longrightarrow {}^6H_{9/2}X_i$ transitions for site 2 in Y_2SiO_5:0.5%Sm^{3+} with a magnetic field applied along the three crystallographic axes of Y_2SiO_5. The top, middle and bottom panels for each $Z_1 \longrightarrow X_i$ transition shows the magnetic splittings with $B \parallel D_1$, $B \parallel D_2$ and $B \parallel b$ respectively. The left panels depicts the experimental splittings, represented by the circles, and the theoretical splittings are represented by the red lines. The right panels shows Zeeman absorption spectra at a magnetic field represented by the vertical line in the left panels. All spectra were measured at 4.2 K. Spectral features labelled with a '#' are transitions not related to site 2 of Y_2SiO_5:0.5%Sm^{3+}.

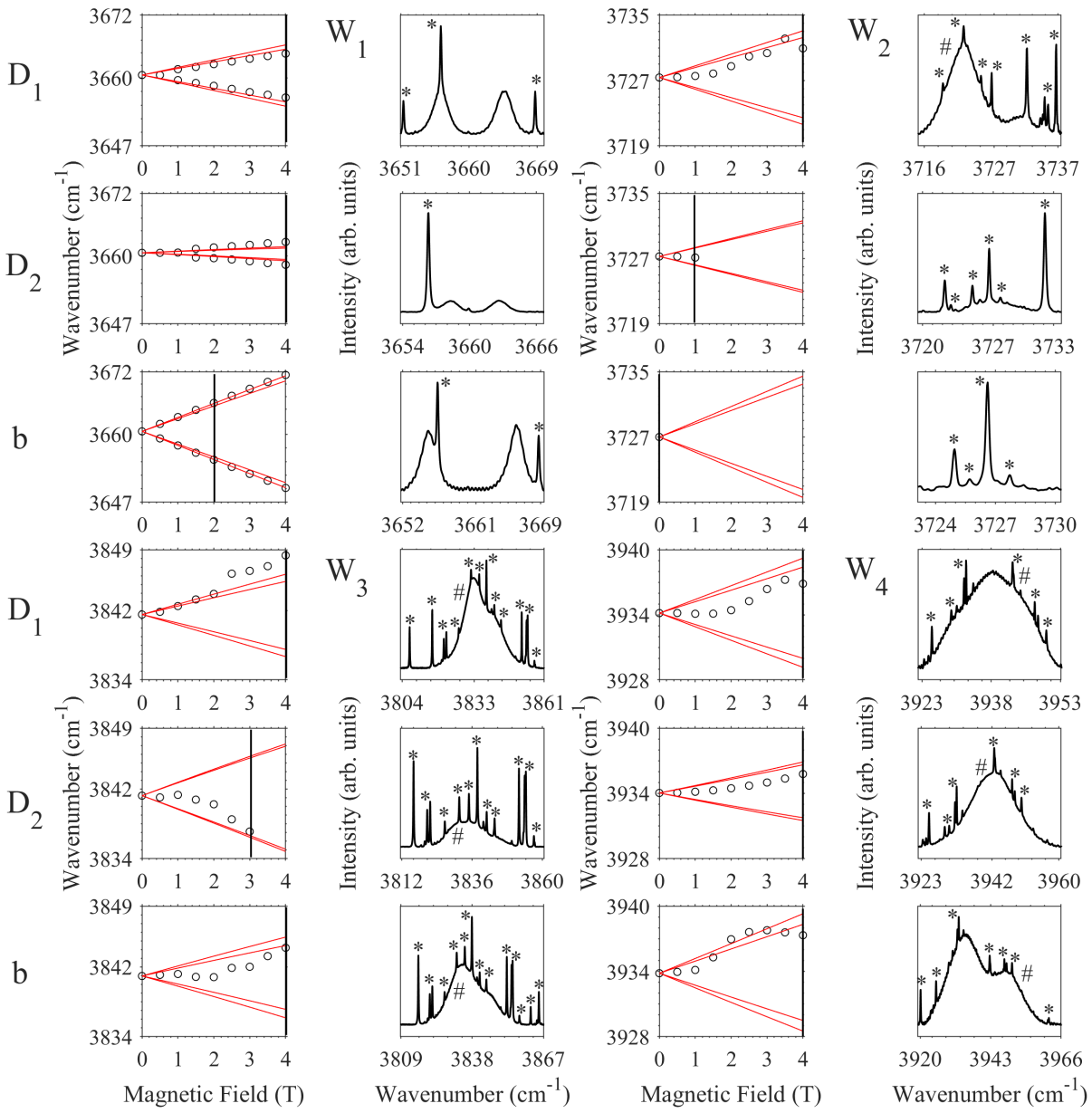

Figure 4.19: Magnetic splittings of the $^6H_{5/2}Z_1 \longrightarrow {}^6H_{11/2}W_i$ transitions for site 1 in Y_2SiO_5:0.5%Sm^{3+} with a magnetic field applied along the three crystallographic axes of Y_2SiO_5. The top, middle and bottom panels for each $Z_1 \longrightarrow W_i$ transition shows the magnetic splittings with $B \parallel D_1$, $B \parallel D_2$ and $B \parallel b$ respectively. The left panels depicts the experimental splittings, represented by the circles, and the theoretical splittings are represented by the red lines. The right panels shows Zeeman absorption spectra at a magnetic field represented by the vertical line in the left panels. All spectra were measured at 4.2 K. Spectral features labelled with a '#' are transitions not related to site 1 of Y_2SiO_5:0.5%Sm^{3+}. Spectral features labelled with an '*' is absorption due to water. Figure is continued over page.

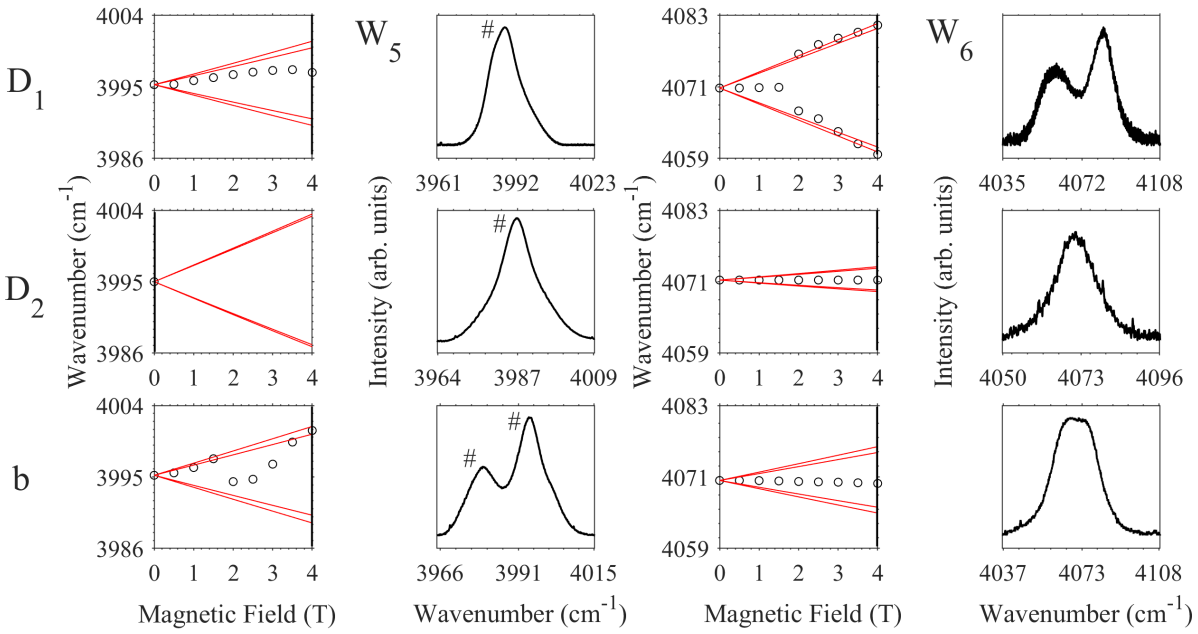

Figure 4.19: Magnetic splittings of the $^6H_{5/2}Z_1 \longrightarrow {}^6H_{11/2}W_i$ transitions for site 1 in Y_2SiO_5:0.5%Sm^{3+} with a magnetic field applied along the three crystallographic axes of Y_2SiO_5. The top, middle and bottom panels for each $Z_1 \longrightarrow W_i$ transition shows the magnetic splittings with $B \parallel D_1$, $B \parallel D_2$ and $B \parallel b$ respectively. The left panels depicts the experimental splittings, represented by the circles, and the theoretical splittings are represented by the red lines. The right panels shows Zeeman absorption spectra at a magnetic field represented by the vertical line in the left panels. All spectra were measured at 4.2 K. Spectral features labelled with a '#' are transitions not related to site 1 of Y_2SiO_5:0.5%Sm^{3+}.

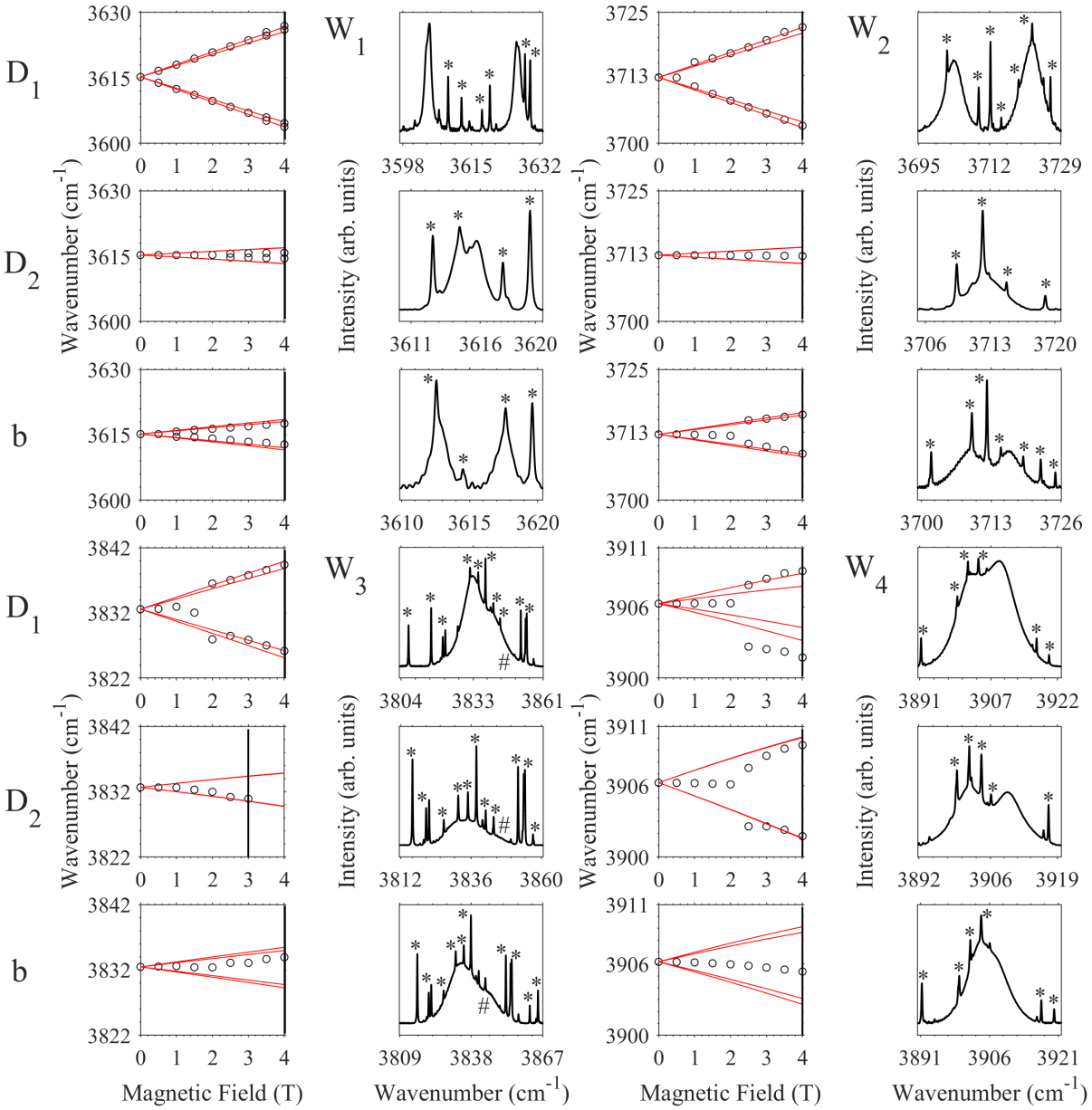

Figure 4.20: Magnetic splittings of the $^6H_{5/2}Z_1 \longrightarrow {}^6H_{11/2}W_i$ transitions for site 2 in Y_2SiO_5:0.5%Sm^{3+} with a magnetic field applied along the three crystallographic axes of Y_2SiO_5. The top, middle and bottom panels for each $Z_1 \longrightarrow W_i$ transition shows the magnetic splittings with $B \parallel D_1$, $B \parallel D_2$ and $B \parallel b$ respectively. The left panels depicts the experimental splittings, represented by the circles, and the theoretical splittings are represented by the red lines. The right panels shows Zeeman absorption spectra at a magnetic field represented by the vertical line in the left panels. All spectra were measured at 4.2 K. Spectral features labelled with a '#' are transitions not related to site 2 of Y_2SiO_5:0.5%Sm^{3+}. Spectral features labelled with an '*' is absorption due to water. Figure is continued over page.

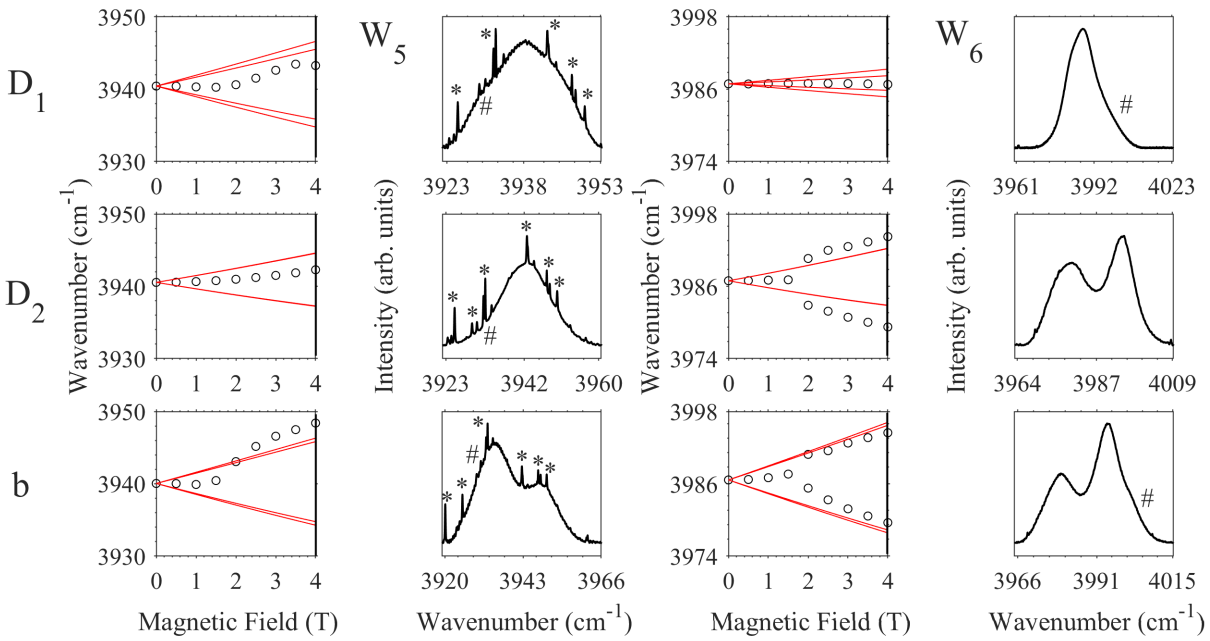

Figure 4.20: Magnetic splittings of the $^6H_{5/2}Z_1 \longrightarrow {}^6H_{11/2}W_i$ transitions for site 2 in Y_2SiO_5:0.5%Sm^{3+} with a magnetic field applied along the three crystallographic axes of Y_2SiO_5. The top, middle and bottom panels for each $Z_1 \longrightarrow W_i$ transition shows the magnetic splittings with $B \parallel D_1$, $B \parallel D_2$ and $B \parallel b$ respectively. The left panels depicts the experimental splittings, represented by the circles, and the theoretical splittings are represented by the red lines. The right panels shows Zeeman absorption spectra at a magnetic field represented by the vertical line in the left panels. All spectra were measured at 4.2 K. Spectral features labelled with a '#' are transitions not related to site 2 of Y_2SiO_5:0.5%Sm^{3+}. Spectral features labelled with an '*' is absorption due to water.

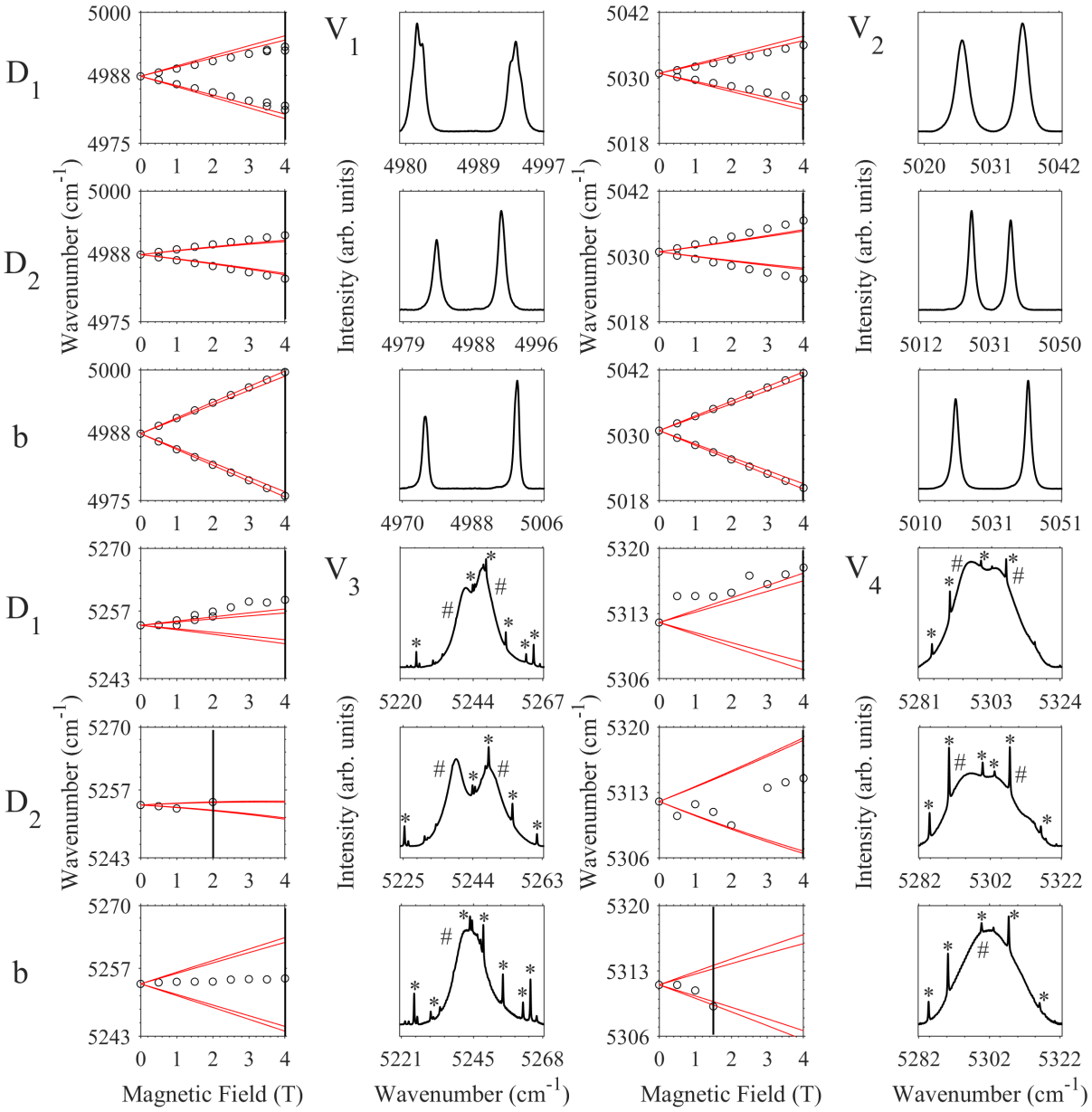

Figure 4.21: Magnetic splittings of the $^6H_{5/2}Z_1 \longrightarrow {}^6H_{13/2}V_i$ transitions for site 1 in Y_2SiO_5:0.5%Sm^{3+} with a magnetic field applied along the three crystallographic axes of Y_2SiO_5. The top, middle and bottom panels for each $Z_1 \longrightarrow V_i$ transition shows the magnetic splittings with $B \parallel D_1$, $B \parallel D_2$ and $B \parallel b$ respectively. The left panels depicts the experimental splittings, represented by the circles, and the theoretical splittings are represented by the red lines. The right panels shows Zeeman absorption spectra at a magnetic field represented by the vertical line in the left panels. All spectra were measured at 4.2 K. Spectral features labelled with a '#' are transitions not related to site 1 of Y_2SiO_5:0.5%Sm^{3+}. Spectral features labelled with an '*' is absorption due to water. Figure is continued over page.

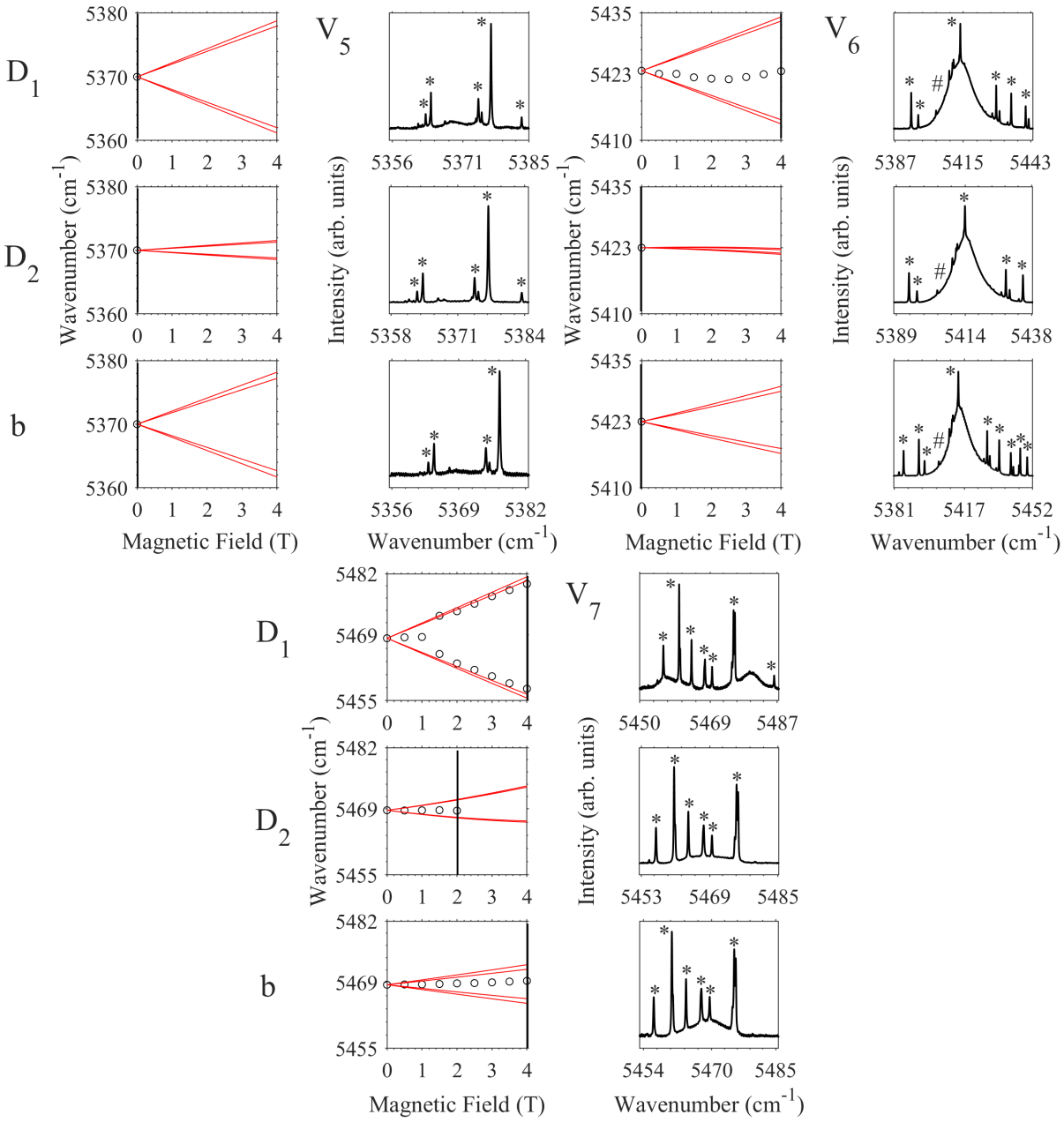

Figure 4.21: Magnetic splittings of the $^6H_{5/2}Z_1 \longrightarrow {}^6H_{13/2}V_i$ transitions for site 1 in Y_2SiO_5:0.5%Sm^{3+} with a magnetic field applied along the three crystallographic axes of Y_2SiO_5. The top, middle and bottom panels for each $Z_1 \longrightarrow V_i$ transition shows the magnetic splittings with $B \parallel D_1$, $B \parallel D_2$ and $B \parallel b$ respectively. The left panels depicts the experimental splittings, represented by the circles, and the theoretical splittings are represented by the red lines. The right panels shows Zeeman absorption spectra at a magnetic field represented by the vertical line in the left panels. All spectra were measured at 4.2 K. Spectral features labelled with a '#' are transitions not related to site 1 of Y_2SiO_5:0.5%Sm^{3+}. Spectral features labelled with an '*' is absorption due to water.

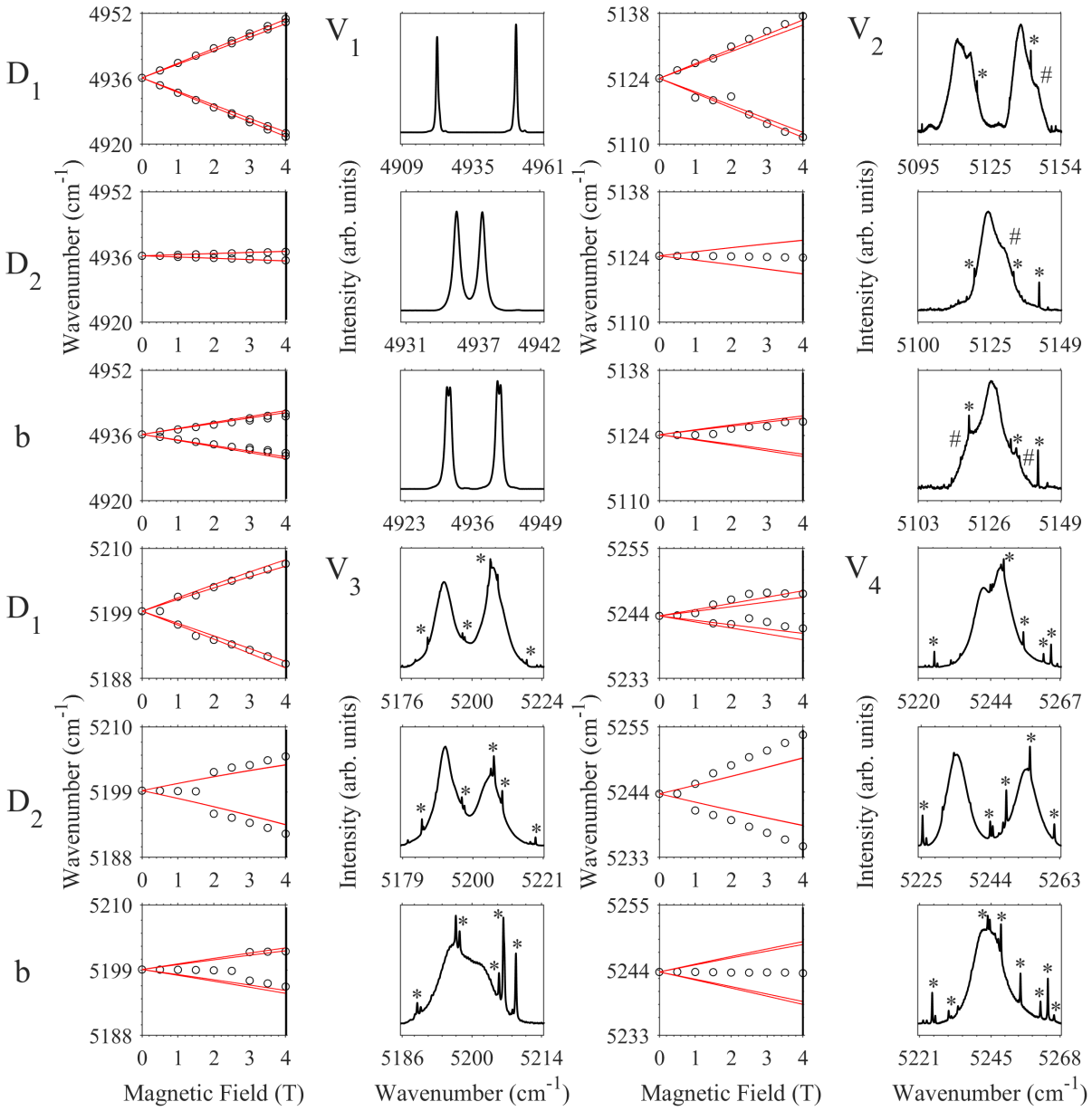

Figure 4.22: Magnetic splittings of the $^6H_{5/2}Z_1 \longrightarrow {}^6H_{13/2}V_i$ transitions for site 2 in Y_2SiO_5:0.5%Sm^{3+} with a magnetic field applied along the three crystallographic axes of Y_2SiO_5. The top, middle and bottom panels for each $Z_1 \longrightarrow V_i$ transition shows the magnetic splittings with $B \parallel D_1$, $B \parallel D_2$ and $B \parallel b$ respectively. The left panels depicts the experimental splittings, represented by the circles, and the theoretical splittings are represented by the red lines. The right panels shows Zeeman absorption spectra at a magnetic field represented by the vertical line in the left panels. All spectra were measured at 4.2 K. Spectral features labelled with a '#' are transitions not related to site 2 of Y_2SiO_5:0.5%Sm^{3+}. Spectral features labelled with an '*' is absorption due to water. Figure is continued over page.

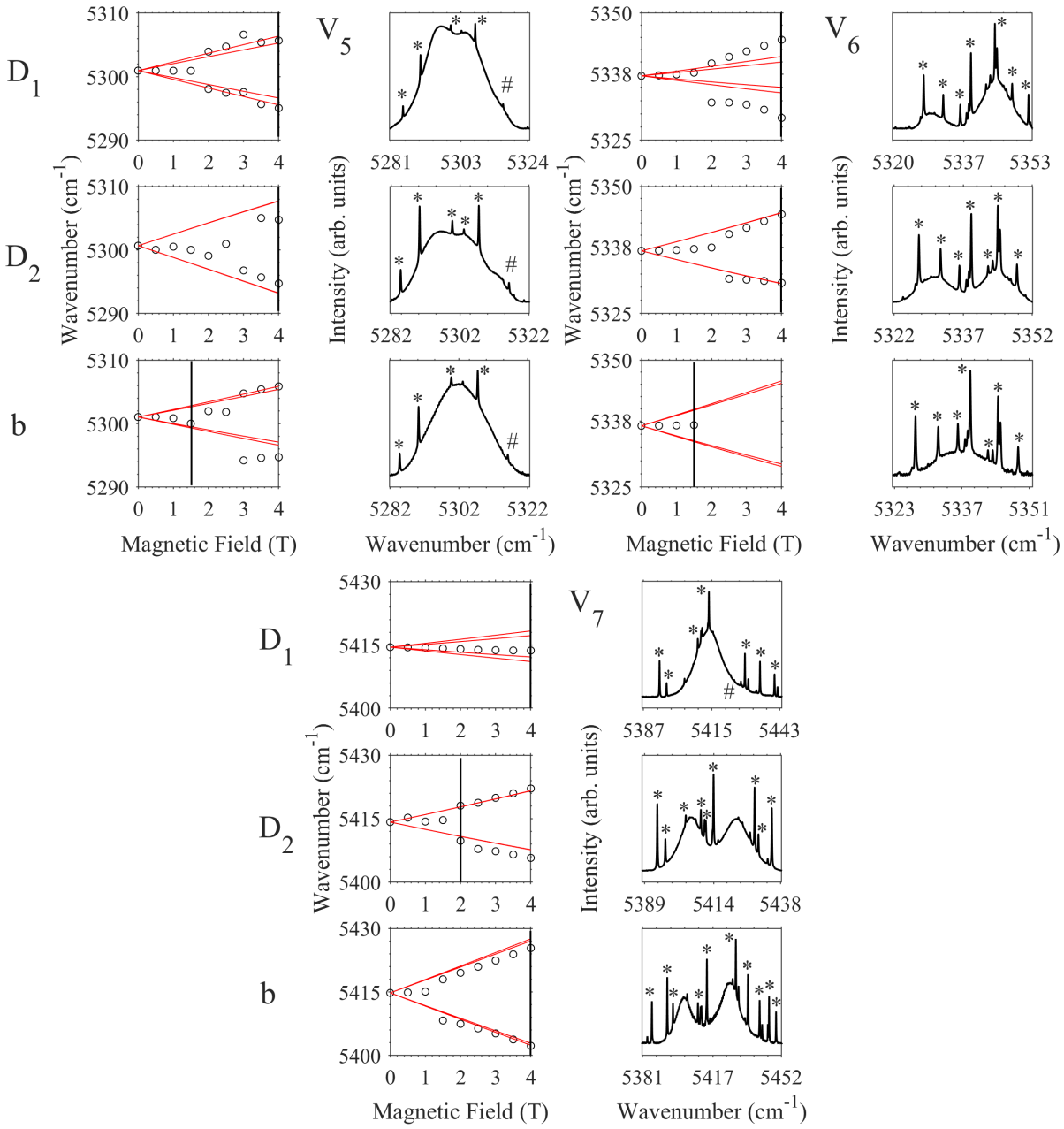

Figure 4.22: Magnetic splittings of the $^6H_{5/2}Z_1 \longrightarrow {}^6H_{13/2}V_i$ transitions for site 2 in Y_2SiO_5:0.5%Sm^{3+} with a magnetic field applied along the three crystallographic axes of Y_2SiO_5. The top, middle and bottom panels for each $Z_1 \longrightarrow V_i$ transition shows the magnetic splittings with $B \parallel D_1$, $B \parallel D_2$ and $B \parallel b$ respectively. The left panels depicts the experimental splittings, represented by the circles, and the theoretical splittings are represented by the red lines. The right panels shows Zeeman absorption spectra at a magnetic field represented by the vertical line in the left panels. All spectra were measured at 4.2 K. Spectral features labelled with a '#' are transitions not related to site 2 of Y_2SiO_5:0.5%Sm^{3+}. Spectral features labelled with an '*' is absorption due to water.

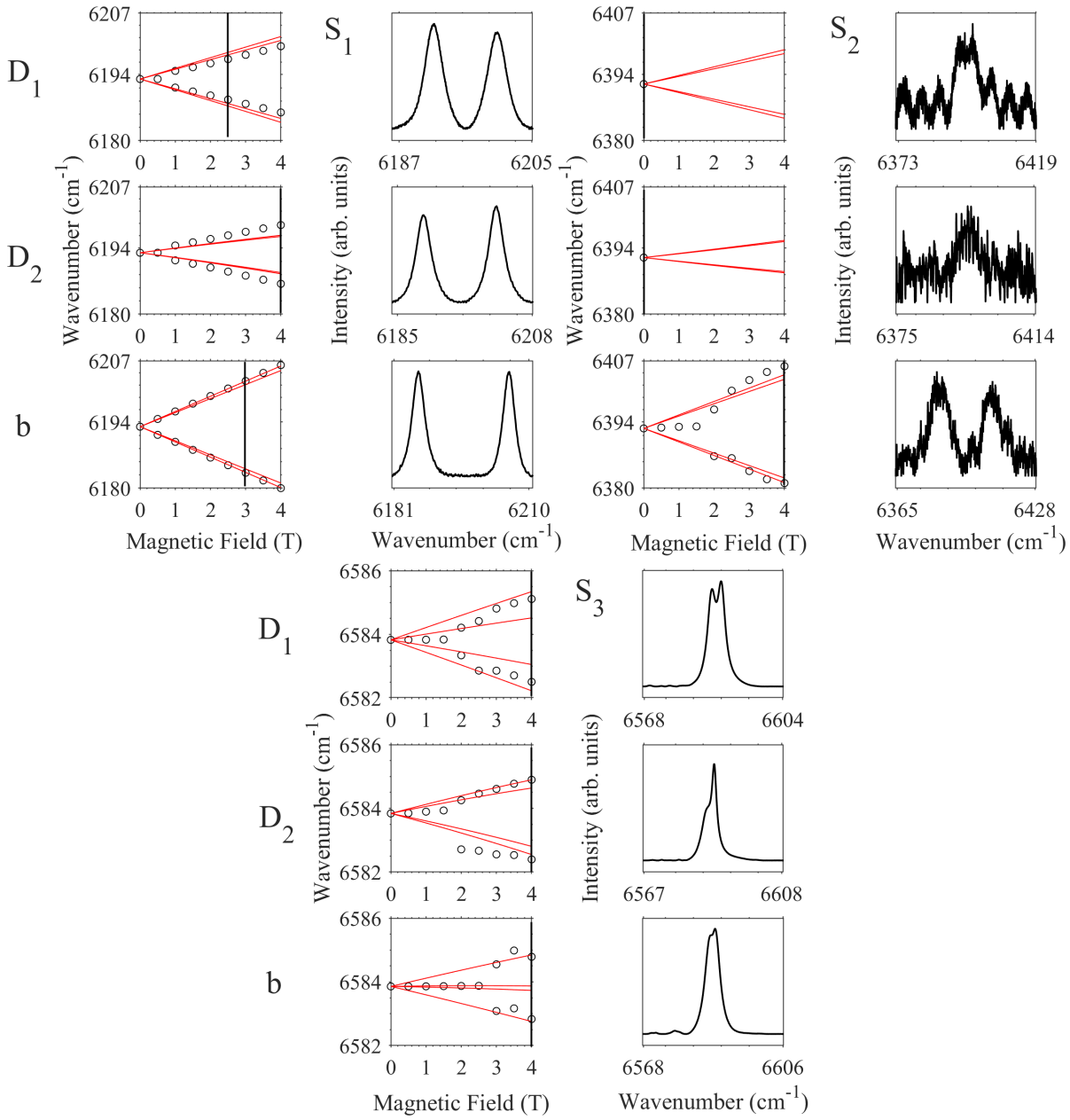

Figure 4.23: Magnetic splittings of the assigned $^6H_{5/2}Z_1 \longrightarrow {}^6F_{1/2}$, $^6F_{3/2}$ and $^6H_{15/2}S_i$ transitions for site 1 in Y_2SiO_5:0.5%Sm^{3+} with a magnetic field applied along the three crystallographic axes of Y_2SiO_5. The top, middle and bottom panels for each $Z_1 \longrightarrow S_i$ transition shows the magnetic splittings with $B \parallel D_1$, $B \parallel D_2$ and $B \parallel b$ respectively. The left panels depicts the experimental splittings, represented by the circles, and the theoretical splittings are represented by the red lines. The right panels shows Zeeman absorption spectra at a magnetic field represented by the vertical line in the left panels. All spectra were measured at 4.2 K.

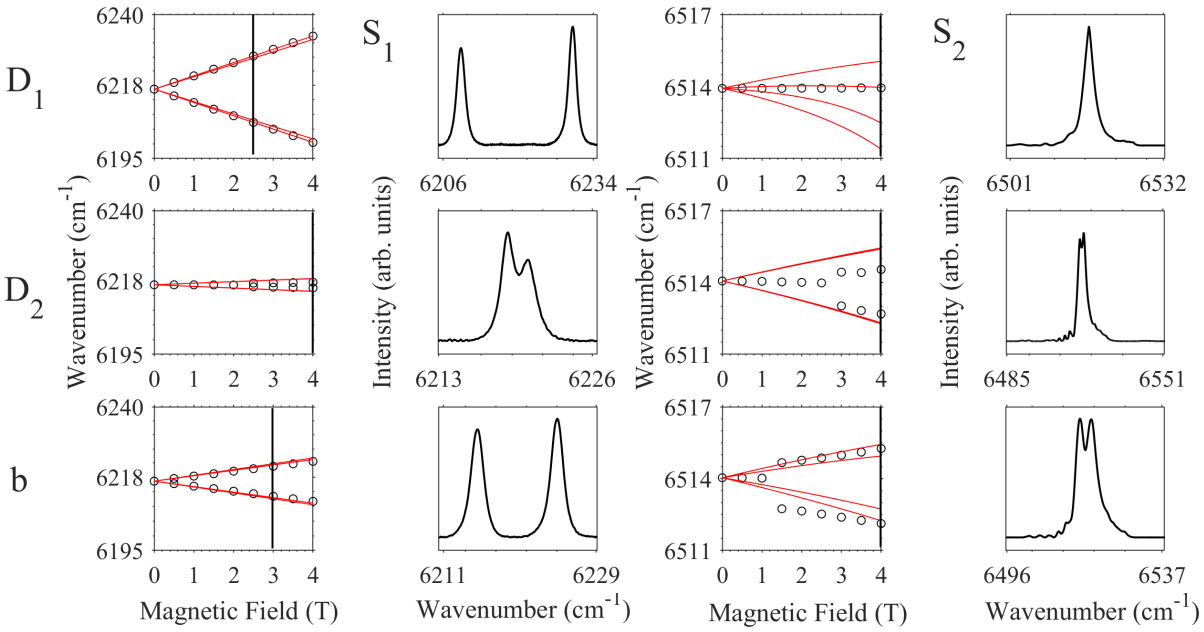

Figure 4.24: Magnetic splittings of the assigned ${}^6H_{5/2}Z_1 \longrightarrow {}^6F_{1/2}$, ${}^6F_{3/2}$ and ${}^6H_{15/2}S_i$ transitions for site 2 in Y_2SiO_5:0.5%Sm^{3+} with a magnetic field applied along the three crystallographic axes of Y_2SiO_5. The top, middle and bottom panels for each $Z_1 \longrightarrow S_i$ transition shows the magnetic splittings with $B \parallel D_1$, $B \parallel D_2$ and $B \parallel b$ respectively. The left panels depicts the experimental splittings, represented by the circles, and the theoretical splittings are represented by the red lines. The right panels shows Zeeman absorption spectra at a magnetic field represented by the vertical line in the left panels. All spectra were measured at 4.2 K.

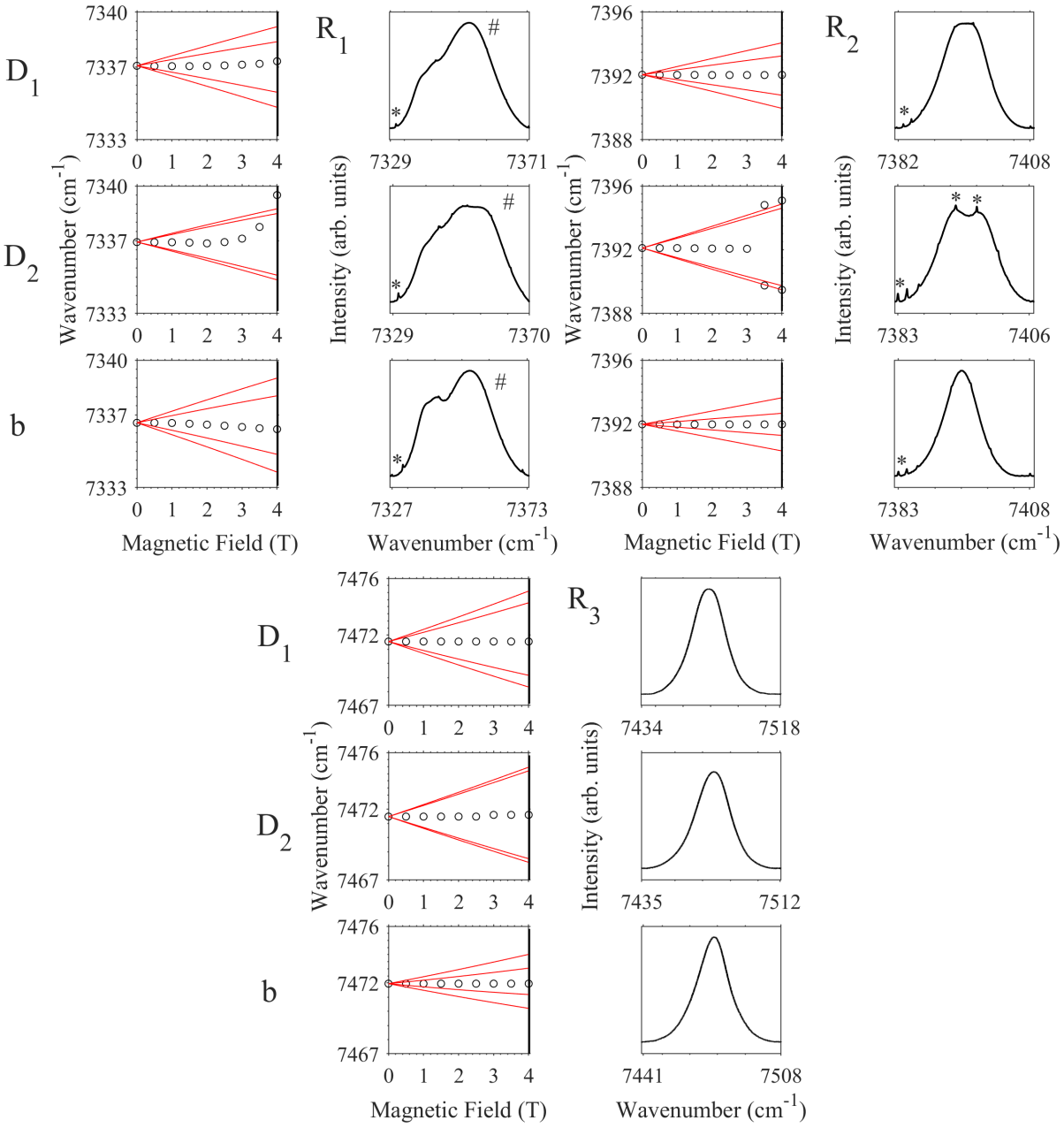

Figure 4.25: Magnetic splittings of the $^6H_{5/2}Z_1 \longrightarrow {}^6F_{5/2}R_i$ transitions for site 1 in Y_2SiO_5:0.5%Sm^{3+} with a magnetic field applied along the three crystallographic axes of Y_2SiO_5. The top, middle and bottom panels for each $Z_1 \longrightarrow R_i$ transition shows the magnetic splittings with $B \parallel D_1$, $B \parallel D_2$ and $B \parallel b$ respectively. The left panels depicts the experimental splittings, represented by the circles, and the theoretical splittings are represented by the red lines. The right panels shows Zeeman absorption spectra at a magnetic field represented by the vertical line in the left panels. All spectra were measured at 4.2 K. Spectral features labelled with a '#' are transitions not related to site 1 of Y_2SiO_5:0.5%Sm^{3+}. Spectral features labelled with an '*' is absorption due to water.

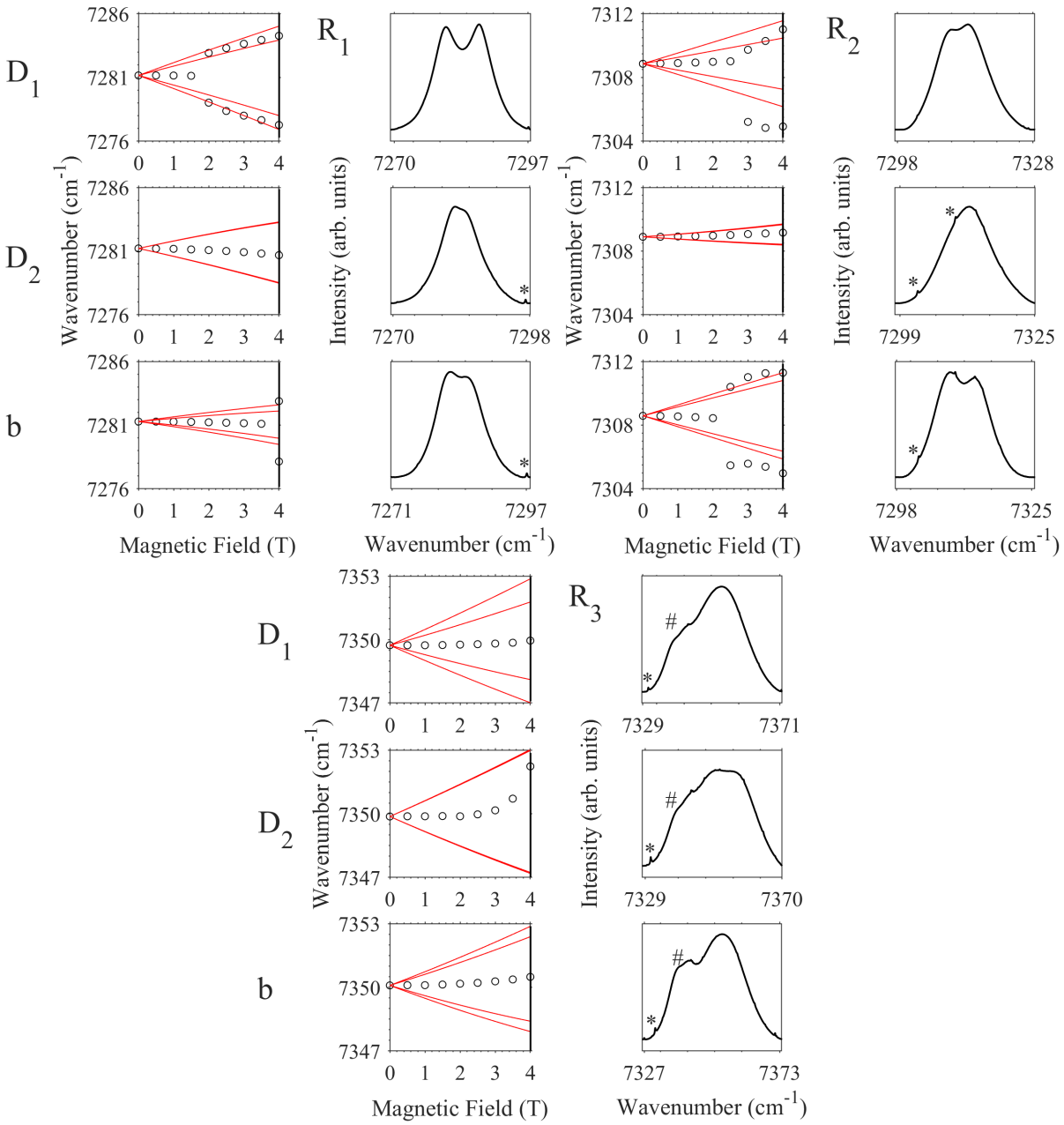

Figure 4.26: Magnetic splittings of the $^6H_{5/2}Z_1 \longrightarrow {}^6F_{5/2}R_i$ transitions for site 2 in Y_2SiO_5:0.5%Sm^{3+} with a magnetic field applied along the three crystallographic axes of Y_2SiO_5. The top, middle and bottom panels for each $Z_1 \longrightarrow R_i$ transition shows the magnetic splittings with $B \parallel D_1$, $B \parallel D_2$ and $B \parallel b$ respectively. The left panels depicts the experimental splittings, represented by the circles, and the theoretical splittings are represented by the red lines. The right panels shows Zeeman absorption spectra at a magnetic field represented by the vertical line in the left panels. All spectra were measured at 4.2 K. Spectral features labelled with a '#' are transitions not related to site 2 of Y_2SiO_5:0.5%Sm^{3+}. Spectral features labelled with an '*' is absorption due to water.

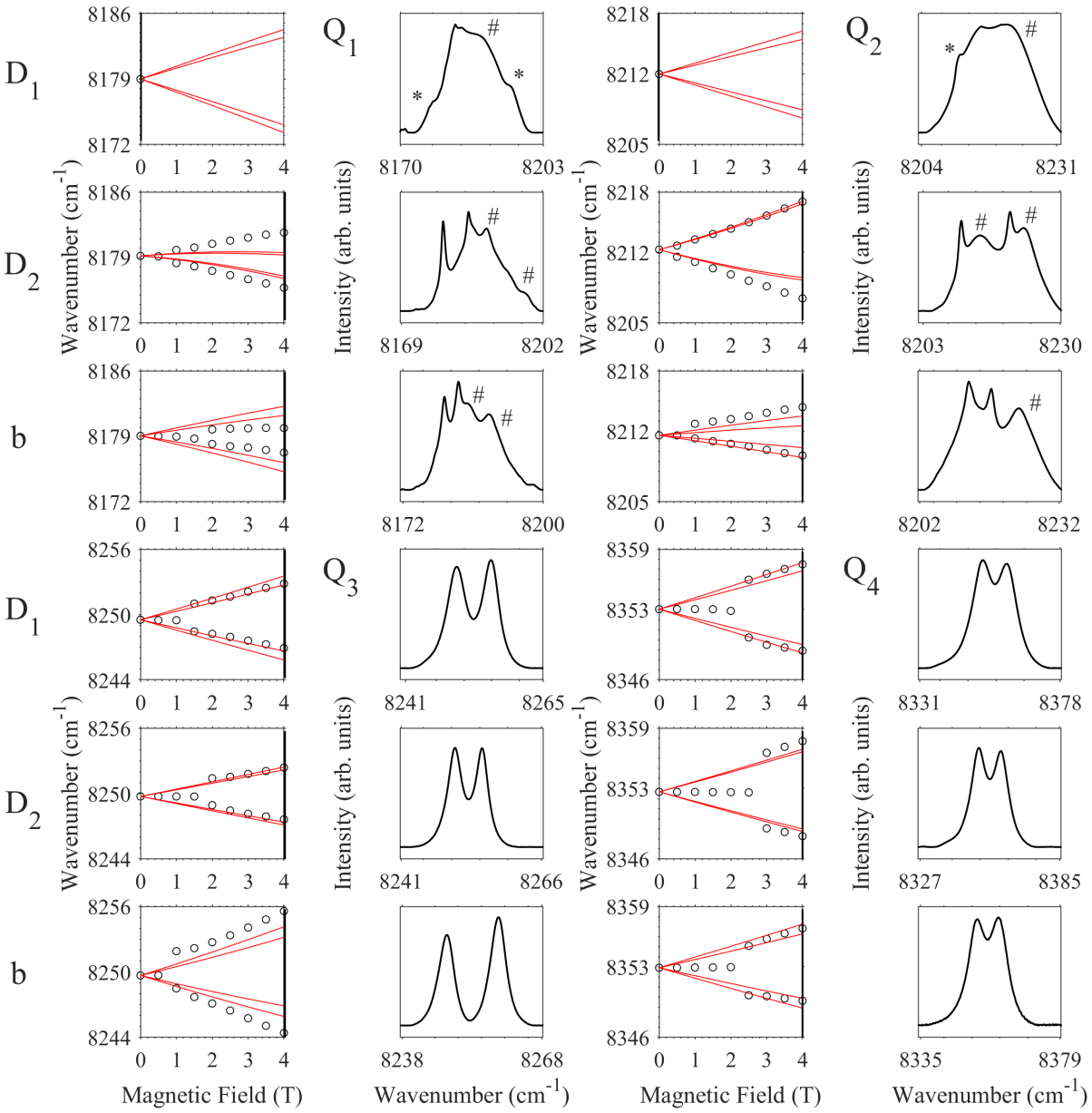

Figure 4.27: Magnetic splittings of the $^6H_{5/2}Z_1 \longrightarrow {}^6F_{7/2}Q_i$ transitions for site 1 in Y_2SiO_5:0.5%Sm^{3+} with a magnetic field applied along the three crystallographic axes of Y_2SiO_5. The top, middle and bottom panels for each $Z_1 \longrightarrow Q_i$ transition shows the magnetic splittings with $B \parallel D_1$, $B \parallel D_2$ and $B \parallel b$ respectively. The left panels depicts the experimental splittings, represented by the circles, and the theoretical splittings are represented by the red lines. The right panels shows Zeeman absorption spectra at a magnetic field represented by the vertical line in the left panels. All spectra were measured at 4.2 K. Spectral features labelled with a '#' are transitions not related to site 1 of Y_2SiO_5:0.5%Sm^{3+}. Spectral features labelled with an '*' is absorption due to cluster sites in Y_2SiO_5:0.5%Sm^{3+}.

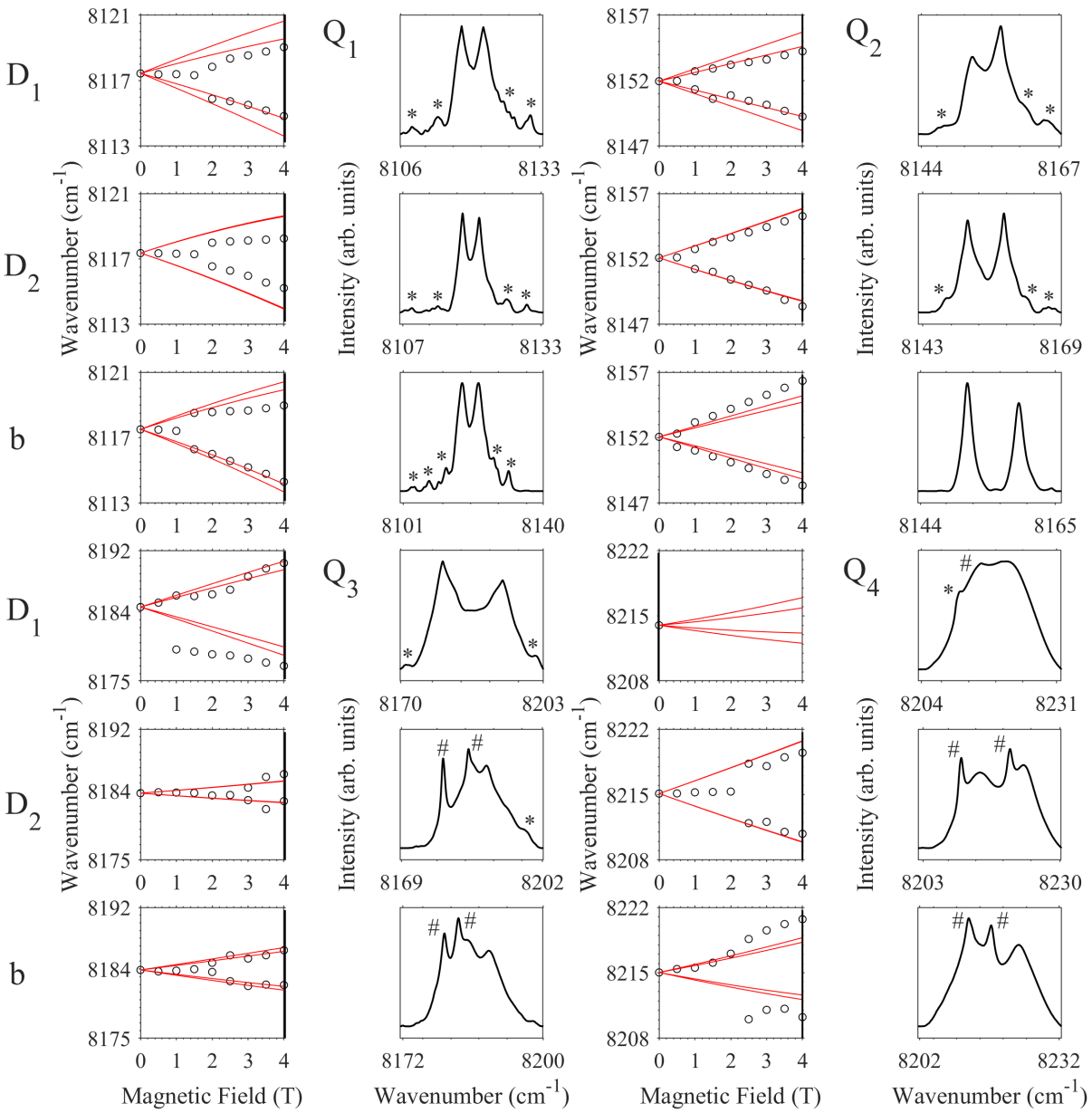

Figure 4.28: Magnetic splittings of the $^6H_{5/2}Z_1 \longrightarrow {}^6F_{7/2}Q_i$ transitions for site 2 in Y_2SiO_5:0.5%Sm^{3+} with a magnetic field applied along the three crystallographic axes of Y_2SiO_5. The top, middle and bottom panels for each $Z_1 \longrightarrow Q_i$ transition shows the magnetic splittings with $B \parallel D_1$, $B \parallel D_2$ and $B \parallel b$ respectively. The left panels depicts the experimental splittings, represented by the circles, and the theoretical splittings are represented by the red lines. The right panels shows Zeeman absorption spectra at a magnetic field represented by the vertical line in the left panels. All spectra were measured at 4.2 K. Spectral features labelled with a '#' are transitions not related to site 2 of Y_2SiO_5:0.5%Sm^{3+}. Spectral features labelled with an '*' is absorption due to cluster sites in Y_2SiO_5:0.5%Sm^{3+}.

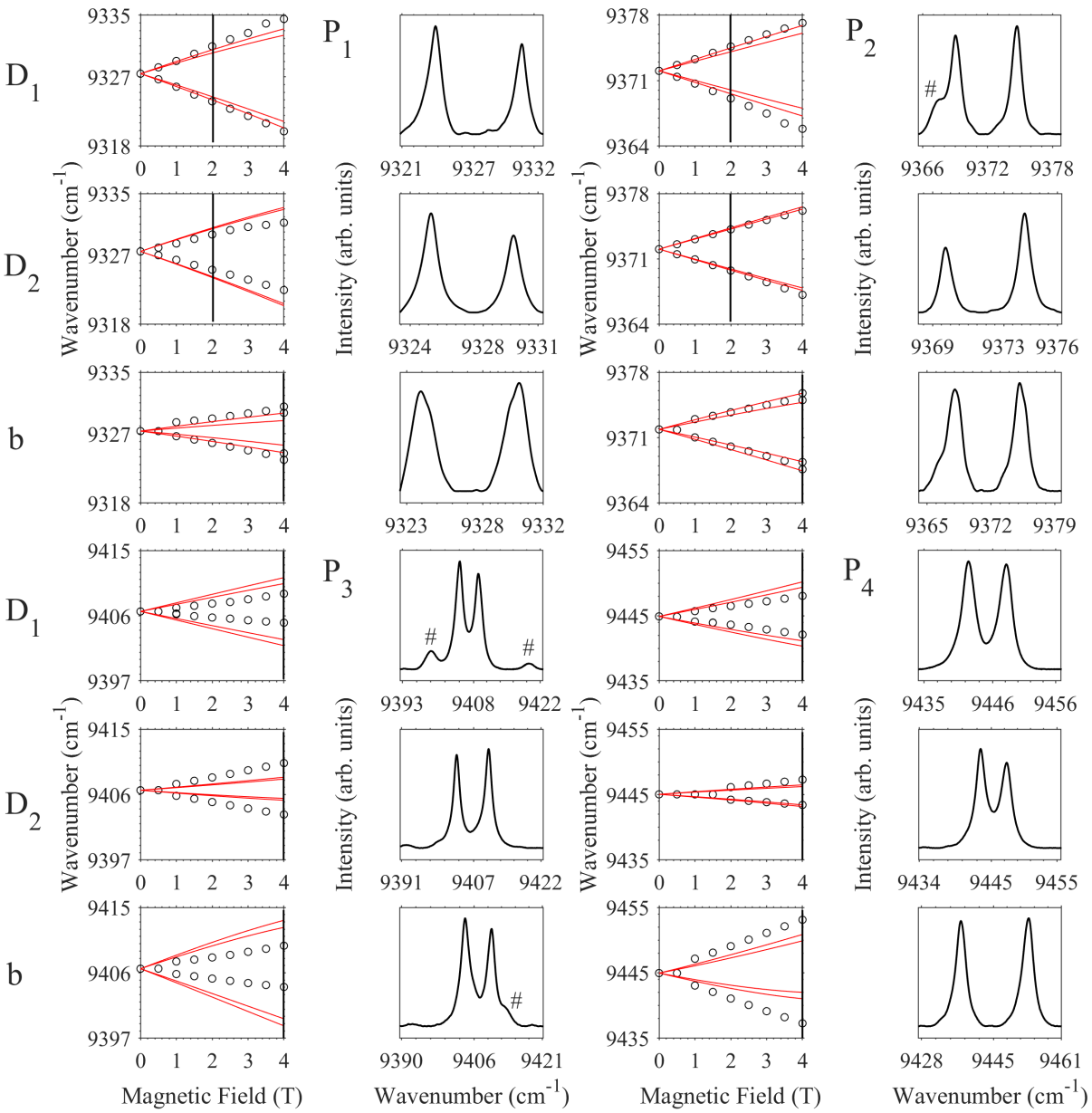

Figure 4.29: Magnetic splittings of the $^6H_{5/2}Z_1 \longrightarrow {}^6F_{9/2}P_i$ transitions for site 1 in Y_2SiO_5:0.5%Sm^{3+} with a magnetic field applied along the three crystallographic axes of Y_2SiO_5. The top, middle and bottom panels for each $Z_1 \longrightarrow P_i$ transition shows the magnetic splittings with $B \parallel D_1$, $B \parallel D_2$ and $B \parallel b$ respectively. The left panels depicts the experimental splittings, represented by the circles, and the theoretical splittings are represented by the red lines. The right panels shows Zeeman absorption spectra at a magnetic field represented by the vertical line in the left panels. All spectra were measured at 4.2 K. Spectral features labelled with a '#' are transitions not related to site 1 of Y_2SiO_5:0.5%Sm^{3+}. Figure is continued over page.

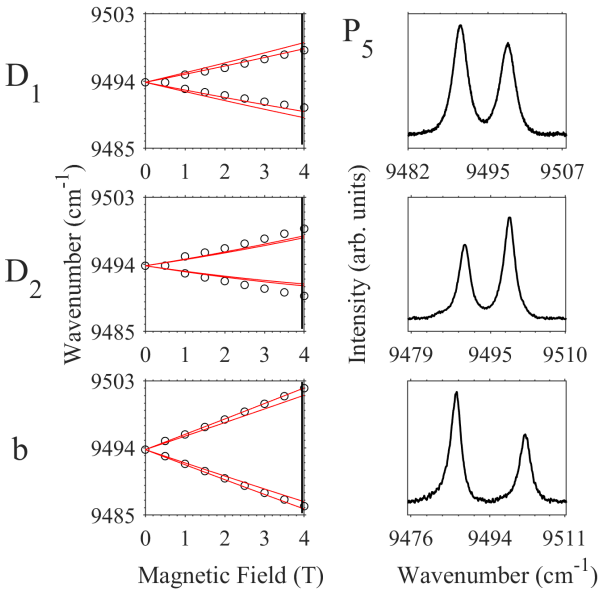

Figure 4.29: Magnetic splittings of the $^6H_{5/2}Z_1 \longrightarrow {}^6F_{9/2}P_i$ transitions for site 1 in Y_2SiO_5:0.5%Sm^{3+} with a magnetic field applied along the three crystallographic axes of Y_2SiO_5. The top, middle and bottom panels for each $Z_1 \longrightarrow P_i$ transition shows the magnetic splittings with $B \parallel D_1$, $B \parallel D_2$ and $B \parallel b$ respectively. The left panels depicts the experimental splittings, represented by the circles, and the theoretical splittings are represented by the red lines. The right panels shows Zeeman absorption spectra at a magnetic field represented by the vertical line in the left panels. All spectra were measured at 4.2 K. Spectral features labelled with a '#' are transitions not related to site 1 of Y_2SiO_5:0.5%Sm^{3+}.

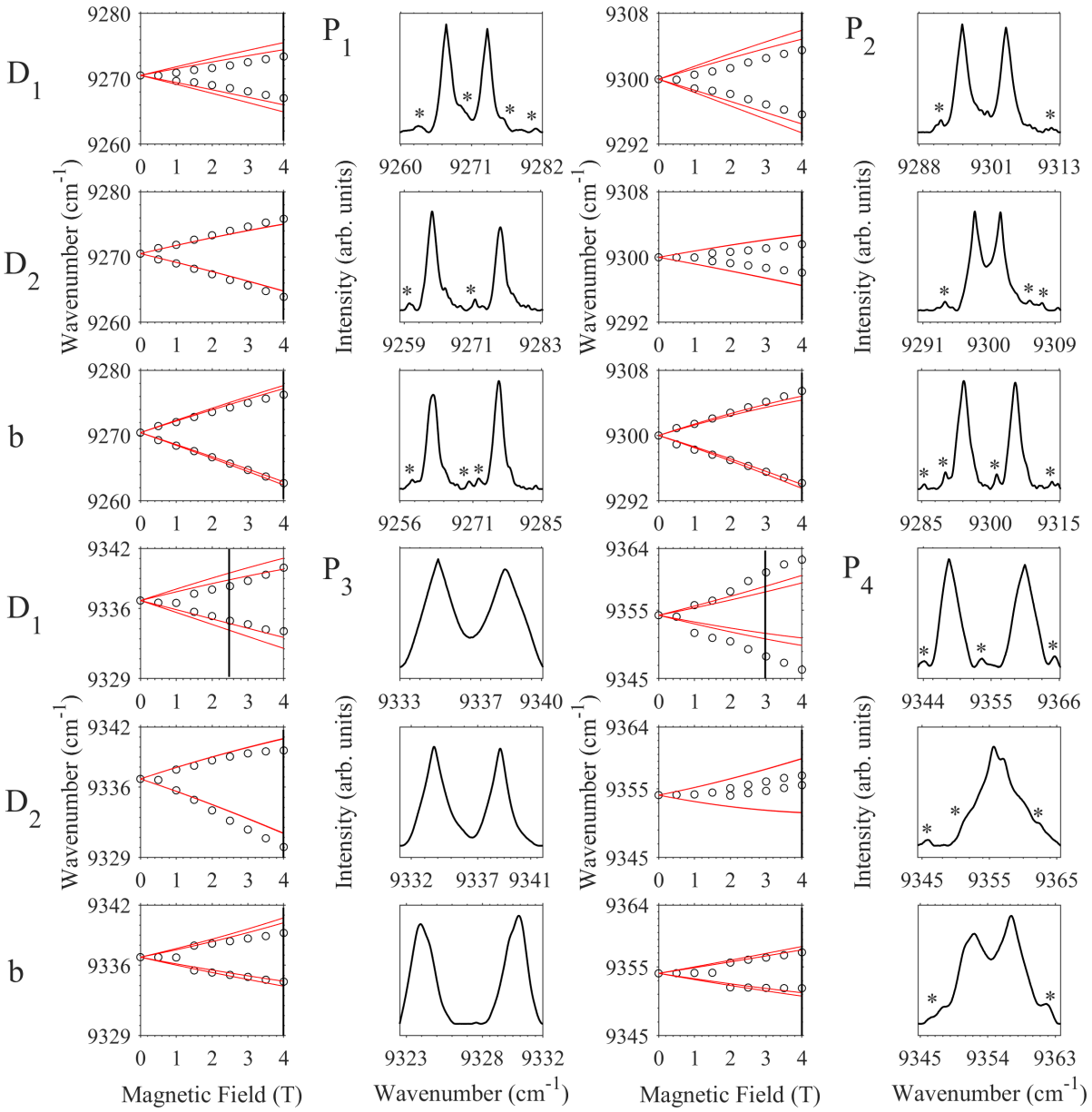

Figure 4.30: Magnetic splittings of the $^6H_{5/2}Z_1 \longrightarrow {}^6F_{9/2}P_i$ transitions for site 2 in Y_2SiO_5:0.5%Sm^{3+} with a magnetic field applied along the three crystallographic axes of Y_2SiO_5. The top, middle and bottom panels for each $Z_1 \longrightarrow P_i$ transition shows the magnetic splittings with $B \parallel D_1$, $B \parallel D_2$ and $B \parallel b$ respectively. The left panels depicts the experimental splittings, represented by the circles, and the theoretical splittings are represented by the red lines. The right panels shows Zeeman absorption spectra at a magnetic field represented by the vertical line in the left panels. All spectra were measured at 4.2 K. Spectral features labelled with a '#' are transitions not related to site 2 of Y_2SiO_5:0.5%Sm^{3+}. Spectral features labelled with an '*' is absorption due to cluster sites in Y_2SiO_5:0.5%Sm^{3+}. Figure is continued over page.

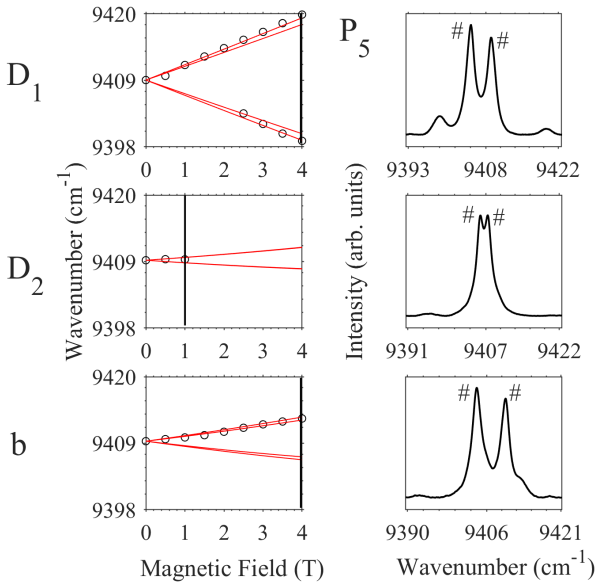

Figure 4.30: Magnetic splittings of the $^6H_{5/2}Z_1 \longrightarrow {}^6F_{9/2}P_i$ transitions for site 2 in Y_2SiO_5:0.5%Sm^{3+} with a magnetic field applied along the three crystallographic axes of Y_2SiO_5. The top, middle and bottom panels for each $Z_1 \longrightarrow P_i$ transition shows the magnetic splittings with $B \parallel D_1$, $B \parallel D_2$ and $B \parallel b$ respectively. The left panels depicts the experimental splittings, represented by the circles, and the theoretical splittings are represented by the red lines. The right panels shows Zeeman absorption spectra at a magnetic field represented by the vertical line in the left panels. All spectra were measured at 4.2 K. Spectral features labelled with a '#' are transitions not related to site 2 of Y_2SiO_5:0.5%Sm^{3+}.

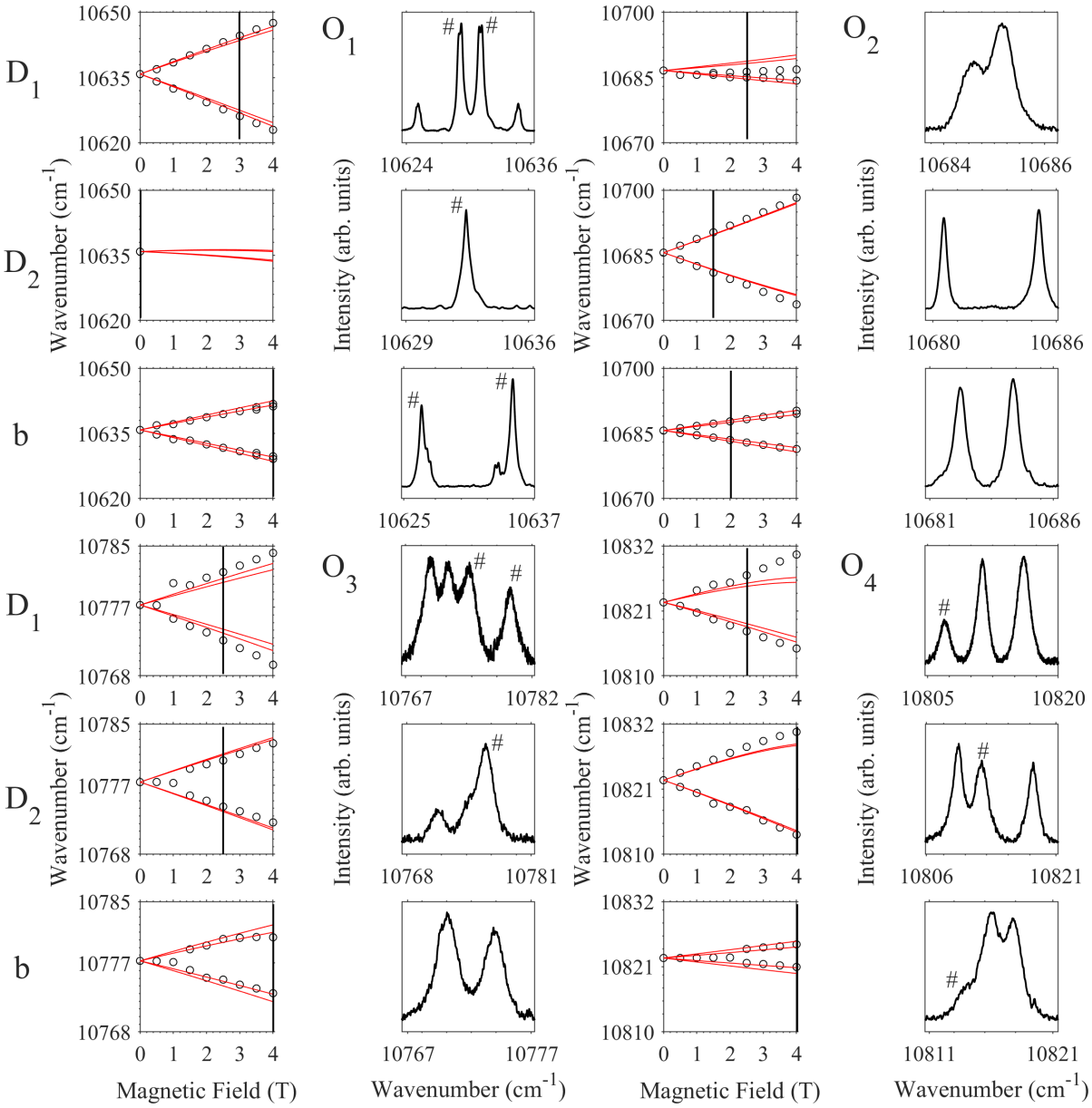

Figure 4.31: Magnetic splittings of the $^6H_{5/2}Z_1 \longrightarrow {}^6F_{11/2}O_i$ transitions for site 1 in Y_2SiO_5:0.5%Sm^{3+} with a magnetic field applied along the three crystallographic axes of Y_2SiO_5. The top, middle and bottom panels for each $Z_1 \longrightarrow O_i$ transition shows the magnetic splittings with $B \parallel D_1$, $B \parallel D_2$ and $B \parallel b$ respectively. The left panels depicts the experimental splittings, represented by the circles, and the theoretical splittings are represented by the red lines. The right panels shows Zeeman absorption spectra at a magnetic field represented by the vertical line in the left panels. All spectra were measured at 4.2 K. Spectral features labelled with a '#' are transitions not related to site 1 of Y_2SiO_5:0.5%Sm^{3+}. Figure is continued over page.

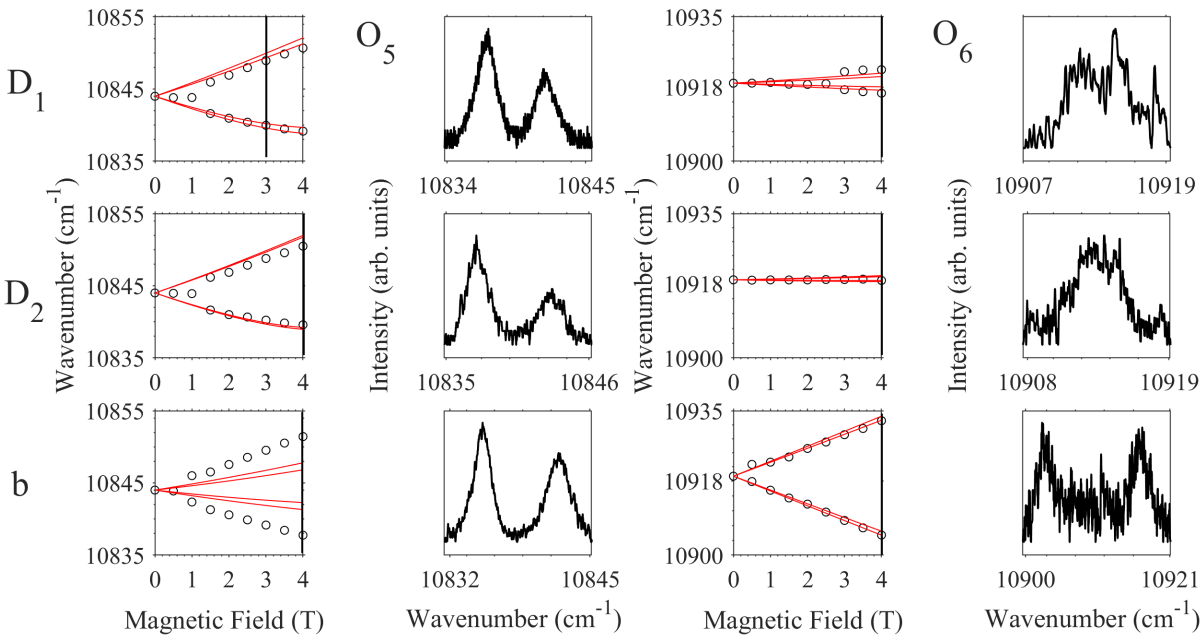

Figure 4.31: Magnetic splittings of the $^6H_{5/2}Z_1 \longrightarrow {}^6F_{11/2}O_i$ transitions for site 1 in Y_2SiO_5:0.5%Sm^{3+} with a magnetic field applied along the three crystallographic axes of Y_2SiO_5. The top, middle and bottom panels for each $Z_1 \longrightarrow O_i$ transition shows the magnetic splittings with $B \parallel D_1$, $B \parallel D_2$ and $B \parallel b$ respectively. The left panels depicts the experimental splittings, represented by the circles, and the theoretical splittings are represented by the red lines. The right panels shows Zeeman absorption spectra at a magnetic field represented by the vertical line in the left panels. All spectra were measured at 4.2 K.

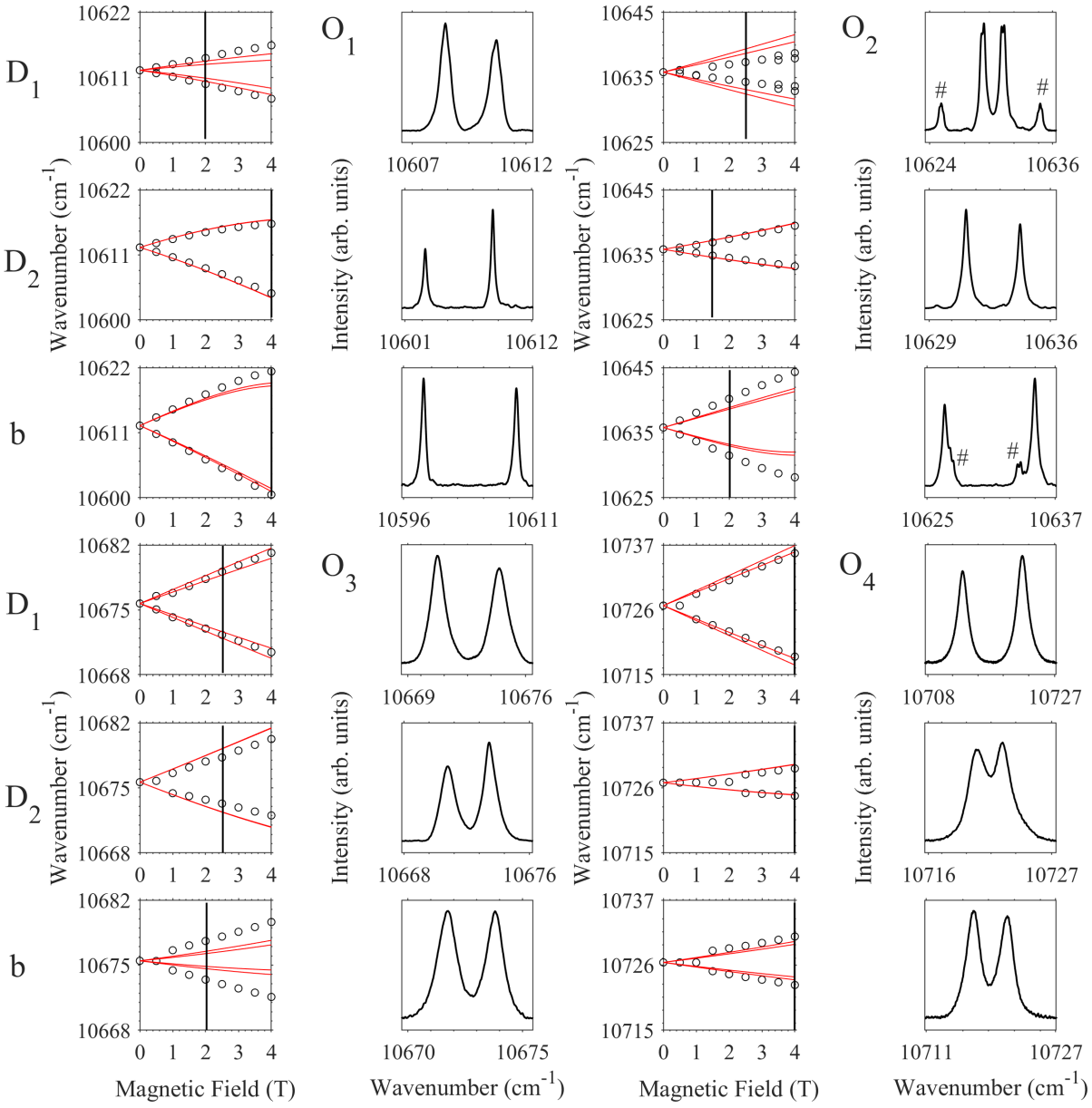

Figure 4.32: Magnetic splittings of the $^6H_{5/2}Z_1 \longrightarrow {}^6F_{11/2}O_i$ transitions for site 2 in Y_2SiO_5:0.5%Sm^{3+} with a magnetic field applied along the three crystallographic axes of Y_2SiO_5. The top, middle and bottom panels for each $Z_1 \longrightarrow O_i$ transition shows the magnetic splittings with $B \parallel D_1$, $B \parallel D_2$ and $B \parallel b$ respectively. The left panels depicts the experimental splittings, represented by the circles, and the theoretical splittings are represented by the red lines. The right panels shows Zeeman absorption spectra at a magnetic field represented by the vertical line in the left panels. All spectra were measured at 4.2 K. Spectral features labelled with a '#' are transitions not related to site 2 of Y_2SiO_5:0.5%Sm^{3+}. Figure is continued over page.

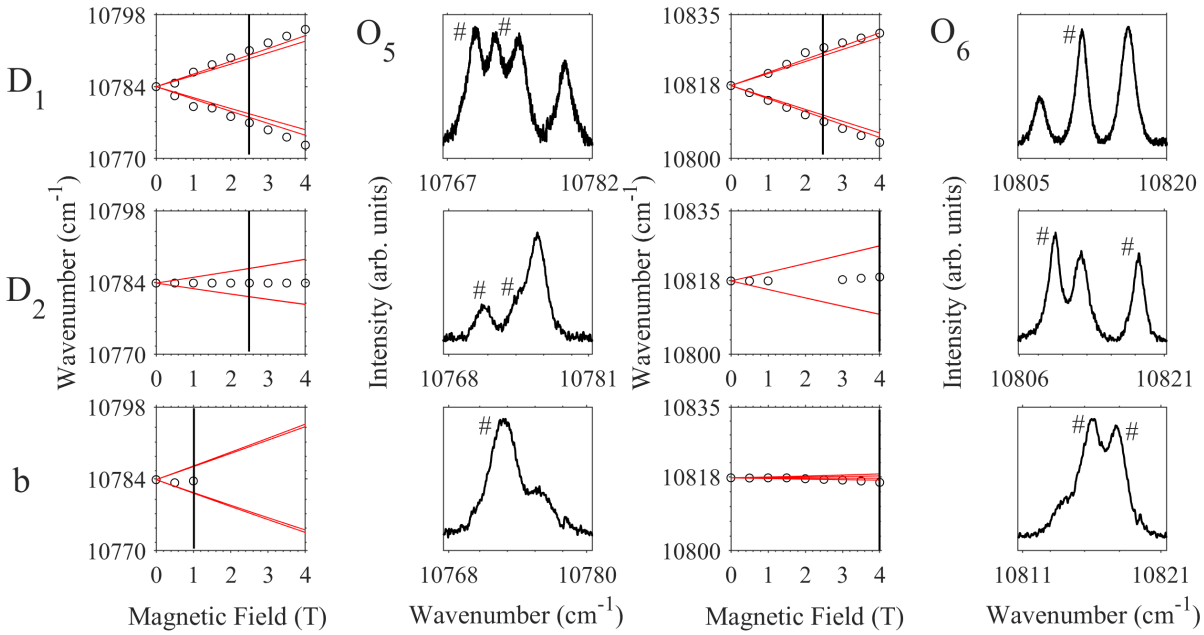

Figure 4.32: Magnetic splittings of the $^6H_{5/2}Z_1 \longrightarrow {}^6F_{11/2}O_i$ transitions for site 2 in Y_2SiO_5:0.5%Sm^{3+} with a magnetic field applied along the three crystallographic axes of Y_2SiO_5. The top, middle and bottom panels for each $Z_1 \longrightarrow O_i$ transition shows the magnetic splittings with $B \parallel D_1$, $B \parallel D_2$ and $B \parallel b$ respectively. The left panels depicts the experimental splittings, represented by the circles, and the theoretical splittings are represented by the red lines. The right panels shows Zeeman absorption spectra at a magnetic field represented by the vertical line in the left panels. All spectra were measured at 4.2 K. Spectral features labelled with a '#' are transitions not related to site 2 of Y_2SiO_5:0.5%Sm^{3+}.

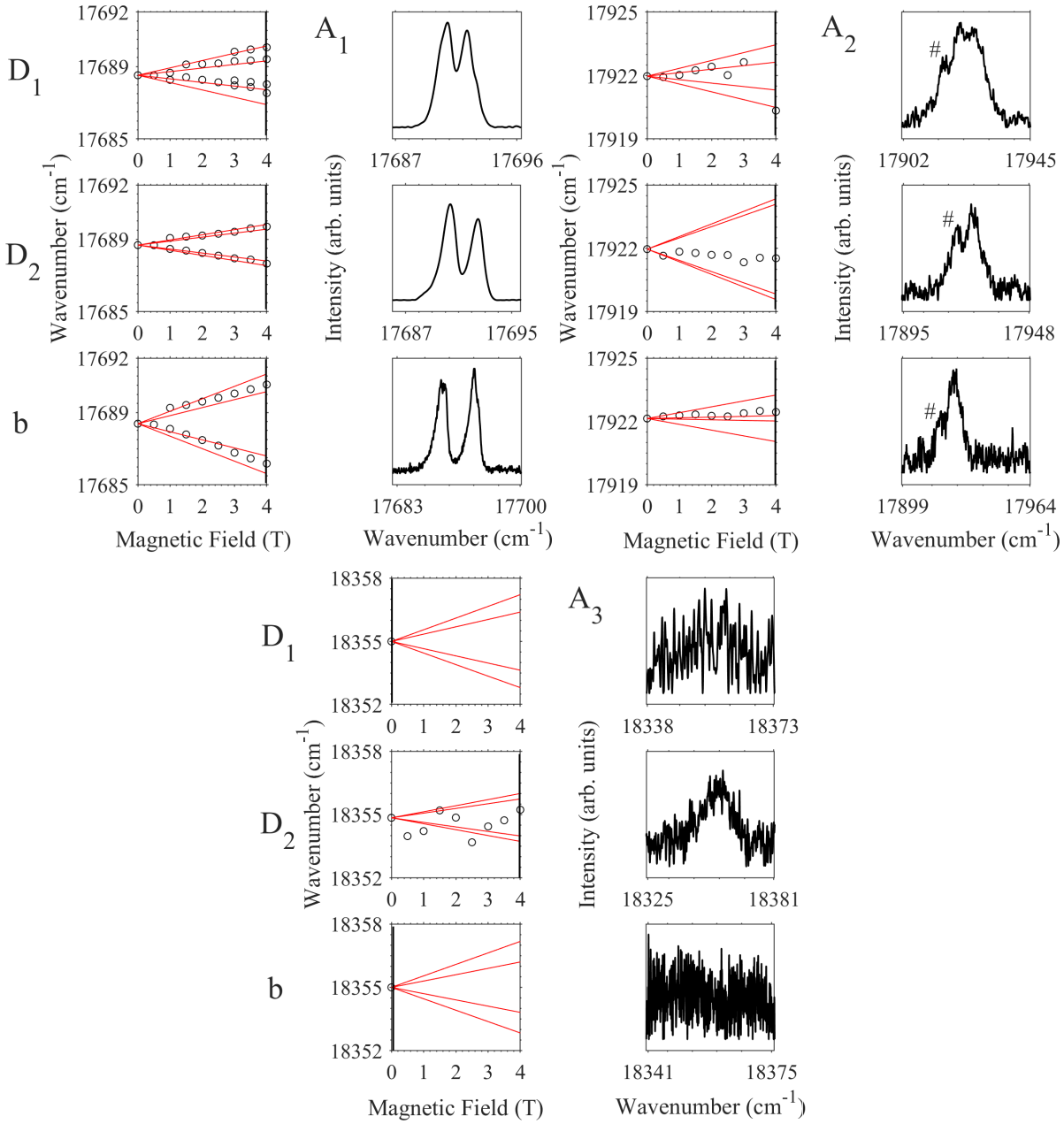

Figure 4.33: Magnetic splittings of the $^6H_{5/2}Z_1 \longrightarrow {}^4G_{5/2}A_i$ transitions for site 1 in Y_2SiO_5:0.5%Sm^{3+} with a magnetic field applied along the three crystallographic axes of Y_2SiO_5. The top, middle and bottom panels for each $Z_1 \longrightarrow A_i$ transition shows the magnetic splittings with $B \parallel D_1$, $B \parallel D_2$ and $B \parallel b$ respectively. The left panels depicts the experimental splittings, represented by the circles, and the theoretical splittings are represented by the red lines. The right panels shows Zeeman absorption spectra at a magnetic field represented by the vertical line in the left panels. All spectra were measured at 4.2 K. Spectral features labelled with a '#' are transitions not related to site 1 of Y_2SiO_5:0.5%Sm^{3+}.

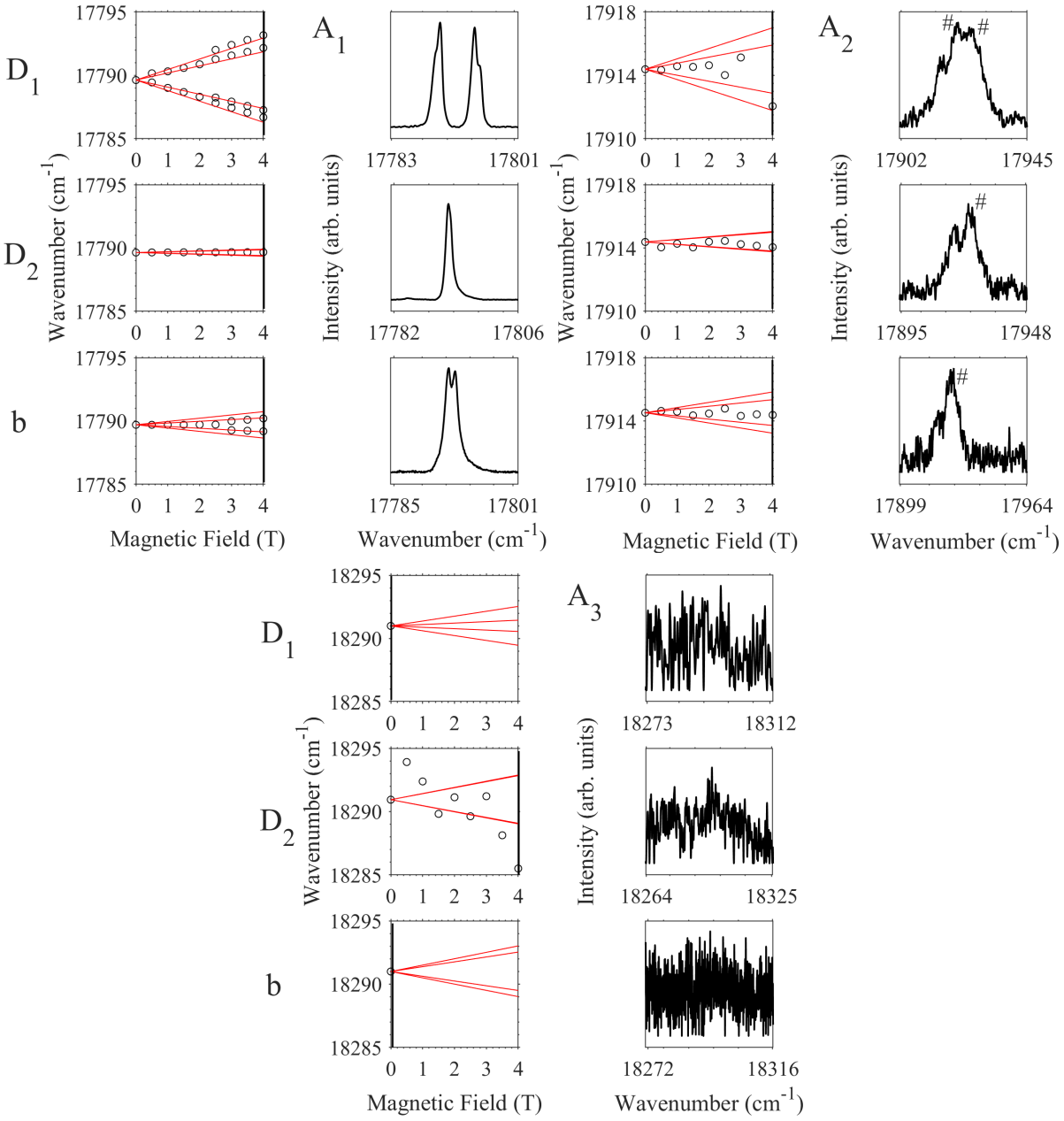

Figure 4.34: Magnetic splittings of the $^6H_{5/2}Z_1 \longrightarrow {}^4G_{5/2}A_i$ transitions for site 2 in Y_2SiO_5:0.5%Sm^{3+} with a magnetic field applied along the three crystallographic axes of Y_2SiO_5. The top, middle and bottom panels for each $Z_1 \longrightarrow A_i$ transition shows the magnetic splittings with $B \parallel D_1$, $B \parallel D_2$ and $B \parallel b$ respectively. The left panels depicts the experimental splittings, represented by the circles, and the theoretical splittings are represented by the red lines. The right panels shows Zeeman absorption spectra at a magnetic field represented by the vertical line in the left panels. All spectra were measured at 4.2 K. Spectral features labelled with a '#' are transitions not related to site 2 of Y_2SiO_5:0.5%Sm^{3+}.

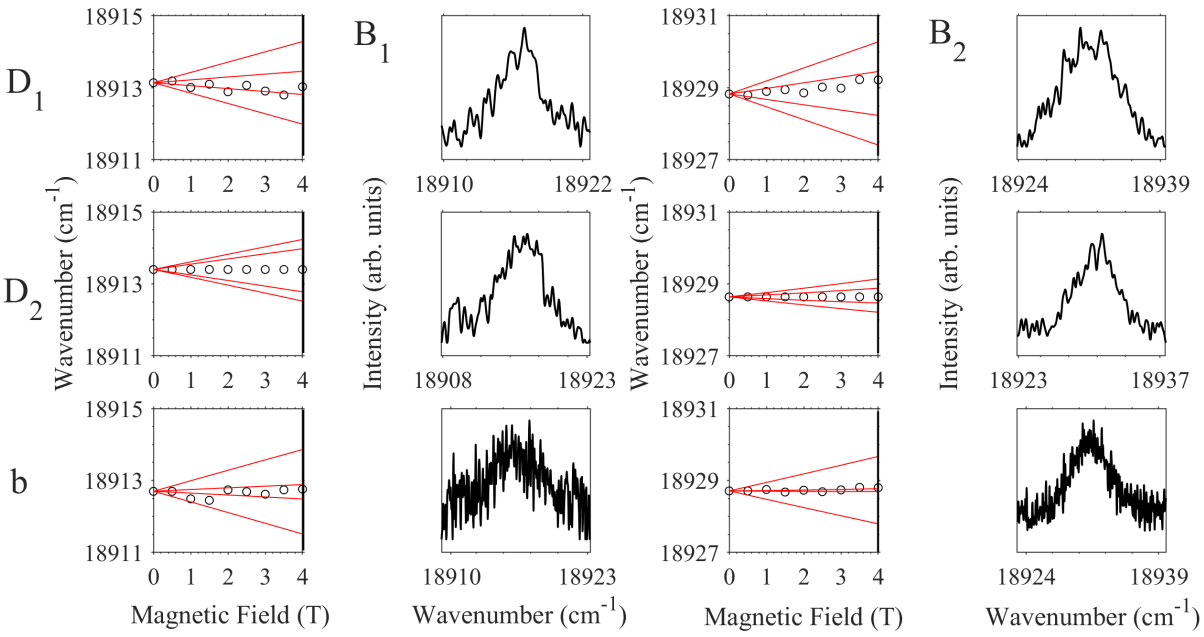

Figure 4.35: Magnetic splittings of the $^6H_{5/2}Z_1 \longrightarrow {}^4F_{3/2}B_i$ transitions for site 1 in Y_2SiO_5:0.5%Sm^{3+} with a magnetic field applied along the three crystallographic axes of Y_2SiO_5. The top, middle and bottom panels for each $Z_1 \longrightarrow B_i$ transition shows the magnetic splittings with $B \parallel D_1$, $B \parallel D_2$ and $B \parallel b$ respectively. The left panels depicts the experimental splittings, represented by the circles, and the theoretical splittings are represented by the red lines. The right panels shows Zeeman absorption spectra at a magnetic field represented by the vertical line in the left panels. All spectra were measured at 4.2 K.

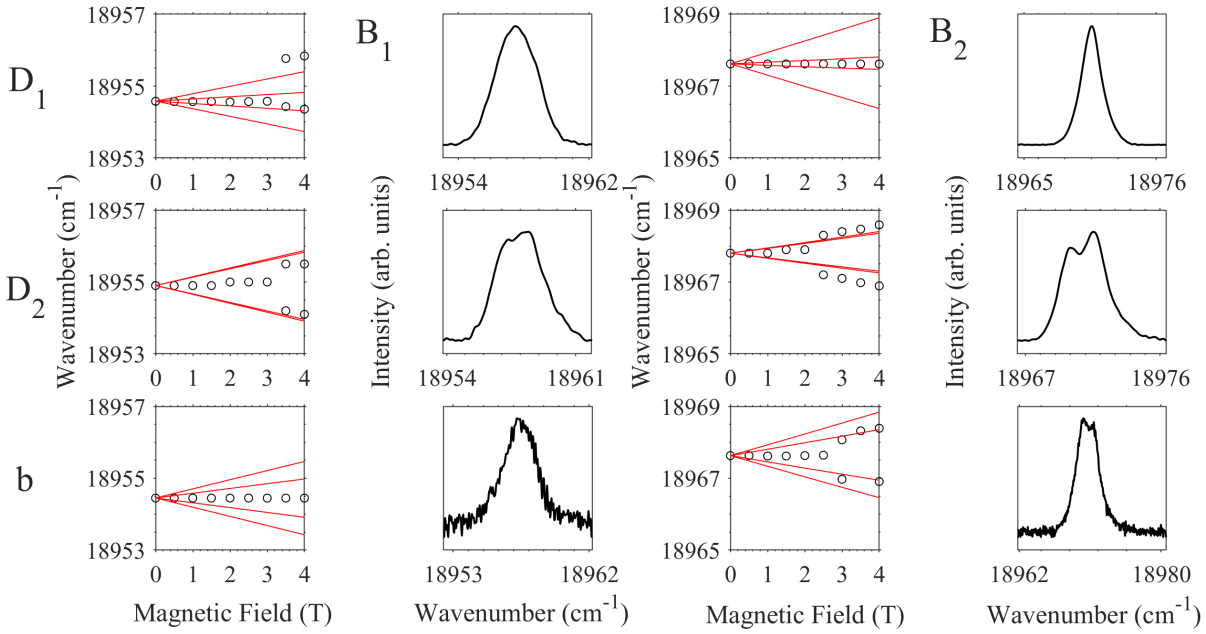

Figure 4.36: Magnetic splittings of the $^6H_{5/2}Z_1 \longrightarrow {}^4F_{3/2}B_i$ transitions for site 2 in Y_2SiO_5:0.5%Sm^{3+} with a magnetic field applied along the three crystallographic axes of Y_2SiO_5. The top, middle and bottom panels for each $Z_1 \longrightarrow B_i$ transition shows the magnetic splittings with $B \parallel D_1$, $B \parallel D_2$ and $B \parallel b$ respectively. The left panels depicts the experimental splittings, represented by the circles, and the theoretical splittings are represented by the red lines. The right panels shows Zeeman absorption spectra at a magnetic field represented by the vertical line in the left panels. All spectra were measured at 4.2 K.

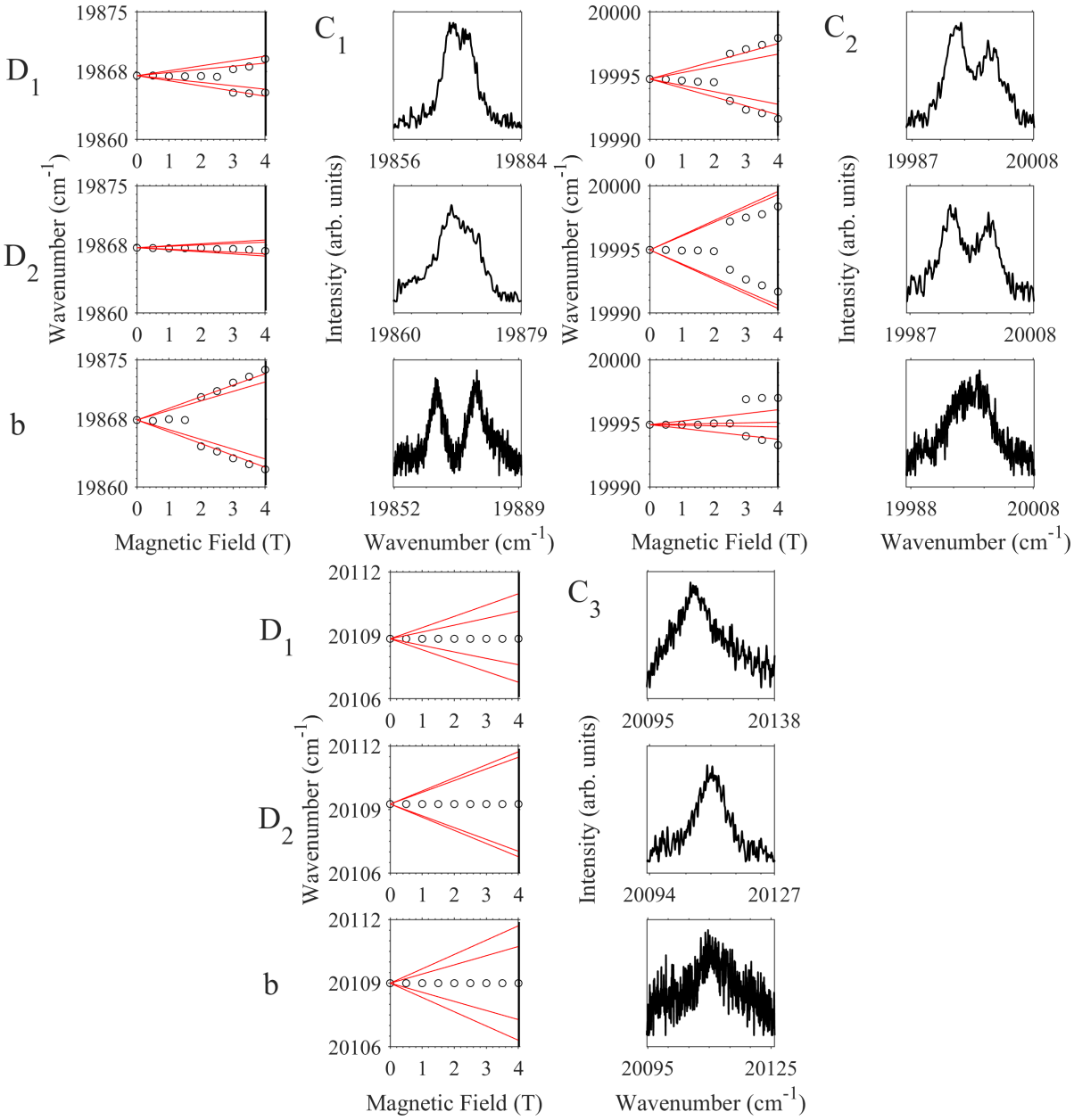

Figure 4.37: Magnetic splittings of the assigned $^6H_{5/2}Z_1 \longrightarrow {}^4G_{7/2}C_i$ transitions for site 1 in Y_2SiO_5:0.5%Sm^{3+} with a magnetic field applied along the three crystallographic axes of Y_2SiO_5. The top, middle and bottom panels for each $Z_1 \longrightarrow C_i$ transition shows the magnetic splittings with $B \parallel D_1$, $B \parallel D_2$ and $B \parallel b$ respectively. The left panels depicts the experimental splittings, represented by the circles, and the theoretical splittings are represented by the red lines. The right panels shows Zeeman absorption spectra at a magnetic field represented by the vertical line in the left panels. All spectra were measured at 4.2 K.

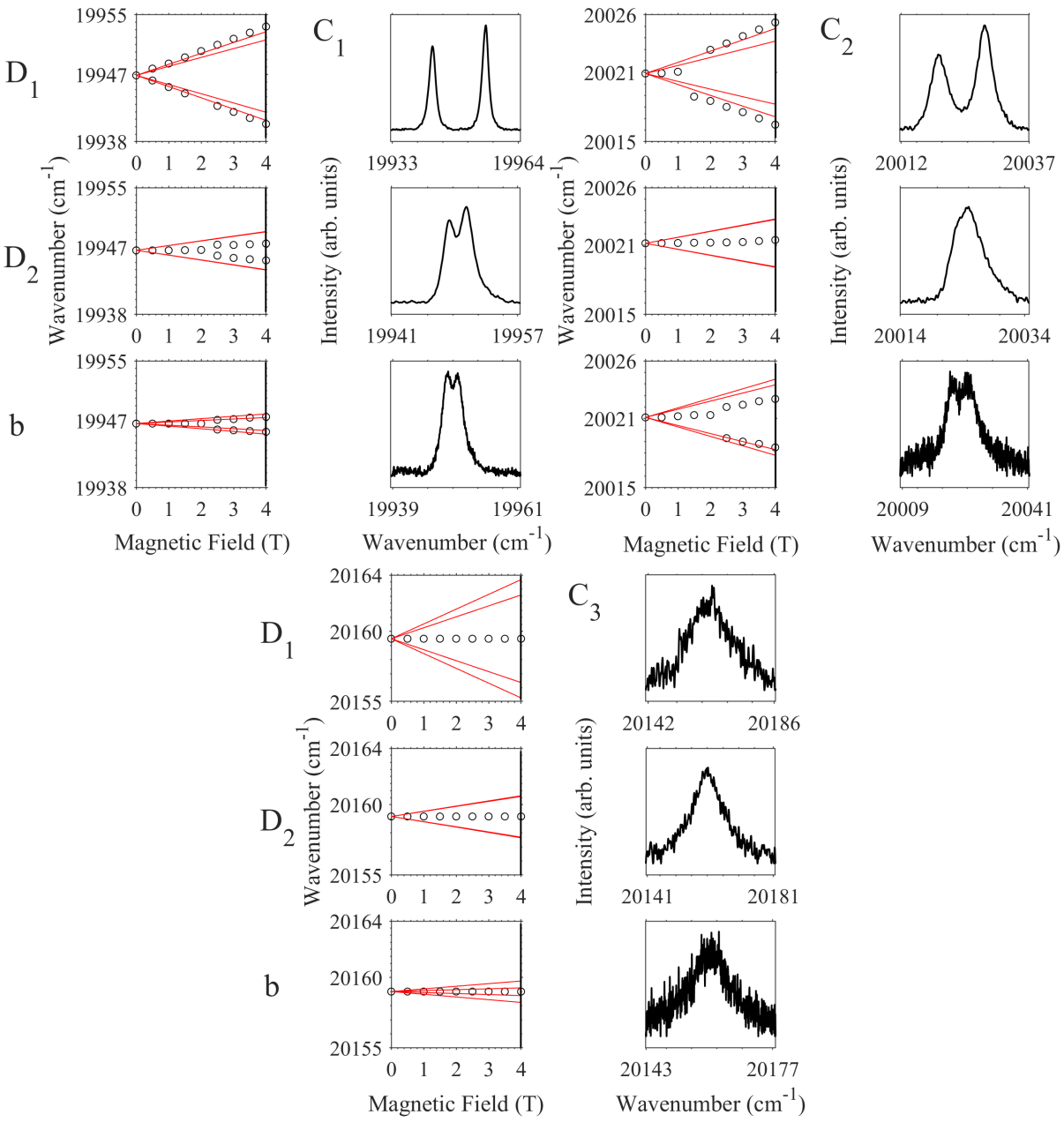

Figure 4.38: Magnetic splittings of the assigned $^6H_{5/2}Z_1 \longrightarrow {}^4G_{7/2}C_i$ transitions for site 2 in Y_2SiO_5:0.5%Sm^{3+} with a magnetic field applied along the three crystallographic axes of Y_2SiO_5. The top, middle and bottom panels for each $Z_1 \longrightarrow C_i$ transition shows the magnetic splittings with $B \parallel D_1$, $B \parallel D_2$ and $B \parallel b$ respectively. The left panels depicts the experimental splittings, represented by the circles, and the theoretical splittings are represented by the red lines. The right panels shows Zeeman absorption spectra at a magnetic field represented by the vertical line in the left panels. All spectra were measured at 4.2 K.

4.4 Raman Heterodyne spectroscopy

The Zeeman spectroscopy given in Section 4.3, provided a large amount of directional data, which is required in order to create a crystal-field model for Sm^{3+}:Y_2SiO_5. However, the three directions monitored is insufficient in determining the g tensor for any state. Therefore, Raman heterodyne spectroscopy was performed at low magnetic field strengths along nine different directions in order to determine the g tensors for the $^6H_{5/2}Z_1$ and $^4G_{5/2}A_1$ states of both sites. The experimental details of Raman heterodyne spectroscopy are given in Section 3.5. The centroid of the $^6H_{5/2}Z_1 \longrightarrow {}^4G_{5/2}A_1$ transition was known to be at around 17 689 cm^{-1} for site 1 and 17 790 cm^{-1} for site 2. However, to find the exact centroid, the laser was scanned across the spectral lines at zero magnetic field strength while simultaneously scanning the R-F frequency as shown in Figure 4.39. The centroids were found to be at 530 298 GHz (17 688.84 cm^{-1}) for site 1 and 533 328 GHz (17 789.91 cm^{-1}) for site 2. Throughout the remainder of this section the transition energies will be cited in terms of their frequencies for convenience. Due to the moderately high concentration of the sample (5000 ppm), the line widths of the hyperfine structure transition are exaggerated forming a high intensity 'background' centered on the transition centroid. This is exacerbated by the isotopic impurity of the sample, with the non-zero nuclear spin isotopes having different hyperfine structure. This prevented the hyperfine structure from being resolved and therefore studied. Also visible either side of the central structure are multiple bands which I attribute to cluster sites which arise from the moderately high concentration of the sample.

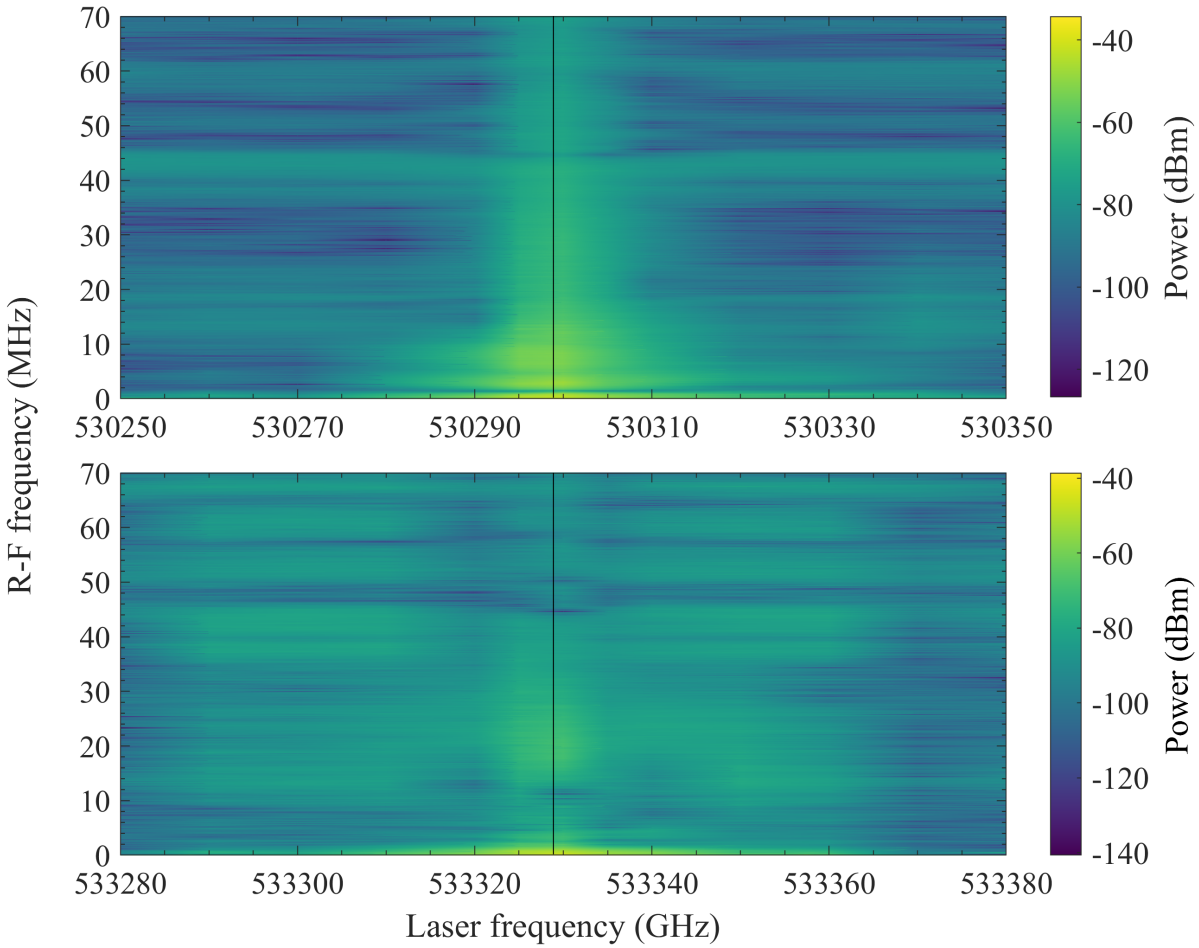

Figure 4.39: Raman heterodyne signal for the $^6H_{5/2}Z_1 \longrightarrow {}^4G_{5/2}A_1$ transition for site 1 (top), and site 2 (bottom) in Sm^{3+}:Y_2SiO_5 as a function of laser and R-F frequency. Note that the signals are plotted on a log scale. The laser excitation wavelengths used throughout this study are represented by the vertical lines at 530 298 GHz for site 1 and 533 328 GHz for site 2. Both spectra were obtained at 3.5 K.

Figures 4.40 and 4.41 shows the Raman heterodyne signal of the $^6H_{5/2}Z_1 \longrightarrow {}^4G_{5/2}A_1$ transition for sites 1 and 2 respectively in Sm^{3+}:Y_2SiO_5. All spectra were obtained at 3.5 K with a magnetic field applied down the three extinction axes and at 45° between two of the axes, resulting in the nine different directions depicted. Note that the applied magnetic field strengths varies between spectra and that the zero offsets are due to a stray magnetic field, which was estimated to be $[-0.2, +0.1, -0.1]$ mT in the $[D_1, D_2, b]$ direction. The Zeeman transitions of interest are the linear lines visible in each spectra. Spectra a) – d) and g) shows two transitions, one representing the splitting of the ground state and the other representing the splitting of the excited state. Spectra e), f), h) and i) shows four transitions, with a pair related to both the ground and excited states, which arises from the two magnetically inequivalent orientations of Y_2SiO_5. In the case of Figure 4.40 i) there are only three transitions visible, this is due to the two magnetically inequivalent orientations for the ground state being close to degenerate in the $D_2, -b$ direction and are therefore unresolvable.

Figures 4.42 and 4.43 depicts the predicted low field hyperfine splittings for site 1 and site 2 respectively, with a magnetic field directed along the D_1 axis. The predictions were made using the crystal-field model presented in Section 4.5. The fields represented matches the fields measured in the Raman heterodyne spectroscopy along the D_1 axis (panel a) in Figures 4.40 and 4.41. Here we see that some states are 'pseudo-doublets' that lineally split as a function of magnetic field, while other states are singlets that are mostly invariant with magnetic field. These two phenomena would explain the additional structure seen in Figures 4.40 and 4.41. In other directions, more complicated magnetic field dependencies may arise, which would explain the remaining non-linear structure.

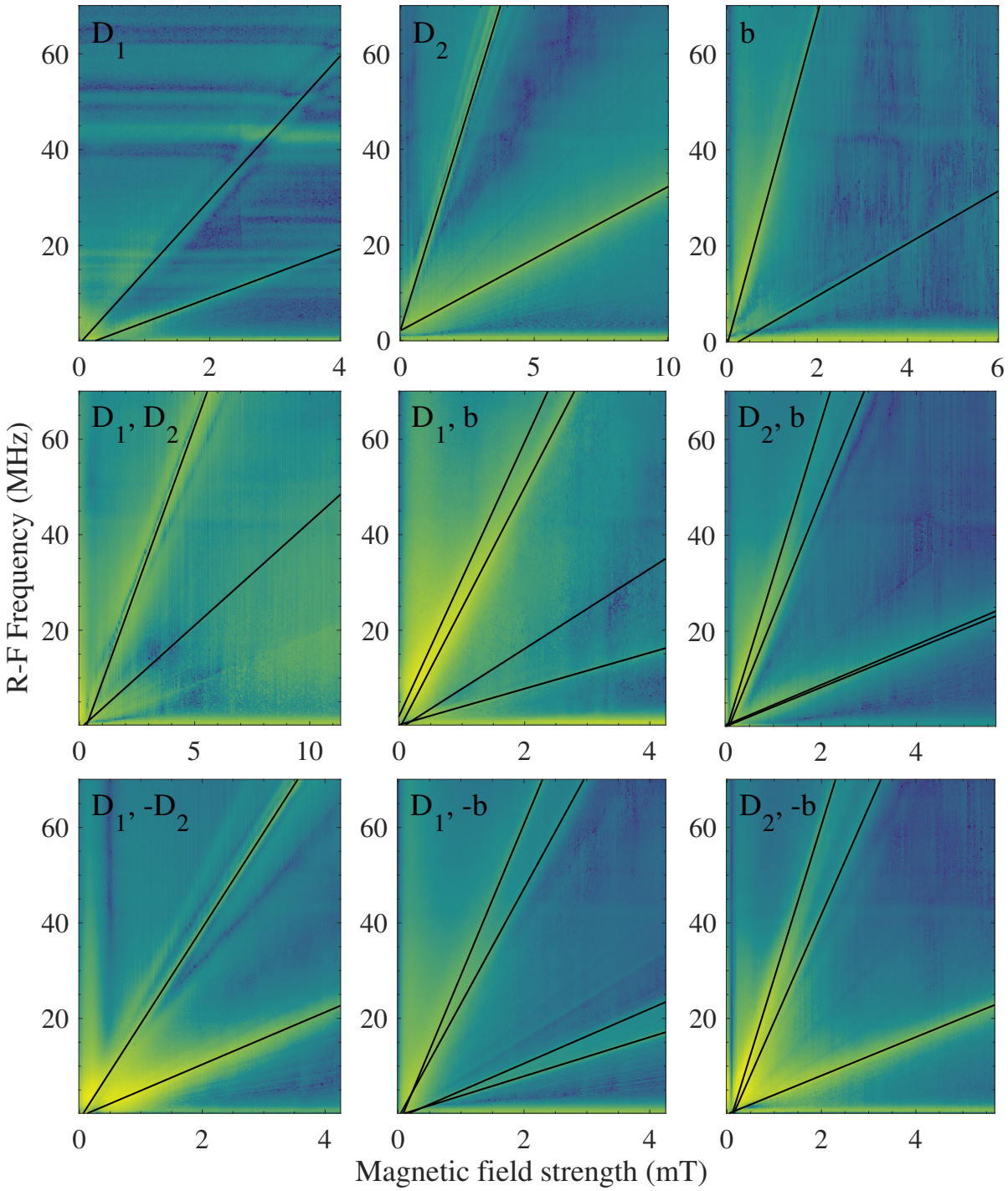

Figure 4.40: 3.5 K Raman heterodyne signal for the site 1, $^6H_{5/2}Z_1 \longrightarrow {}^4G_{5/2}A_1$ transition of Sm^{3+}:Y_2SiO_5 along nine different magnetic field directions. The applied magnetic field direction is stated on each panel. The lines represents linear least-squares fits that correspond to the Zeeman transitions along each direction. The laser excitation wavelength was 530 298 GHz. Note that the intensity is plotted on a log scale. The zero offsets are due to a stray magnetic field.

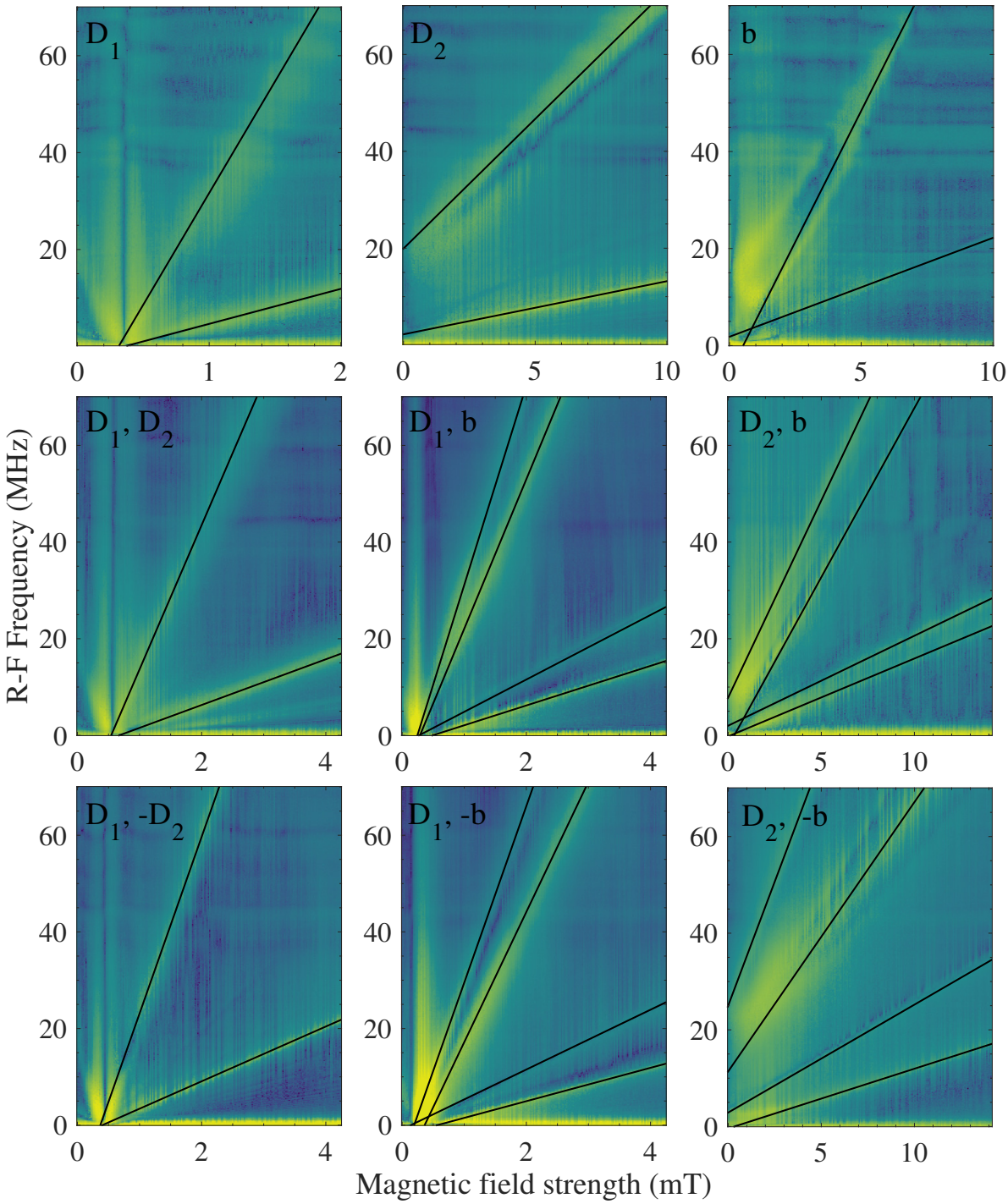

Figure 4.41: 3.5 K Raman heterodyne signal for the site 2, $^6H_{5/2}Z_1 \longrightarrow {}^4G_{5/2}A_1$ transition of Sm^{3+}:Y_2SiO_5 along nine different magnetic field directions. The applied magnetic field direction is stated on each panel. The lines represents linear least-squares fits that correspond to the Zeeman transitions along each direction. The laser excitation wavelength was 533 533 GHz. Note that the intensity is plotted on a log scale. The zero offsets are due to a stray magnetic field.

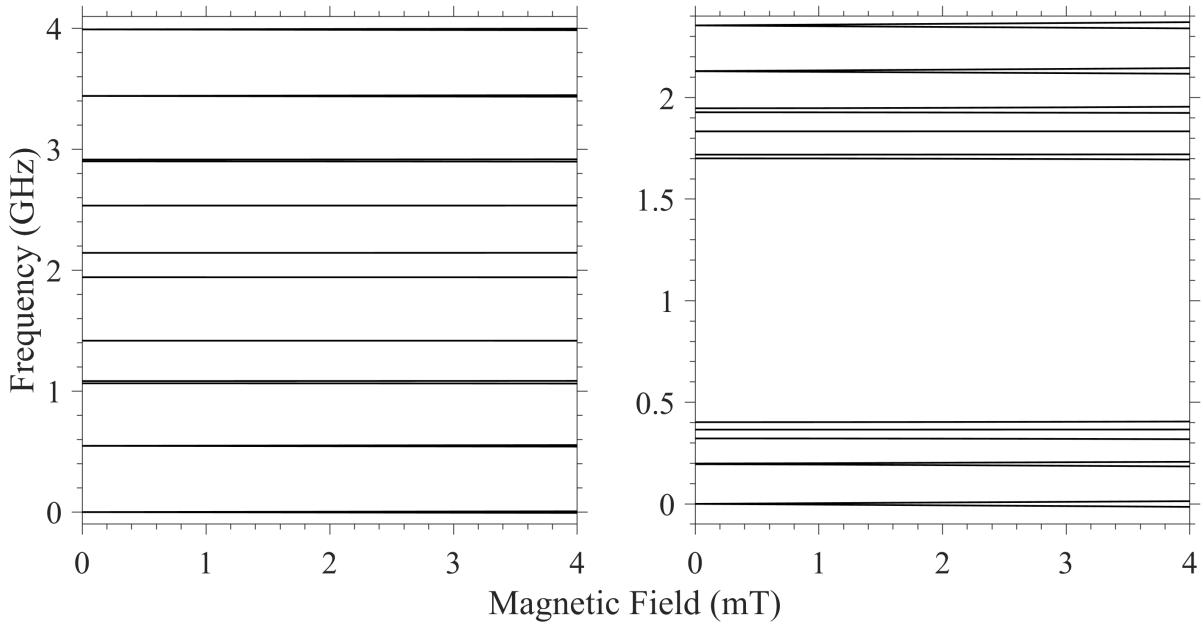

Figure 4.42: Predicted low field hyperfine splittings of the $^6H_{5/2}Z_1$ (left) and $^4G_{5/2}A_1$ (right) states for site 2 in Sm^{3+}:Y_2SiO_5 with a magnetic field applied down the D_1 axis.

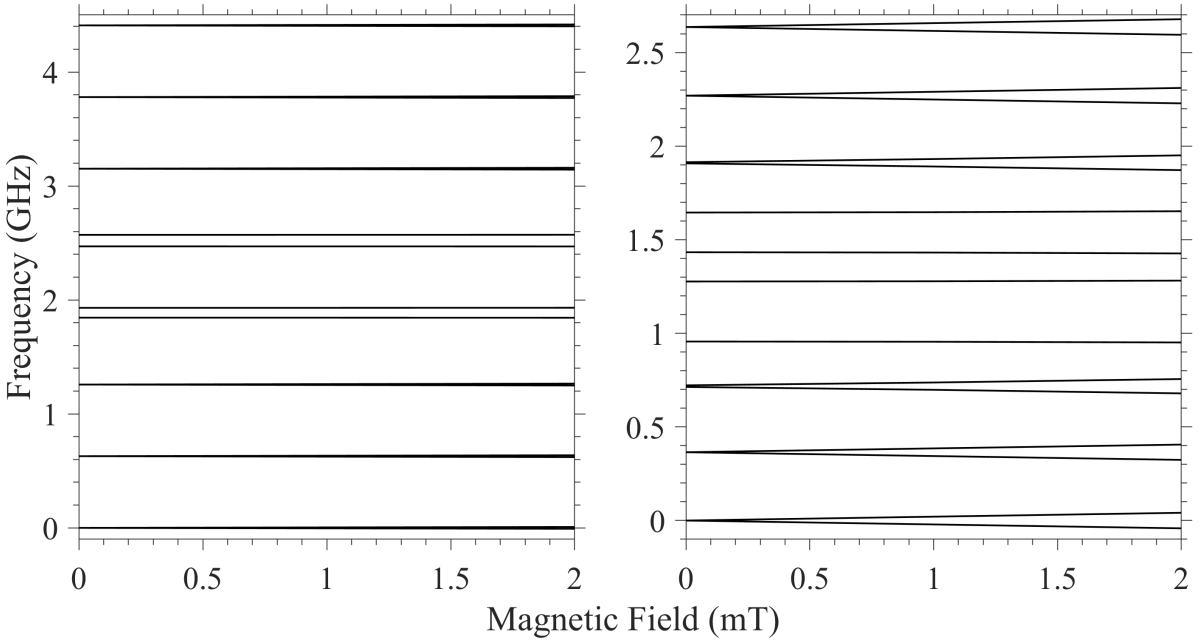

Figure 4.43: Predicted low field hyperfine splittings of the $^6H_{5/2}Z_1$ (left) and $^4G_{5/2}A_1$ (right) states for site 2 in Sm^{3+}:Y_2SiO_5 with a magnetic field applied down the D_1 axis.

The g values of the $^6H_{5/2}Z_1$ ground and $^4G_{5/2}A_1$ excited states were determined using Equation (4.1) and are summarised in Tables 4.1 and 4.2 for sites 1 and 2 respectively. These g values agree with those found in Zeeman absorption spectroscopy. Each state in the $D_1, \pm b$ and $D_2, \pm b$ directions have two related g values which arises from the two magnetically inequivalent orientations. In the case of Y_2SiO_5, the $D_1, +b$ and $D_1, -b$ directions, in addition to the the $D_2, +b$ and the $D_2, -b$ directions are degenerate. Therefore, the average of the two g values were used in determining the g tensors. Preliminary crystal-field analyses performed on Sm^{3+}:Y_2SiO_5 have shown that the g values for the ground state are significantly smaller than those of the excited state in most directions, and therefore distinguishing their g values is trivial. The exception to this are the g values in the D_2, b, and $D_2, \pm b$ directions for site 2 where both the ground and excited states have g values significantly less than one. These g values were assigned as belonging to that of either the ground or excited state by constructing a g tensor for every remaining combination of g values and determining the g tensor that provided the closest agreement to the experimental data.

Table 4.1: Experimentally determined g values of the $^6H_{5/2}Z_1$ ground and $^4G_{5/2}A_1$ excited states, obtained from the splittings depicted in Figure 4.40, along each magnetic field direction for site 1 in Sm^{3+}:Y_2SiO_5. The numbers in parentheses are uncertainties.

Direction	Ground	Excited
D_1	0.36 (0.04)	1.07 (0.31)
D_2	0.21 (0.09)	1.29 (0.21)
b	0.39 (0.02)	2.46 (0.19)
$D_1, +D_2$	0.31 (0.05)	0.94 (0.14)
$D_1, -D_2$	0.39 (0.18)	1.43 (0.34)
$D_1, \pm b$	0.28, 0.50 (0.01, 0.15)	1.77, 2.16 (0.08, 0.42)
$D_2, \pm b$	0.29, 0.29 (0.12, 0.12)	1.68, 2.29 (0.23, 0.49)

Table 4.2: Experimentally determined g values of the $^6H_{5/2}Z_1$ ground and $^4G_{5/2}A_1$ excited states, obtained from the splittings depicted in Figure 4.41, along each magnetic field direction for site 2 in Sm^{3+}:Y_2SiO_5. The numbers in parentheses are uncertainties.

Direction	Ground	Excited
D_1	0.52 (0.05)	3.29 (0.51)
D_2	0.078 (0.005)	0.38 (0.11)
b	0.15 (0.01)	0.77 (0.11)
$D_1, +D_2$	0.34 (0.05)	2.13 (0.16)
$D_1, -D_2$	0.41 (0.05)	2.61 (0.09)
$D_1, \pm b$	0.27, 0.44 (0.05, 0.02)	2.40, 2.42 (0.24, 0.35)
$D_2, \pm b$	0.10, 0.146 (0.01, 0.005)	0.50, 0.66 (0.08, 0.06)

Following Weil *et al.*, we relate the g values, g, with a magnetic field applied along an arbitrary direction $\mathbf{n}$ to the g tensor, $\mathbf{g}$, through the following relationship [141]:

$$g^2(\mathbf{n}) = \mathbf{n}^T \cdot (\mathbf{g} \cdot \mathbf{g}^T) \cdot \mathbf{n} \tag{4.2}$$

For a particular magnetic field direction, Equation (4.2) is transformed to:

$$g^2(\mathbf{n}_\alpha) = (\mathbf{g} \cdot \mathbf{g}^T)_{\alpha\alpha} \tag{4.3}$$

and

$$g^2(\mathbf{n}_{\alpha\pm\beta}) = \frac{1}{2}\Big[(\mathbf{g} \cdot \mathbf{g}^T)_{\alpha\alpha} + (\mathbf{g} \cdot \mathbf{g}^T)_{\beta\beta} \pm 2(\mathbf{g} \cdot \mathbf{g}^T)_{\alpha\beta}\Big] \tag{4.4}$$

Here $\mathbf{n}_\alpha$ and $\mathbf{n}_\beta$ are the basis vectors of the Cartesian coordinate system and $\mathbf{n}_{\alpha\pm\beta}$ are the unit vectors in the $\mathbf{n}_\alpha \pm \mathbf{n}_\beta$ directions. From Equations (4.3) and (4.4), the squares of the off-diagonal components of the g tensor can be expressed as:

$$(\mathbf{g} \cdot \mathbf{g}^T)_{\alpha\beta} = \frac{g^2(\mathbf{n}_{\alpha+\beta}) - g^2(\mathbf{n}_{\alpha-\beta})}{2} \tag{4.5}$$

Using Equations (4.3) and (4.5) the full g tensors were determined. The g tensor is symmetric and therefore requires six independent components to be determined. Due to the two magnetically inequivalent orientations and the ambiguity between the ground and excited states there are 16 possible combinations of g values for site 1 and 256 possible combination for site 2. Equations (4.6) and (4.7) show the g tensors of the ${}^6\mathrm{H}_{5/2}\mathrm{Z}_1$ ground ($\mathbf{g}_{g1}$ for site 1 and $\mathbf{g}_{g2}$ for site 2) and ${}^4\mathrm{G}_{5/2}\mathrm{A}_1$ excited ($\mathbf{g}_{e1}$ for site 1 and $\mathbf{g}_{e2}$ for site 2) states in Sm^{3+}:$\mathrm{Y}_2\mathrm{SiO}_5$ that provided the closest agreement to the experimental data.

$$\mathbf{g}_{g1} = \begin{pmatrix} 0.351 & -0.016 & 0.078 \\ -0.016 & 0.209 & -0.007 \\ 0.078 & -0.007 & 0.382 \end{pmatrix}, \qquad \mathbf{g}_{e1} = \begin{pmatrix} 1.025 & -0.257 & 0.166 \\ -0.257 & 1.248 & 0.202 \\ 0.166 & 0.202 & 2.446 \end{pmatrix} \tag{4.6}$$

$$\mathbf{g}_{g2} = \begin{pmatrix} 0.512 & -0.040 & -0.054 \\ -0.040 & 0.067 & 0.009 \\ -0.054 & 0.009 & 0.135 \end{pmatrix}, \qquad \mathbf{g}_{e2} = \begin{pmatrix} 3.264 & -0.311 & 0.262 \\ -0.311 & 0.183 & 0.125 \\ 0.262 & 0.125 & 0.714 \end{pmatrix} \tag{4.7}$$

Table 4.3 shows the principal axes and related direction cosines obtained by diagonalising the g tensors given in Equations (4.3) and (4.5). The principal axes are the eigenvectors of the g tensor while the principal g values are their corresponding eigenvalues. The principal axes are labelled x', y' and z' with the maximum and minimum g value directions labelled as z' and x' respectively.

Table 4.3: Principal g values and direction cosines of the ground and excited state g tensors for both sites in Sm^{3+}:Y_2SiO_5. The principal axes are labelled x', y' and z' with the maximum and minimum g values directions labelled as z' and x' respectively.

		Ground state				Excited state			
		Prin. g	l	m	n	Prin. g	l	m	n
Site 1	$g_{z'}$	0.447	0.635	−0.066	0.770	2.490	0.087	0.143	0.986
	$g_{y'}$	0.288	−0.764	0.093	0.639	1.411	0.573	−0.817	0.068
	$g_{x'}$	0.208	0.114	0.994	−0.009	0.818	0.815	0.559	−0.152
Site 2	$g_{z'}$	0.523	−0.986	0.088	0.140	3.319	−0.991	0.095	−0.095
	$g_{y'}$	0.128	−0.144	−0.045	−0.989	0.730	−0.068	0.259	0.964
	$g_{x'}$	0.063	0.081	0.995	−0.057	0.113	0.116	0.961	−0.251

Figure 4.44 gives a visual representation of the directional splittings of the $^6H_{5/2}Z_1$ ground state and the $^4G_{5/2}A_1$ excited state for both sites in Y_2SiO_5. The g tensors derived in Equations (4.3) and (4.5) were used to derive the effective g values in terms of the extinction axes. The black dots are the experimentally determined g values given in Tables 4.1 and 4.2. The extinction and principal axes are depicted as the solid and dash-dotted lines respectively.

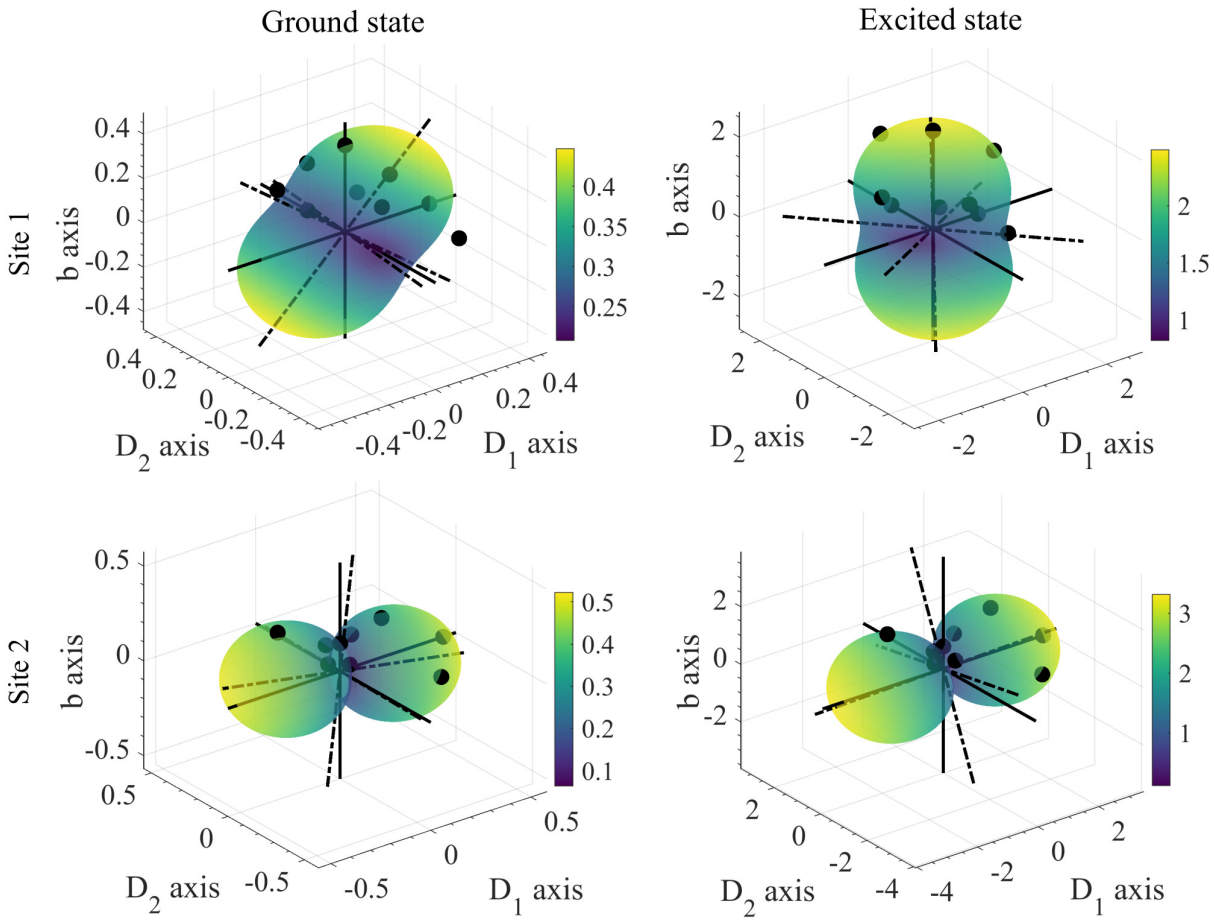

Figure 4.44: The effective g values for the ground (left panels) and excited (right panels) for site 1 (top panels) and site 2 (bottom panels) in Sm^{3+}:Y_2SiO_5. The experimental values are given by the black data points whereas the extinction and principal axes are given as the solid and dash-dotted lines respectively.

Figures 4.45 and 4.46 shows the angular dependence of the g values for the $^6H_{5/2}Z_1$ ground (left panels) and $^4G_{5/2}A_1$ excited states (right panels) of sites 1 and 2 respectively in Sm^{3+}:Y_2SiO_5. The top panels depict a rotation in the D_1-D_2 ($\theta = 90°$) plane with $\phi = 0°$ corresponding to the D_1 axis and $\phi = 90°$ corresponding to the D_2 axis. The middle panels depict a rotation in the b-D_1 ($\phi = 0°$) plane with $\theta = 0°$ corresponding to the b axis and $\theta = 90°$ corresponding to the D_1 axis. The bottom panels depict a rotation in the b-D_2 ($\phi = 90°$) plane with $\theta = 0°$ corresponding to the b axis and $\theta = 90°$ corresponding to the D_2 axis. The site 2 rotation curves for both the ground and excited states have a very similar shape, with only the magnitude that varies. This is confirmed by inspecting Figure 4.44 where both states have their g tensors orientated in a very similar direction.

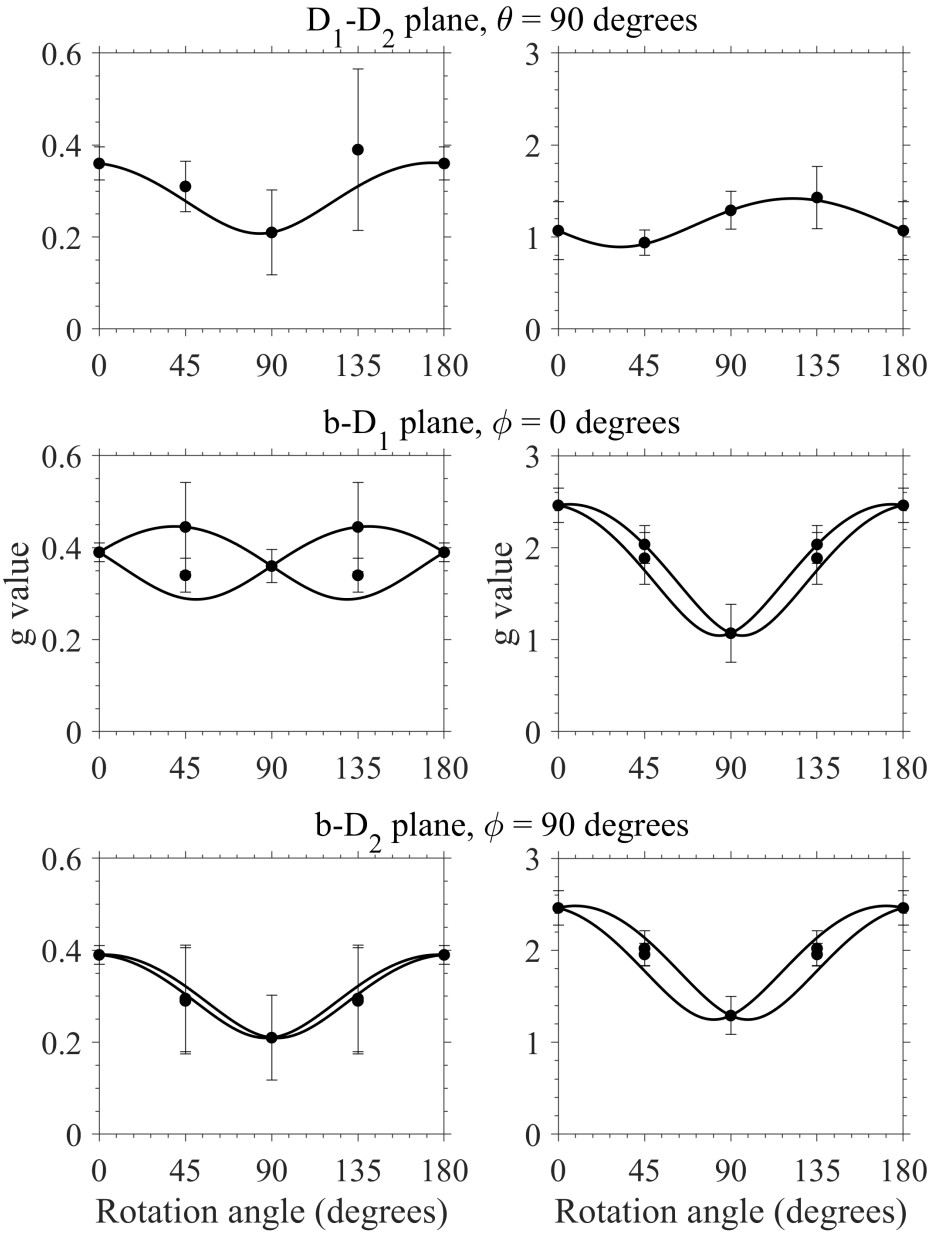

Figure 4.45: The g value rotation curves in the: D_1-D_2 ($\theta = 90°$) plane (top panels), b-D_1 ($\phi = 0°$) plane (middle panels) and b-D_2 ($\phi = 90°$) plane (bottom panels) for the $^6H_{5/2}Z_1$ ground state (left panels) and the $^4G_{5/2}A_1$ excited state (right panels) for site 1 in Sm^{3+}:Y_2SiO_5. The solid lines are calculated g values based on the g tensors given in Equation (4.7), while the circles are the experimentally determined g values.

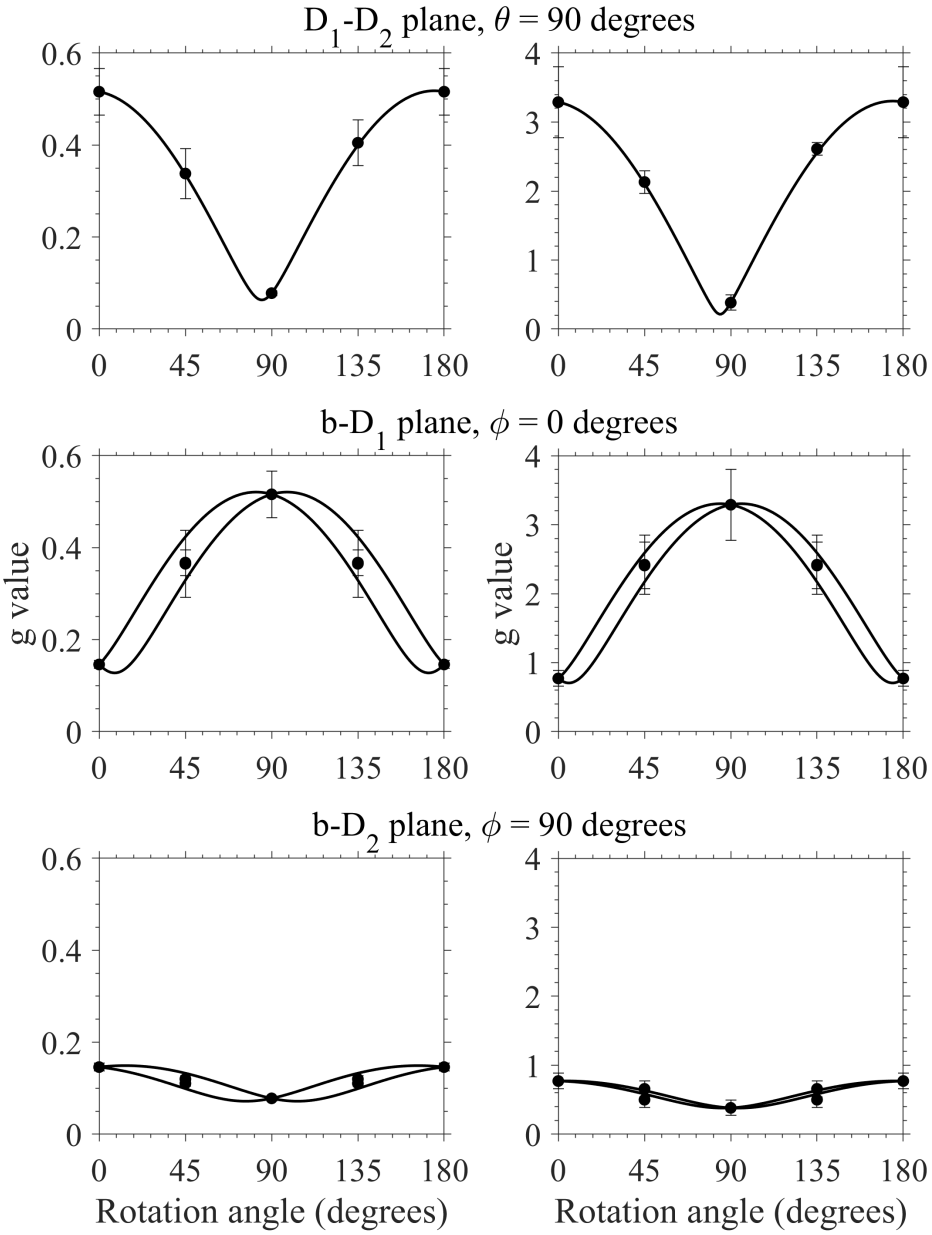

Figure 4.46: The g value rotation curves in the: D_1-D_2 ($\theta = 90°$) plane (top panels), b-D_1 ($\phi = 0°$) plane (middle panels) and b-D_2 ($\phi = 90°$) plane (bottom panels) for the $^6H_{5/2}Z_1$ ground state (left panels) and the $^4G_{5/2}A_1$ excited state (right panels) for site 2 in Sm^{3+}:Y_2SiO_5. The solid lines are calculated g values based on the g tensors given in Equation (4.7), while the circles are the experimentally determined g values.

4.5 Crystal-field analysis

A crystal-field model was developed for both sites of Sm^{3+}:Y_2SiO_5 by fitting five free-ion parameters and 27 crystal-field parameters to experimental data. As no hyperfine structure could be observed, the hyperfine parameters could not be determined. In order to reduce the computational time, the matrix elements of the Stark levels were truncated to 30 000 cm^{-1}. The initial crystal-field parameters used in the optimisation routine were set to those found by Horvath *et al.* for Er^{3+}:Y_2SiO_5, while the initial free-ion parameters were set to those found by Carnall *et al.* [49,55,106]. The two- and three-body interactions and higher order effects in the free-ion Hamiltonian were held fixed to the values obtained by Carnall *et al.* for Sm^{3+}:LnF_3 [49]. A coarse fit was performed using a basin-hopping algorithm, which allowed for the addition of uncertain assignments in the $^6F_{1/2}$, $^6F_{3/2}$, and $^6H_{15/2}$ multiplets, followed by a final fit using simulated annealing. The details of the crystal-field fitting procedure and the algorithms used are given in Section 2.5. Table 4.4 shows the weightings used for the various parameters sets during the fitting process. These weightings were chosen to reflect the uncertainties in the relevant measurements. It should be noted that different weightings would yield different parameters as the fit prioritises different data sets. A separate Hamiltonian was created for each set of data at a specific magnetic field in order to allow for parallelisation, thus further reducing the computing time required. The magnetic fields chosen were given by the parametric spiral:

$$\mathbf{B} = B_0 \begin{bmatrix} \sqrt{1-t^2}\cos(6\pi t) \\ \sqrt{1-t^2}\sin(6\pi t) \\ t \end{bmatrix}, \quad t \in [-1, 1] \tag{4.8}$$

With B_0 being the magnitude of the magnetic field vector.

For site 1 a total of 150 experimental data points were fitted simultaneously and are as follows:

- 54 electronic energy levels up to the $^4G_{7/2}$ multiplet at ∼20 000 cm^{-1}.
- 72 g values (25 along the D_1 axis, 22 along the D_2 axis and 25 along the b axis) corresponding to states up to the $^4G_{7/2}$ multiplet at ∼20 000 cm^{-1}.
- 12 data points for the magnetic splittings of the $^6H_{5/2}Z_1$ state, calculated from the $\mathbf{g}_{g1}$ tensor given in Equation (4.6), sampled at equally spaced intervals according to Equation (4.8), with $B_0 = 0.05$ T.
- 12 data points for the magnetic splittings of the $^4G_{5/2}A_1$ state, calculated from the $\mathbf{g}_{e1}$ tensor given in Equation (4.6), sampled at equally spaced intervals according to Equation (4.8), with $B_0 = 0.05$ T.

For site 2 a total of 169 experimental data points were fitted simultaneously and are as follows:

- 53 electronic energy levels up to the $^4G_{7/2}$ multiplet at ∼20 000 cm^{-1}.
- 92 g values (34 along the D_1 axis, 28 along the D_2 axis and 30 along the b axis) corresponding to states up to the $^4G_{7/2}$ multiplet at ∼20 000 cm^{-1}.

- 12 data points for the magnetic splittings of the $^6H_{5/2}Z_1$ state, calculated from the $\mathbf{g}_{g2}$ tensor given in Equation (4.7), sampled at equally spaced intervals according to Equation (4.8), with $B_0 = 0.05$ T.
- 12 data points for the magnetic splittings of the $^4G_{5/2}A_1$ state, calculated from the $\mathbf{g}_{e2}$ tensor given in Equation (4.7), sampled at equally spaced intervals according to Equation (4.8), with $B_0 = 0.05$ T.

Table 4.4: Weightings used for different parameter sets during the fitting process for both sites in Sm^{3+}:Y_2SiO_5.

Data set	Weighting
Electronic levels	1
g values	1×10^3
$^6H_{5/2}Z_1$ and $^4G_{5/2}A_1$ $\mathbf{g}$ tensors	1×10^4

Tables 4.5 and 4.6 shows the theoretical and experimental energy levels and g values up to the $^4G_{7/2}$ multiplet at $\sim$20 000 cm^{-1} for both sites in Y_2SiO_5. The theoretical values were estimated using the fitted crystal field parameters. The standard deviations between theoretical and experimental electronic energy levels were found to be 7.9 cm^{-1} for site 1 and 5.2 cm^{-1} for site 2. Furthermore, our study accurately reproduces the magnetic structure across the entire $4f^5$ configuration of Sm^{3+}:Y_2SiO_5.

Table 4.5: Theoretical and experimental electronic energies and corresponding g values along the D_1, D_2 and b axes for site 1 up to the $^4G_{7/2}$ multiplet of Sm^{3+}:Y_2SiO_5. The theoretical g values were calculated using the determined crystal-field Hamiltonian. Levels marked with a '–' could not be assigned. The experimentally determined energy levels have an associated uncertainty of 1 cm^{-1}.

		Energies			g values					
					D_1 axis		D_2 axis		b axis	
Multiplet	State	Theory	Exp.	Diff.	Theory	Exp.	Theory	Exp.	Theory	Exp.
$^6H_{5/2}$	Z_1	-3	0	3	0.44	0.36	0.14	0.21	0.52	0.39
	Z_2	301	287	−14	1.30	–	0.20	–	1.09	–
	Z_3	502	486	−16	1.23	–	0.54	–	0.31	–
$^6H_{7/2}$	Y_1	1161	1154	−7	2.12	–	1.31	–	3.70	–
	Y_2	1273	1275	2	2.06	–	3.73	–	1.28	–
	Y_3	1480	1484	4	1.18	–	2.88	–	1.88	–
	Y_4	1553	1551	−2	4.09	–	0.79	–	2.59	–
$^6H_{9/2}$	X_1	2352	2351	−1	3.86	2.70	1.48	–	7.77	7.76
	X_2	2452	2461	9	4.02	–	3.84	–	3.84	–
	X_3	2538	2539	1	2.44	–	2.99	–	2.92	–
	X_4	2699	2702	3	1.87	–	6.56	–	3.47	–
	X_5	2761	2762	1	7.65	–	1.40	–	4.22	–
$^6H_{11/2}$	W_1	3654	3661	7	5.84	4.50	1.30	2.34	10.96	11.58
	W_2	3720	3727	7	5.70	–	4.56	–	7.44	–
	W_3	3855	3841	−14	4.62	–	6.50	–	4.44	–
	W_4	3930	3934	4	4.93	–	2.74	–	5.25	–
	W_5	3998	3995	−3	5.24	–	8.83	–	5.99	–
	W_6	4068	4071	3	11.11	11.62	2.10	–	5.45	–
$^6H_{13/2}$	V_1	4983	4988	5	8.02	6.05	3.39	4.44	12.35	12.65
	V_2	5039	5031	−8	6.77	5.27	3.78	5.74	10.99	11.27
	V_3	5244	5254	10	3.39	–	1.81	–	9.81	–
	V_4	5303	5312	9	5.12	–	6.56	–	5.52	–
	V_5	5373	5370	−3	9.01	–	1.49	–	8.32	–
	V_6	5423	5423	0	10.84	–	0.54	–	6.54	–
	V_7	5469	5469	0	13.36	11.90	4.07	–	3.85	–

Continued over page.

		Energies			g values					
					D_1 axis		D_2 axis		b axis	
Multiplet	State	Theory	Exp.	Diff.	Theory	Exp.	Theory	Exp.	Theory	Exp.
$^6F_{1/2}$,	S_1	6202	6193	−9	9.29	7.15	4.24	6.67	13.29	13.96
$^6F_{3/2}$,	S_2	6393	6392	−1	7.35	–	3.55	–	11.74	–
$^6H_{15/2}$	S_3	6599	6583	−16	1.23	1.39	1.11	1.34	0.60	1.05
	S_4	6637	–	–	3.82	–	9.78	–	6.90	–
	S_5	6707	–	–	11.95	–	3.75	–	9.30	–
	S_6	6817	–	–	3.31	–	3.51	–	3.93	–
	S_7	6835	–	–	1.66	–	3.67	–	5.62	–
	S_8	6856	–	–	1.08	–	1.59	–	1.54	–
	S_9	6916	–	–	5.84	–	2.63	–	10.29	–
	S_{10}	7016	–	–	14.93	–	8.22	–	3.64	–
	S_{11}	7119	–	–	10.82	–	14.51	–	0.87	–
$^6F_{5/2}$	R_1	7337	7337	0	1.93	–	1.96	–	2.24	–
	R_2	7385	7392	7	1.76	–	2.75	3.00	1.27	–
	R_3	7479	7472	−7	3.19	–	3.46	–	1.52	–
$^6F_{7/2}$	Q_1	8170	8179	9	5.49	–	1.30	3.15	3.21	1.66
	Q_2	8195	8212	17	4.21	–	4.17	5.14	1.71	2.58
	Q_3	8246	8250	4	3.68	3.16	2.71	2.54	3.87	5.97
	Q_4	8362	8353	−9	4.37	4.59	4.24	5.06	3.95	3.85
$^6F_{9/2}$	P_1	9317	9327	10	6.53	7.82	6.79	4.69	2.22	3.91
	P_2	9366	9372	6	4.83	6.06	4.72	4.82	3.95	4.19
	P_3	9401	9406	5	4.62	2.14	1.61	3.79	7.63	3.04
	P_4	9432	9445	13	4.89	3.17	1.62	2.07	5.06	8.48
	P_5	9494	9494	0	4.96	4.12	3.48	4.82	8.18	8.46
$^6F_{11/2}$	O_1	10651	10635	−16	12.00	13.17	1.33	–	6.98	6.46
	O_2	10684	10685	1	3.05	1.37	11.64	13.14	4.64	4.53
	O_3	10773	10777	4	5.68	7.81	6.32	5.52	4.88	3.90
	O_4	10835	10822	−13	6.10	8.49	8.48	9.28	2.42	2.04
	O_5	10859	10844	−15	7.35	6.17	7.46	5.83	2.96	7.31
	O_6	10931	10919	−12	1.76	3.05	0.63	–	14.94	14.84
$^4G_{5/2}$	A_1	17691	17689	−2	1.29	1.07	1.08	1.29	2.43	2.46
	A_2	17919	17922	3	1.15	–	2.41	–	0.66	–
	A_3	18350	18355	5	1.91	–	1.08	–	1.80	–
$^4F_{3/2}$	B_1	18910	18913	3	0.79	–	0.78	–	0.74	–
	B_2	18932	18929	−3	1.09	–	0.36	–	0.48	–
$^4G_{7/2}$	C_1	19868	19868	0	2.08	2.12	0.88	–	5.38	6.28
	C_2	20000	19995	−5	2.55	3.40	4.79	3.58	0.72	1.98
	C_3	20109	20109	0	1.79	–	2.51	–	2.37	–
	C_4	20256	–	–	7.67	–	1.75	–	5.58	–

Table 4.6: Theoretical and experimental electronic energies and corresponding g values along the D_1, D_2 and b axes for site 2 up to the $^4G_{7/2}$ multiplet of Sm^{3+}:Y_2SiO_5. The theoretical g values were calculated using the determined crystal-field Hamiltonian. Levels marked with a '–' could not be assigned. The experimentally determined energy levels have an associated uncertainty of 1 cm^{-1}.

		Energies			g values					
					D_1 axis		D_2 axis		b axis	
Multiplet	State	Calc.	Exp.	Diff.	Calc.	Exp.	Calc.	Exp.	Calc.	Exp.
$^6H_{5/2}$	Z_1	1	0	−1	0.58	0.52	0.03	0.08	0.26	0.15
	Z_2	302	300	−2	0.67	–	0.87	–	0.60	–
	Z_3	437	429	−8	0.35	–	0.87	–	1.29	–
$^6H_{7/2}$	Y_1	1118	1119	1	4.42	–	1.54	–	1.37	–
	Y_2	1262	1256	−6	3.50	–	1.25	–	1.86	–
	Y_3	1418	1421	3	2.84	–	3.42	–	1.47	–
	Y_4	1467	1463	−4	1.11	–	2.30	–	3.40	–
$^6H_{9/2}$	X_1	2318	2322	4	8.17	7.92	2.35	1.48	1.81	1.63
	X_2	2410	2415	5	6.52	6.15	1.06	–	4.00	4.32
	X_3	2562	2564	2	4.37	–	3.29	–	1.69	–
	X_4	2625	2627	2	3.74	–	5.86	–	4.14	6.49
	X_5	2662	2660	−2	2.14	–	3.79	6.07	5.55	–
$^6H_{11/2}$	W_1	3611	3615	4	11.68	11.93	1.93	0.69	3.47	2.56
	W_2	3709	3713	4	9.68	10.10	1.67	–	4.25	4.00
	W_3	3837	3833	−4	7.32	7.06	2.74	–	3.05	–
	W_4	3903	3906	3	2.46	3.90	4.61	4.10	3.26	–
	W_5	3940	3940	0	5.80	–	3.93	–	6.30	–
	W_6	3985	3987	2	1.87	–	5.12	8.02	9.64	7.99
$^6H_{13/2}$	V_1	4937	4936	−1	14.78	15.01	1.24	1.12	6.05	5.17
	V_2	5128	5124	−4	12.90	13.89	3.86	–	4.41	–
	V_3	5199	5199	0	9.24	9.01	5.40	6.97	3.86	3.17
	V_4	5246	5244	−2	3.85	3.12	6.09	10.04	5.44	–
	V_5	5300	5301	1	5.28	5.68	7.81	–	4.72	–
	V_6	5343	5337	−6	3.29	8.23	7.50	7.23	8.81	–
	V_7	5414	5414	0	3.27	–	7.47	8.76	13.20	12.35

Continued over page.

		Energies			g values					
					D_1 axis		D_2 axis		b axis	
Multiplet	State	Theory	Exp.	Diff.	Theory	Exp.	Theory	Exp.	Theory	Exp.
$^6F_{1/2}$,	S_1	6217	6217	0	17.26	17.86	2.14	0.95	7.57	6.70
$^6F_{3/2}$,	S_2	6528	6514	−14	1.03	–	1.63	0.99	1.44	1.68
$^6H_{15/2}$	S_3	6546	–	–	12.75	–	3.36	–	4.59	–
	S_4	6592	–	–	3.15	–	12.33	–	3.63	–
	S_5	6652	–	–	5.05	–	5.58	–	5.83	–
	S_6	6740	–	–	3.53	–	6.32	–	7.07	–
	S_7	6771	–	–	2.92	–	2.20	–	2.45	–
	S_8	6801	–	–	1.32	–	2.86	–	1.22	–
	S_9	6843	–	–	2.17	–	4.48	–	8.48	–
	S_{10}	6870	–	–	8.46	–	10.96	–	2.63	–
	S_{11}	6940	–	–	4.62	–	5.70	–	15.16	–
$^6F_{5/2}$	R_1	7280	7281	1	3.76	3.75	2.57	–	1.39	2.54
	R_2	7305	7308	3	2.30	3.27	0.66	–	2.67	2.38
	R_3	7356	7350	−6	2.54	–	3.11	–	2.41	–
$^6F_{7/2}$	Q_1	8105	8117	12	3.21	2.26	3.09	1.55	3.35	2.50
	Q_2	8144	8152	8	3.47	2.67	3.84	3.44	3.19	4.29
	Q_3	8184	8184	0	6.00	7.16	1.50	1.88	2.73	2.42
	Q_4	8219	8214	−5	2.00	–	5.80	4.64	3.32	5.61
$^6F_{9/2}$	P_1	9265	9270	5	5.14	2.80	5.55	6.40	7.95	7.24
	P_2	9300	9300	0	6.27	3.39	3.41	1.86	5.94	6.03
	P_3	9325	9337	12	4.38	3.38	5.07	5.32	3.25	2.59
	P_4	9349	9354	5	4.97	8.55	4.37	–	3.68	2.79
	P_5	9406	9408	2	10.27	11.18	1.89	–	3.57	–
$^6F_{11/2}$	O_1	10623	10612	−11	3.08	4.83	7.45	6.57	10.64	11.93
	O_2	10645	10635	−10	5.36	2.69	3.67	2.70	6.26	8.66
	O_3	10682	10675	−7	5.82	5.72	5.92	4.40	1.74	4.32
	O_4	10728	10726	−2	10.29	9.35	2.87	2.48	3.19	4.39
	O_5	10779	10783	4	9.83	10.07	4.73	–	11.08	–
	O_6	10823	10817	−6	13.05	14.24	8.94	–	0.56	–
$^4G_{5/2}$	A_1	17794	17790	−4	2.98	3.29	0.26	0.38	0.85	0.77
	A_2	17921	17915	−7	2.22	–	0.66	–	1.13	–
	A_3	18283	18291	8	1.06	–	2.04	–	1.88	–
$^4F_{3/2}$	B_1	18951	18955	4	0.31	0.79	1.03	0.75	0.83	–
	B_2	18972	18968	−4	0.77	–	0.59	0.91	1.02	0.79
$^4G_{7/2}$	C_1	19945	19947	2	5.79	6.99	2.74	1.21	1.19	1.07
	C_2	20017	20021	4	3.52	4.75	2.22	–	3.26	2.25
	C_3	20157	20159	2	3.91	–	1.57	–	0.55	–
	C_4	20300	–	–	1.62	–	4.17	–	3.22	–

Table 4.7 shows the fitted free-ion and crystal-field parameters for both sites in Sm^{3+}:Y_2SiO_5. The two- and three-body interactions and higher order effects in the free-ion Hamiltonian were held fixed to the values obtained by Carnall *et al.* for Sm^{3+}:LaF_3 and are given by the square brackets [49]. The uncertainties of the fitted parameters were estimated through the use of the MCMC techniques by sampling the posterior probability distribution [128]. A total of 5 000 000 trials were attempted for both sites with 423 818 accepted steps for site 1 and 401 830 accepted steps for site 2. This aligns with the Metropolis algorithms ∼10 % acceptance rate recommended for this technique, which was fine tuned through altering the step size in the optimisation routine [128]. Of the accepted steps, the last 50 000 steps were used to allow the algorithm to 'burn in' (become confined within the area of the global minimum). Every 10^{th} element was then selected from the remaining points to ensure that the samples were not correlated.

Figures 4.47 and 4.48 shows the variation of the fitted free-ion and crystal field parameters for site 1 and site 2 respectively once the algorithm was allowed to 'burn in'. The standard deviation of this variation was used as the parameter uncertainties. The first panel of both figures depicts the χ^2 value of the model as a function of accepted step. The final χ^2 values were found to be 4260 for site 1 and 2550 for site 2. Many of the free-ion and crystal-field parameters were found to be composed of multiple distributions, which is indicative of multiple equally valid local minima that the model moves between, instead of a single global minimum. This is a reflection of the complex parameter space that is present in the C_1 symmetry environment of Y_2SiO_5.

Table 4.7: Fitted values and their related uncertainties for the free-ion and crystal-field parameters of site 1 and site 2 in Sm^{3+}:Y_2SiO_5. All values are in cm^{-1}, and the square brackets indicates the parameters that were held fixed during the fitting process.

Parameter	Site 1	Site 1 Uncer.	Site 2	Site 2 Uncer.
E_{avg}	47318.63	0.4	47336.56	0.6
F^2	78304.67	2.7	78382.86	2.6
F^4	56472.48	4.7	56603.73	5.3
F^6	39718.79	4.1	39875.75	5.5
ζ	1165.98	0.3	1169.16	0.5
α	[20.16]	–	[20.16]	–
β	[−566.90]	–	[−566.90]	–
γ	[1500.00]	–	[1500.00]	–
T^2	[300.00]	–	[300.00]	–
T^3	[36.00]	–	[36.00]	–
T^4	[56.00]	–	[56.00]	–
T^6	[−347.00]	–	[−347.00]	–
T^7	[373.00]	–	[373.00]	–
T^8	[348.00]	–	[348.00]	–
M^{tot}	[2.60]	–	[2.60]	–
P^{tot}	[357.00]	–	[357.00]	–
B_0^2	−507.86	4.9	382.22	9.1
B_1^2	$619.26 + 216.98i$	$5.6 + 4.8i$	$366.20 - 106.59i$	$8.4 + 8.2i$
B_2^2	$71.49 - 90.84i$	$5.4 + 4.1i$	$-451.24 - 121.22i$	$6.8 + 8.0i$
B_0^4	2113.11	7.2	799.08	8.0
B_1^4	$135.67 + 445.01i$	$4.7 + 12.6i$	$-639.84 + 100.40i$	$9.9 + 8.4i$
B_2^4	$-75.29 + 374.32i$	$5.8 + 7.0i$	$-86.57 - 815.64i$	$7.6 + 10.9i$
B_3^4	$-251.33 - 41.37i$	$4.0 + 2.0i$	$-156.21 + 328.67i$	$9.0 + 9.8i$
B_4^4	$-853.86 + 1083.85i$	$6.4 + 2.9i$	$-843.47 - 8.48i$	$9.9 + 8.8i$
B_0^6	44.88	5.0	358.59	8.7
B_1^6	$463.50 - 60.99i$	$3.1 + 7.6i$	$-77.81 + 1.30i$	$11.2 + 4.5i$
B_2^6	$113.14 + 400.51i$	$3.8 + 2.3i$	$-482.57 + 104.00i$	$11.8 + 9.3i$
B_3^6	$175.64 + 152.02i$	$5.0 + 6.4i$	$143.65 + 121.80i$	$6.7 + 6.9i$
B_4^6	$171.12 - 263.75i$	$5.7 + 4.8i$	$-51.59 + 46.72i$	$7.8 + 9.5i$
B_5^6	$-231.81 + 39.04i$	$11.9 + 7.5i$	$149.96 + 33.42i$	$7.5 + 13.9i$
B_6^6	$205.51 + 108.20i$	$5.1 + 7.3i$	$329.98 + 299.65i$	$5.9 + 7.3i$

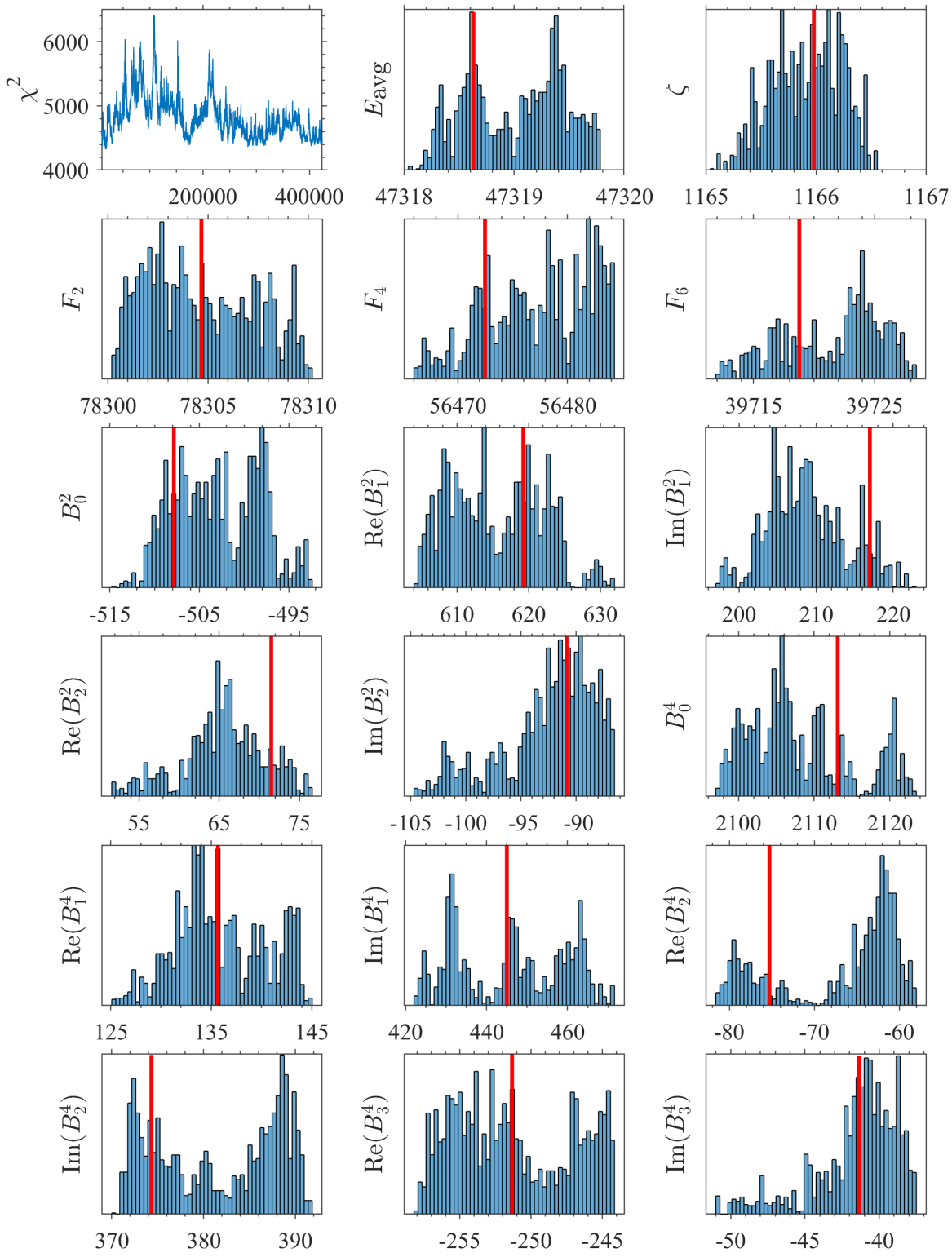

Figure 4.47: Variation of the free-ion and crystal-field parameters for site 1 of Sm^{3+}:Y_2SiO_5 after the algorithm has been allowed to 'burn in'. The histograms represent approximations to the posterior probability distribution for the parameters. The red lines indicate the fitted value for each parameter. All parameters have units of cm^{-1}. Figure is continued over page.

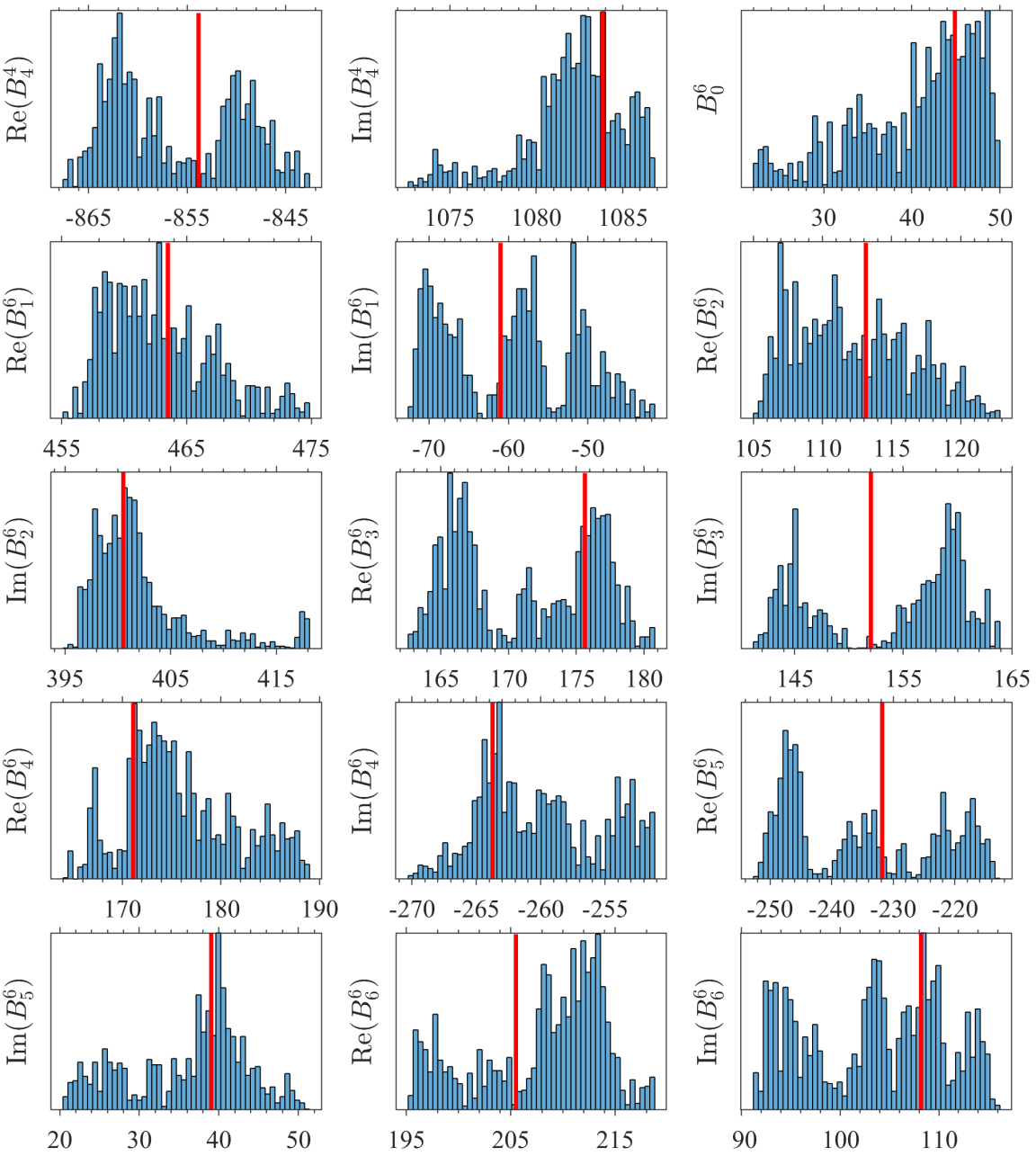

Figure 4.47: Variation of the free-ion and crystal-field parameters for site 1 in Sm^{3+}:Y_2SiO_5 after the algorithm has been allowed to 'burn in'. The histograms represent approximations to the posterior probability distribution for the parameters. The red lines indicate the fitted value for each parameter. All parameters have units of cm^{-1}.

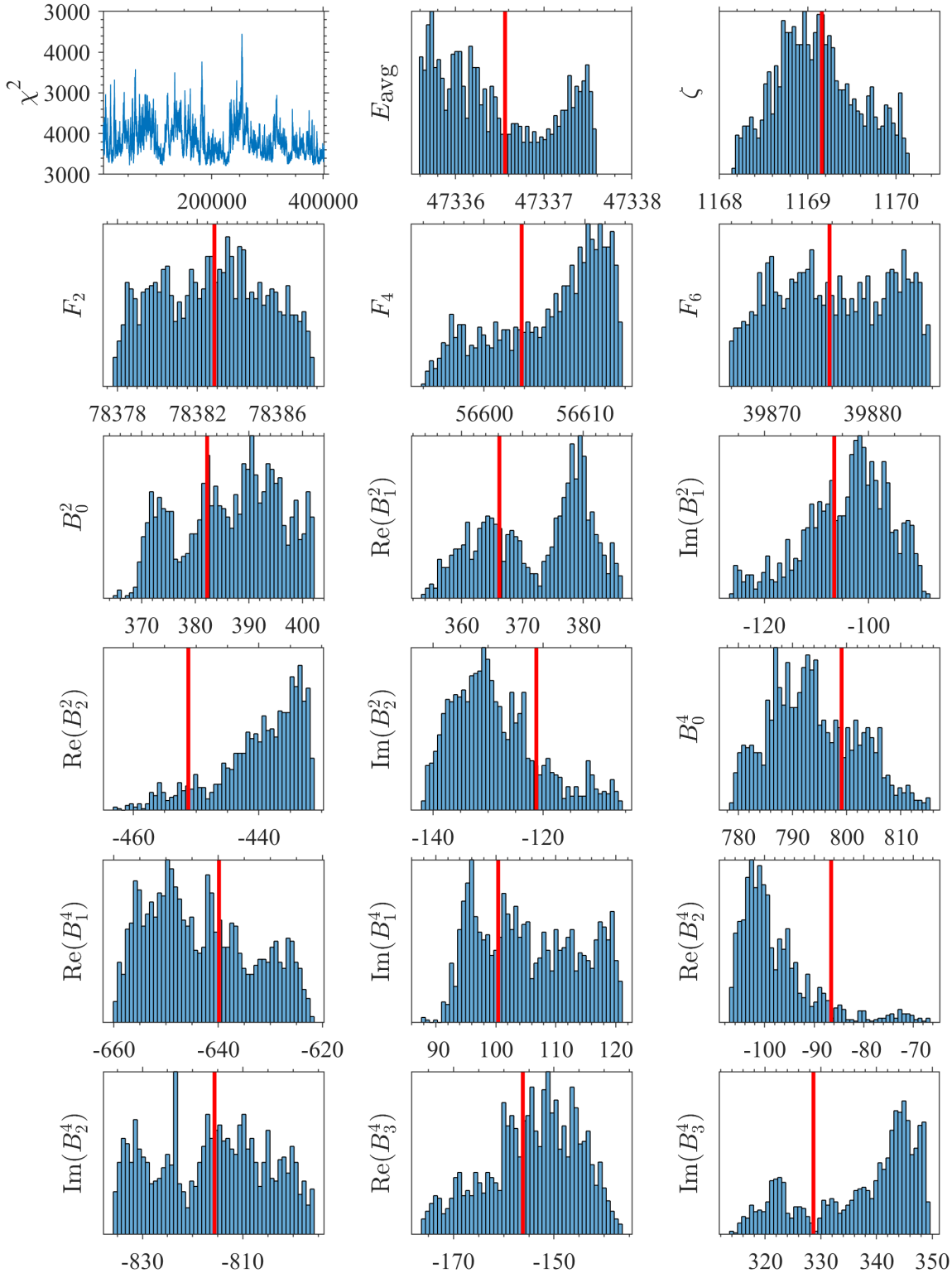

Figure 4.48: Variation of the free-ion and crystal-field parameters for site 2 of Sm^{3+}:Y_2SiO_5 after the algorithm has been allowed to 'burn in'. The histograms represent approximations to the posterior probability distribution for the parameters. The red lines indicate the fitted value for each parameter. All parameters have units of cm^{-1}. Figure is continued over page.

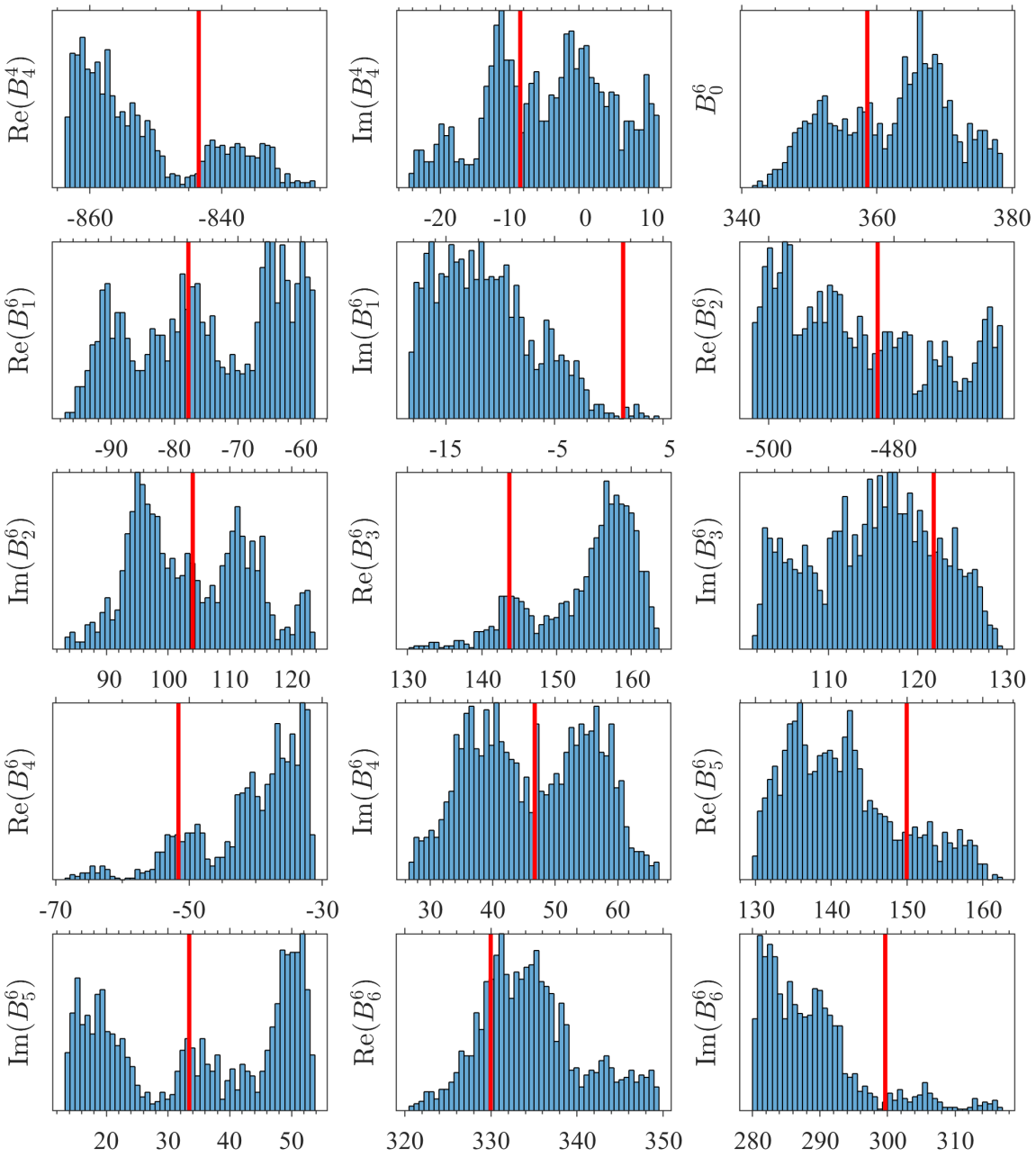

Figure 4.48: Variation of the free-ion and crystal-field parameters for site 2 of Sm^{3+}:Y_2SiO_5 after the algorithm has been allowed to 'burn in'. The histograms represent approximations to the posterior probability distribution for the parameters. The red lines indicate the fitted value for each parameter. All parameters have units of cm^{-1}.

Tables 4.8 and 4.9 shows the g tensors reproduced from our crystal-field model for the $^6H_{5/2}Z_1$ and $^4G_{5/2}A_1$ states for site 1 and site 2 respectively. The theoretical g tensors given in Equations (4.6) and (4.7) are also presented for comparison.

Table 4.8: Theoretical and experimental g tensors for the $^6H_{5/2}Z_1$ and $^4G_{5/2}A_1$ states for site 1 in Sm^{3+}:Y_2SiO_5.

State		g_{xx}	g_{yy}	g_{zz}	g_{xy}	g_{xz}	g_{yz}
$^6H_{5/2}Z_1$	Theoretical	0.425	0.060	0.514	−0.108	0.049	0.062
	Experimental	0.351	0.209	0.382	−0.016	0.078	−0.007
$^4G_{5/2}A_1$	Theoretical	1.209	0.978	2.398	−0.375	−0.265	0.207
	Experimental	1.025	1.248	2.446	−0.257	0.166	0.202

Table 4.9: Theoretical and experimental g tensors for the $^6H_{5/2}Z_1$ and $^4G_{5/2}A_1$ states for site 2 in Sm^{3+}:Y_2SiO_5.

State		g_{xx}	g_{yy}	g_{zz}	g_{xy}	g_{xz}	g_{yz}
$^6H_{5/2}Z_1$	Theoretical	0.559	0.023	0.203	−0.010	−0.163	0.002
	Experimental	0.512	0.067	0.135	−0.040	−0.054	0.009
$^4G_{5/2}A_1$	Theoretical	2.937	0.107	0.671	−0.259	−0.470	−0.122
	Experimental	3.264	0.183	0.714	−0.311	0.262	0.125

While no hyperfine structure was observed for Sm^{3+}:Y_2SiO_5, this structure is able to be predicted using our crystal-field model, which will prove useful for any future studies into Sm^{3+}:Y_2SiO_5. As the hyperfine parameters are largely host invariant, the hyperfine parameter determined by Horvath *et al.* for Sm^{3+}:CaF_2, co-doped with Na^{3+} ions, was used in our predictions [138]. It should be noted that the nuclear-quadrupole parameter could not be determined by Horvath *et al.* and was set to zero in our predictions. Table 4.10 shows the predicted zero-field hyperfine splittings of the $^6H_{5/2}Z_1$ ground and $^4G_{5/2}A_1$ excited states for both sites in Sm^{3+}:Y_2SiO_5. The ground state hyperfine structure is predicted to span about 4 GHz for both sites, while the excited state of both sites is expected to span about 2.5 GHz. These are splittings on the same order as that of Er^{3+}:Y_2SiO_5, and are much larger that the hyperfine splittings of Eu^{3+}:Y_2SiO_5, resulting in Sm^{3+}:Y_2SiO_5 being an attractive candidate for high-bandwidth quantum memories [55, 61].

Table 4.10: Theoretical zero-field hyperfine splittings of the $^6H_{5/2}Z_1$ and $^4G_{5/2}A_1$ states for both sites in Sm^{3+}:Y_2SiO_5. Level 1 is defined as the zero point for both states. All values are in GHz.

	Site 1		Site 2	
Level	$^6H_{5/2}Z_1$	$^4G_{5/2}A_1$	$^6H_{5/2}Z_1$	$^4G_{5/2}A_1$
1	0	0	0	0
2	0	0.00003	0	0
3	0.54790	0.19534	0.62911	0.36488
4	0.54808	0.19849	0.62911	0.36494
5	1.06477	0.32207	1.25751	0.71354
6	1.08351	0.36557	1.25760	0.72217
7	1.41730	0.40214	1.84447	0.95619
8	1.94206	1.70051	1.93060	1.27670
9	2.14361	1.71895	2.47002	1.43298
10	2.53457	1.83347	2.57117	1.64502
11	2.90016	1.92746	3.15139	1.90764
12	2.91521	1.94715	3.15151	1.91388
13	3.44117	2.12952	3.77975	2.26925
14	3.44129	2.13030	3.77975	2.26931
15	3.99141	2.35496	4.40887	2.63587
16	3.99141	2.35496	4.40887	2.63587

Figures 4.49 and 4.50 depicts the predicted magnetic dependence of the hyperfine structure of the $^6H_{5/2}Z_1$ and $^4G_{5/2}A_1$ states for site 1 and site 2 respectively. Visible at low fields are a number of avoided crossings followed by the hyperfine levels splitting into two groups of near-parallel levels at higher fields, which is expected of a Kramers system such as Sm^{3+}:Y_2SiO_5. Avoided crossings appear at magnetic fields up to 1 T, particularly in the ground state for site 1. This is at much higher field strengths than what has been observed for Er^{3+}:Y_2SiO_5, which has been observed to occur at field strengths less than 100 mT [31]. The presence of avoided crossings at higher field strengths for Sm^{3+}:Y_2SiO_5 is attributed to the low g values of the ground state relative to Er^{3+}:Y_2SiO_5, and so requires higher field strengths in order to split the Kramers doublet into two non-degenerate singlets.

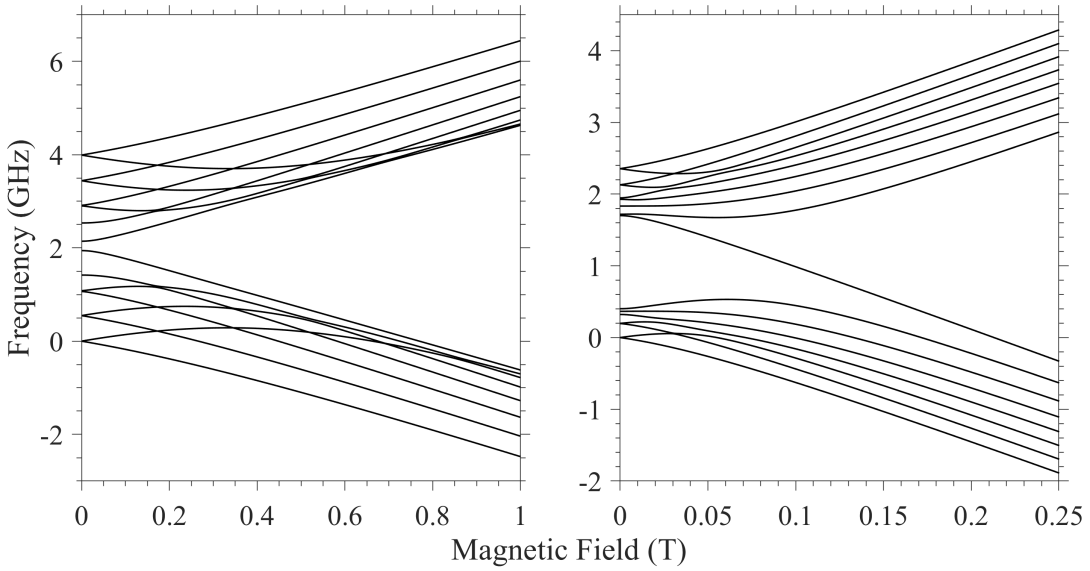

Figure 4.49: Predicted hyperfine splittings of the $^6H_{5/2}Z_1$ (left) and $^4G_{5/2}A_1$ (right) states for site 1 in Sm^{3+}:Y_2SiO_5 with a magnetic field applied down the D_1 axis.

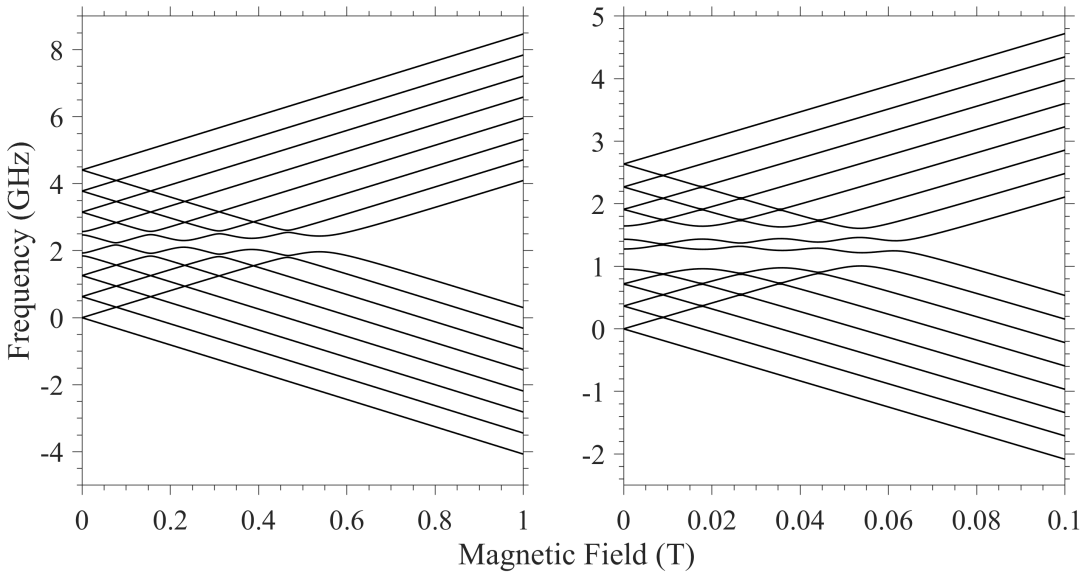

Figure 4.50: Predicted hyperfine splittings of the $^6H_{5/2}Z_1$ (left) and $^4G_{5/2}A_1$ (right) states for site 2 in Sm^{3+}:Y_2SiO_5 with a magnetic field applied down the D_1 axis.

4.6 Conclusion

The results presented in this chapter are the first investigation of the spectroscopic properties of bulk crystal Sm^{3+}:Y_2SiO_5. Multiple spectroscopic techniques were employed in determining the electronic and magnetic structure of Sm^{3+}:Y_2SiO_5. A total of 54 electronic energy levels and 72 g values (25 along the D_1 axis, 22 along the D_2 axis and 25 along the b axis) were determined corresponding to various states up to the $^4G_{7/2}$ multiplet at ∼20 000 cm^{-1} for site 1. For site 2, a total of 53 electronic energy levels and 92 g values (34 along the D_1 axis, 28 along the D_2 axis and 30 along the b axis) were determined for the same region. Additionally, the full g tensors of the $^6H_{5/2}Z_1$ and $^4G_{5/2}A_1$ states for both sites were determined through the use of Raman heterodyne spectroscopy.

A crystal-field fit to the obtained experimental data was performed for Sm^{3+}:Y_2SiO_5. To date, the model developed here is one of the very few produced for a C_1 symmetry material, with other crystal-field models developed for Ce^{3+}:Y_2SiO_5, Nd^{3+}:Y_2SiO_5, Er^{3+}:Y_2SiO_5 and Yb^{3+}:Y_2SiO_5 [55, 106, 142–144]. The determined free-ion and crystal-field parameters accurately models the energies of the electronic states up to the $^4G_{7/2}$ multiplet at ∼20 000 cm^{-1} in addition to reproducing the magnetic splitting of many of these states in multiple magnetic field directions.

Future work involves the investigation of the hyperfine structure, particularly of the readily accessible $^6H_{5/2}Z_1$ and $^4G_{5/2}A_1$ states. The addition of such data in a crystal-field model will allow for predictions of the hyperfine structure across the entire $4f^5$ configuration of Sm^{3+}:Y_2SiO_5. The hyperfine structure is easily probed through the use of electron-paramagnetic resonance and Raman heterodyne measurements. However, as the hyperfine structure is very complex, due to the large number of hyperfine states present in Sm^{3+}:Y_2SiO_5, any future studies will greatly benefit from having an isotopically pure, low concentration sample. This will vastly minimise the number of possible interactions, as each isotope has a unique hyperfine structure, simplifying any future analyses.

Chapter 5

Energy Transfer Processes in Sm^{3+}:Y_2SiO_5

In this chapter, the energy transfer processes within our Sm^{3+}:Y_2SiO_5 sample are investigated through the use of site-selective laser spectroscopic techniques. Trivalent samarium has been extensively studied across a large variety of hosts in the context of phonon assisted energy transfer [102, 145–147]; in some cases leading to complete quenching of emission from the $^4G_{5/2}$ multiplet [148, 149]. This behaviour arises from the rich density of multiplets within the ^6F_J and ^6H_J manifolds below 12 000 cm^{-1} as seen in Figure 4.1. In particular, it is notable that the energy separation between the $^4G_{5/2}$ and $^6F_{11/2}$ multiplets is comparable to that between $^6H_{5/2}$ and $^6F_{5/2}$ at approximately 7000 cm^{-1}. Likewise, the energy separation between the $^4G_{5/2}$ and $^6F_{5/2}$ multiplets is comparable to the energy separation between $^6H_{5/2}$ and $^6F_{11/2}$ at approximately 10 500 cm^{-1} - with any energy mismatches readily bridged by lattice band phonons. In the case of Sm^{3+}:Y_2SiO_5, energy transfer can occur between ions of the same crystallographic site, known as intra-site energy transfer, or between individual ions of distinct crystallographic sites, known as inter-site energy transfer. Figure 5.1 shows a simplified schematic diagram of the energy levels of Sm^{3+} including some possible energy transfer pathways between Sm^{3+} ions in the case of: a) intra-site cross relaxation (depicted as (I) and (II)) and b) inter-site energy transfer.

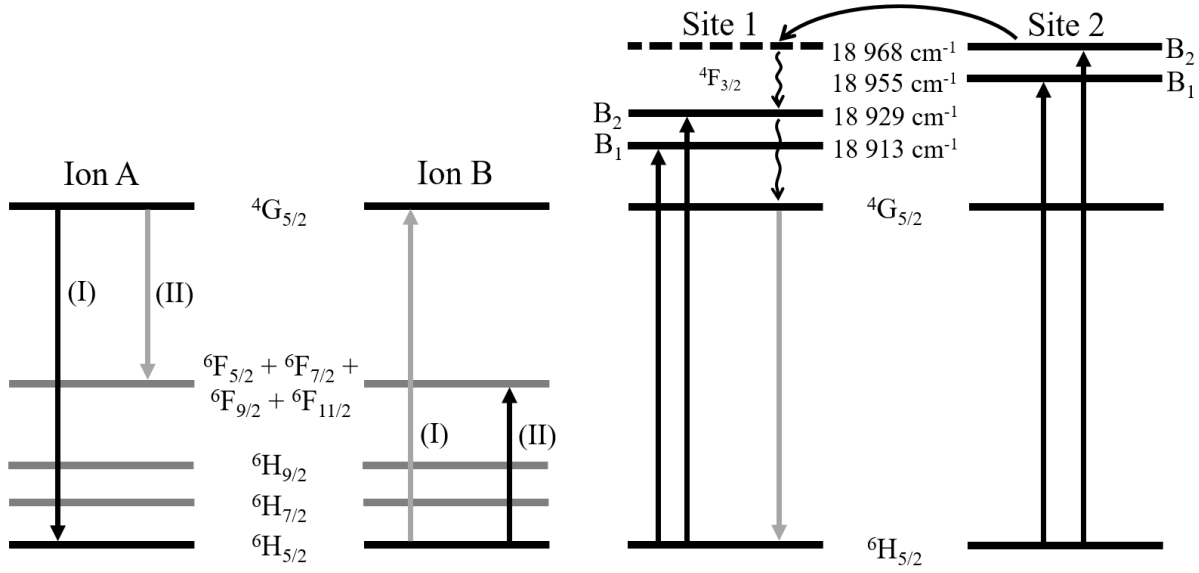

Figure 5.1: Simplified energy level diagram for Sm^{3+}:Y_2SiO_5 indicating: (left panel) the possible cross relaxation pathways (labelled as (I) and (II)), and (right panel) the likely pathways for inter-site energy transfer.

As energy transfer becomes more favourable as the separation between the donor and acceptor decreases, the more highly doped a system is, the more likely that it exhibits energy transfer behaviours. As our Sm^{3+}:Y_2SiO_5 sample has a moderately high dopant concentration at 0.5 %, it serves as an excellent candidate to observe such phenomena. The experimental setup relevant to this chapter is outlined in Chapter 3.2.

5.1 Cross relaxation between Sm^{3+} ions within a single crystallographic site

While monitoring the fluorescence transients from the $^4G_{5/2}A_1$ state to the $^6H_{7/2}$ and $^6H_{9/2}$ multiplets, required to obtain the fluorescence spectrum seen in Figures 4.4 and 4.5, the transients for both sites were observed to be multi-exponential. These transients show a short time scale decay on the order of 100 μs and a longer time scale decay, relating to isolated ions, on the order of a few ms. The presence of a short timescale decay is indicative of intra-site energy transfer, which arises from distortions experienced by a small number of the Sm^{3+} ions induced by neighbouring Sm^{3+} ions. These distortions induces an electric dipole moment which results in the nominally parity forbidden $4f \longrightarrow 4f$ to be more allowed, resulting in broader linewidths and shorter lifetimes [145].

In order to quantify this observed energy transfer, and to determine the radiative and non-radiative rates, a discrete atomic model was created using the unit cell of Y_2SiO_5 as an input. $5 \times 7 \times 5$ unit cells was used, which accounts for all interactions up to a radius of 20 Å. As Sm^{3+} has a larger ionic radius than Y^{3+}, as summarised in Table 2.1, the Sm^{3+} ions tend to preferentially occupy the higher co-ordinate site 2. Through averaging the integrals of spectral lines found in absorption, site 2 was estimated to be more populated relative to site 1 by a factor of 1.63. This led us to create a 3090 and 5490 ppm random distribution of acceptors around a central donor for both sites 1 and

2 respectively. Note that the effects of preferential clustering could be neglected due to the doping of Sm^{3+} ion into Y_2SiO_5 does not require charge compensation. One such configuration is shown in Figure 5.2.

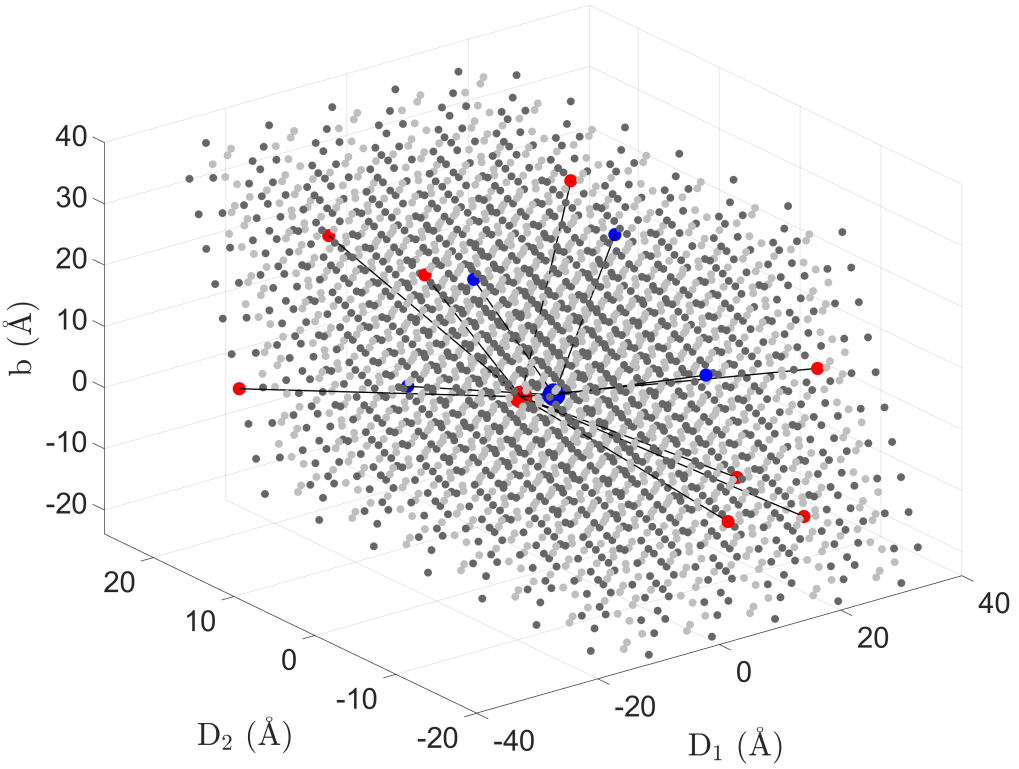

Figure 5.2: Sample random distribution of acceptors around a single donor for both sites in 0.5% Sm^{3+}:Y_2SiO_5. The light and dark grey dots are the Y^{3+} ions for site 1 and site 2 respectively and the blue and red dots are the acceptor Sm^{3+} ions (small dots) around a central donor (large central dots) for sites 1 site 2 respectively.

Using the Monte-Carlo methods outlined in Section 2.6, 50 000 random configurations of acceptors around a single donor was created for both sites and was found to be sufficient to obtain convergence in the fit described. The average nearest donor-acceptor distance was found to be 18.0 Å for site 1 and 14.9 Å for site 2. Figure 5.3 depicts the fitted fluorescence transients for both sites in 0.5% Sm^{3+}:Y_2SiO_5. The left panel depicts the fitted fluorescence transient for the $^4G_{5/2}A_1 \longrightarrow {}^6H_{9/2}X_1$ transition at 15 338 cm^{-1} for site 1 while the right panel depicts the fitted transient fluorescent decay of the $^4G_{5/2}A_1 \longrightarrow {}^6H_{7/2}Y_1$ transition for site 2 at 16 671 cm^{-1}. Both fluorescence transients were recorded at 10 K and were normalised such that they have an intensity of 1 at $t = 0$. The 10 K fluorescence transients were fitted using Equation (2.63) with the multipole-multipole and exchange interactions given from Equations (2.61) and (2.62). The excitation was to the $^4G_{5/2}A_1$ state at 17 689 and 17 790 cm^{-1} for sites 1 and 2 respectively.

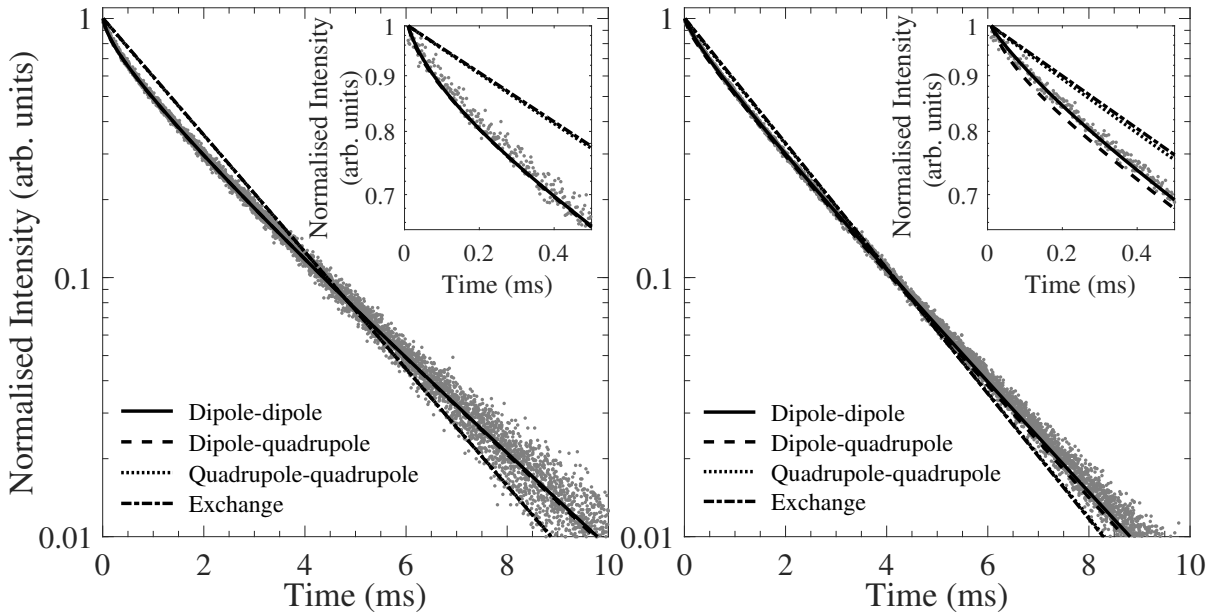

Figure 5.3: 10 K fluorescent transients for the $^4G_{5/2}A_1$ state for site 1 (left) and site 2 (right) in 0.5% Sm^{3+}:Y_2SiO_5. The solid, dashed, dotted and dash-dotted lines are the simulated curves using the dipole-dipole, dipole-quadrupole, quadrupole-quadrupole and exchange mechanisms respectively. The inset shows a magnified region of the first 0.5 ms displaying the different interactions more clearly. It should be noted that that the different interactions for site 1 do lie on top of each other and can not be clearly distinguished.

The dipole-dipole (solid line) mechanism has the closest fit to the fluorescence transients as depicted in Figure 5.3 whereas the dipole-quadrupole, quadrupole-quadrupole and exchange mechanisms (dashed, dotted and dash-dotted lines respectively) do not. This is expected as the typical distance scales of interest are on the order of ∼10 Å, which the dipole-quadrupole, quadrupole-quadrupole and exchange mechanisms struggle to model due to their higher radial dependencies relative to the dipole-dipole mechanism.

The fitted radiative relaxation rates and energy transfer parameters, derived from the 10 K fluorescence transients of both sites are given in Table 5.1. The intra-site nearest neighbour distances, r_0, was set to 3.459 Å for site 1 and 3.621 Å for site 2. There is a large variation between the different interactions, by multiple orders of magnitude in the case of the energy transfer parameter, owing to the dipole-quadrupole, quadrupole-quadrupole and exchange mechanisms providing a poor fit to the experimental transients, especially on short time scales.

Table 5.1: Radiative relaxation rates and energy transfer parameters of the $^4G_{5/2}A_1$ state in Sm^{3+}:Y_2SiO_5:0.5%, determined using Monte-Carlo methods on the luminescence decay curves for both site 1 and site 2 using the dipole-dipole, dipole-quadrupole, quadrupole-quadrupole and exchange mechanisms.

	γ_r (s^{-1})		C_{nr} (s^{-1})	
Mechanism	Site 1	Site 2	Site 1	Site 2
Dipole-Dipole	357 ± 17	447 ± 11	$(2.0 \pm 0.3)\times10^6$	$(1.8 \pm 0.2)\times10^5$
Dipole-Quadrupole	386 ± 17	471 ± 12	$(7.4 \pm 1.2)\times10^8$	$(3.1 \pm 0.6)\times10^7$
Quadrupole-Quadrupole	518 ± 44	551 ± 26	$(8.9 \pm 3.9)\times10^5$	$(1.3 \pm 1.0)\times10^4$
Exchange	520 ± 65	557 ± 48	$(6.7 \pm 3.4)\times10^5$	$(6.4 \pm 3.9)\times10^4$

The fluorescence transients were then monitored as a function of sample temperature from 10 K - 300 K at the same excitation and fluorescence wavelengths for both sites. Each transient was fitted using a dipole-dipole interaction, given by Equation (2.61) (s = 6), and the determined radiative rates and energy transfer parameters were obtained. Figure 5.4 shows the inferred radiative rate and energy transfer parameter as a function of temperature for both sites.

Important while performing any temperature dependent studies is spectral line broadening and shifts, which is a function of temperature. These effects can be described by phonon interactions assuming a Debye distribution of phonons [150–152]. The effect of spectral line broadening on this study can be seen in Figure 5.4, where spectral broadening results in a lesser proportion of the ions being on resonance with the laser excitation, resulting in a large spread in the radiative relation rates and energy transfer parameters. Also present is a shift of the spectral lines as temperature is increased. This was compensated for by periodically changing the laser wavelength to remain on resonance with the peak of the $^4G_{5/2}A_1$ spectral lines for both sites as temperature was increased.

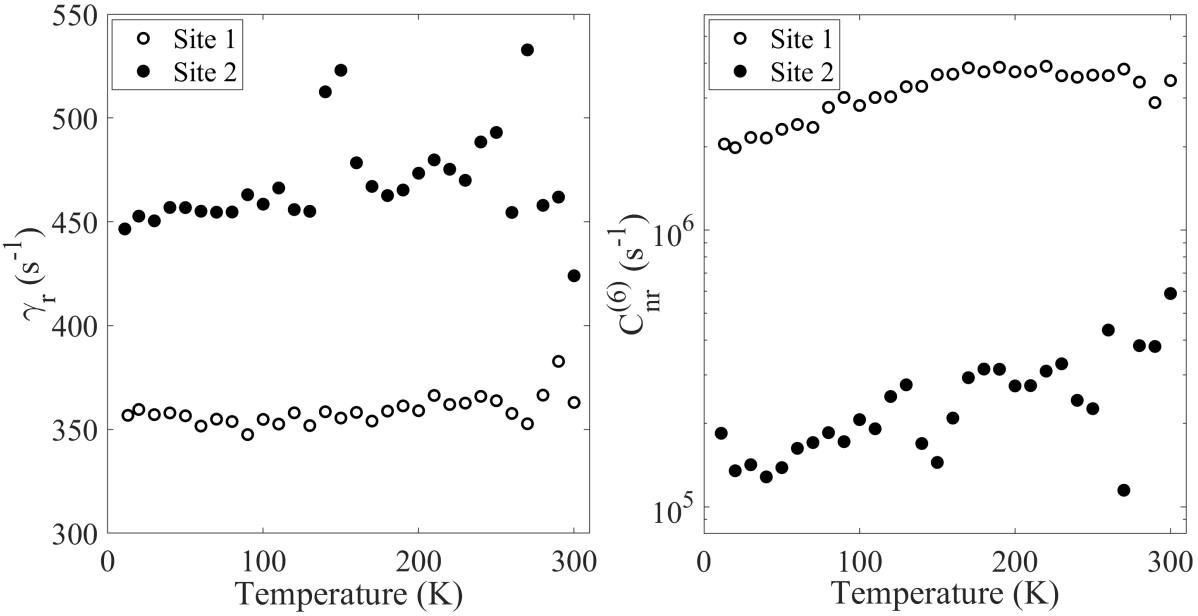

Figure 5.4: Radiative relaxation rates (left) and energy transfer parameters (right) of the Sm^{3+} $^4G_{5/2}A_1$ state as a function of temperature for site 1 and site 2 respectively. The rates and parameters were determined by fitting the experimental data to Equation (2.63) using a dipole-dipole interaction ($s = 6$). Note that the left panel has a linear scale while the right panel has a log scale.

The left panel of Figure 5.4 depicts the determined radiative rates for both sites of 0.5% Sm^{3+}:Y_2SiO_5 as a function of temperature. Aside for some noticeable excursions of some data points, the radiative rates for both sites appear to remain constant as a function of temperature, with site 1 remaining constant at $\sim$360 s^{-1} and site 2, at $\sim$450 s^{-1}.

The energy transfer parameters of 0.5% Sm^{3+}:Y_2SiO_5, shown in the right panel of Figure 5.4 does show variation as a function of temperature. This is expected due to the necessity for small energy mismatches to be bridged by lattice band phonons. The site 1 energy transfer parameter was found to increase from 2.0×10^6 s^{-1} to 4.0×10^6 s^{-1} as the sample temperature increased from 10 K - 300 K. The site 2 energy transfer parameter was found to increase from 1.3×10^5 s^{-1} to 4.0×10^5 s^{-1} over the same temperature range.

5.2 Energy transfer between ions occupying distinct crystallographic sites

Energy transfer between ions of the same site in 0.5% Sm^{3+}:Y_2SiO_5 has been discussed. I will now consider the energy transfer between ions of different sites within 0.5% Sm^{3+}:Y_2SiO_5. As mentioned in Section 4.2.2, close analysis of the middle panel of Figure 4.14 reveals fluorescence from the site 1 $^4G_{5/2}A_1$ state while exciting the $^4F_{3/2}B_1$ and B_2 states of site 2, seen as the small peaks at 18 955 cm^{-1} and 18 968 cm^{-1} respectively. This is indicative of energy transfer between the two sites. At 10 K this appears to be a one-way phenomenon as there are no corresponding peaks that relate to emission from the site 2 $^4G_{5/2}A_1$ state while exciting the $^4F_{3/2}B_1$ and B_2 states for site 1. This is attributed to the $^4F_{3/2}B_1$ and B_2 states for site 2 having higher energies than that of site 1 so lattice band phonons can only be created, allowing an excitation to only decrease in energy, from site 2 to site 1. The energy difference between the higher lying site 2 $^4F_{3/2}B_1$ state and the site 1 $^4F_{3/2}B_2$ state is 26 cm^{-1}.

Figure 5.5 shows temperature dependent excitation spectra of the $^4F_{3/2}$ multiplet in 0.5% Sm^{3+}:Y_2SiO_5. The left panel depicts the $^4F_{3/2}$ excitation spectra while monitoring site 1, $^4G_{5/2}A_1 \longrightarrow {}^6H_{5/2}Z_1$ fluorescence at 17 689 cm^{-1}. The right panel depicts the $^4F_{3/2}$ excitation spectra while monitoring site 2, $^4G_{5/2}A_1 \longrightarrow {}^6H_{5/2}Z_1$ fluorescence at 17 790 cm^{-1}. The individual spectra have been normalised so that the B_1 site 1 and the B_2 site 2 spectral lines has constant intensity across all temperatures for the left and right panels respectively.

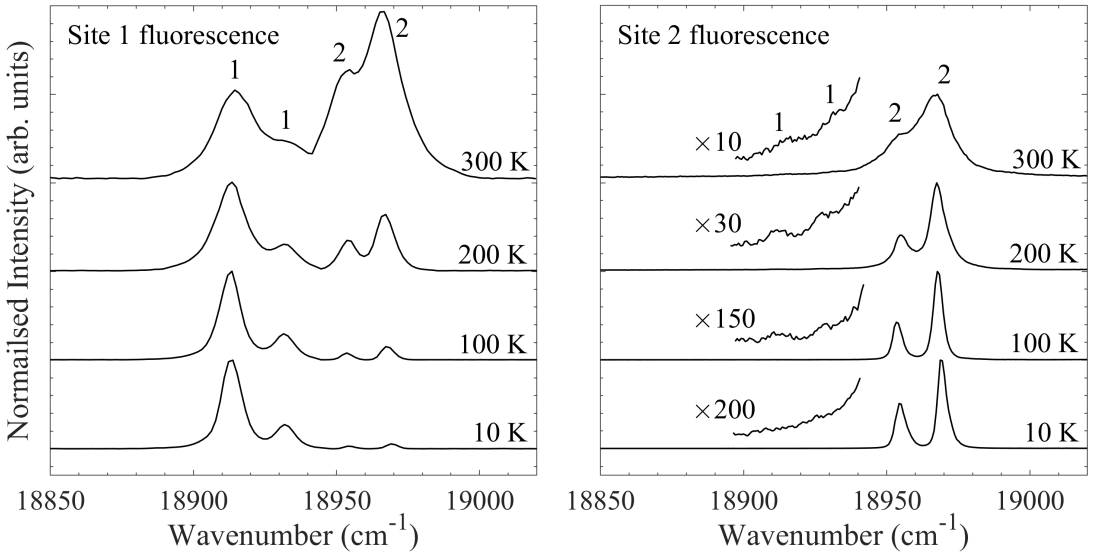

Figure 5.5: Excitation spectra of the $^4F_{3/2}$ multiplet in 0.5% Sm^{3+}:Y_2SiO_5 as a function of temperature while monitoring fluorescence from site 1 (left) and site 2 (right). Fluorescence from the $^4G_{5/2}A_1 \longrightarrow {}^6H_{5/2}Z_1$ transition was monitored at 17 689 cm^{-1} for site 1 and at 17 790 cm^{-1} for site 2. Each spectrum was normalised so that the B_1 site 1 and the B_2 site 2 spectral lines has constant intensity across all temperatures for the left and right panels respectively. The numbers depicts which site each spectral line belongs to.

Figure 5.6 shows the ratio of the integrated areas of the most intense site 1 line relative to the most intense site 2 line of the $^4F_{3/2}$ multiplet in 0.5% Sm^{3+}:Y_2SiO_5 as a function of temperature while measuring the site 1 fluorescence (left panel) and the site 2 fluorescence (right panel).

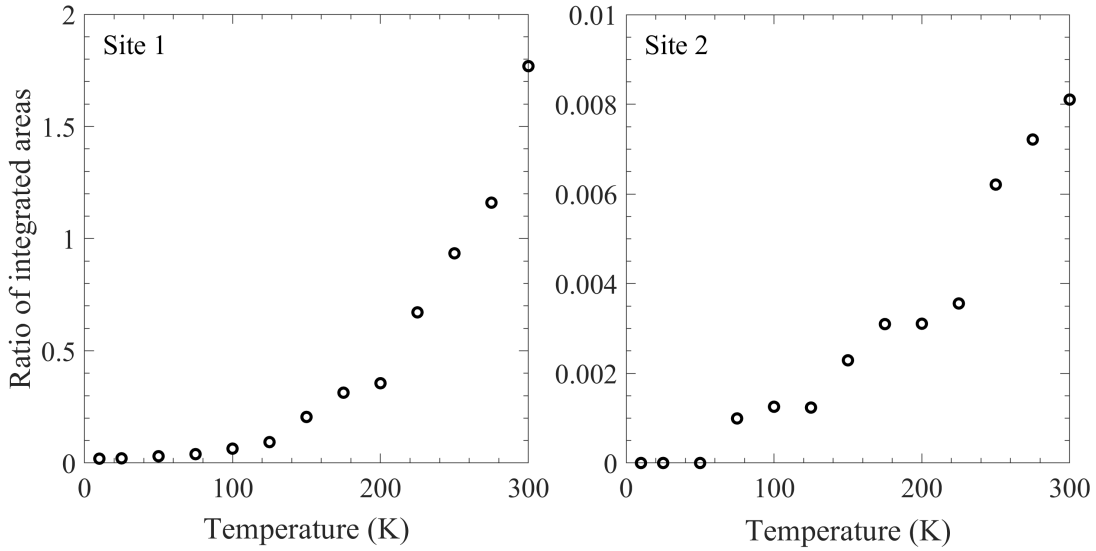

Figure 5.6: Ratio of integrated areas of selected spectral features for the $^4F_{3/2}$ multiplet in 0.5% Sm^{3+}:Y_2SiO_5 as a function of temperature. The left panel shows the ratio of the integrated area of the site 2 B_2 spectral line relative to the integrated area of the site 1 B_1 spectral line as a function of temperature. The right panel shows the ratio of the integrated area of the site 1 B_1 spectral line relative to the integrated area of the site 2 B_2 spectral line as a function of temperature.

From the left panel of Figures 5.5 and 5.6 we see that the energy transfer from site 2 to site 1 becomes exceptionally more efficient as temperature approaches 300 K, even becoming more dominant than the direct emission of site 1 itself. The reverse is not true however, as the direct emission from site 2 remains the dominate source of site 2 fluorescence as temperature increases, as seen in the right panel of Figures 5.5 and 5.6. This is attributed to the possible phonon assisted pathways for energy transfer in Sm^{3+}:Y_2SiO_5. The phonon density of states has been previously determined up to 37.5 THz ($\sim$1250 cm^{-1}) by Luo *et al.* [139]. There also exists further phonon vibration bands at $\sim$1350 - 1400 cm^{-1} as determined by Zheng *et al.* [140]. Table 5.2 depicts the energy differences between site 1 and site 2 of states within the $^4G_{5/2}$ and $^4F_{3/2}$ multiplets. As energy transfer can only proceed through the production of phonons at cryogenic temperatures, an excitation is restricted to transitioning from a higher to lower energy state through phonon assisted non-radiative energy transfer. Therefore, at cryogenic temperatures, energy transfer from site 1 to site 2 is represented by the upper right triangle of Table 5.2 while the reverse direction is represented by the lower left triangle. Comparing the phonon density of states with the energy differences between the site 1 and site 2 states in the $^4G_{5/2}$ and $^4F_{3/2}$ multiplets we see that there are many more allowed phonon assisted transitions from site 2 to site 1 than the reverse. Namely the site 1 $\longrightarrow$ site 2, $^4F_{3/2}B_1 \longrightarrow {}^4G_{5/2}A_3$ and $^4F_{3/2}B_2 \longrightarrow {}^4G_{5/2}A_3$ transitions at 622 cm^{-1} and 638 cm^{-1} respectively are forbidden as the energy difference between these states lines up with zero phonon density of states. However, the same transitions from site 2 to site 1, do line up with a non-zero phonon density of states, resulting in this direction being much more allowed.

Table 5.2: Energy differences between the site 1 and site 2 states in the $^4G_{5/2}$ and $^4F_{3/2}$ multiplets.

		Site 1				
	State	A_1	A_2	A_3	B_1	B_2
Site 2	A_1	101	132	565	1123	1139
	A_2	226	7	420	998	1014
	A_3	602	369	64	622	638
	B_1	1266	1033	600	42	26
	B_2	1279	1046	613	55	39

5.3 Conclusion

Site-selective laser spectroscopy was used to study the energy transfer mechanics of 0.5% Sm^{3+}:Y_2SiO_5. The intra-site energy transfer mechanics was quantified using Monte-Carlo methods in order to produce 50 000 random configurations of acceptors around a single donor. Intra-site energy transfer was found to proceed via a dipole-dipole mechanism for both sites. The radiative fluorescence rates of the $^4G_{5/2}A_1$ state was found to be 360 s^{-1} for site 1 and 450 s^{-1} site 2 and were insensitive to temperature. The site 1 energy transfer parameter was found to increase from 2.0×10^6 s^{-1} to 4.0×10^6 s^{-1} as the sample temperature is increased from 10 K – 300 K. The site 2 energy transfer parameter was found to increase from 1.3×10^5 s^{-1} to 4.0×10^5 s^{-1} over the same temperature range. Inter-site energy transfer can be observed for excitation of the $^4F_{3/2}$ multiplet of site 2, with the resultant fluorescence observed from the $^4G_{5/2}$ multiplet of site 1. While the process becomes very efficient as a function of temperature, the reverse process remains very weak. Further investigations would involve repeating the studies performed here on additional samples of Sm^{3+}:Y_2SiO_5 with varying dopant concentrations as dopant concentration is directly linked to the efficiency of energy transfer.

Chapter 6

Spectroscopy and Crystal-field analysis of Er^{3+}:Y_2SiO_5

Triply ionised erbium-doped materials are of specific interest for applications in QIP due to the ion having strong absorption in the well established 1550 nm telecommunications band. The existence of such a transition has allowed the use of erbium to become entrenched in our modern classical optical telecommunication infrastructures [153], with trialing underway for its use in quantum optical telecommunication infrastructure [34,38,154]. Er^{3+}:Y_2SiO_5 has the narrowest optical homogeneous linewidth observed to date of 50 Hz [7], in addition to a coherence time of over one second [28]. Furthermore, Er^{3+} is a Kramers ion and therefore has a large hyperfine splitting relative to Pr^{3+} and Eu^{3+}, which allows for larger memory bandwidths within these hyperfine transitions whilst still obtaining reasonably long coherence times. The electronic structure of Er^{3+}:Y_2SiO_5 [31, 55, 62, 106, 110, 155–158] and the dynamics [28, 159–165] have been the subject of many investigations.

In this chapter, I aim to further the crystal-field analyses that have recently been undertaken by Horvath on Er^{3+}:Y_2SiO_5 [55, 106]. These analyses included the electronic level structure of Er^{3+}:Y_2SiO_5 up to the $^2H_{11/2}$ multiplet at ∼20 000 cm^{-1}, determined by Doualan *et al.* [158], magnetic **g** tensors of the $^4I_{13/2}Z_1$ and $^4I_{11/2}Y_1$ states, determined by Sun *et al.* [110] and the spin Hamiltonian **A** and **Q** tensors of the $^4I_{13/2}Z_1$ ground states [62]. While Horvath focused on modelling the hyperfine structure of the $^4I_{13/2}Z_1$ and $^4I_{11/2}Y_1$ states, this study aims to create a crystal-field model for the full electronic structure of Er^{3+}:Y_2SiO_5. This was achieved by extending the electronic level structure, determined by Doualan *et al.*, up to 27 000 cm^{-1} to include the $^4F_{7/2}$, $^4F_{5/2}$, $^2H_{9/2}$ and $^4G_{11/2}$ multiplets through the use of temperature dependent absorption spectroscopy. Additionally, the magnetic g values along the D_1, D_2 and b axes for many states up to the $^4F_{5/2}$ multiplet at 22 500 cm^{-1}, determined through the use of Zeeman spectroscopy, was also introduced in our model.

6.1 Spectroscopic properties of Er^{3+}:Y_2SiO_5

Erbium is located towards the end of the lanthanide series, with an atomic number of 68. Triply ionised erbium, Er^{3+}, has an electronic configuration given as $[Xe]4f^{11}$. This results in Er^{3+}:Y_2SiO_5 having 182 doubly-degenerate Kramers states, split into 41 multiplets, which is doubled to 364 non-degenerate states upon the application of a magnetic field. ^{167}Er is the only naturally occurring isotope to have a non-zero nuclear spin, with a natural abundance of 22.9 % and a nuclear spin of $I = \frac{7}{2}$. This leads to a total of 2912 hyperfine states within the $4f^{11}$ configuration of Er^{3+}:Y_2SiO_5. The energy level structure of Er^{3+}:Y_2SiO_5 up to 30 000 cm^{-1} is given in Figure 6.1. Er^{3+} has an ionic radius similar to that of Y^{3+}, resulting in even populations between the two sites and balanced spectral features.

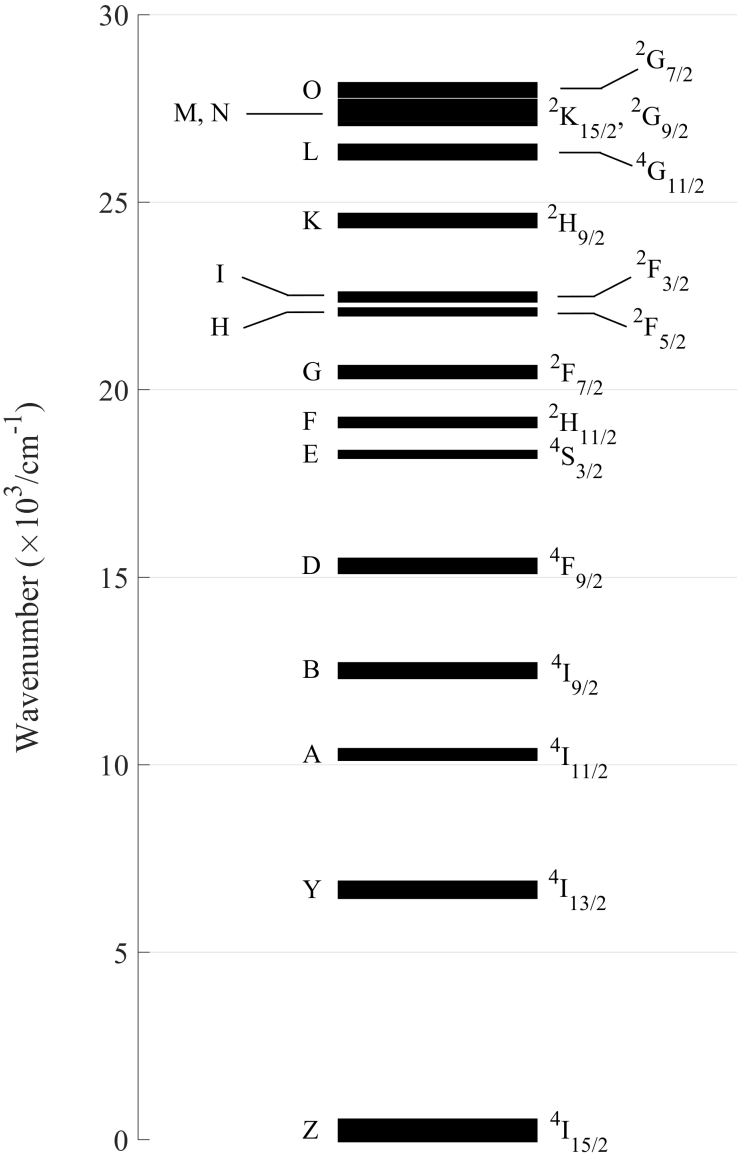

Figure 6.1: Energy level structure of Er^{3+}:Y_2SiO_5 up to 30 000 cm^{-1} with the $^{2S+1}L_J$ multiplets labelled. The thickness of each line indicates the crystal-field splittings within each multiplet.

6.2 Temperature dependent absorption spectroscopy

A previous study by Doualan *et al.* determined the electronic structure of Er^{3+}:Y_2SiO_5 up to the $^2H_{11/2}$ multiplet at ∼20 000 cm^{-1} [158]. The present study extends the determined electronic structure up to the $^4G_{11/2}$ multiplet at ∼26 500 cm^{-1} by performing temperature dependent absorption spectroscopy. The experimental details of such an experiment are discussed in detail in Section 3.3. This is a powerful spectroscopic technique that allows for site assignments without the need for performing site selective fluorescence spectroscopy as excited states within the ground state multiplet become thermally populated as the temperature increases. In the case of Er^{3+}:Y_2SiO_5, with the presence of multiple excited states below 100 cm^{-1}, the thermal population of states up to the $^4I_{15/2}Z_4$ state for both sites is evident at temperatures as low as 100 K. Each spectral line found in absorption therefore has a number of related transitions at lower energies which originates from the excited states. As the two sites of Er^{3+}:Y_2SiO_5 have an electronic energy level structure that are distinct from each other, each site therefore has a unique pattern which can be used to assign each spectral line found in absorption.

Figures 6.2 – 6.11 depicts 12 K and 100 K absorption spectra of most excited multiplets up to the $^4G_{11/2}$ multiplet of Y_2SiO_5:0.005%Er^{3+}, with each transition labelled. These states were assigned by monitoring hot lines as the sample temperature was increased to 100 K. Site 1 transitions are labelled in blue and site 2, in red. The $^4F_{3/2}$ multiplet and two states for site 1 of the $^2H_{9/2}$ multiplet were too weak to be monitored. Most spectra are split into two portions for ease of reading. The extra structure seen in the 6 700 – 6 900 cm^{-1} range of the $^4I_{13/2}$ multiplet is absorption due to water vapour. Spectral features that could not be assigned as belonging to Er^{3+}:Y_2SiO_5 are marked with an '*'.

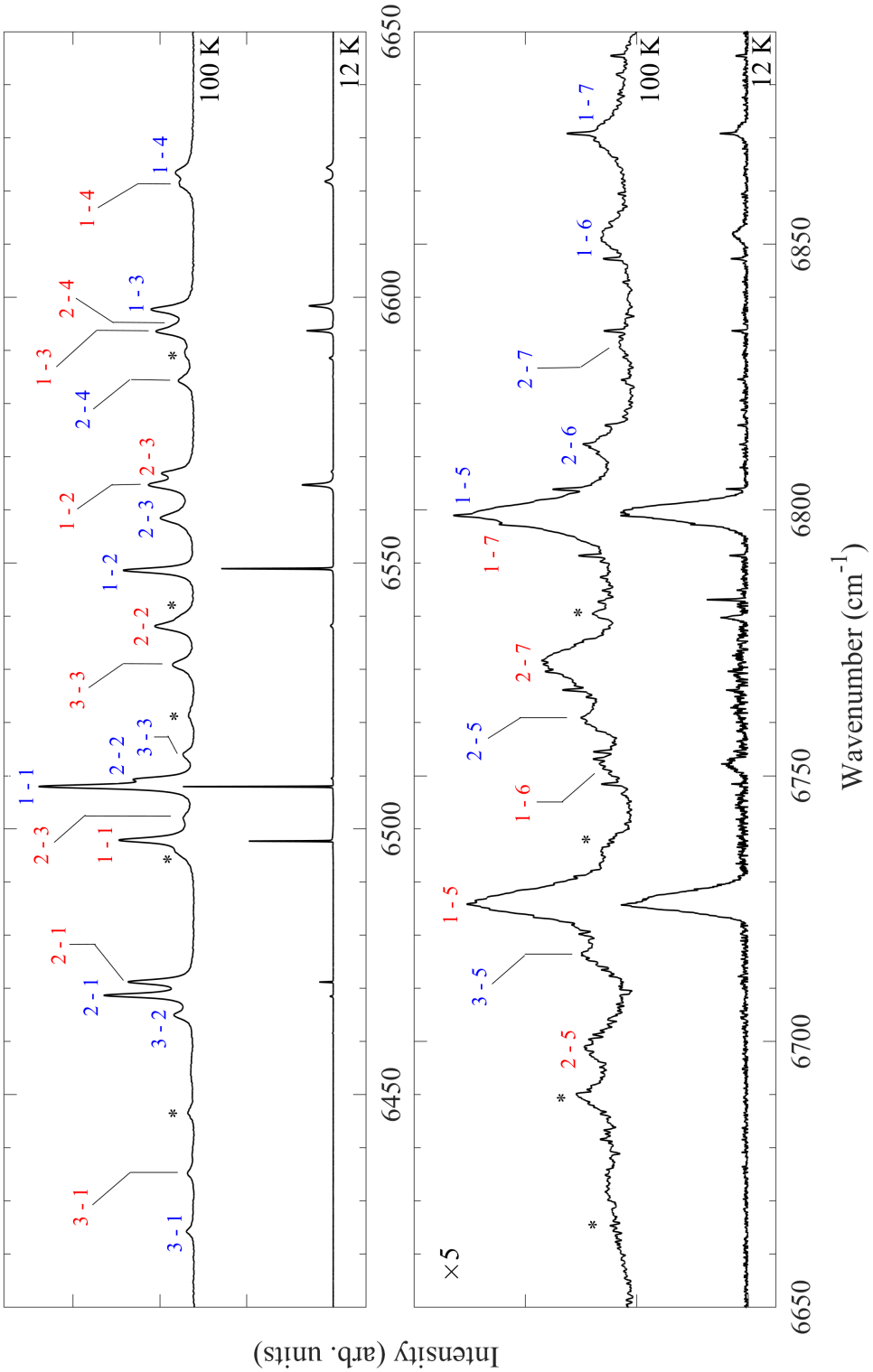

Figure 6.2: 12 K and 100 K absorption spectra of the $^4I_{13/2}$ multiplet in Y_2SiO_5:0.005%Er^{3+} with the $Z_i \longrightarrow Y_j$ transitions labelled. Site 1 transitions are labelled in blue and site 2, in red. Spectral features labelled with an '*' are unrelated to Er^{3+}:Y_2SiO_5. The narrow structure seen in the 6 700 – 6 900 cm^{-1} range is absorption due to water vapour.

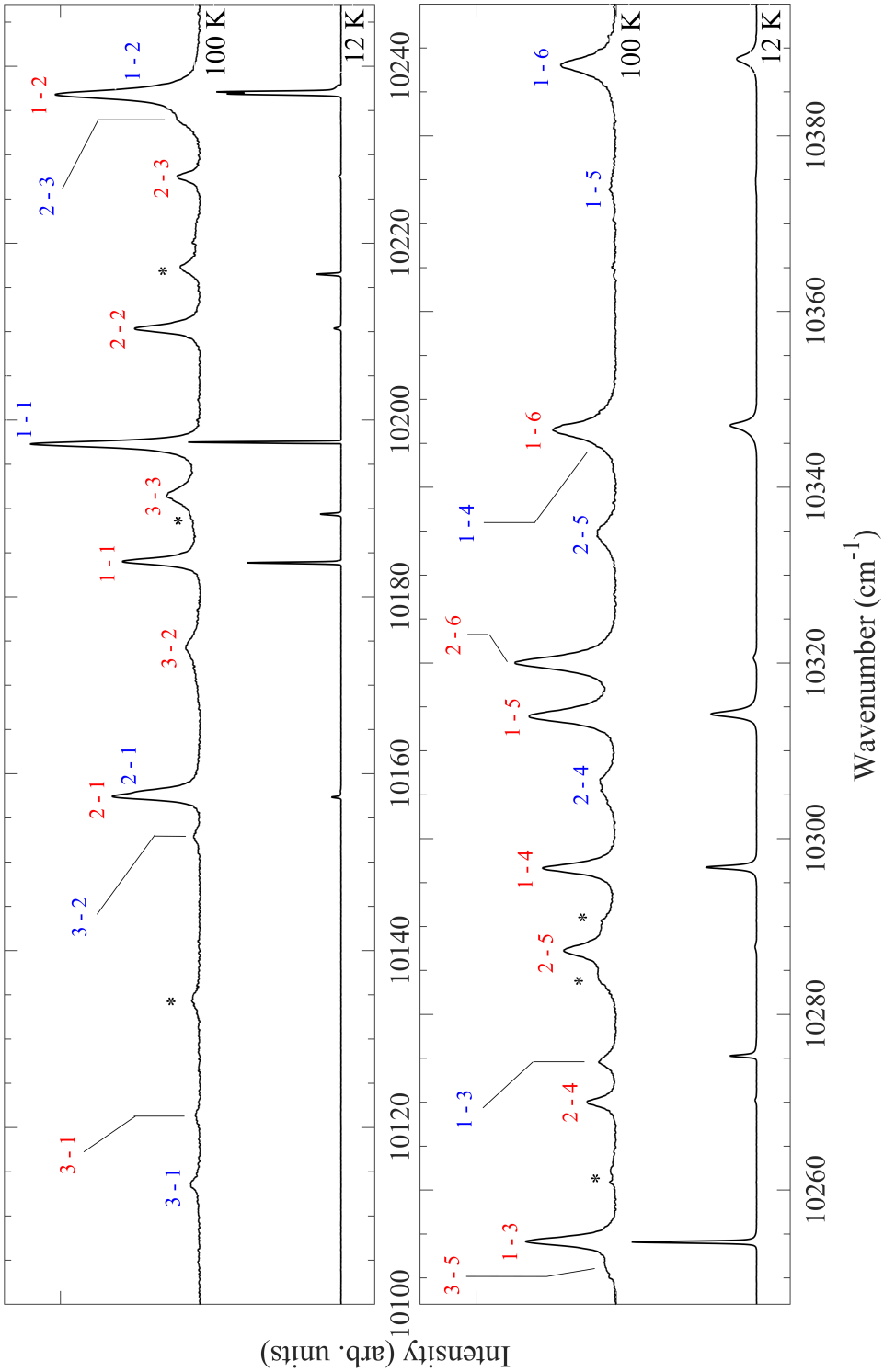

Figure 6.3: 12 K and 100 K absorption spectra of the $^4I_{11/2}$ multiplet in Y_2SiO_5:0.005%Er^{3+} with the $Z_i \longrightarrow A_j$ transitions labelled. Site 1 transitions are labelled in blue and site 2, in red. Spectral features labelled with an '*' are unrelated to Er^{3+}:Y_2SiO_5.

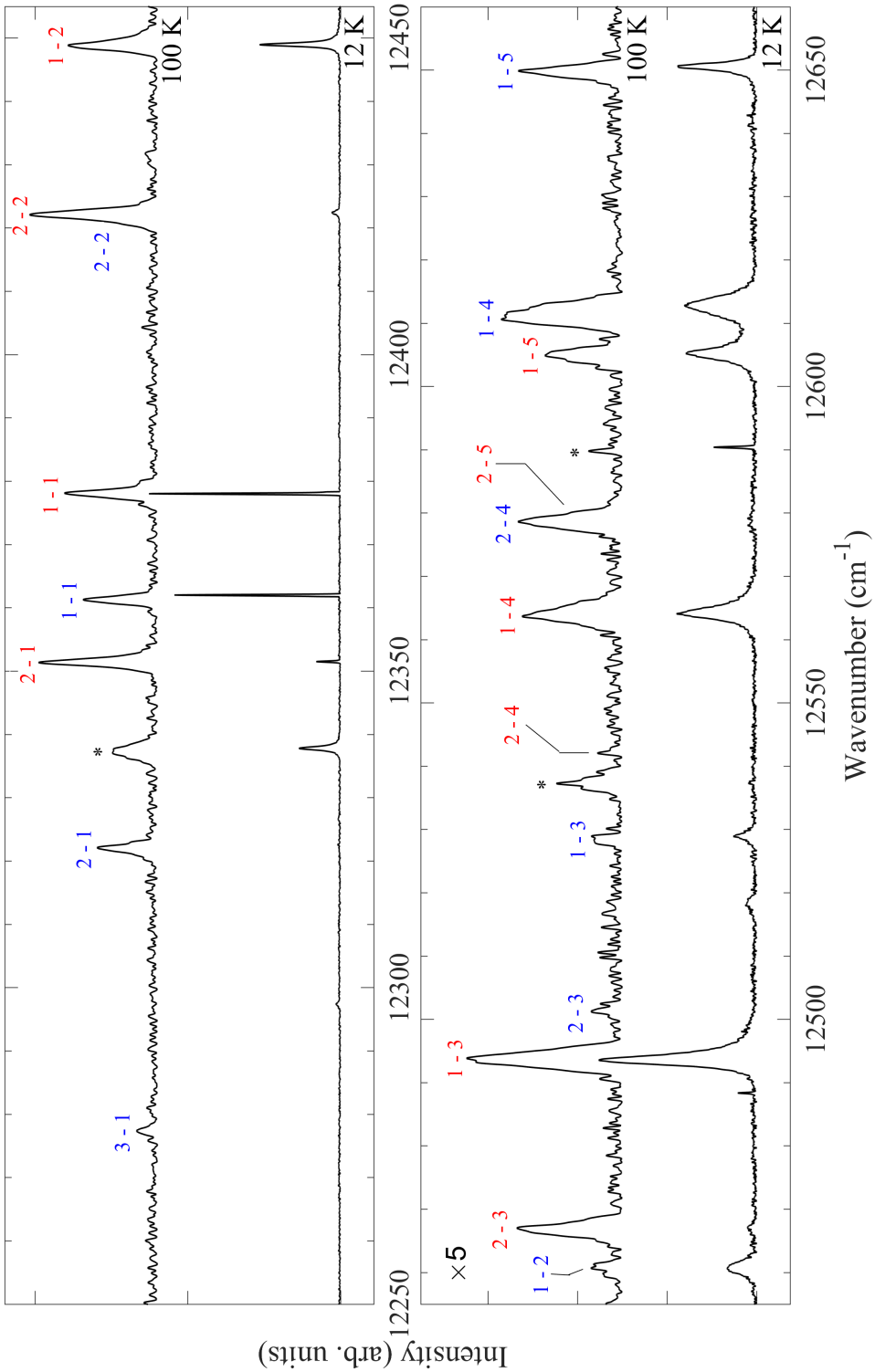

Figure 6.4: 12 K and 100 K absorption spectra of the $^4I_{9/2}$ multiplet in Y_2SiO_5:0.005%Er^{3+} with the $Z_i \longrightarrow B_j$ transitions labelled. Site 1 transitions are labelled in blue and site 2, in red. Spectral features labelled with an '*' are unrelated to Er^{3+}:Y_2SiO_5.

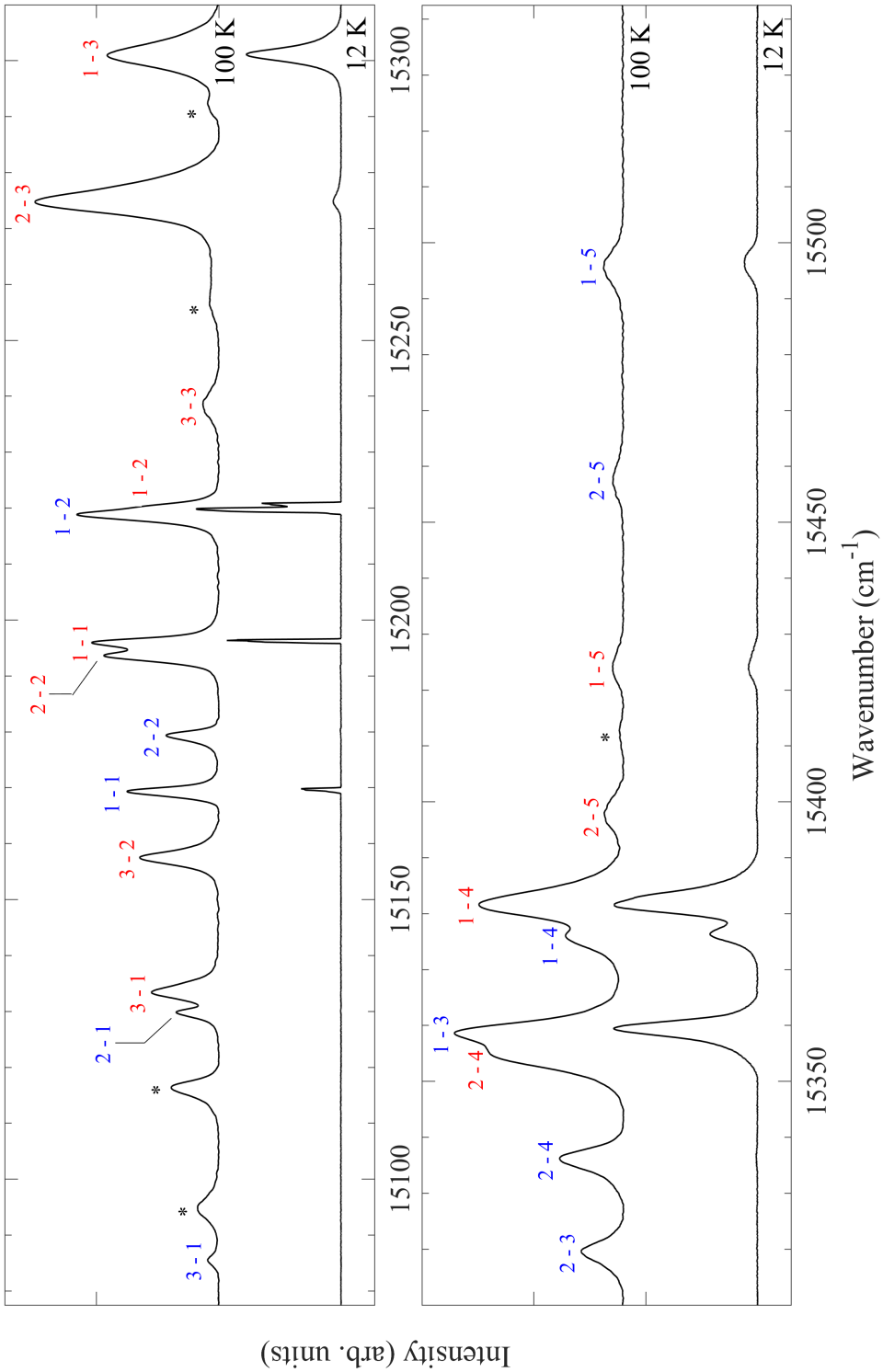

Figure 6.5: 12 K and 100 K absorption spectra of the $^4F_{9/2}$ multiplet in Y_2SiO_5:0.005%Er^{3+} with the $Z_i \longrightarrow D_j$ transitions labelled. Site 1 transitions are labelled in blue and site 2, in red. Spectral features labelled with an '*' are unrelated to Er^{3+}:Y_2SiO_5.

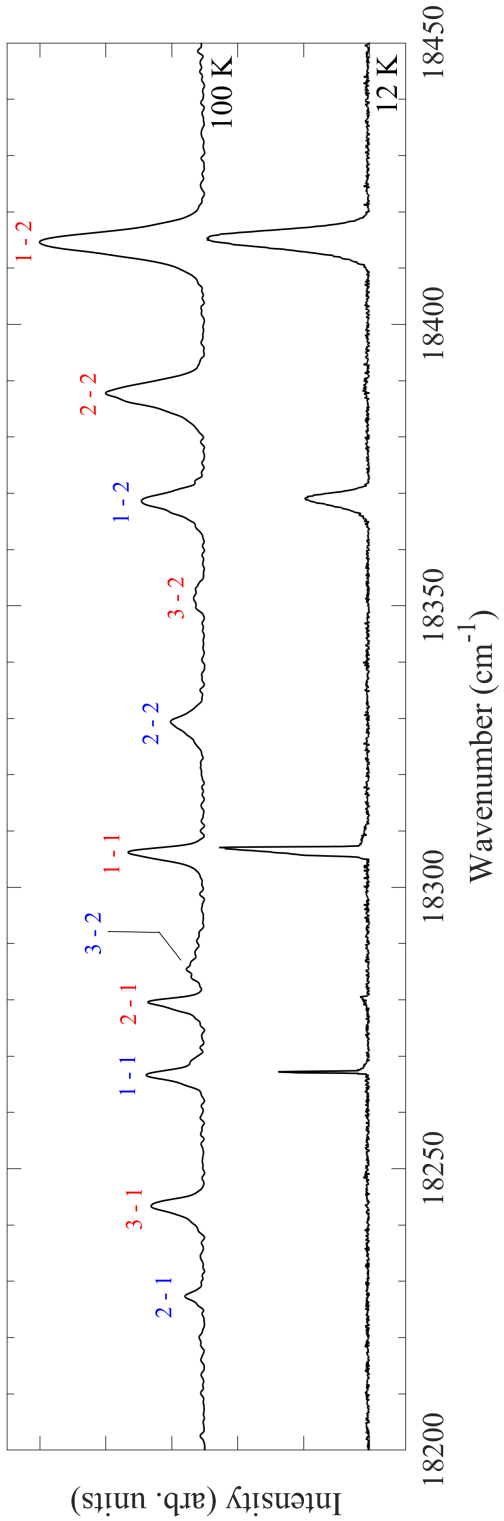

Figure 6.6: 12 K and 100 K absorption spectra of the $^4S_{3/2}$ multiplet in Y_2SiO_5:0.005%Er^{3+} with the $Z_i \longrightarrow E_j$ transitions labelled. Site 1 transitions are labelled in blue and site 2, in red.

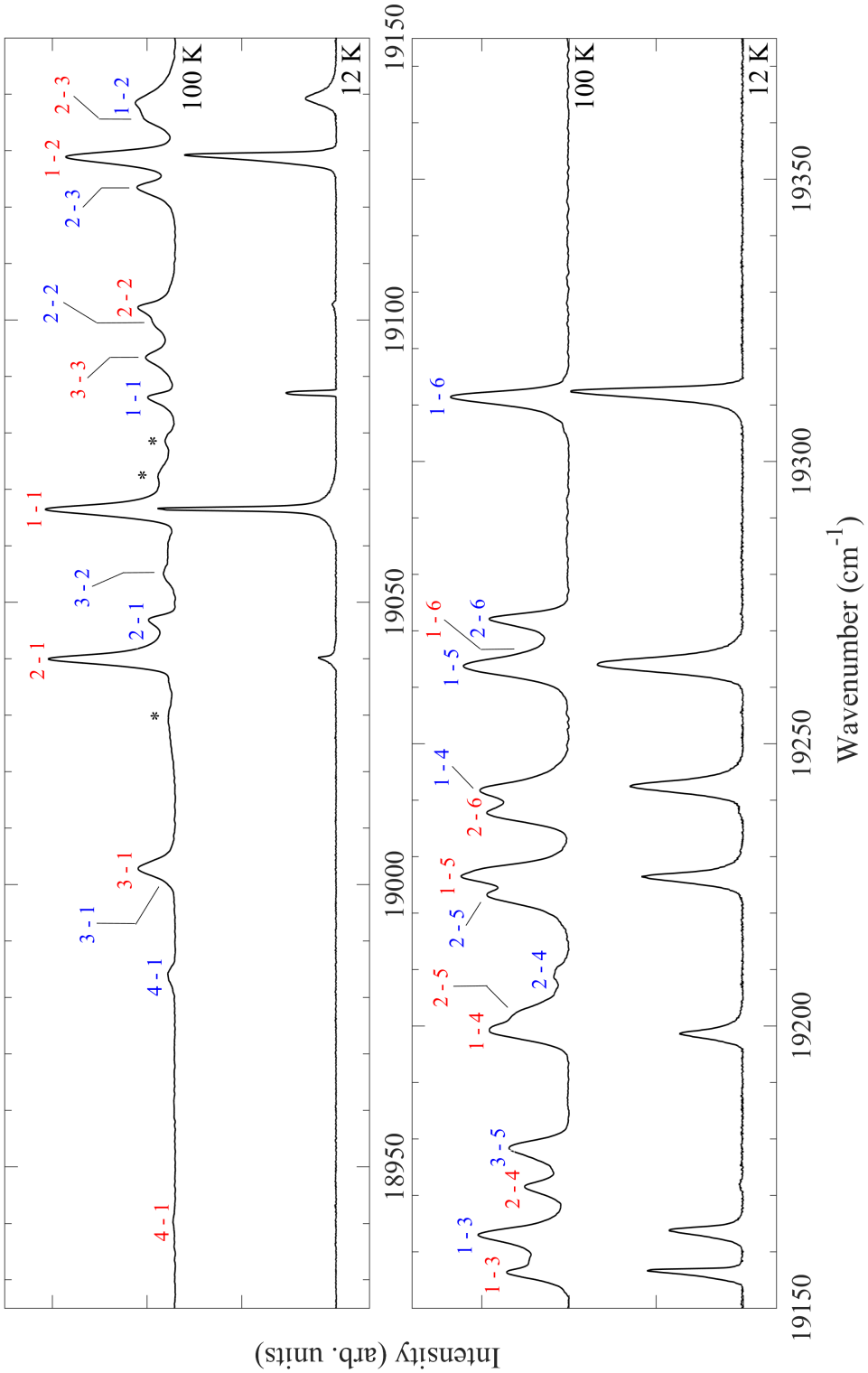

Figure 6.7: 12 K and 100 K absorption spectra of the $^2H_{11/2}$ multiplet in Y_2SiO_5:0.005%Er^{3+} with the $Z_i \longrightarrow F_j$ transitions labelled. Site 1 transitions are labelled in blue and site 2, in red. Spectral features labelled with an '*' are unrelated to Er^{3+}:Y_2SiO_5.

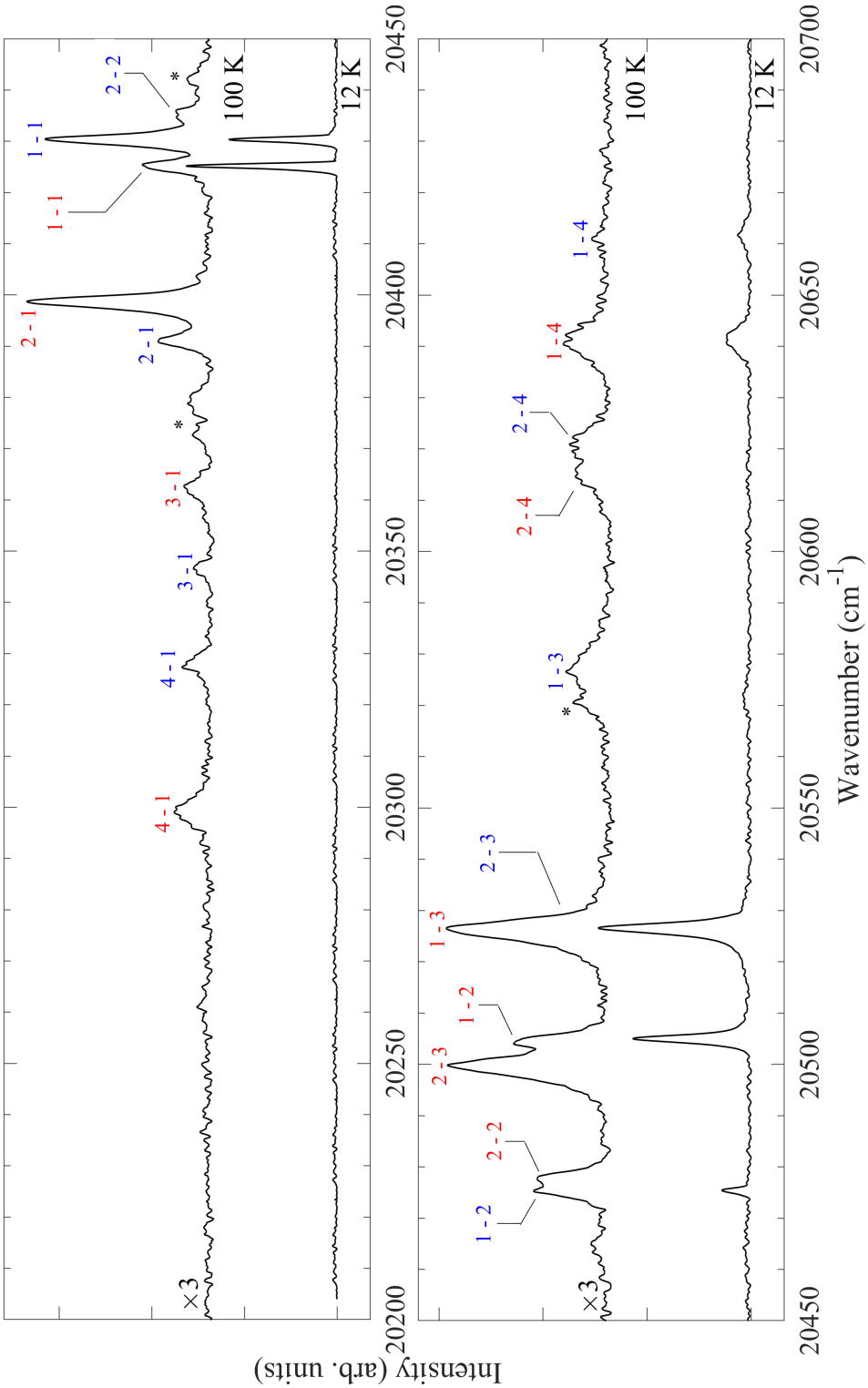

Figure 6.8: 12 K and 100 K absorption spectra of the $^4F_{7/2}$ multiplet in Y_2SiO_5:0.005%Er^{3+} with the $Z_i \longrightarrow G_j$ transitions labelled. Site 1 transitions are labelled in blue and site 2, in red. Spectral features labelled with an '*' are unrelated to Er^{3+}:Y_2SiO_5.

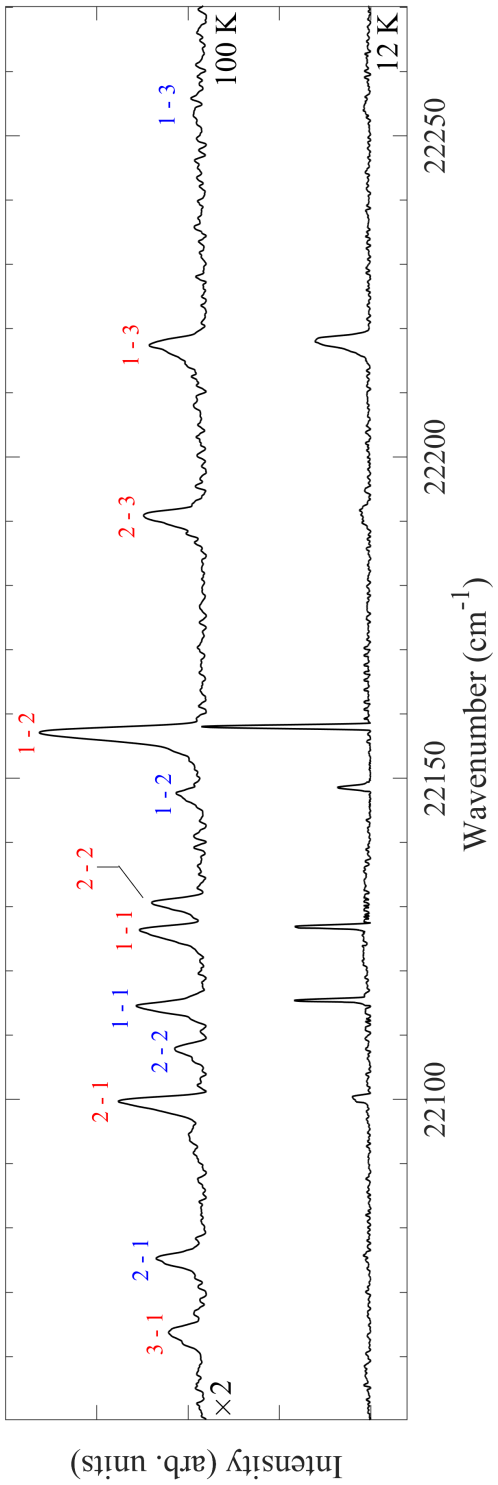

Figure 6.9: 12 K and 100 K absorption spectra of the $^4F_{5/2}$ multiplet in Y_2SiO_5:0.005%Er^{3+} with the $Z_i \longrightarrow H_j$ transitions labelled. Site 1 transitions are labelled in blue and site 2, in red.

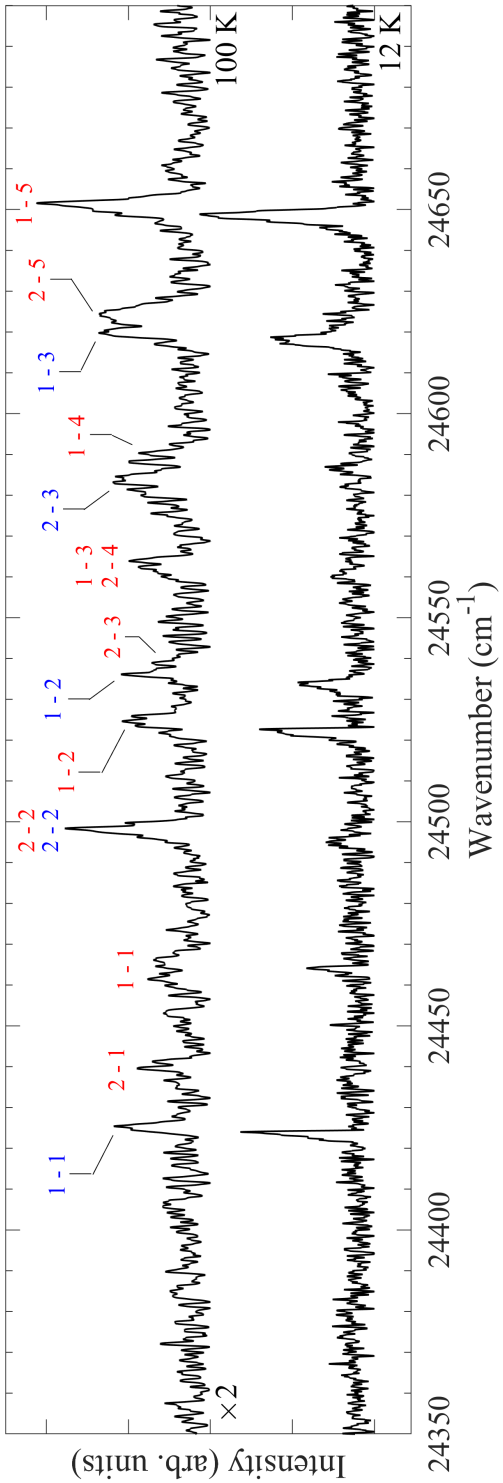

Figure 6.10: 12 K and 100 K absorption spectra of the $^2H_{9/2}$ multiplet in Y_2SiO_5:0.005%Er^{3+} with the $Z_i \longrightarrow K_j$ transitions labelled. Site 1 transitions are labelled in blue and site 2, in red.

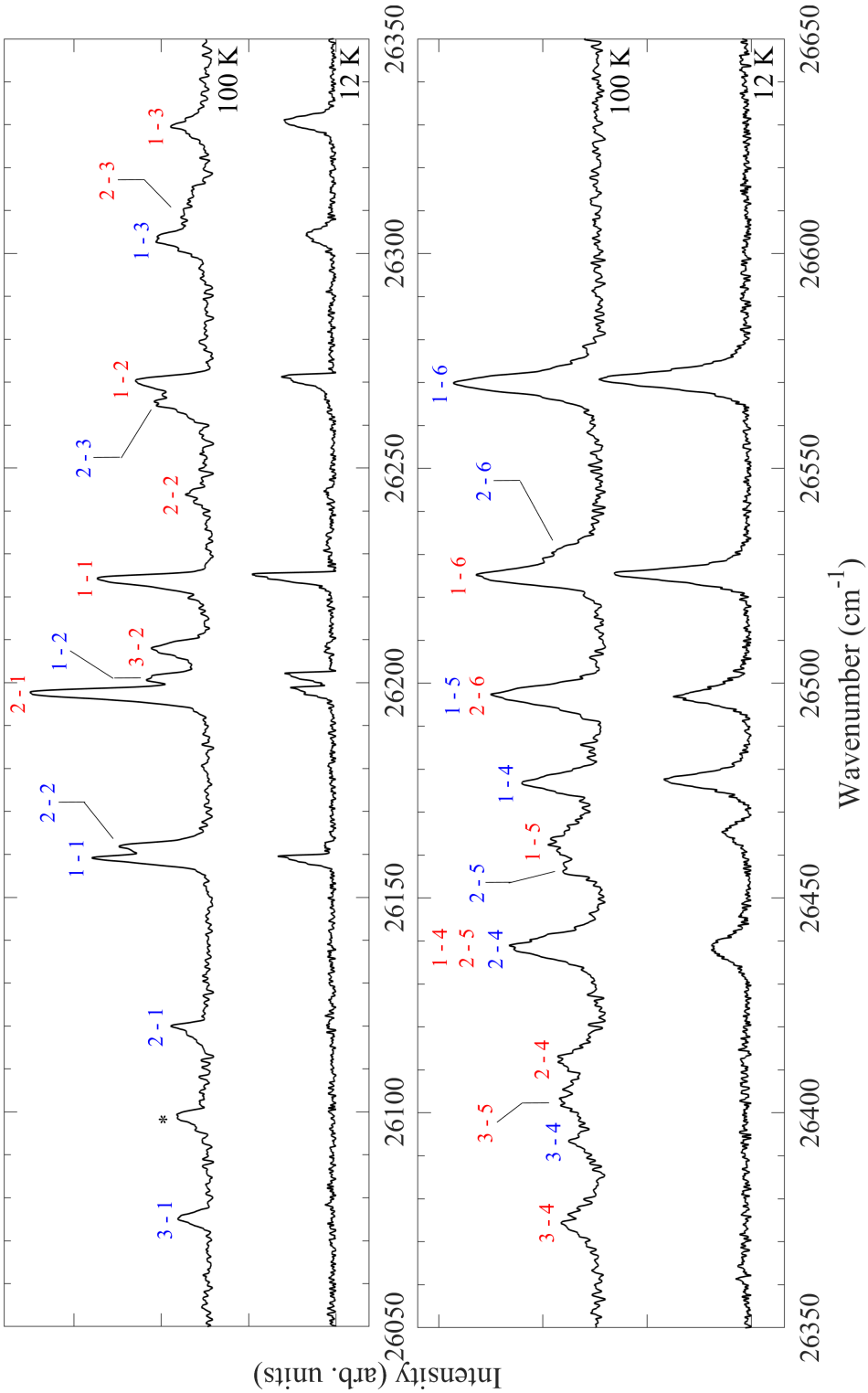

Figure 6.11: 12 K and 100 K absorption spectra of the $^4G_{11/2}$ multiplet in Y_2SiO_5:0.005%Er^{3+} with the $Z_i \longrightarrow L_j$ transitions labelled. Site 1 transitions are labelled in blue and site 2, in red. Spectral features labelled with an '*' are unrelated to Er^{3+}:Y_2SiO_5.

A total of 51 and 53 electronic states were assigned to site 1 and site 2 respectively. The $^4I_{15/2}Z_5$ – $^4I_{15/2}Z_8$ states of Er^{3+}:Y_2SiO_5 could not be determined due to phonon absorption in this region, and the negligible thermal population of such states at cryogenics temperatures. The assignments made by Doualan *et al.* were used for these states in the crystal-field fit [158]. It should be noted that our site assignments differ from that of Doualan *et al.* on the order of a few wavenumbers, which I attribute to the uncertainty of the site assignments. One notable exception to this is the $^4I_{11/2}$ multiplet, where our assignments and the assignments of Doualan *et al.* differ significantly, which arises from a number of uncertain assignments.

6.3 Zeeman absorption spectroscopy

While previous studies have included the magnetic structure of a select few states in crystal-field fits, here I present the approach of complimenting the crystal-field fit with g values from many states, obtained through Zeeman spectroscopy. Zeeman absorption spectroscopy was performed at 4.2 K along all three axes on most excited state multiplets up to the $^4F_{5/2}$ multiplet at ∼22 000 cm^{-1}. The experimental details of Zeeman absorption spectroscopy are given in Section 3.4. For states above 22 000 cm^{-1}, the g values could not be determined due to insufficient signal. Spectra were obtained at field strengths of 0 T – 0.5 T in steps of 0.1 T, followed by field strengths of 0.5 T – 4 T in steps of 0.5 T. The low-field steps were required in order monitor all four transitions, as in a few cases, the transitions vanish at high fields. This is due to the large ground state g values of Er^{3+}:Y_2SiO_5 which results in the upper state of the Kramers doublet becoming thermally depopulated, even at modest magnetic field strengths, while at 4.2 K.

Figure 6.12 shows representative spectra of the $^4I_{15/2}Z_1 \rightarrow {}^4I_{13/2}Y_1$ transition of both sites in Y_2SiO_5:0.005%Er^{3+} under the influence of a magnetic field. The top, middle and bottom panels show the splittings when the magnetic field was directed parallel to the D_1, D_2 and b axes respectively. The left panels depict the spectra that were obtained at magnetic field strengths of 0 T – 0.5 T in steps of 0.1 T and 0.5 T – 4 T in steps of 0.5 T. All spectra were recorded at 4.2 K. The right panels show the experimental splittings, represented by circles, and the theoretical splittings, calculated from our crystal-field model, are represented by the red lines. The theoretical splittings were shifted so that they lined up with the zero-field experimental energies. Due the two magnetically inequivalent orientations, many transitions, including those depicted in Figure 6.12 split into eight transitions, which is indicative of a small misalignment of the crystal.

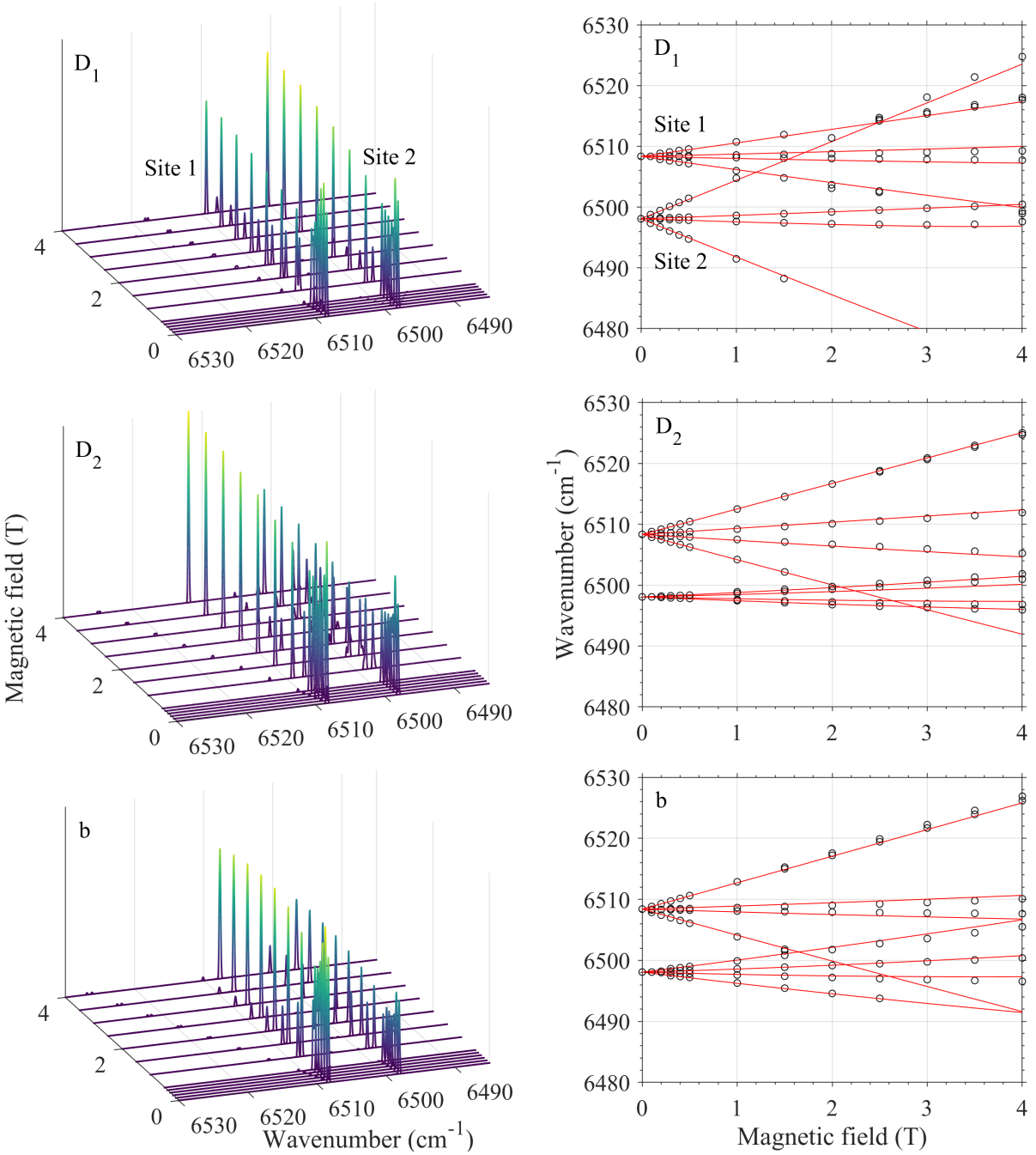

Figure 6.12: Magnetic splittings of the $^4I_{15/2}Z_1 \rightarrow {}^4I_{13/2}Y_1$ transition of both sites in Y_2SiO_5:0.005%Er^{3+} with a magnetic field applied along the three crystallographic axes of Y_2SiO_5. The top, middle and bottom panels shows $B \parallel D_1$, $B \parallel D_2$ and $B \parallel b$ respectively. The left panels show Zeeman absorption spectra at magnetic fields ranging from 0 T $\longrightarrow$ 4 T, all measured at 4.2 K. The right panels show the experimental splittings, represented by the circles, and the theoretical splittings are represented by the red lines.

Of particular note in Figure 6.12 is asymmetries in the spectra resulting from the quadratic Zeeman effect. Most notably in the site 2 transition along the D_2 and b axes, where the splitting is very asymmetric about the zero field transition at ∼6498 cm^{-1}. This is due to the interaction between the $^4I_{15/2}Z_1$ and Z_2 states, causing both states to bend away from each other. Figures 6.13 and 6.14 shows this effect clearly for site 1 and site 2 respectively. The left panels show the magnetic splittings of the $^4I_{15/2}Z_1$ and Z_2 states while the right panels depicts magnetic splittings of the $^4I_{13/2}Y_1$ and Y_2 states, with a magnetic field applied along the D_1 (top panels), D_2 (middle panels) and b (bottom panels) axes of Y_2SiO_5. We see that the $^4I_{15/2}Z_1$ and Z_2 states have minimal interaction along any direction for site 1, while these two states extensively interact for site 2 when the magnetic field is applied along the D_2 or b axes, as seen by the asymmetries about the zero-field energies (dashed horizontal lines). For the $^4I_{13/2}Y_1$ and Y_2 states, we see that there is minimal interactions along any axis for both sites.

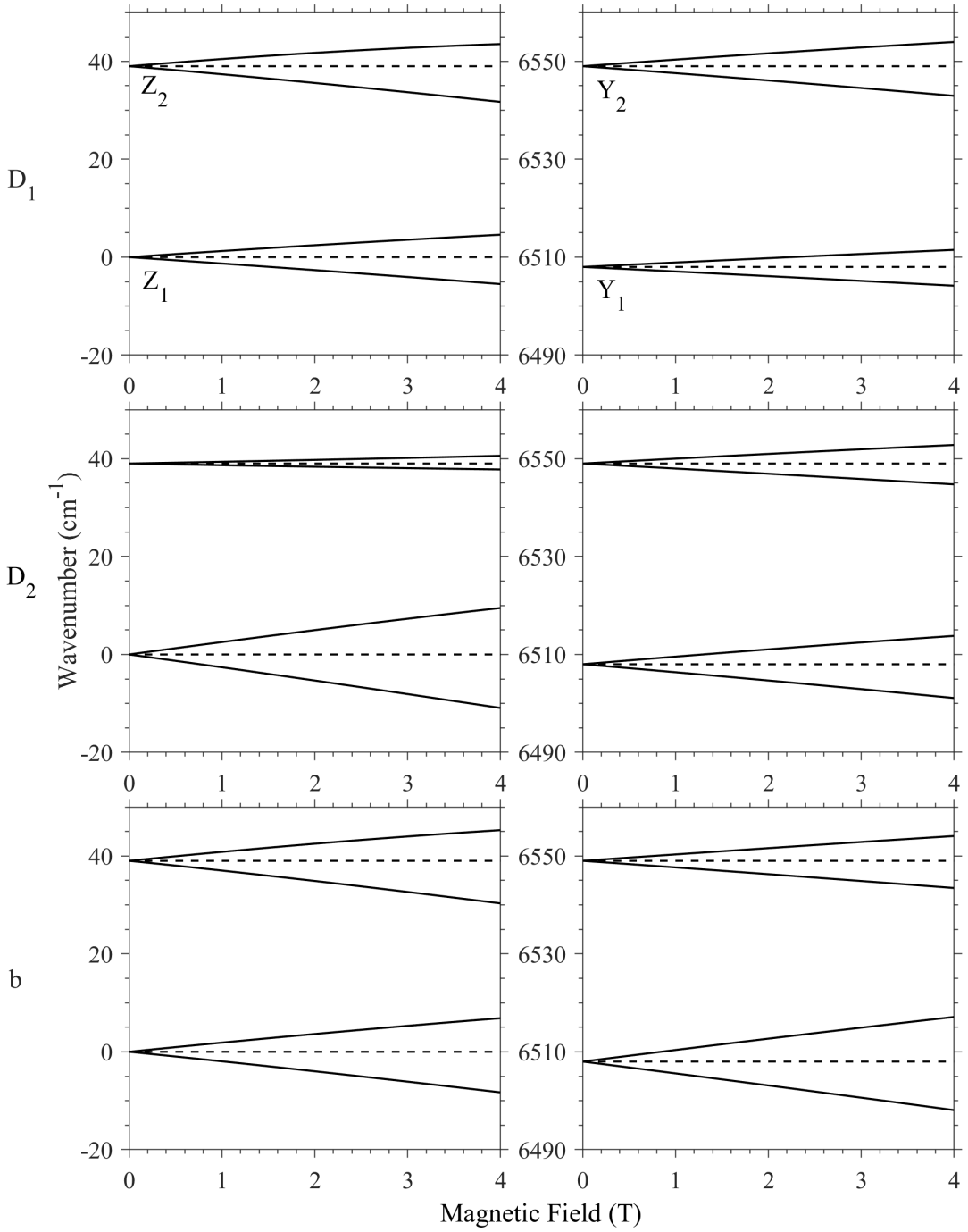

Figure 6.13: Theoretical magnetic splittings of the $^4I_{15/2}Z_1$ and Z_2 states (left panels) and the $^4I_{13/2}Y_1$ and Y_2 states (right panels) for site 1 in Y_2SiO_5:0.005%Er^{3+} with a magnetic field applied along the three crystallographic axes of Y_2SiO_5. The top, middle and bottom panels shows $B \parallel D_1$, $B \parallel D_2$ and $B \parallel b$ respectively. The splittings were calculated from the crystal-field model developed in this study. The dashed horizontal lines represent the zero-field energy levels and were added to assist the reader.

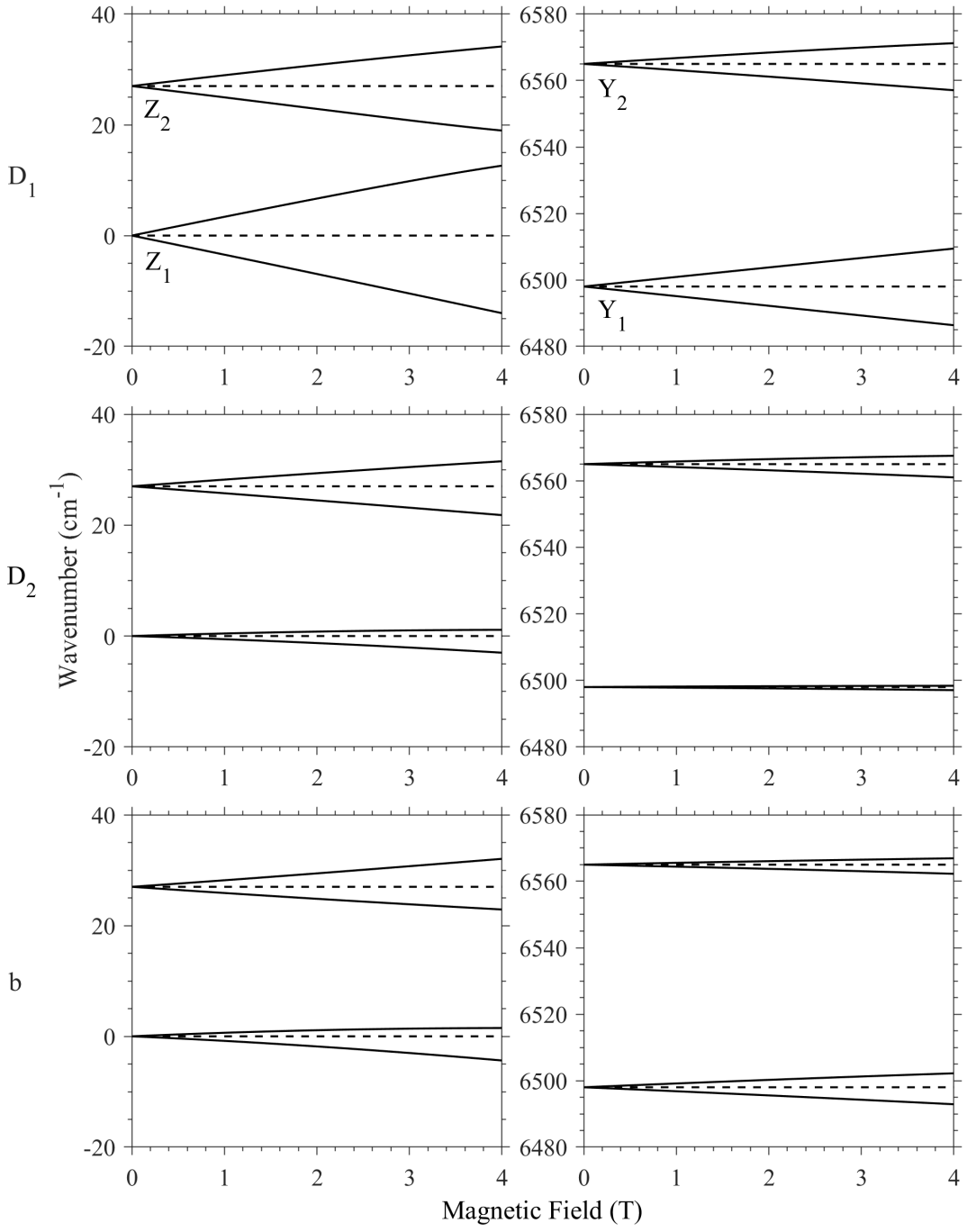

Figure 6.14: Theoretical magnetic splittings of the $^4I_{15/2}Z_1$ and Z_2 states (left panels) and the $^4I_{13/2}Y_1$ and Y_2 states (right panels) for site 2 in Y_2SiO_5:0.005%Er^{3+} with a magnetic field applied along the three crystallographic axes of Y_2SiO_5. The top, middle and bottom panels shows $B \parallel D_1$, $B \parallel D_2$ and $B \parallel b$ respectively. The splittings were calculated from the crystal-field model developed in this study. The dashed horizontal lines represent the zero-field energy levels and were added to assist the reader.

Figures 6.15 – 6.30 depicts the magnetic splittings from the $^4I_{15/2}Z_1$ ground state to each excited state up to the $^4F_{5/2}$ multiplet for both sites in Y_2SiO_5:0.005%Er^{3+}. For each transition the top, middle and bottom panels shows the magnetic splittings with $B \parallel D_1$, $B \parallel D_2$ and $B \parallel b$ respectively. The left panels of each transition show the experimental splittings, represented by the circles, and the theoretical splittings, calculated from our crystal-field model, are represented by the red lines. The right panels of each transition show Zeeman absorption spectra at a magnetic field represented by the vertical line in the left panels. Spectral features labelled with a '#' are related to other transitions of Er^{3+}:Y_2SiO_5 while spectral features labelled with an '*' is absorption due to water.

A total of 68 g values (20 along the D_1 axis, 23 along the D_2 axis and 25 along the b axis) for site 1 and 70 g values (25 along the D_1 axis, 24 along the D_2 axis and 21 along the b axis) for site 2 were determined utilising Zeeman spectroscopy. These values are summarised in Tables 6.2 and 6.3 respectively. The g values were determined by applying Equations (3.1) and (3.2) to spectra that are at sufficient magnetic field strengths where each state has resolved into 4 transitions but not too high where the transitions split further into 8 transitions due to the magnetically inequivalent orientations, or becomes noticeably non-linear due to the quadratic Zeeman effect. g values could only be found for states that have a g value large enough for the splitting to be resolved relative to the transitions line width.

As the splitting pattern of any transition should be linear at low fields about the zero-field transition, a g value could still be extracted in case where only two of the four expected transitions could be observed. One such example of this is the $^4I_{13/2}Y_4$ transition for site 1 with the magnetic field applied along the D_2 axis as depicted in Figure 6.15. In this case only the two higher energy transitions could be observed due to the lower transitions being obscured by a site 2 transition. However, as the splitting of these two upper transitions remain linear as the magnetic field strength increases, it could be assumed there would be a related pair of transitions at lower energies resulting in the four transitions required to calculate the g values. In the cases where a g value could not be determined, the monitored splittings are, in general, well described by our crystal field model.

In some cases the spectral features of both sites happen to lie very close to each other ($\Delta E \leq 2$ cm^{-1}), such as the $^4I_{13/2}Y_4$ transitions for both sites, the $^4I_{11/2}A_2$ transitions for both sites, the $^4I_{11/2}A_4$ and $^4I_{11/2}A_6$ transitions for site 1 and site 2 respectively, the $^4F_{9/2}D_2$ transitions for both sites and the $^2H_{11/2}F_5$ and $^2H_{11/2}F_6$ transitions for site 1 and site 2 respectively. In many of these cases it appears as a single spectral line has split into eight, however each could be separated into two groups four transitions and assigned as belonging to either one of the two sites. The exception to this was the $^2H_{11/2}F_6$ transitions (see Figures 6.25 and 6.26) where less than eight of the expected transitions could be resolved and therefore the g values could not be extracted.

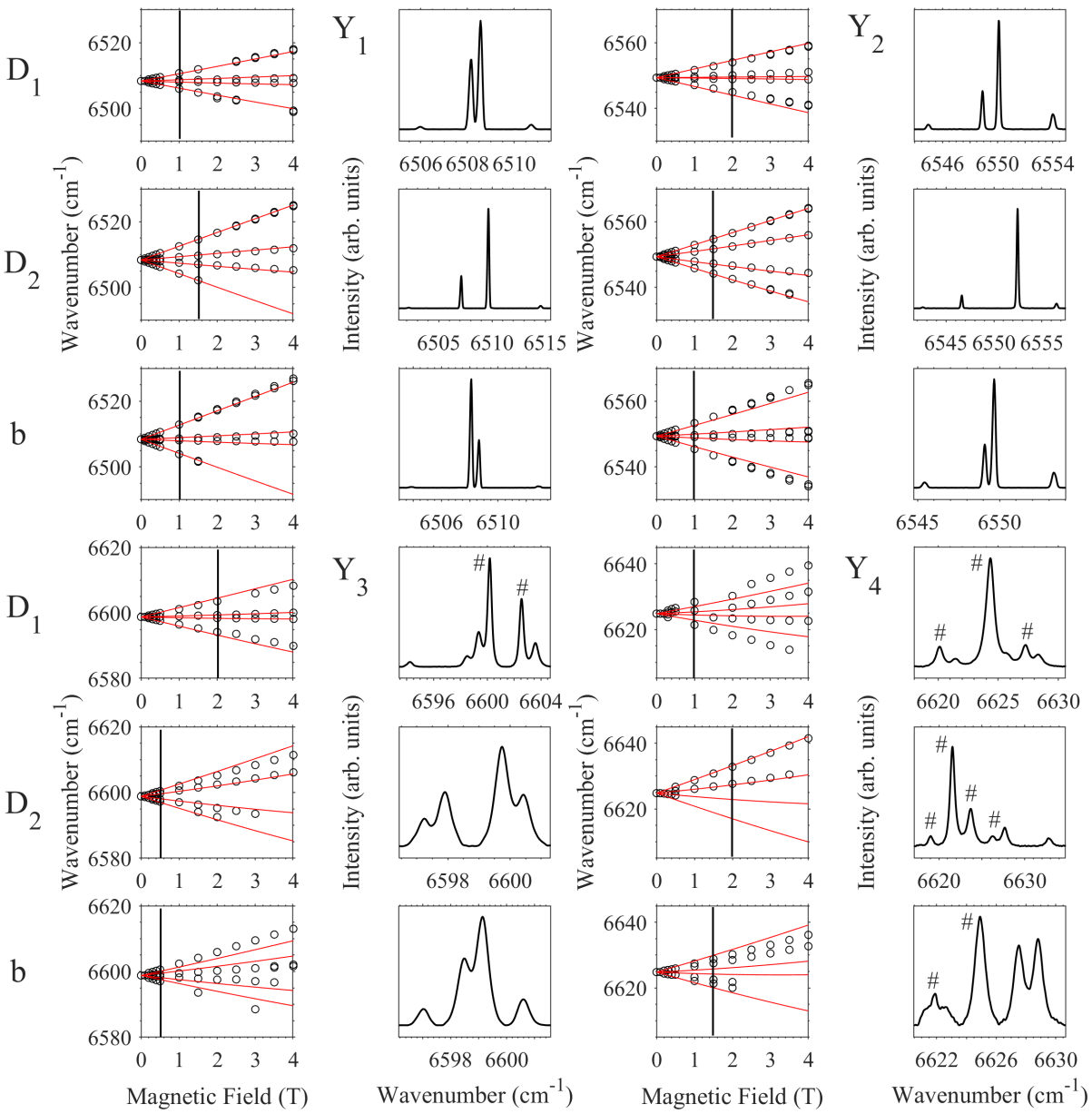

Figure 6.15: Magnetic splittings of the $^4I_{15/2}Z_1 \rightarrow {}^4I_{13/2}Y_i$ transitions of site 1 in Y_2SiO_5:0.005%Er^{3+} with a magnetic field applied along the three crystallographic axes of Y_2SiO_5. The top, middle and bottom panels for each $Z_1 \longrightarrow Y_i$ transition shows the magnetic splittings with $B \parallel D_1$, $B \parallel D_2$ and $B \parallel b$ respectively. The left panels of each transition show the experimental splittings, represented by the circles, and the theoretical splittings are represented by the red lines. The right panels of each transition show Zeeman absorption spectra at a magnetic field represented by the vertical line in the left panels. All spectra were measured at 4.2 K. Spectral features labelled with a '#' are transitions related to site 2. Figure is continued over page.

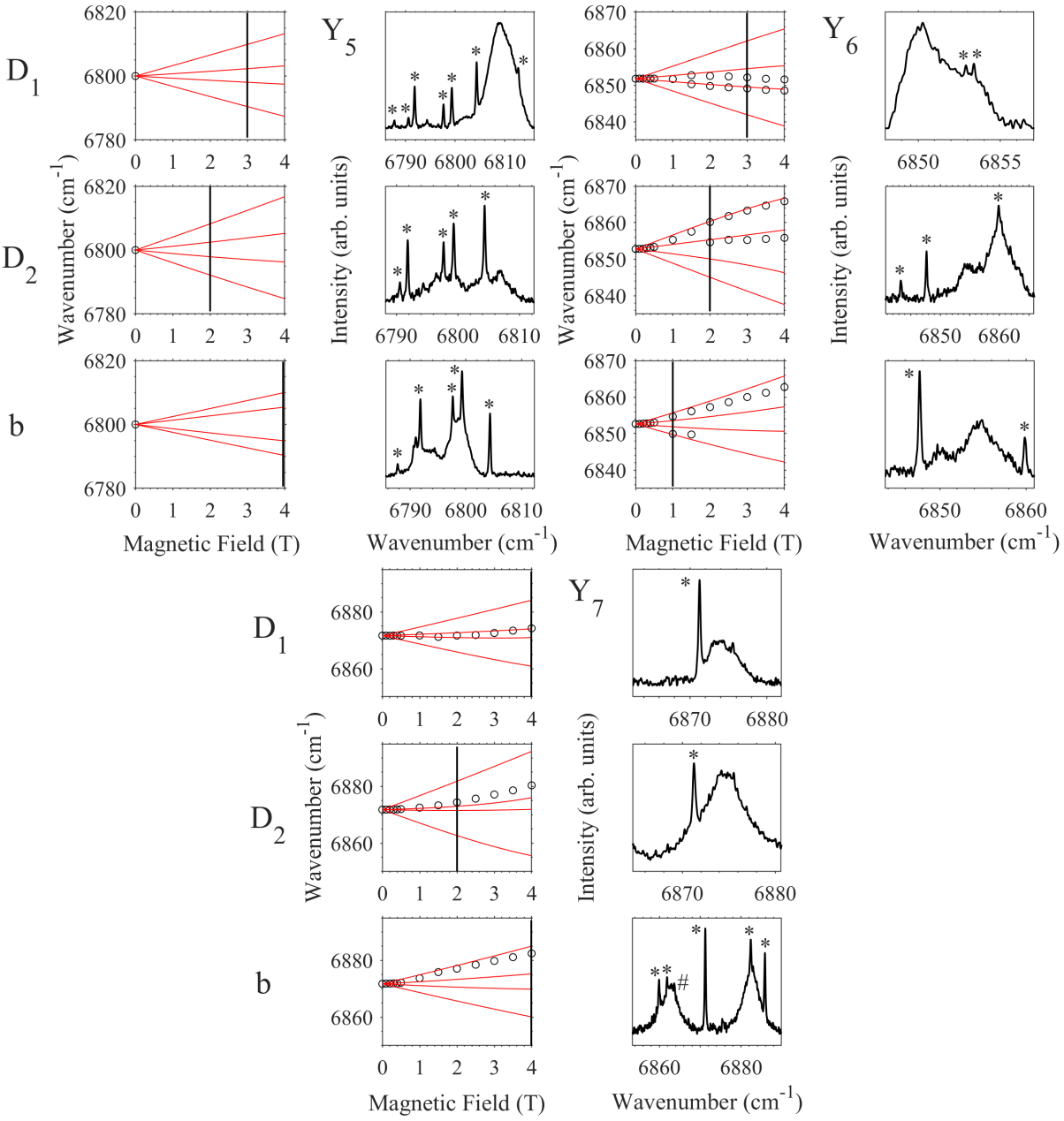

Figure 6.15: Magnetic splittings of the $^4I_{15/2}Z_1 \rightarrow {}^4I_{13/2}Y_i$ transitions of site 1 in Y_2SiO_5:0.005%Er^{3+} with a magnetic field applied along the three crystallographic axes of Y_2SiO_5. The top, middle and bottom panels for each $Z_1 \longrightarrow Y_i$ transition shows the magnetic splittings with $B \parallel D_1$, $B \parallel D_2$ and $B \parallel b$ respectively. The left panels of each transition show the experimental splittings, represented by the circles, and the theoretical splittings are represented by the red lines. The right panels of each transition show Zeeman absorption spectra at a magnetic field represented by the vertical line in the left panels. All spectra were measured at 4.2 K. Spectral features labelled with an '#' are transitions related to site 2. Spectral features labelled with an '*' is absorption due to water.

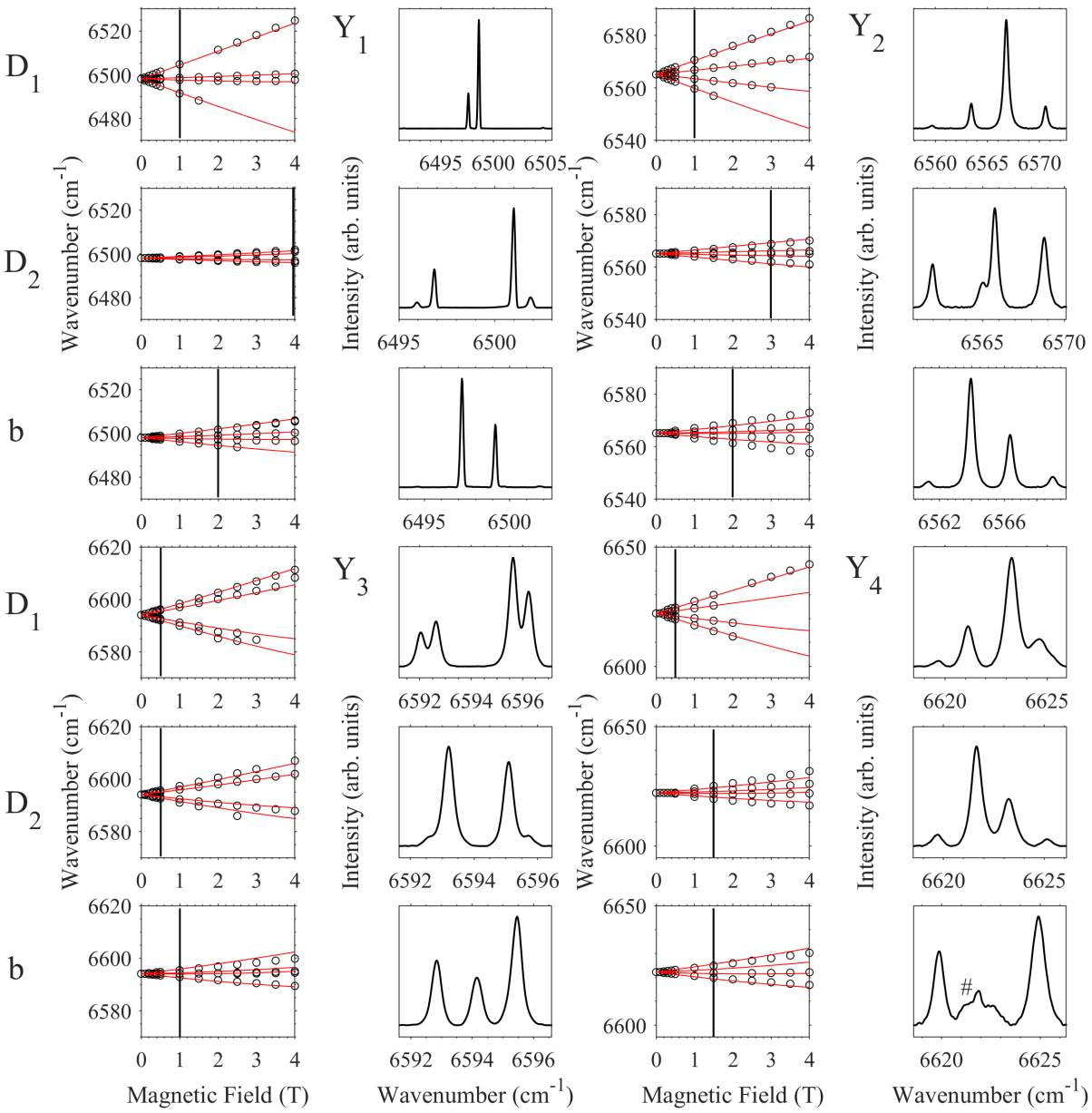

Figure 6.16: Magnetic splittings of the $^4I_{15/2}Z_1 \rightarrow {}^4I_{13/2}Y_i$ transitions of site 2 in Y_2SiO_5:0.005%Er^{3+} with a magnetic field applied along the three crystallographic axes of Y_2SiO_5. The top, middle and bottom panels for each $Z_1 \longrightarrow Y_i$ transition shows the magnetic splittings with $B \parallel D_1$, $B \parallel D_2$ and $B \parallel b$ respectively. The left panels of each transition show the experimental splittings, represented by the circles, and the theoretical splittings are represented by the red lines. The right panels of each transition show Zeeman absorption spectra at a magnetic field represented by the vertical line in the left panels. All spectra were measured at 4.2 K. Spectral features labelled with a '#' are transitions related to site 1. Figure is continued over page.

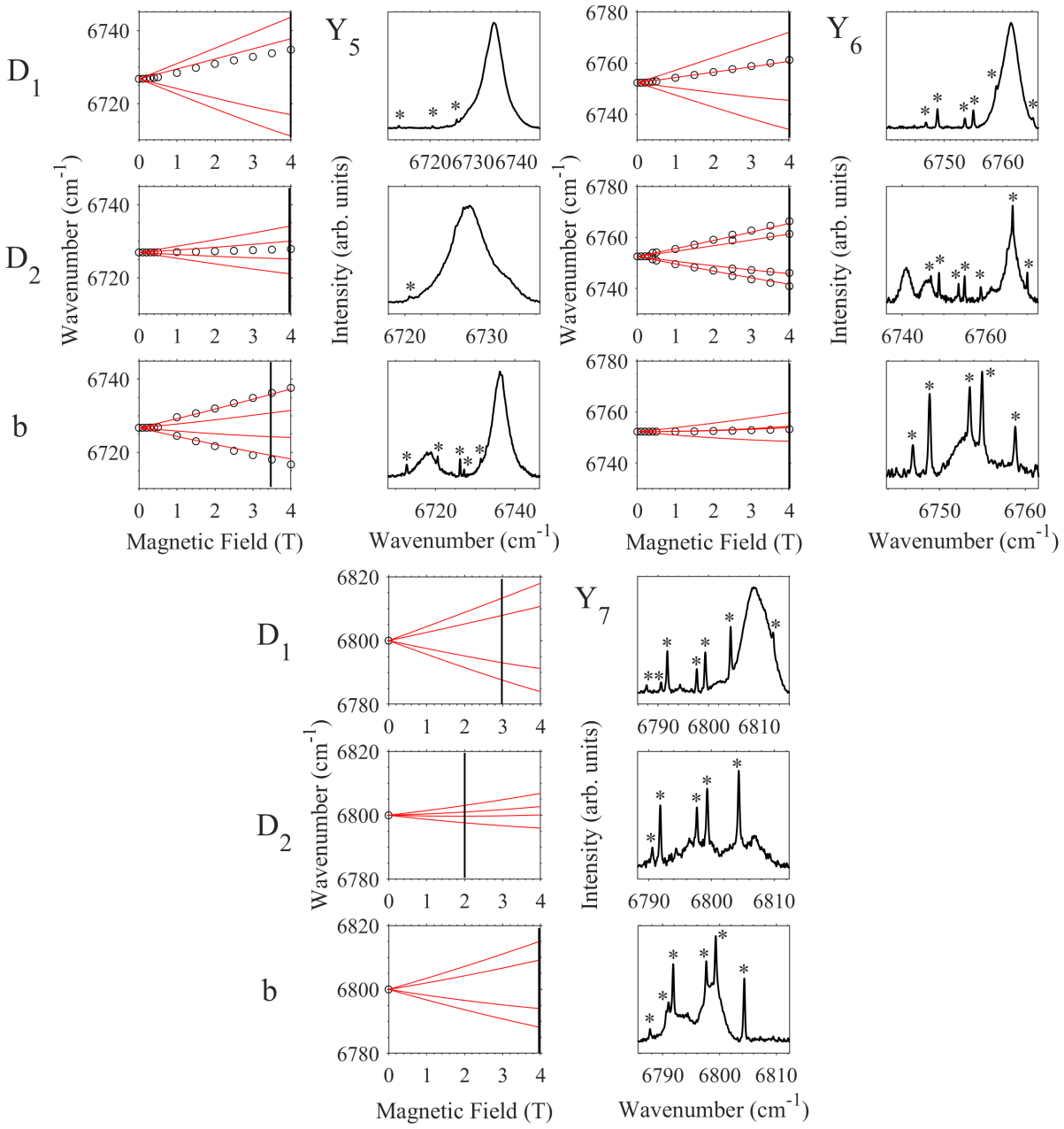

Figure 6.16: Magnetic splittings of the $^4I_{15/2}Z_1 \rightarrow {}^4I_{13/2}Y_i$ transitions of site 2 in Y_2SiO_5:0.005%Er^{3+} with a magnetic field applied along the three crystallographic axes of Y_2SiO_5. The top, middle and bottom panels for each $Z_1 \longrightarrow Y_i$ transition shows the magnetic splittings with $B \parallel D_1$, $B \parallel D_2$ and $B \parallel b$ respectively. The left panels of each transition show the experimental splittings, represented by the circles, and the theoretical splittings are represented by the red lines. The right panels of each transition show Zeeman absorption spectra at a magnetic field represented by the vertical line in the left panels. All spectra were measured at 4.2 K. Spectral features labelled with an '*' is absorption due to water.

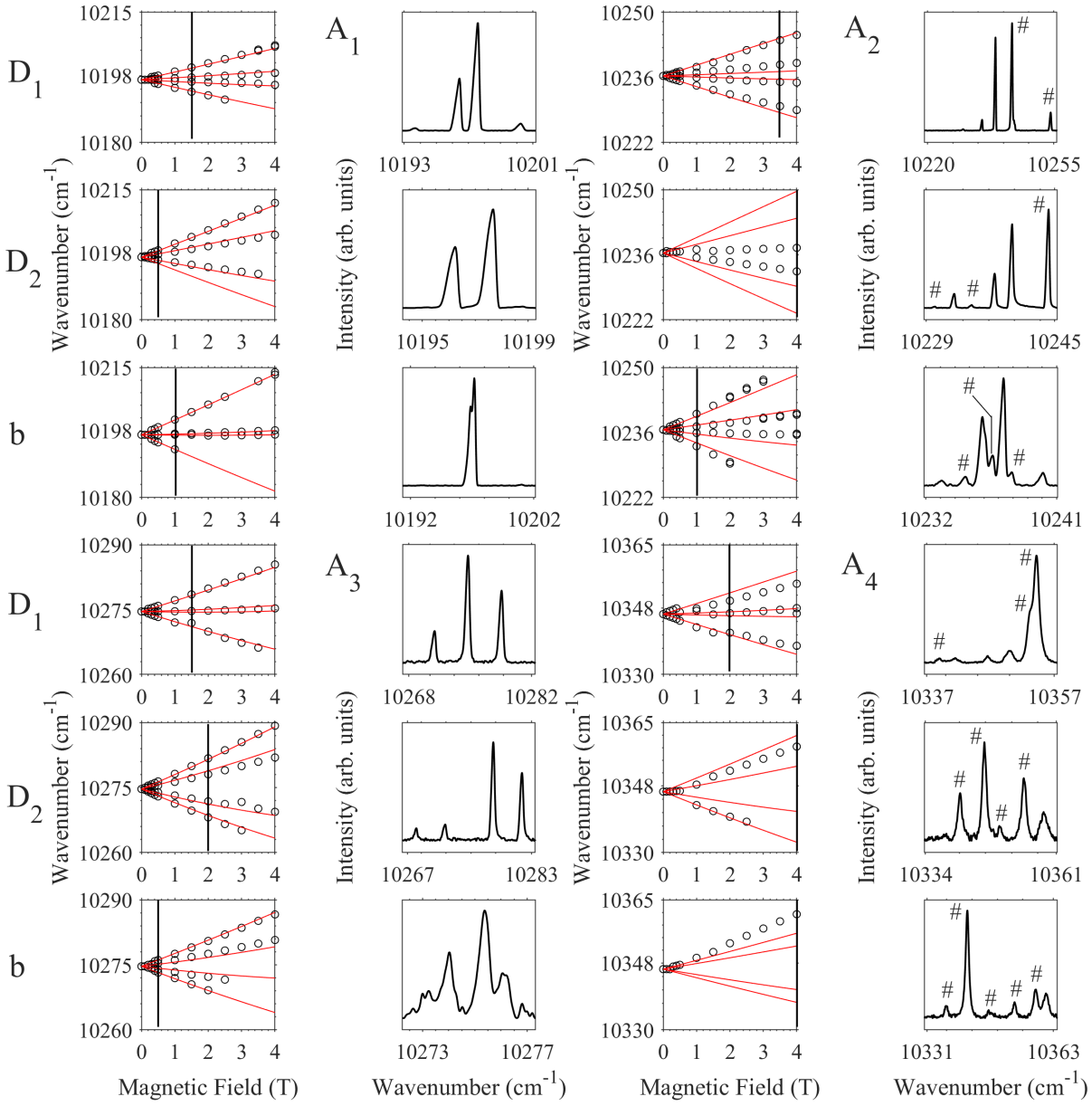

Figure 6.17: Magnetic splittings of the $^4I_{15/2}Z_1 \rightarrow {}^4I_{11/2}A_i$ transitions of site 1 in Y_2SiO_5:0.005%Er^{3+} with a magnetic field applied along the three crystallographic axes of Y_2SiO_5. The top, middle and bottom panels for each $Z_1 \longrightarrow A_i$ transition shows the magnetic splittings with $B \parallel D_1$, $B \parallel D_2$ and $B \parallel b$ respectively. The left panels of each transition show the experimental splittings, represented by the circles, and the theoretical splittings are represented by the red lines. The right panels of each transition show Zeeman absorption spectra at a magnetic field represented by the vertical line in the left panels. All spectra were measured at 4.2 K. Spectral features labelled with an '#' are transitions related to site 2. Figure is continued over page.

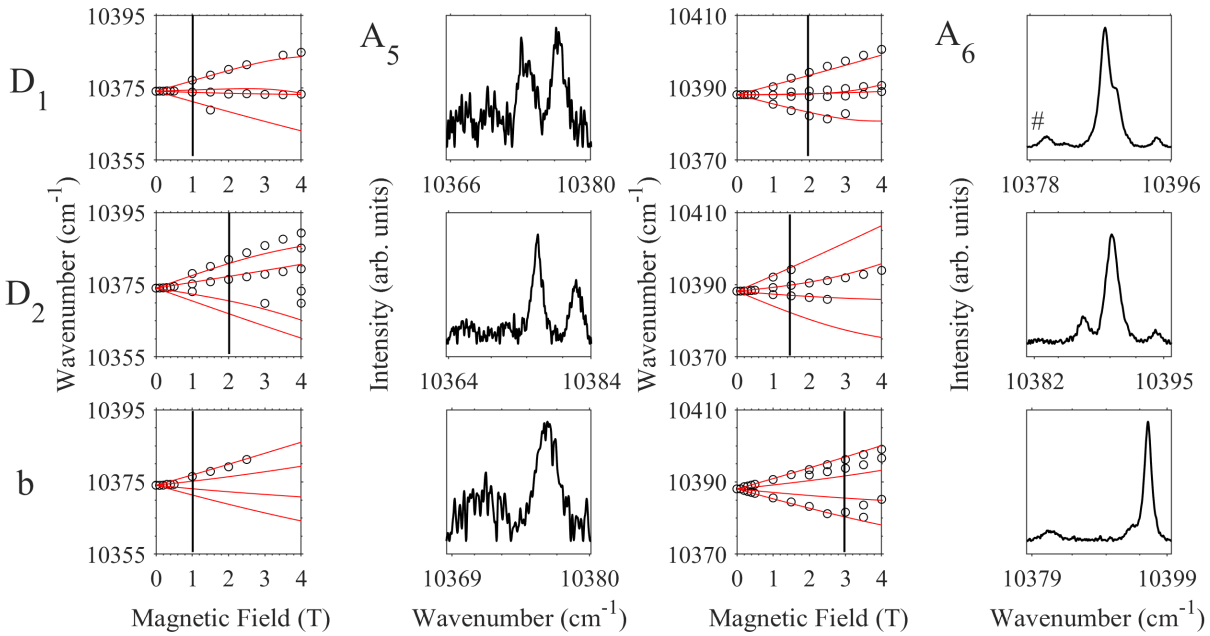

Figure 6.17: Magnetic splittings of the $^4I_{15/2}Z_1 \rightarrow {}^4I_{11/2}A_i$ transitions of site 1 in Y_2SiO_5:0.005%Er^{3+} with a magnetic field applied along the three crystallographic axes of Y_2SiO_5. The top, middle and bottom panels for each $Z_1 \longrightarrow A_i$ transition shows the magnetic splittings with $B \parallel D_1$, $B \parallel D_2$ and $B \parallel b$ respectively. The left panels of each transition show the experimental splittings, represented by the circles, and the theoretical splittings are represented by the red lines. The right panels of each transition show Zeeman absorption spectra at a magnetic field represented by the vertical line in the left panels. All spectra were measured at 4.2 K. Spectral features labelled with an '#' are transitions related to the $^4I_{11/2}A_5$ site 1 spectral lines.

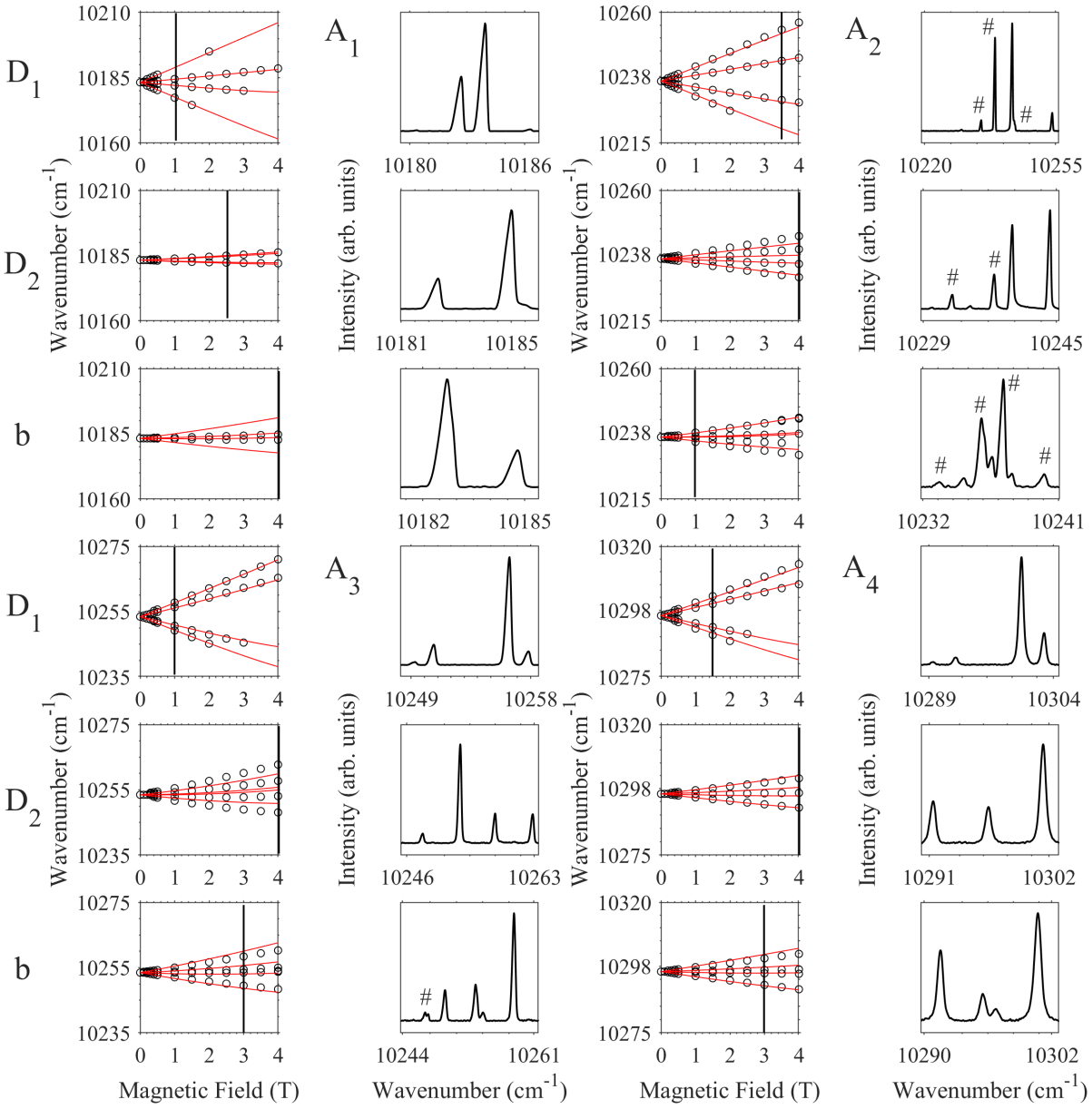

Figure 6.18: Magnetic splittings of the $^4I_{15/2}Z_1 \rightarrow {}^4I_{11/2}A_i$ transitions of site 2 in Y_2SiO_5:0.005%Er^{3+} with a magnetic field applied along the three crystallographic axes of Y_2SiO_5. The top, middle and bottom panels for each $Z_1 \longrightarrow A_i$ transition shows the magnetic splittings with $B \parallel D_1$, $B \parallel D_2$ and $B \parallel b$ respectively. The left panels of each transition show the experimental splittings, represented by the circles, and the theoretical splittings are represented by the red lines. The right panels of each transition show Zeeman absorption spectra at a magnetic field represented by the vertical line in the left panels. All spectra were measured at 4.2 K. Spectral features labelled with an '#' are transitions related to site 1. Figure is continued over page.

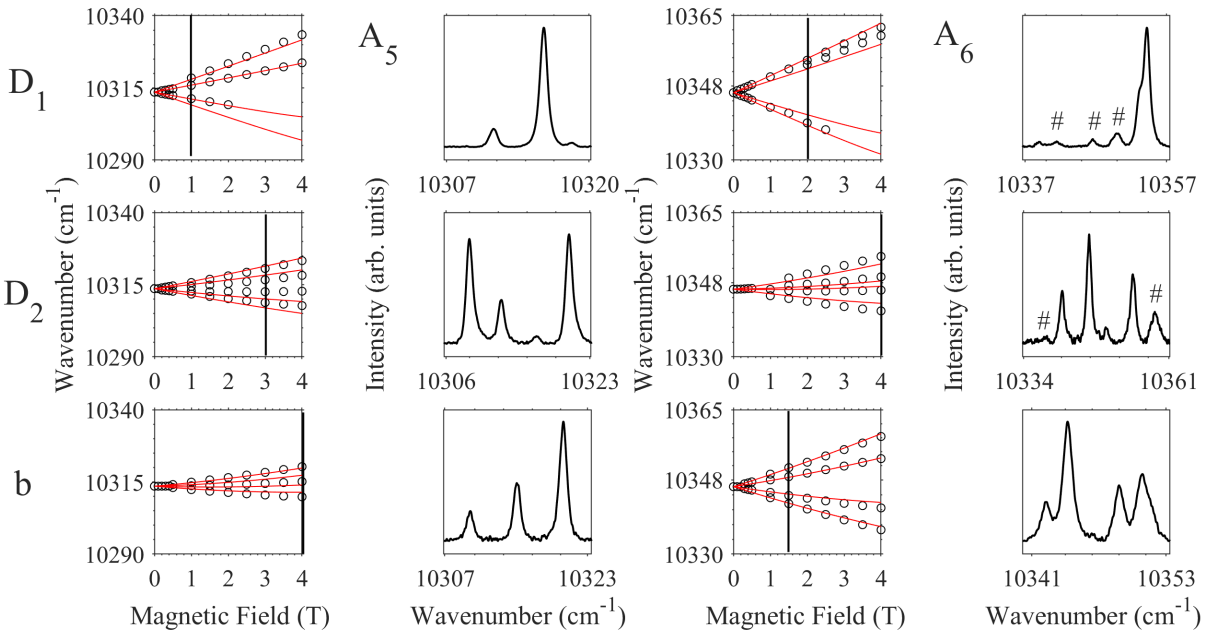

Figure 6.18: Magnetic splittings of the $^4I_{15/2}Z_1 \rightarrow {}^4I_{11/2}A_i$ transitions of site 2 in Y_2SiO_5:0.005%Er^{3+} with a magnetic field applied along the three crystallographic axes of Y_2SiO_5. The top, middle and bottom panels for each $Z_1 \longrightarrow A_i$ transition shows the magnetic splittings with $B \parallel D_1$, $B \parallel D_2$ and $B \parallel b$ respectively. The left panels of each transition show the experimental splittings, represented by the circles, and the theoretical splittings are represented by the red lines. The right panels of each transition show Zeeman absorption spectra at a magnetic field represented by the vertical line in the left panels. All spectra were measured at 4.2 K. Spectral features labelled with an '#' are transitions related to site 1.

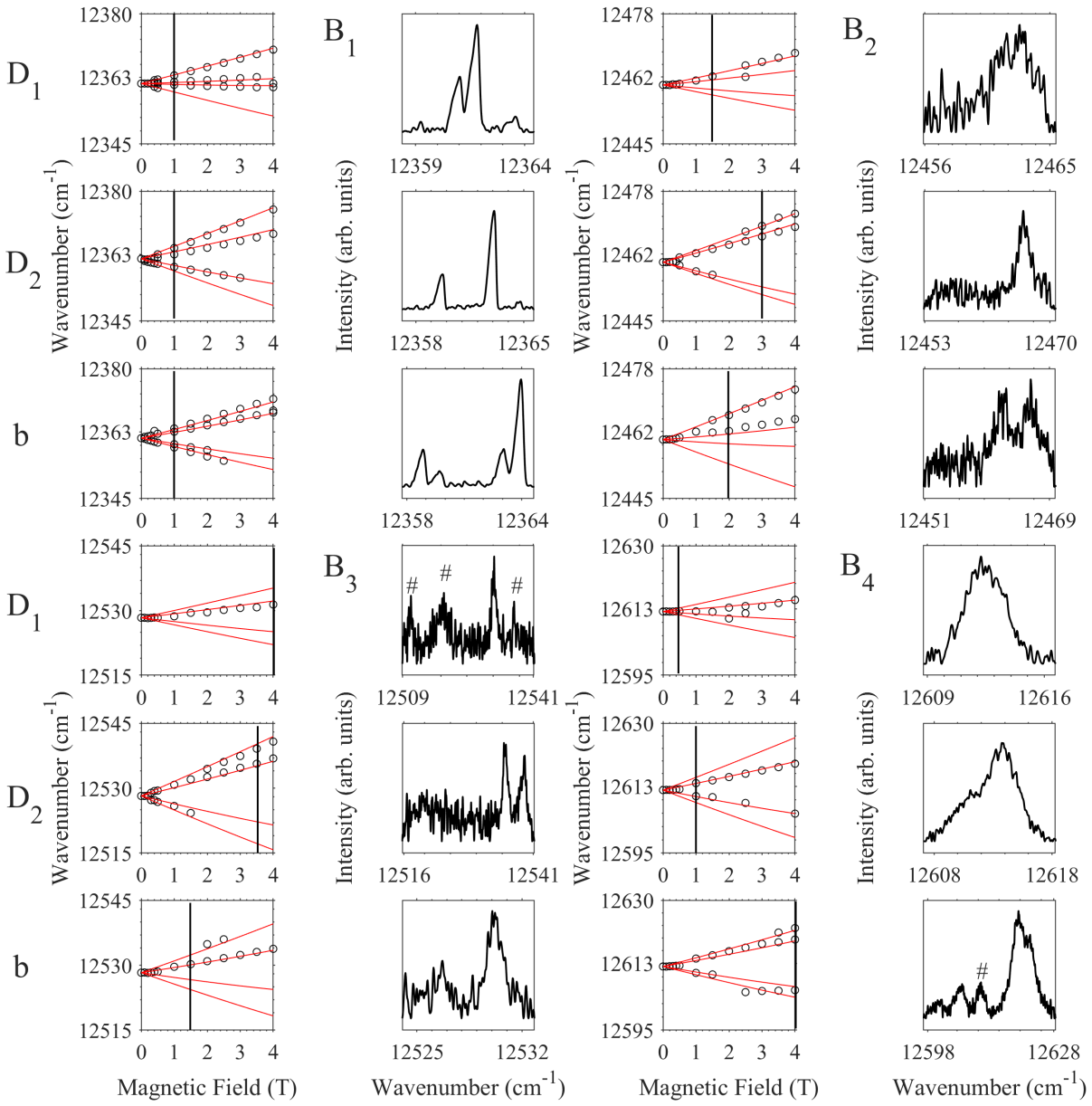

Figure 6.19: Magnetic splittings of the $^4I_{15/2}Z_1 \rightarrow {}^4I_{9/2}B_i$ transitions of site 1 in Y_2SiO_5:0.005%Er^{3+} with a magnetic field applied along the three crystallographic axes of Y_2SiO_5. The top, middle and bottom panels for each $Z_1 \longrightarrow B_i$ transition shows the magnetic splittings with $B \parallel D_1$, $B \parallel D_2$ and $B \parallel b$ respectively. The left panels of each transition show the experimental splittings, represented by the circles, and the theoretical splittings are represented by the red lines. The right panels of each transition show Zeeman absorption spectra at a magnetic field represented by the vertical line in the left panels. All spectra were measured at 4.2 K. Spectral features labelled with an '#' are transitions related to site 2. Figure is continued over page.

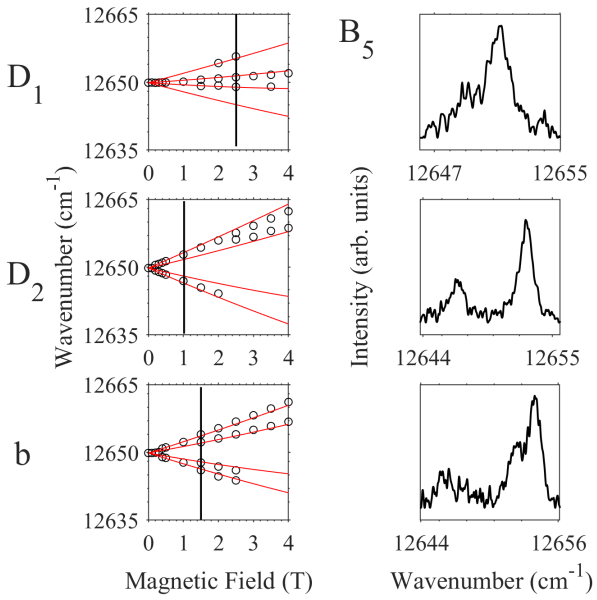

Figure 6.19: Magnetic splittings of the $^4I_{15/2}Z_1 \rightarrow {}^4I_{9/2}B_i$ transitions of site 1 in Y_2SiO_5:0.005%Er^{3+} with a magnetic field applied along the three crystallographic axes of Y_2SiO_5. The top, middle and bottom panels for each $Z_1 \longrightarrow B_i$ transition shows the magnetic splittings with $B \parallel D_1$, $B \parallel D_2$ and $B \parallel b$ respectively. The left panels of each transition show the experimental splittings, represented by the circles, and the theoretical splittings are represented by the red lines. The right panels of each transition show Zeeman absorption spectra at a magnetic field represented by the vertical line in the left panels. All spectra were measured at 4.2 K.

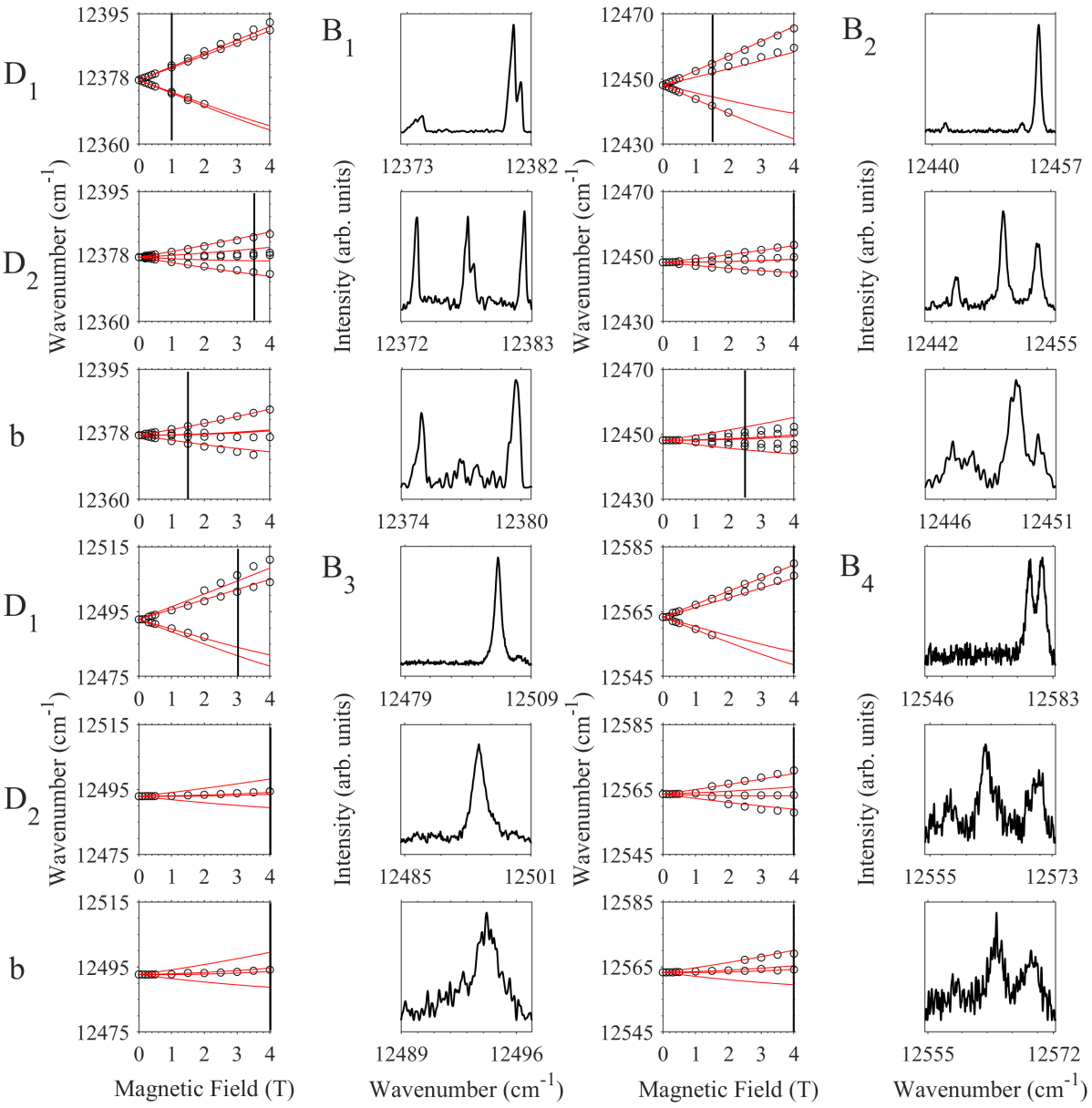

Figure 6.20: Magnetic splittings of the $^4I_{15/2}Z_1 \rightarrow {}^4I_{9/2}B_i$ transitions of site 2 in Y_2SiO_5:0.005%Er^{3+} with a magnetic field applied along the three crystallographic axes of Y_2SiO_5. The top, middle and bottom panels for each $Z_1 \longrightarrow B_i$ transition shows the magnetic splittings with $B \parallel D_1$, $B \parallel D_2$ and $B \parallel b$ respectively. The left panels of each transition show the experimental splittings, represented by the circles, and the theoretical splittings are represented by the red lines. The right panels of each transition show Zeeman absorption spectra at a magnetic field represented by the vertical line in the left panels. All spectra were measured at 4.2 K. Figure is continued over page.

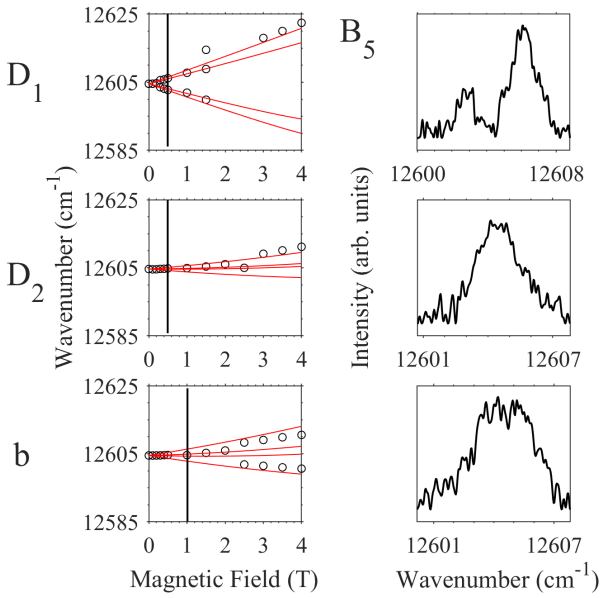

Figure 6.20: Magnetic splittings of the $^4I_{15/2}Z_1 \rightarrow {}^4I_{9/2}B_i$ transitions of site 2 in Y_2SiO_5:0.005%Er^{3+} with a magnetic field applied along the three crystallographic axes of Y_2SiO_5. The top, middle and bottom panels for each $Z_1 \longrightarrow B_i$ transition shows the magnetic splittings with $B \parallel D_1$, $B \parallel D_2$ and $B \parallel b$ respectively. The left panels of each transition show the experimental splittings, represented by the circles, and the theoretical splittings are represented by the red lines. The right panels of each transition show Zeeman absorption spectra at a magnetic field represented by the vertical line in the left panels. All spectra were measured at 4.2 K.

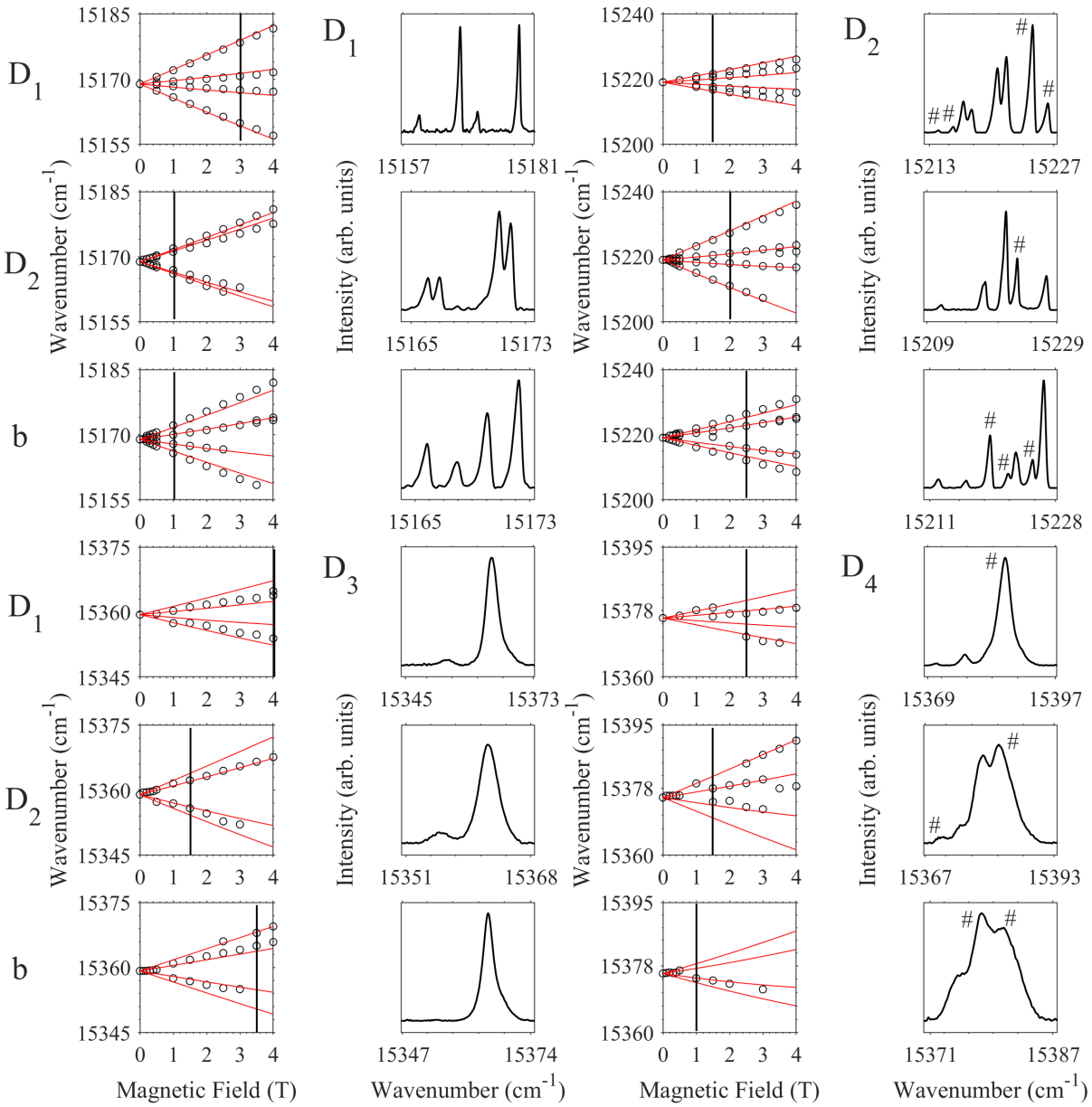

Figure 6.21: Magnetic splittings of the $^4I_{15/2}Z_1 \rightarrow {}^4F_{9/2}D_i$ transitions of site 1 in Y_2SiO_5:0.005%Er^{3+} with a magnetic field applied along the three crystallographic axes of Y_2SiO_5. The top, middle and bottom panels for each $Z_1 \longrightarrow D_i$ transition shows the magnetic splittings with $B \parallel D_1$, $B \parallel D_2$ and $B \parallel b$ respectively. The left panels of each transition show the experimental splittings, represented by the circles, and the theoretical splittings are represented by the red lines. The right panels of each transition show Zeeman absorption spectra at a magnetic field represented by the vertical line in the left panels. All spectra were measured at 4.2 K. Spectral features labelled with an '#' are transitions related to site 2. Figure is continued over page.

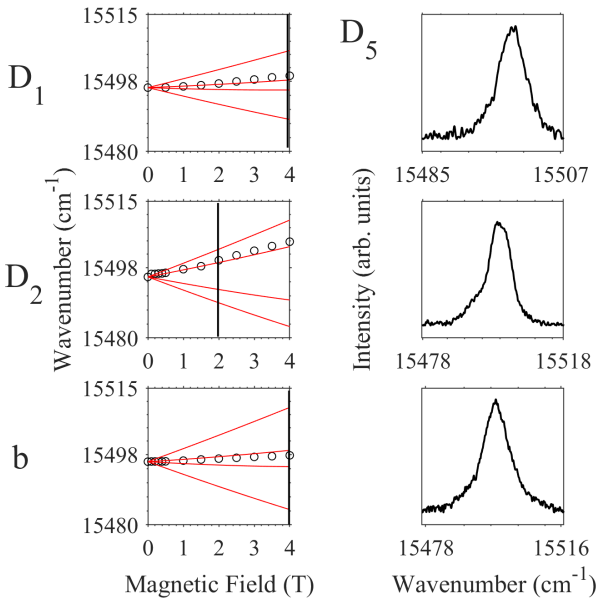

Figure 6.21: Magnetic splittings of the $^4I_{15/2}Z_1 \rightarrow {}^4F_{9/2}D_i$ transitions of site 1 in Y_2SiO_5:0.005%Er^{3+} with a magnetic field applied along the three crystallographic axes of Y_2SiO_5. The top, middle and bottom panels for each $Z_1 \longrightarrow D_i$ transition shows the magnetic splittings with $B \parallel D_1$, $B \parallel D_2$ and $B \parallel b$ respectively. The left panels of each transition show the experimental splittings, represented by the circles, and the theoretical splittings are represented by the red lines. The right panels of each transition show Zeeman absorption spectra at a magnetic field represented by the vertical line in the left panels. All spectra were measured at 4.2 K.

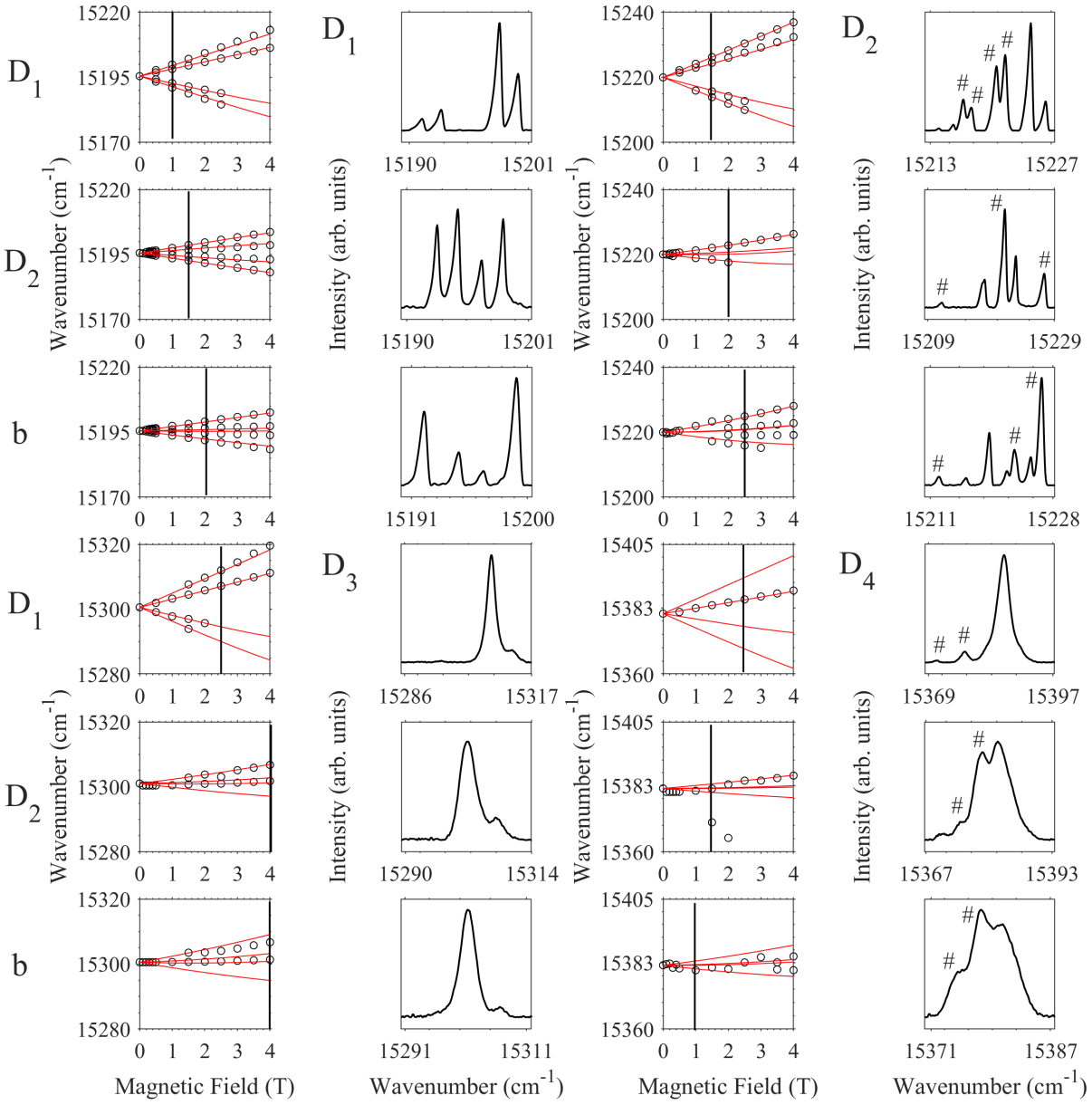

Figure 6.22: Magnetic splittings of the $^4I_{15/2}Z_1 \rightarrow {}^4F_{9/2}D_i$ transitions of site 2 in Y_2SiO_5:0.005%Er^{3+} with a magnetic field applied along the three crystallographic axes of Y_2SiO_5. The top, middle and bottom panels for each $Z_1 \longrightarrow D_i$ transition shows the magnetic splittings with $B \parallel D_1$, $B \parallel D_2$ and $B \parallel b$ respectively. The left panels of each transition show the experimental splittings, represented by the circles, and the theoretical splittings are represented by the red lines. The right panels of each transition show Zeeman absorption spectra at a magnetic field represented by the vertical line in the left panels. All spectra were measured at 4.2 K. Spectral features labelled with an '#' are transitions related to site 1. Figure is continued over page.

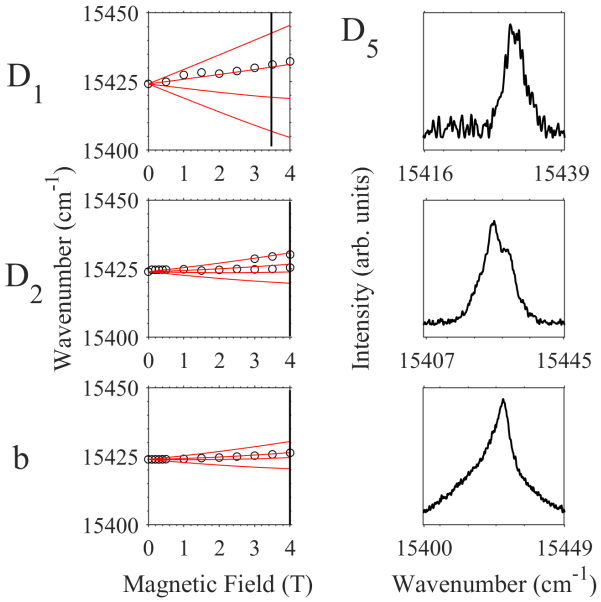

Figure 6.22: Magnetic splittings of the $^4I_{15/2}Z_1 \rightarrow {}^4F_{9/2}D_i$ transitions of site 2 in Y_2SiO_5:0.005%Er^{3+} with a magnetic field applied along the three crystallographic axes of Y_2SiO_5. The top, middle and bottom panels for each $Z_1 \longrightarrow D_i$ transition shows the magnetic splittings with $B \parallel D_1$, $B \parallel D_2$ and $B \parallel b$ respectively. The left panels of each transition show the experimental splittings, represented by the circles, and the theoretical splittings are represented by the red lines. The right panels of each transition show Zeeman absorption spectra at a magnetic field represented by the vertical line in the left panels. All spectra were measured at 4.2 K.

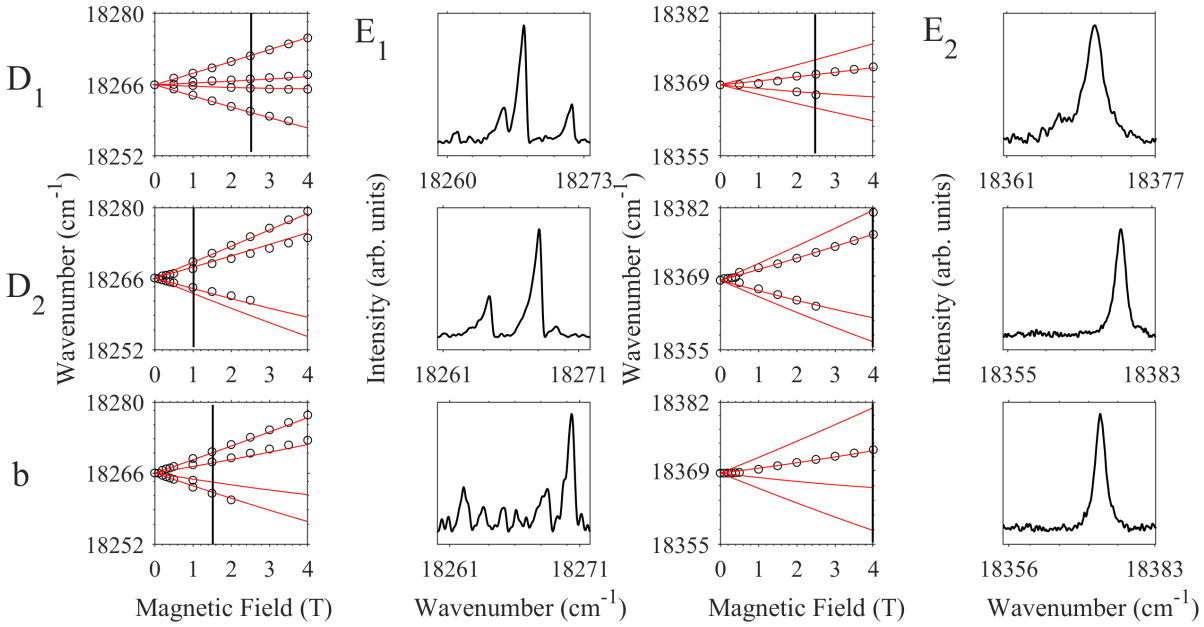

Figure 6.23: Magnetic splittings of the $^4I_{15/2}Z_1 \rightarrow {}^4S_{3/2}E_i$ transitions of site 1 in Y_2SiO_5:0.005%Er^{3+} with a magnetic field applied along the three crystallographic axes of Y_2SiO_5. The top, middle and bottom panels for each $Z_1 \longrightarrow E_i$ transition shows the magnetic splittings with $B \parallel D_1$, $B \parallel D_2$ and $B \parallel b$ respectively. The left panels of each transition show the experimental splittings, represented by the circles, and the theoretical splittings are represented by the red lines. The right panels of each transition show Zeeman absorption spectra at a magnetic field represented by the vertical line in the left panels. All spectra were measured at 4.2 K.

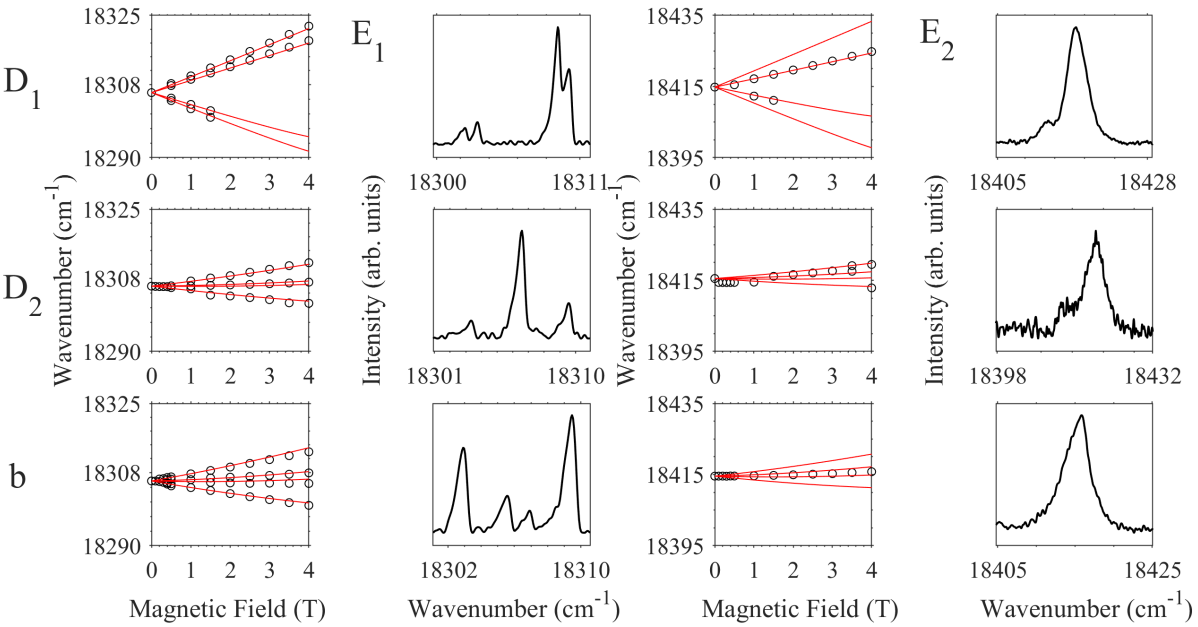

Figure 6.24: Magnetic splittings of the $^4I_{15/2}Z_1 \rightarrow {}^4S_{3/2}E_i$ transitions of site 2 in Y_2SiO_5:0.005%Er^{3+} with a magnetic field applied along the three crystallographic axes of Y_2SiO_5. The top, middle and bottom panels for each $Z_1 \longrightarrow E_i$ transition shows the magnetic splittings with $B \parallel D_1$, $B \parallel D_2$ and $B \parallel b$ respectively. The left panels of each transition show the experimental splittings, represented by the circles, and the theoretical splittings are represented by the red lines. The right panels of each transition show Zeeman absorption spectra at a magnetic field represented by the vertical line in the left panels. All spectra were measured at 4.2 K.

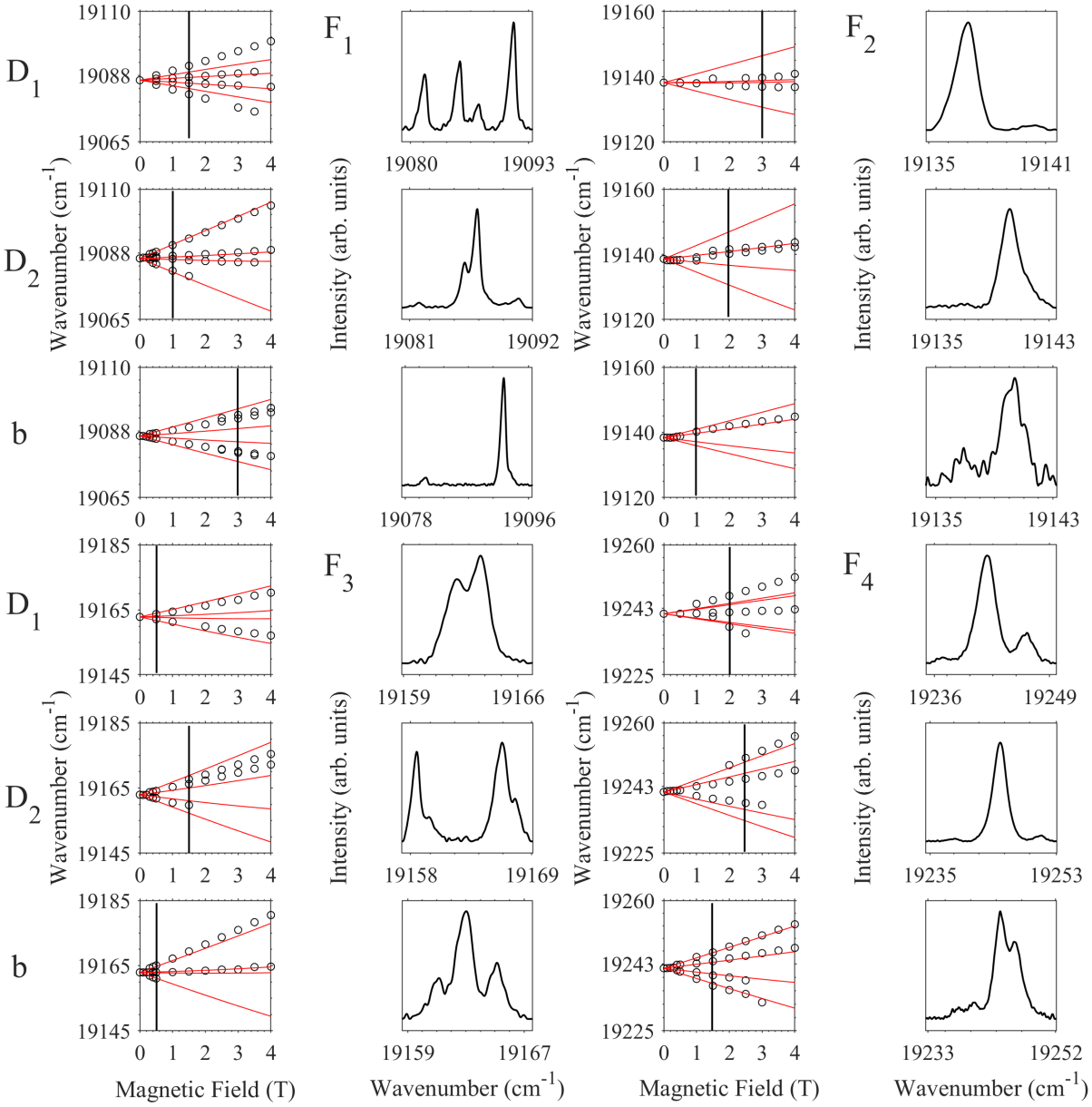

Figure 6.25: Magnetic splittings of the $^4I_{15/2}Z_1 \rightarrow {}^2H_{11/2}F_i$ transitions of site 1 in Y_2SiO_5:0.005%Er^{3+} with a magnetic field applied along the three crystallographic axes of Y_2SiO_5. The top, middle and bottom panels for each $Z_1 \longrightarrow F_i$ transition shows the magnetic splittings with $B \parallel D_1$, $B \parallel D_2$ and $B \parallel b$ respectively. The left panels of each transition show the experimental splittings, represented by the circles, and the theoretical splittings are represented by the red lines. The right panels of each transition show Zeeman absorption spectra at a magnetic field represented by the vertical line in the left panels. All spectra were measured at 4.2 K. Figure is continued over page.

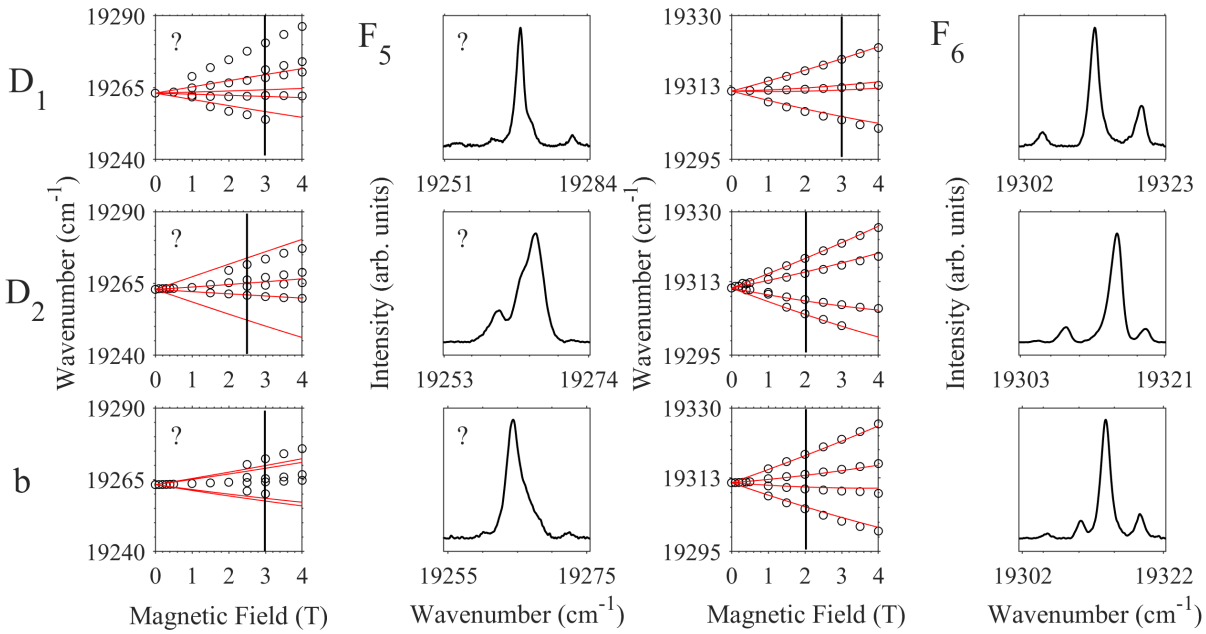

Figure 6.25: Magnetic splittings of the $^4I_{15/2}Z_1 \rightarrow {}^2H_{11/2}F_i$ transitions of site 1 in Y_2SiO_5:0.005%Er^{3+} with a magnetic field applied along the three crystallographic axes of Y_2SiO_5. The top, middle and bottom panels for each $Z_1 \longrightarrow F_i$ transition shows the magnetic splittings with $B \parallel D_1$, $B \parallel D_2$ and $B \parallel b$ respectively. The left panels of each transition show the experimental splittings, represented by the circles, and the theoretical splittings are represented by the red lines. The right panels of each transition show Zeeman absorption spectra at a magnetic field represented by the vertical line in the left panels. All spectra were measured at 4.2 K. The $^4I_{15/2}Z_1 \rightarrow {}^2H_{11/2}F_5$ transitions could not be assigned as belonging to either site.

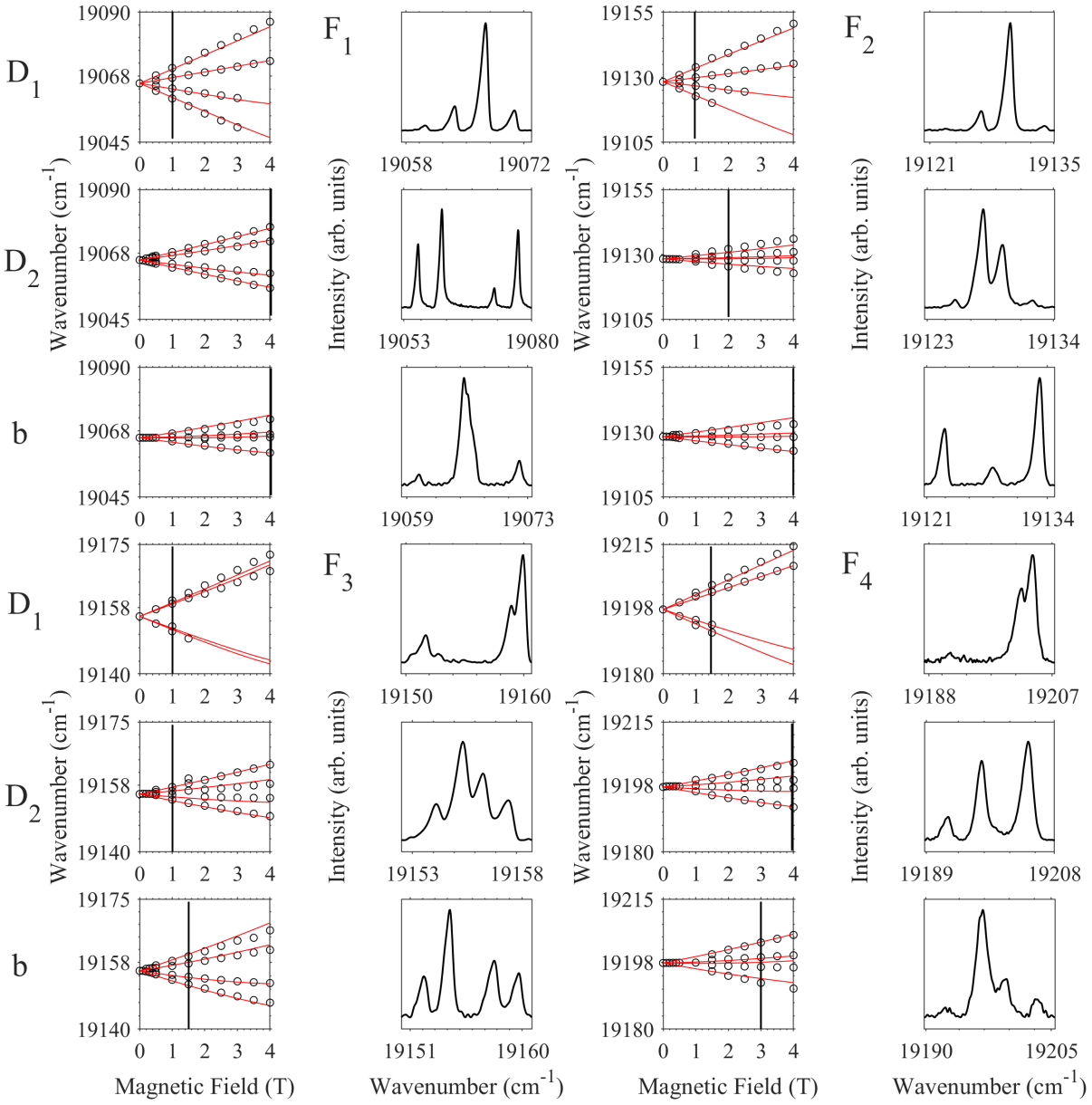

Figure 6.26: Magnetic splittings of the $^4I_{15/2}Z_1 \rightarrow {}^2H_{11/2}F_i$ transitions of site 2 in Y_2SiO_5:0.005%Er^{3+} with a magnetic field applied along the three crystallographic axes of Y_2SiO_5. The top, middle and bottom panels for each $Z_1 \longrightarrow F_i$ transition shows the magnetic splittings with $B \parallel D_1$, $B \parallel D_2$ and $B \parallel b$ respectively. The left panels of each transition show the experimental splittings, represented by the circles, and the theoretical splittings are represented by the red lines. The right panels of each transition show Zeeman absorption spectra at a magnetic field represented by the vertical line in the left panels. All spectra were measured at 4.2 K. Figure is continued over page.

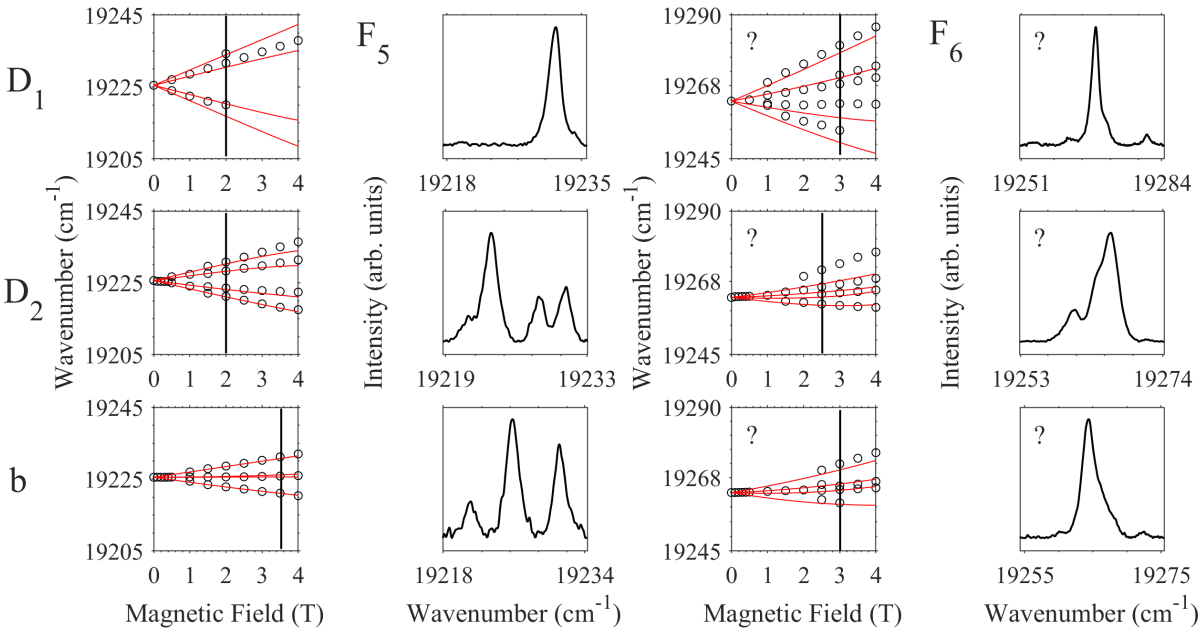

Figure 6.26: Magnetic splittings of the $^4I_{15/2}Z_1 \rightarrow {}^2H_{11/2}F_i$ transitions of site 2 in Y_2SiO_5:0.005%Er^{3+} with a magnetic field applied along the three crystallographic axes of Y_2SiO_5. The top, middle and bottom panels for each $Z_1 \longrightarrow F_i$ transition shows the magnetic splittings with $B \parallel D_1$, $B \parallel D_2$ and $B \parallel b$ respectively. The left panels of each transition show the experimental splittings, represented by the circles, and the theoretical splittings are represented by the red lines. The right panels of each transition show Zeeman absorption spectra at a magnetic field represented by the vertical line in the left panels. All spectra were measured at 4.2 K. The $^4I_{15/2}Z_1 \rightarrow {}^2H_{11/2}F_6$ transitions could not be assigned as belonging to either site.

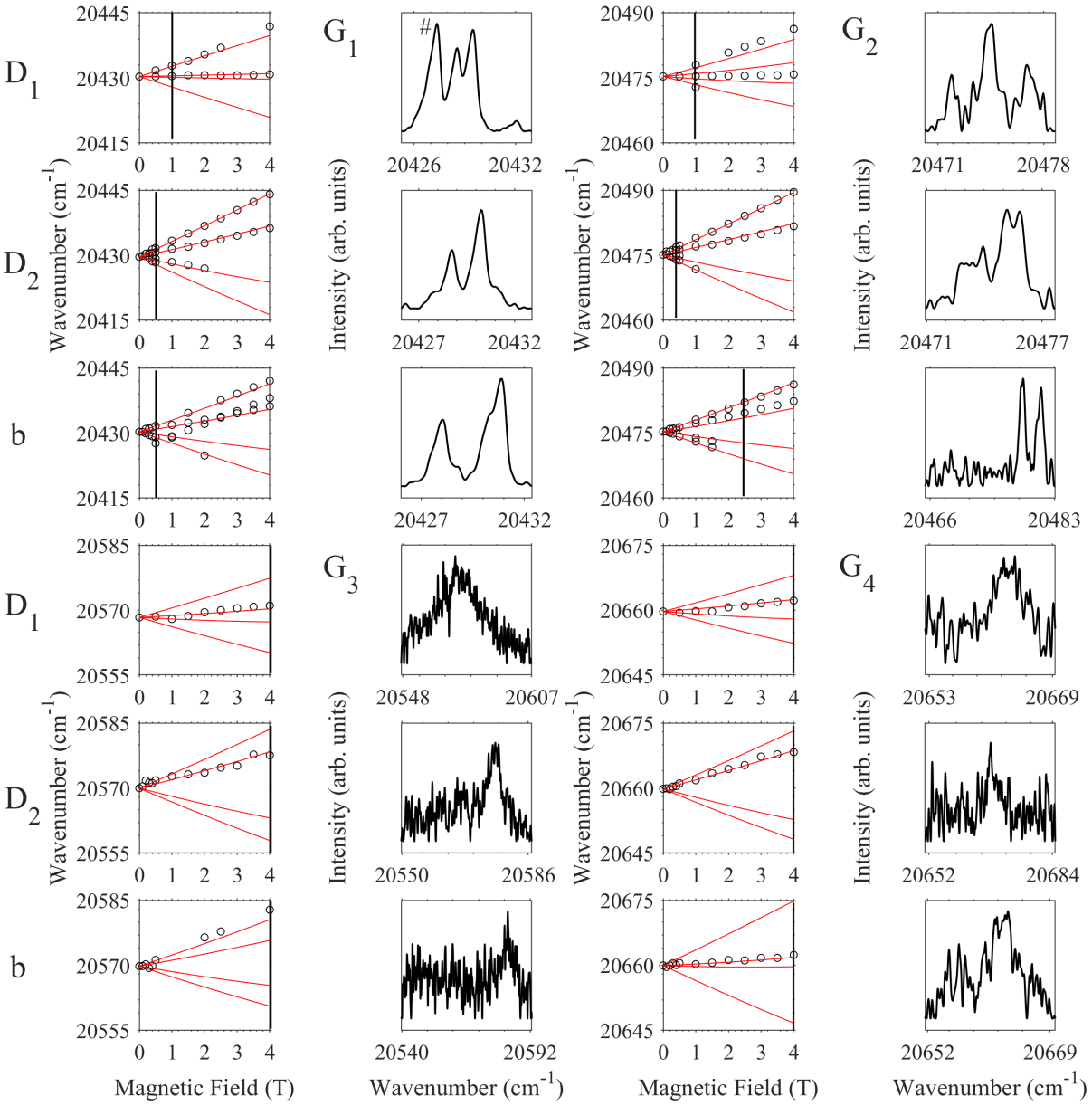

Figure 6.27: Magnetic splittings of the $^4I_{15/2}Z_1 \rightarrow {}^4F_{7/2}G_i$ transitions of site 1 in Y_2SiO_5:0.005%Er^{3+} with a magnetic field applied along the three crystallographic axes of Y_2SiO_5. The top, middle and bottom panels for each $Z_1 \longrightarrow G_i$ transition shows the magnetic splittings with $B \parallel D_1$, $B \parallel D_2$ and $B \parallel b$ respectively. The left panels of each transition show the experimental splittings, represented by the circles, and the theoretical splittings are represented by the red lines. The right panels of each transition show Zeeman absorption spectra at a magnetic field represented by the vertical line in the left panels. All spectra were measured at 4.2 K. Spectral features labelled with an '#' are transitions related to site 2.

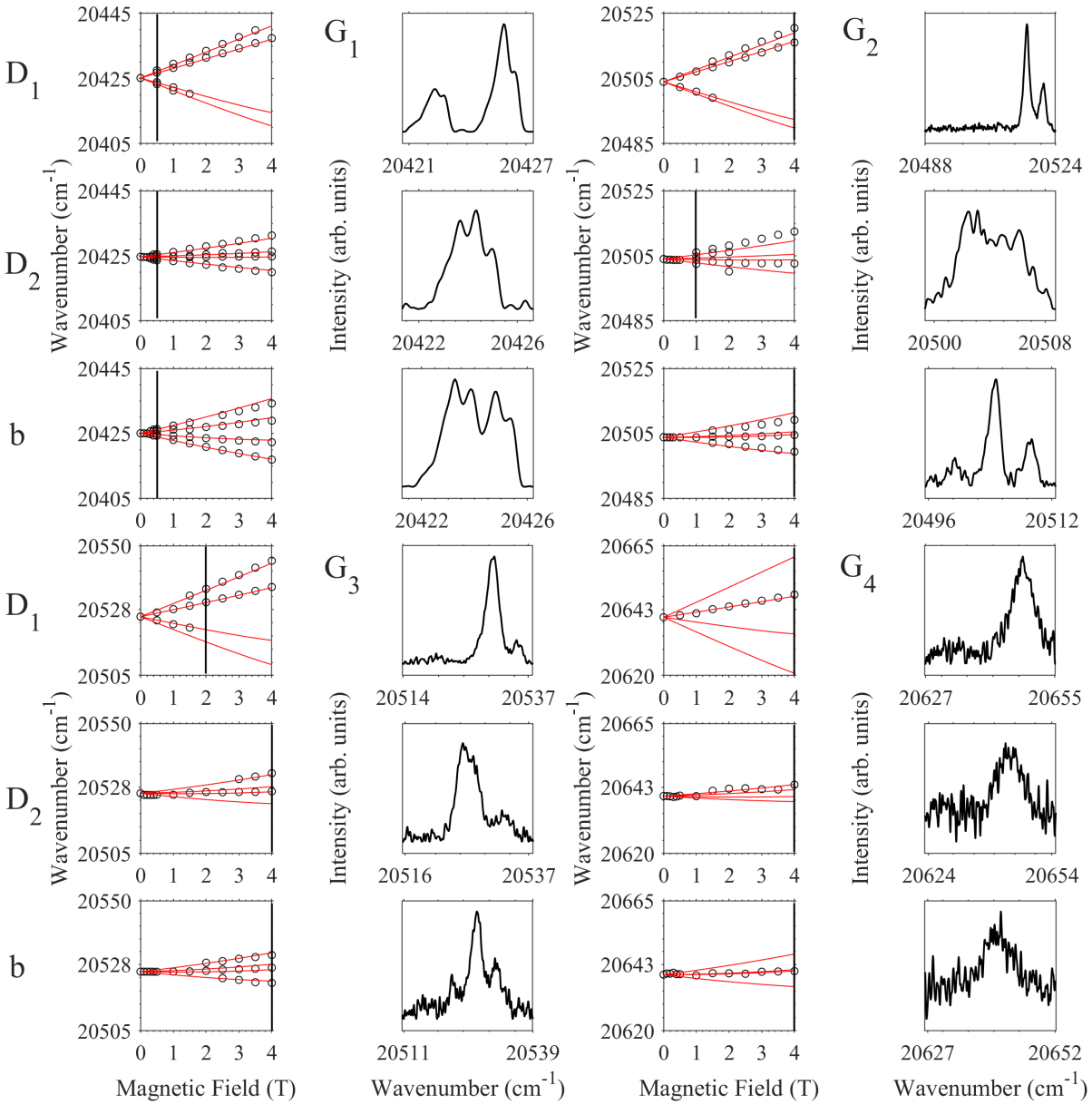

Figure 6.28: Magnetic splittings of the $^4I_{15/2}Z_1 \rightarrow {}^4F_{7/2}G_i$ transitions of site 2 in Y_2SiO_5:0.005%Er^{3+} with a magnetic field applied along the three crystallographic axes of Y_2SiO_5. The top, middle and bottom panels for each $Z_1 \longrightarrow G_i$ transition shows the magnetic splittings with $B \parallel D_1$, $B \parallel D_2$ and $B \parallel b$ respectively. The left panels of each transition show the experimental splittings, represented by the circles, and the theoretical splittings are represented by the red lines. The right panels of each transition show Zeeman absorption spectra at a magnetic field represented by the vertical line in the left panels. All spectra were measured at 4.2 K.

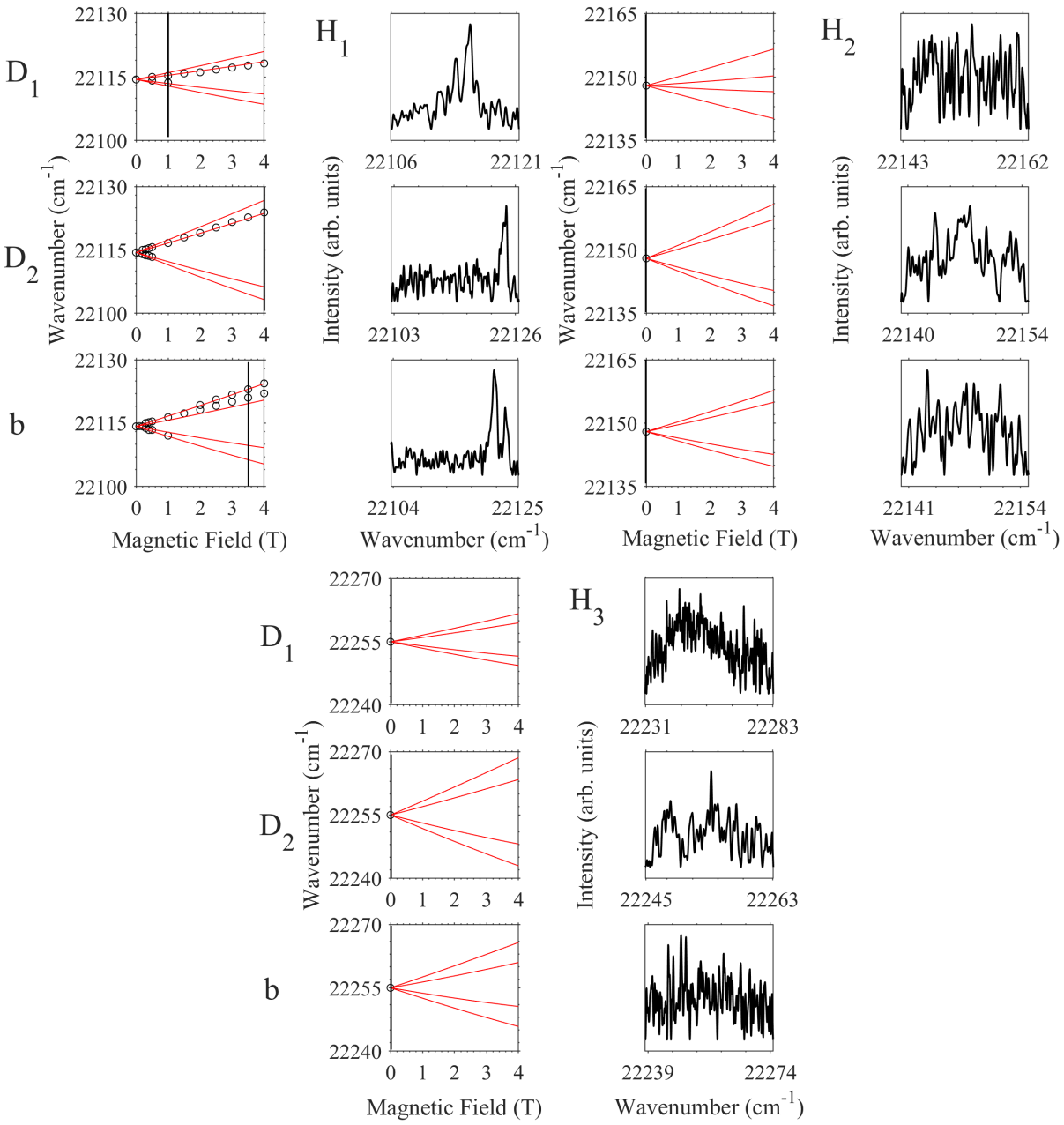

Figure 6.29: Magnetic splittings of the $^4I_{15/2}Z_1 \rightarrow {}^4F_{5/2}H_i$ transitions of site 1 in Y_2SiO_5:0.005%Er^{3+} with a magnetic field applied along the three crystallographic axes of Y_2SiO_5. The top, middle and bottom panels for each $Z_1 \longrightarrow H_i$ transition shows the magnetic splittings with $B \parallel D_1$, $B \parallel D_2$ and $B \parallel b$ respectively. The left panels of each transition show the experimental splittings, represented by the circles, and the theoretical splittings are represented by the red lines. The right panels of each transition show Zeeman absorption spectra at a magnetic field represented by the vertical line in the left panels. All spectra were measured at 4.2 K.

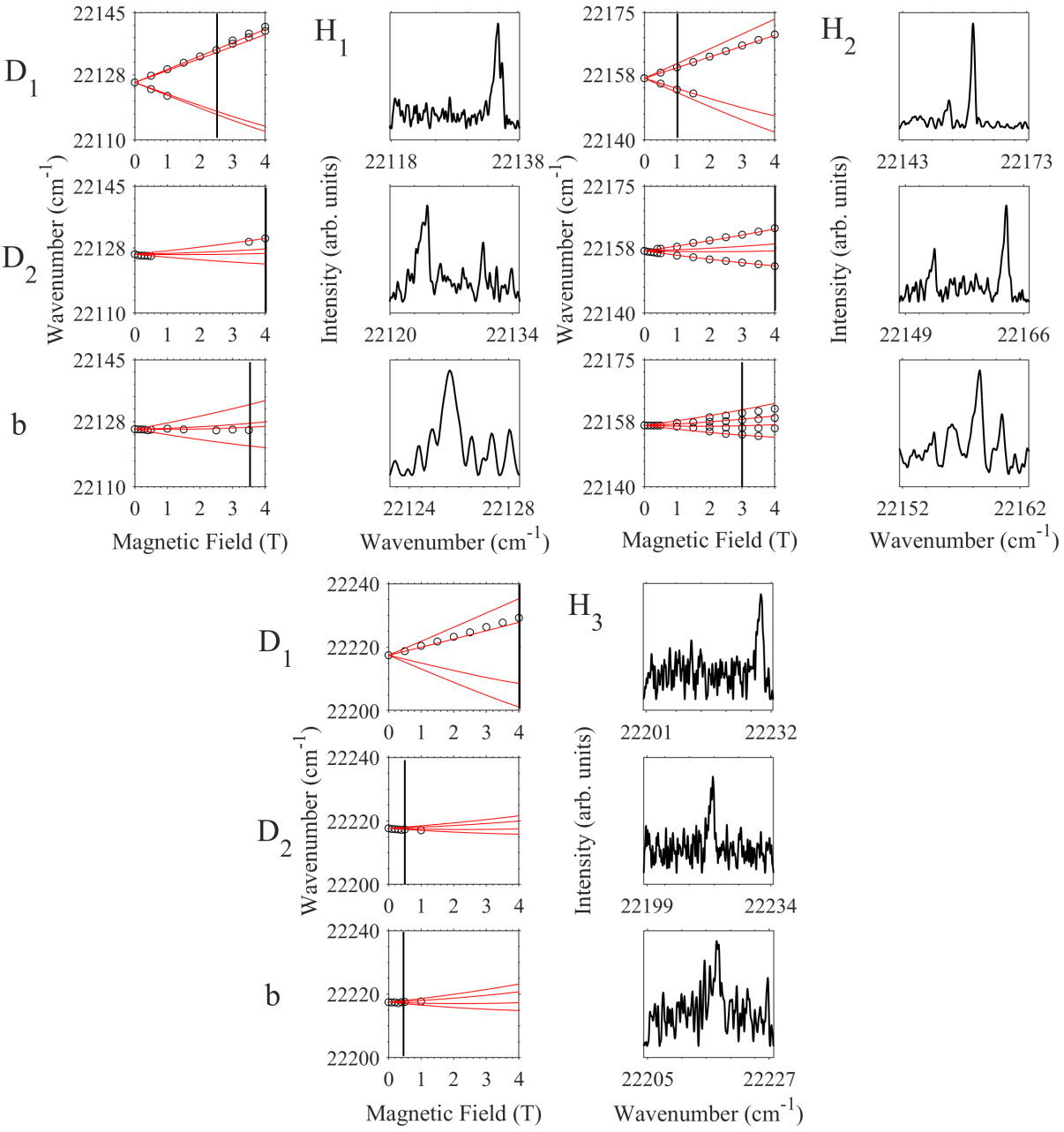

Figure 6.30: Magnetic splittings of the $^4I_{15/2}Z_1 \rightarrow {}^4F_{5/2}H_i$ transitions of site 2 in Y_2SiO_5:0.005%Er^{3+} with a magnetic field applied along the three crystallographic axes of Y_2SiO_5. The top, middle and bottom panels for each $Z_1 \longrightarrow H_i$ transition shows the magnetic splittings with $B \parallel D_1$, $B \parallel D_2$ and $B \parallel b$ respectively. The left panels of each transition show the experimental splittings, represented by the circles, and the theoretical splittings are represented by the red lines. The right panels of each transition show Zeeman absorption spectra at a magnetic field represented by the vertical line in the left panels. All spectra were measured at 4.2 K.

6.4 Crystal-field analysis

A crystal-field model was produced by fitting five free-ion parameters, 27 crystal-field parameters and two hyperfine parameters to experimental data. As multiple data sets were required to be diagonalised simultaneously, the hyperfine portion of the fit used an intermediate coupled effective Hamiltonian in a basis spanning only the $^4I_{15/2}$ and $^4I_{13/2}$ multiplets. This reduced the dimension of the hyperfine Hamiltonian from 2912 to 224 states, minimising the computational power required to perform the fit. The matrix elements of the Stark levels were truncated to 40 000 cm^{-1} to further increase performance. The initial crystal-field parameters in the optimisation routine were set to those found by Horvath *et al.* [55, 106]. The two- and three-body interactions and higher order effects in the free-ion Hamiltonian were held fixed to the values obtained by Carnall *et al.* for Er^{3+}:LnF_3 [49]. A coarse fit was performed using a basin-hopping algorithm and following this, a final fit was performed using simulated annealing. The details of the crystal-field fitting procedure and the algorithms used are summarised in Section 2.5. Table 6.1 shows the weightings used for the various parameters sets during the fitting process. These weightings were chosen to reflect the uncertainties in the relevant measurements.

For site 1 a total of 350 experimental data points were fitted simultaneously and are as follows:

- 55 electronic energy levels up to the $^4G_{11/2}$ multiplet at ∼26 500 cm^{-1} including the $^4I_{15/2}Z_5$ – Z_8 states determined by Doualan *et al.* [158].
- 68 g values (20 along the D_1 axis, 23 along the D_2 axis and 25 along the b axis) corresponding to various states up to the $^4F_{5/2}$ multiplet at ∼20 500 cm^{-1}.
- 180 data points for the hyperfine splittings of the $^4I_{15/2}Z_1$ state, calculated from the **g**, **A** and **Q** tensors determined by Chen *et al.* [62]. The energy of each hyperfine state besides the ground state (which was set as zero) was sampled at equally spaced intervals according to Equation (4.8), with $B_0 = 0.05$ T.
- 12 data points for the magnetic splittings of the $^4I_{13/2}Y_1$ state, calculated from the **g** tensor determined by Sun *et al.* [110], also sampled at equally spaced intervals according to Equation (4.8), with $B_0 = 0.05$ T.
- 4 data points from low-frequency Raman heterodyne measurements, calculated from a three dimensional curvature tensor of transition energy with respect to a magnetic field, obtained from [55]. The four data points were sampled at magnetic fields of [0 0 0], [0.5 0 0], [0 0.5 0], [0 0 0.5] (with axes [D_1, D_2, b] and units of mT).
- 31 data points of high frequency Raman heterodyne spectroscopy along the D_2 direction as determined in [55]. Second order polynomials were fitted and sampled at magnetic fields strengths of 0.0, 0.3 and 0.5 mT. Nine transitions were fitted using this method whereas four of the transitions have a very steep gradient around zero field and therefore were only sampled at 0.5 mT.

To date, no studies have observed the hyperfine structure of the $^4I_{13/2}Y_1$ state of site 2 in Er^{3+}:Y_2SiO_5 and therefore a lesser amount of 319 experimental data points were fitted simultaneously and are as follows:

- 57 electronic energy levels up to the $^4G_{11/2}$ multiplet at ∼26 500 cm^{-1} including the $^4I_{15/2}Z_5$ – Z_8 states determined by Doualan *et al.* [158].
- 70 g values (25 along the D_1 axis, 24 along the D_2 axis and 21 along the b axis) corresponding to various states up to the $^4F_{5/2}$ multiplet at ∼20 500 cm^{-1}.
- 180 data points for the magnetic-hyperfine splittings of the $^4I_{15/2}Z_1$ state, calculated from the **g**, **A** and **Q** tensors determined by Chen *et al.* [62]. The energy of each hyperfine state besides the ground state (which was set as zero) was sampled at equally spaced intervals according to Equation (4.8), with $B_0 = 0.05$ T.
- 12 data points for the magnetic splittings of the $^4I_{13/2}Y_1$ state, calculated from the **g** tensor determined by Sun *et al.* [110], also sampled at equally spaced intervals according to Equation (4.8), with $B_0 = 0.05$ T.

Table 6.1: Weightings used for different parameter sets during the fitting process for both sites in Er^{3+}:Y_2SiO_5.

Data set	Weighting
Electronic levels	1
g values	1×10^4
$^4I_{15/2}Z_1$ **g**, **A** and **Q** tensors	1×10^5
$^4I_{13/2}Y_1$ **g** tensors	1×10^5
Raman heterodyne data	1×10^6

The theoretical energy levels and g values up to the $^4G_{11/2}$ multiplet of Er^{3+}:Y_2SiO_5 were estimated using the fitted crystal field parameters for site 1 and site 2 and are given in Tables 6.2 and 6.3 respectively along with the determined experimental energy levels and g values. We see that the standard deviation between theoretical and experimental electronic energy levels found in this study are comparable to previous studies, 16 cm^{-1} compared to 17 cm^{-1} [55] and 14 cm^{-1} [106] for site 1 and 13 cm^{-1} compared to 9 cm^{-1} [106] for site 2. Furthermore, we see that our study also accurately predicts the magnetic structure across the entire $4f^{11}$ configuration of Er^{3+}:Y_2SiO_5 with the experimentally determined g values matching closely with the g values theoretically determined from our crystal-field model.

Table 6.2: Theoretical and experimental electronic energy levels and g values up to 27 000 cm^{-1} for site 1 in Er^{3+}:Y_2SiO_5. The theoretical electronic energies and g values were calculated using the determined crystal-field Hamiltonian. All energies are in cm^{-1}. Levels marked with a '–' were not assigned. Levels marked with an '*' are assignments made by Doualan *et al.* [158]. The experimentally determined energy levels have an associated uncertainty of 1 cm^{-1}.

		Energies			g values					
					D_1 axis		D_2 axis		b axis	
Multiplet	State	Theory	Exp.	Diff.	Theory	Exp.	Theory	Exp.	Theory	Exp.
$^4I_{15/2}$	Z_1	-10	0	10	5.47	5.46	11.06	10.91	8.18	8.36
	Z_2	39	39	0	6.67	–	1.50	–	8.19	–
	Z_3	72	84	12	3.98	–	7.07	–	2.35	–
	Z_4	111	102	−9	3.93	–	9.34	–	4.23	–
	Z_5	179	172*	−7	4.08	–	8.58	–	7.35	–
	Z_6	416	424*	8	10.22	–	7.62	–	3.68	–
	Z_7	474	481*	7	10.79	–	7.14	–	4.42	–
	Z_8	509	513*	4	8.30	–	12.08	–	6.50	–
$^4I_{13/2}$	Y_1	6518	6508	−10	3.93	4.64	6.82	6.90	10.24	10.00
	Y_2	6564	6549	−15	5.93	4.24	4.35	4.41	5.69	7.77
	Y_3	6599	6598	−1	6.59	4.54	4.73	3.04	2.56	6.10
	Y_4	6637	6624	−13	3.43	9.32	6.29	5.44	5.97	1.87
	Y_5	6805	6800	−5	8.47	–	6.16	–	2.43	–
	Y_6	6866	6852	−14	9.13	–	5.57	–	4.56	–
	Y_7	6887	6871	−16	7.32	–	9.66	–	5.23	–
$^4I_{11/2}$	A_1	10189	10197	8	3.30	3.89	3.67	4.80	8.75	8.23
	A_2	10231	10237	6	4.43	3.31	3.15	–	4.04	5.99
	A_3	10258	10275	17	4.76	5.41	2.84	4.00	4.27	3.30
	A_4	10345	10347	2	6.58	3.51	4.44	–	1.82	–
	A_5	10386	10375	−11	6.87	5.33	4.13	5.31	3.73	–
	A_6	10396	10389	−7	5.65	7.28	7.11	6.21	3.79	1.66
$^4I_{9/2}$	B_1	12337	12362	25	4.39	3.75	3.16	3.68	1.64	1.87
	B_2	12430	12461	31	1.99	–	1.40	2.10	5.51	4.03
	B_3	12532	12529	−3	1.61	–	3.08	2.01	3.27	3.73
	B_4	12606	12613	7	2.60	–	3.47	–	1.55	1.65
	B_5	12656	12651	−5	3.31	3.66	3.27	1.98	2.26	2.44
$^4F_{9/2}$	D_1	15185	15170	−15	8.60	7.86	0.68	1.76	3.42	4.61
	D_2	15236	15220	−16	2.68	1.39	7.51	6.84	2.05	3.21
	D_3	15360	15360	0	2.54	0.54	2.66	–	2.72	2.30
	D_4	15402	15377	−25	2.41	–	4.90	–	2.67	–
	D_5	15493	15497	4	4.04	–	3.64	–	5.88	–

Continued over page.

		Energies			g values					
					D_1 axis		D_2 axis		b axis	
Multiplet	State	Theory	Exp.	Diff.	Theory	Exp.	Theory	Exp.	Theory	Exp.
$^4S_{3/2}$	E_1	18272	18267	−5	4.13	3.64	2.03	3.00	2.84	2.77
	E_2	18359	18369	10	2.43	–	2.44	2.24	4.37	–
$^2H_{11/2}$	F_1	19115	19087	−28	2.66	8.47	9.21	7.93	4.89	0.89
	F_2	19152	19139	−13	5.97	–	6.51	–	2.62	–
	F_3	19177	19164	−13	4.12	–	5.45	2.08	7.23	10.36
	F_4	19242	19242	0	0.38	–	2.60	4.72	3.67	3.79
	F_5	19277	19264	−13	3.88	–	7.64	–	0.68	–
	F_6	19302	19312	10	4.64	4.93	3.52	4.80	5.15	5.20
$^4F_{7/2}$	G_1	20424	20430	6	4.77	5.91	3.99	3.92	3.16	3.25
	G_2	20468	20475	7	2.91	–	3.84	4.58	3.16	1.90
	G_3	20557	20570	13	3.79	–	2.79	–	2.56	–
	G_4	20633	20660	27	3.00	–	2.43	–	6.97	–
$^4F_{5/2}$	H_1	22099	22115	16	1.29	–	1.64	–	2.08	1.18
	H_2	22130	22148	18	3.40	–	1.96	–	1.51	–
	H_3	22217	22255	38	1.18	–	2.76	–	2.54	–
$^4F_{3/2}$	I_1	22470	–	–	1.90	–	1.08	–	0.72	–
	I_2	22601	–	–	0.80	–	0.85	–	1.36	–
$^2H_{9/2}$	K_1	24403	24423	20	5.70	–	3.49	–	2.49	–
	K_2	24515	24534	19	2.18	–	1.79	–	5.53	–
	K_3	24594	24618	24	2.08	–	2.41	–	4.51	–
	K_4	24639	–	–	2.18	–	3.77	–	3.69	–
	K_5	24686	–	–	3.88	–	3.78	–	2.66	–
$^4G_{11/2}$	L_1	26207	26159	−48	4.51	–	8.68	–	5.03	–
	L_2	26223	26202	−21	6.93	–	5.44	–	4.47	–
	L_3	26322	26304	−18	4.74	–	3.95	–	2.72	–
	L_4	26469	26477	8	1.88	–	3.85	–	4.04	–
	L_5	26514	26497	−17	4.58	–	6.93	–	1.13	–
	L_6	26577	26571	−6	3.82	–	5.95	–	3.43	–

Table 6.3: Theoretical and experimental electronic energy levels and g values up to 27 000 cm^{-1} for site 2 in Er^{3+}:Y_2SiO_5. The theoretical electronic energies and g values were calculated using the determined crystal-field Hamiltonian. All energies are in cm^{-1}. Levels marked with a '–' were not assigned. Levels marked with an '*' are assignments made by Doualan *et al.* [158]. The experimentally determined energy levels have an associated uncertainty of 1 cm^{-1}.

		Energies			g values					
					D_1 axis		D_2 axis		b axis	
Multiplet	State	Theory	Exp.	Diff.	Theory	Exp.	Theory	Exp.	Theory	Exp.
$^4I_{15/2}$	Z_1	-1	0	1	14.65	15.31	2.21	2.66	3.13	2.84
	Z_2	29	27	−2	8.58	–	5.27	–	4.93	–
	Z_3	66	62	−4	3.07	–	6.40	–	6.95	–
	Z_4	129	126	−3	5.21	–	11.48	–	4.50	–
	Z_5	170	169*	−1	6.52	–	4.03	–	6.98	–
	Z_6	313	314*	1	3.71	–	7.17	–	7.18	–
	Z_7	347	350*	3	6.57	–	11.73	–	3.72	–
	Z_8	408	415*	7	5.18	–	4.11	–	13.96	–
$^4I_{13/2}$	Y_1	6515	6498	−17	12.37	13.14	0.70	0.46	5.01	4.93
	Y_2	6570	6565	−5	7.82	8.23	3.61	2.16	2.46	5.45
	Y_3	6596	6594	−2	3.36	2.61	9.33	10.75	4.04	2.63
	Y_4	6637	6622	−15	5.73	6.04	3.35	4.75	5.72	4.36
	Y_5	6733	6726	−7	3.15	–	4.85	–	7.24	–
	Y_6	6767	6752	−15	6.11	–	10.58	10.88	3.04	–
	Y_7	6813	6800	−13	3.88	–	3.60	–	11.37	–
$^4I_{11/2}$	A_1	10176	10184	8	9.60	10.04	0.30	–	4.07	–
	A_2	10223	10237	14	5.82	6.71	3.80	5.19	2.81	3.92
	A_3	10243	10254	11	3.36	3.06	2.66	5.44	5.02	–
	A_4	10296	10297	1	2.80	3.91	3.78	3.05	4.71	3.71
	A_5	10317	10314	−3	4.34	5.53	8.12	5.95	1.49	–
	A_6	10347	10347	0	2.74	1.14	2.88	4.42	8.95	9.35
$^4I_{9/2}$	B_1	12357	12378	21	0.62	1.17	4.17	3.08	3.00	4.02
	B_2	12424	12449	25	4.23	3.23	2.24	2.05	2.87	1.05
	B_3	12471	12494	23	1.85	3.54	2.52	–	2.61	–
	B_4	12542	12564	22	2.18	2.00	3.67	3.63	2.54	3.53
	B_5	12599	12605	6	2.27	–	1.76	–	4.39	–
$^4F_{9/2}$	D_1	15211	15196	−15	2.79	3.72	6.26	5.83	3.89	5.02
	D_2	15234	15221	−13	2.90	2.40	3.00	–	3.35	5.20
	D_3	15309	15302	−7	3.90	4.41	3.03	4.11	4.44	3.73
	D_4	15390	15382	−8	6.66	–	1.99	–	2.68	–
	D_5	15437	15425	−12	7.66	–	3.76	–	2.17	–

Continued over page.

		Energies			g values					
					D_1 axis		D_2 axis		b axis	
Multiplet	State	Theory	Exp.	Diff.	Theory	Exp.	Theory	Exp.	Theory	Exp.
$^4S_{3/2}$	E_1	18307	18306	−1	1.91	1.83	2.66	2.99	4.14	7.22
	E_2	18405	18415	10	4.77	–	1.30	–	1.91	–
$^2H_{11/2}$	F_1	19093	19067	−26	6.29	7.39	8.74	8.77	3.89	3.42
	F_2	19143	19129	−14	7.92	8.47	2.68	4.57	3.91	2.75
	F_3	19166	19157	−9	0.76	2.36	5.58	4.72	8.98	8.04
	F_4	19203	19199	−4	2.24	2.16	4.47	3.97	3.89	4.41
	F_5	19242	19226	−16	3.65	–	7.81	8.00	3.04	–
	F_6	19255	19264	9	5.70	–	3.82	–	4.86	–
$^4F_{7/2}$	G_1	20421	20424	3	2.19	2.74	3.08	3.57	6.85	6.47
	G_2	20489	20504	15	1.44	–	3.16	5.01	3.61	–
	G_3	20519	20526	7	4.55	–	3.22	–	2.11	–
	G_4	20623	20640	17	7.30	–	0.95	–	2.90	–
$^4F_{5/2}$	H_1	22109	22126	17	0.76	0.62	1.55	–	3.79	–
	H_2	22146	22157	11	2.39	–	3.24	–	1.85	1.35
	H_3	22196	22218	22	3.98	–	0.89	–	1.31	–
$^4F_{3/2}$	I_1	22454	–	–	0.74	–	1.36	–	1.59	–
	I_2	22584	–	–	1.54	–	0.22	–	0.71	–
$^2H_{9/2}$	K_1	24442	24464	22	1.40	–	5.75	–	3.23	–
	K_2	24513	24522	9	3.28	–	3.05	–	3.11	–
	K_3	24556	24557	1	3.42	–	2.73	–	3.28	–
	K_4	24605	24587	−18	1.99	–	4.23	–	3.14	–
	K_5	24657	24649	−8	3.22	–	3.62	–	3.87	–
$^4G_{11/2}$	L_1	26251	26225	−26	6.43	–	9.77	–	3.78	–
	L_2	26278	26271	−7	5.74	–	2.34	–	8.61	–
	L_3	26335	26331	−4	3.36	–	2.77	–	5.10	–
	L_4	26435	26438	3	3.29	–	4.59	–	3.57	–
	L_5	26485	26465	−20	3.46	–	8.73	–	2.76	–
	L_6	26519	26525	6	6.70	–	4.91	–	2.70	–

Tables 6.4 and 6.5 shows the fitted free-ion, crystal-field and hyperfine parameters for site 1 and site 2 respectively in Er^{3+}:Y_2SiO_5. Also added for comparison are the values obtained by Horvath *et al.* [55, 106]. The two- and three-body interactions and higher order effects in the free-ion Hamiltonian were held fixed to the values obtained by Carnall *et al.* in Er^{3+}:LaF_3 for all crystal-field models and are given in Table 6.6 [49]. The uncertainties of the fitted parameters were estimated through the use of the MCMC techniques in order to sample the posterior probability distribution [128]. A total of 3 000 000 trials were undertaken for both sites with 343 158 accepted steps for site 1 and 278 705 accepted steps for site 2. This aligns with the Metropolis algorithms ∼10 % acceptance rate recommended for this technique which was fine tuned through

altering the step size in the optimisation routine [128]. Of the accepted steps, the last 30 000 steps were used to allow the algorithm to 'burn in'. Every 10^{th} element was then selected from the remaining points to ensure that the samples were not correlated. As discussed in Section 2.3.2, the odd-q B_q^k parameters are free to swap signs while leaving the eigenvalues unchanged. Therefore, the odd-q B_q^k parameters found for site 2 have had their signs swapped in order to reflect the signs of the 2^{nd} rank crystal-field parameters of Horvath [106].

Table 6.4: Fitted values for the free-ion, crystal-field and hyperfine parameters and their related uncertainties of site 1 in Er^{3+}:Y_2SiO_5. All values are in cm^{-1}. Parameters determined by Horvath *et al.* are also included for comparison [55, 106].

Parameter	This study	Uncertainty	Horvath et al. [55]	Horvath [106]
E_{avg}	35491.3	0.1	35503.5	–
F^2	95805.7	1.0	96029.6	95346
F^4	67869.7	3.4	67670.6	68525
F^6	53148.2	2.5	53167.1	52804
ζ	2360.5	0.1	2362.9	2358
B_0^2	-479.6	6.1	-149.8	-563
B_1^2	$471.4 + 143.8i$	$2.9 + 3.0i$	$420.6 + 396.0i$	$558 + 280i$
B_2^2	$125.5 - 2.0i$	$2.8 + 2.3i$	$-228.5 + 27.6i$	$143 - 121i$
B_0^4	-640.6	31.3	1131.2	-125
B_1^4	$288.8 + 924.1i$	$7.2 + 25.3i$	$985.7 + 34.2i$	$225 - 831i$
B_2^4	$-273.9 + 320.9i$	$11.1 + 16.7i$	$296.8 + 145.0i$	$-48 - 945i$
B_3^4	$-873.7 - 367.8i$	$20.7 + 9.7i$	$-402.3 - 381.7i$	$-615 - 688i$
B_4^4	$-600.8 + 1210.5i$	$23.7 + 9.2i$	$-282.3 + 1114.3i$	$744 - 102i$
B_0^6	145.7	13.2	-263.2	-28
B_1^6	$-105.9 - 329.0i$	$2.9 + 4.0i$	$111.9 + 222.9i$	$49 + 199i$
B_2^6	$-119.9 + 164.1i$	$7.7 + 8.8i$	$124.7 + 195.9i$	$120 - 107i$
B_3^6	$1.1 + 133.3i$	$6.7 + 4.5i$	$-97.9 + 139.7i$	$195 - 55i$
B_4^6	$-84.6 + 36.9i$	$5.0 + 4.5i$	$-93.7 - 145.0i$	$-287 - 161i$
B_5^6	$75.5 + 6.9i$	$4.3 + 6.6i$	$13.9 + 109.5i$	$-117 + 162i$
B_6^6	$-48.5 + 118.0i$	$6.2 + 4.2i$	$3.0 - 108.6i$	$136 + 186i$
a_l	0.005306	0.000008	0.005466	0.0059
a_Q	0.0554	0.0020	0.0716	0.0800

Table 6.5: Fitted values for the free-ion, crystal-field and hyperfine parameters and their related uncertainties of site 2 in Er^{3+}:Y_2SiO_5. All values are in cm^{-1}. Parameters determined by Horvath are also included for comparison [106].

Parameter	This study	Uncertainty	Horvath [106]
E_{avg}	35507.5	0.1	–
F^2	96121.9	1.3	95721
F^4	67722.4	4.5	68564
F^6	53241.2	3.1	52999
ζ	2362.3	0.1	2356
B_0^2	389.0	3.7	354
B_1^2	$325.7 + 95.8i$	$2.7 + 3.0i$	$498.6807 + 274i$
B_2^2	$-368.5 + 53.7i$	$1.8 + 2.0i$	$-75.8028 + 60i$
B_0^4	17.2	15.5	226
B_1^4	$378.7 + 519.5i$	$5.1 + 9.3i$	$-657.8381 + 593i$
B_2^4	$-72.0 - 146.0i$	$5.7 + 6.7i$	$335.7827 + 253i$
B_3^4	$890.8 - 570.4i$	$9.5 + 7.3i$	$-71.3262 - 46i$
B_4^4	$-198.7 - 567.9i$	$7.8 + 5.2i$	$-813.9654 + 64i$
B_0^6	73.4	4.3	219
B_1^6	$37.5 - 49.9i$	$3.4 + 5.7i$	$-127 + 197i$
B_2^6	$135.5 + 60.6i$	$4.5 + 1.5i$	$-36 - 47i$
B_3^6	$166.7 - 131.8i$	$2.6 + 4.0i$	$17 - 108i$
B_4^6	$227.2 + 47.6i$	$1.2 + 3.0i$	$-100 + 77i$
B_5^6	$-119.5 - 64.3i$	$3.7 + 3.2i$	$-263 + 103i$
B_6^6	$37.6 - 41.3i$	$3.5 + 2.8i$	$12 - 26i$
a_l	0.005389	0.000012	0.0069
a_Q	0.0240	0.0024	0.0808

Table 6.6: Free-ion parameters that were held fixed during the fitting process and were set to those found by Carnall *et al.* in Er^{3+}:LaF_3 [49].

Parameter	Value (cm^{-1})
α	17.79
β	−582.10
γ	1800.00
T^2	400.00
T^3	43.00
T^4	73.00
T^6	−271.00
T^7	308.00
T^8	299.00
M^{tot}	3.86
P^{tot}	594.00

Figures 6.31 and 6.32 shows the variation of the fitted free-ion, crystal field and hyperfine parameters for site 1 and site 2 respectively once the algorithm was allowed to 'burn in'. The standard deviation of this variation was used as the parameters uncertainties. The first panel of both figures depicts the χ^2 value of the model as a function of accepted step. The model converges very well for both sites, as seen by the 'flatness' of the χ^2 panel after ∼300 000 accepted steps, with the final χ^2 values being 15 602 for site 1 and 9823 for site 2. These values are larger than those determined in Section 4.5 for Sm^{3+}:Y_2SiO_5 due to the larger data set fitted simultaneously for Er^{3+}:Y_2SiO_5. It should be noted that a few of the crystal-field parameters converges to a value on the very edge of the given distribution. A possible explanation for this behaviour is that these parameters vary within an asymmetric region of a minimum, with the minimum being located close to the region wall. Like Sm^{3+}:Y_2SiO_5, some free-ion and hyperfine parameters were found to converge to be composed of multiple distributions which is further evidence of the complex parameter space that is present in the C_1 symmetry environment of Y_2SiO_5.

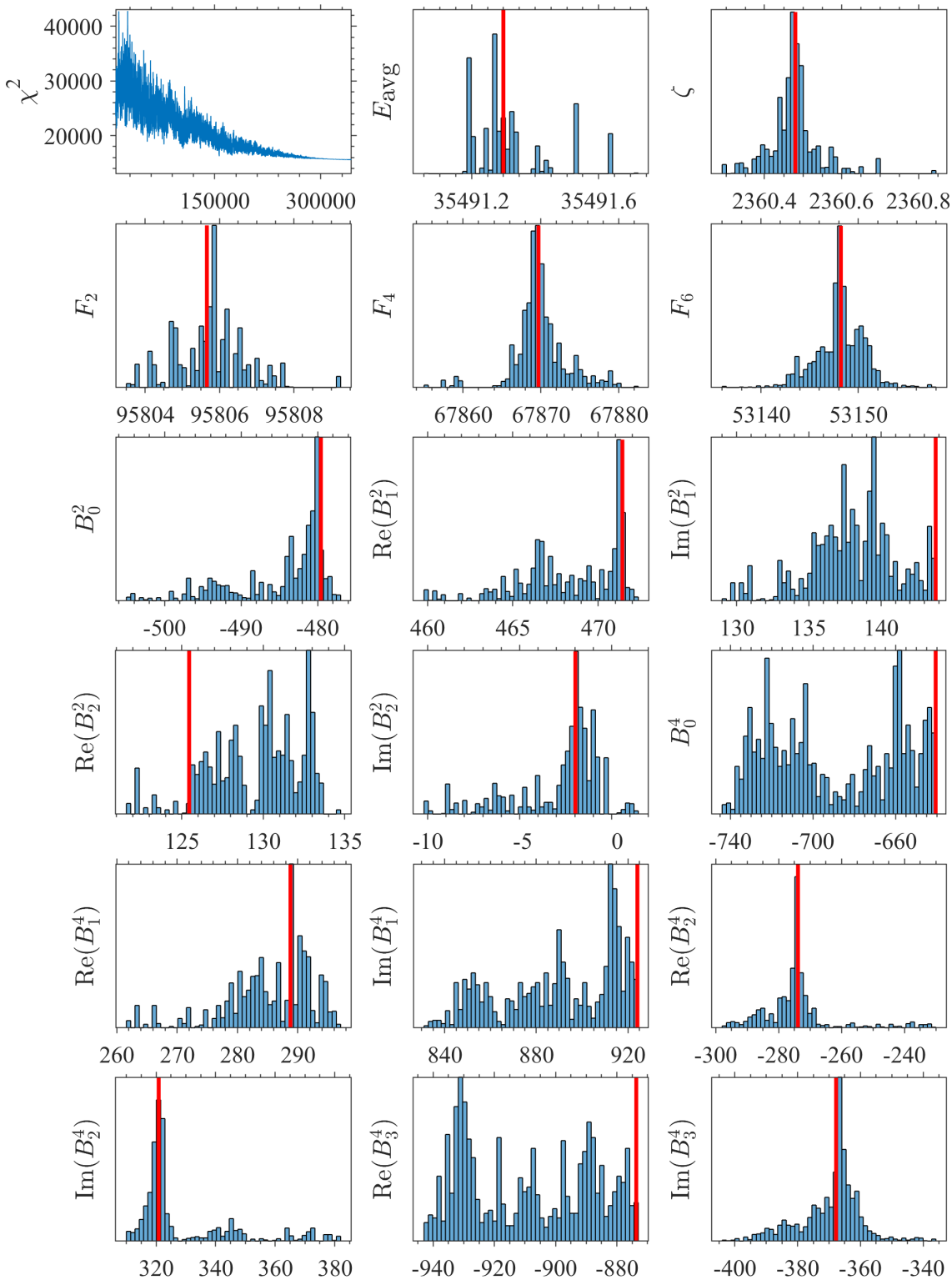

Figure 6.31: Variation of the free-ion, crystal-field and hyperfine parameters for site 1 in Er^{3+}:Y_2SiO_5 after the algorithm has been allowed to 'burn in'. The histograms represent approximations to the posterior probability distribution for the parameters. The red lines indicate the fitted value for each parameter. All parameters have units of cm^{-1}. Figure is continued over page.

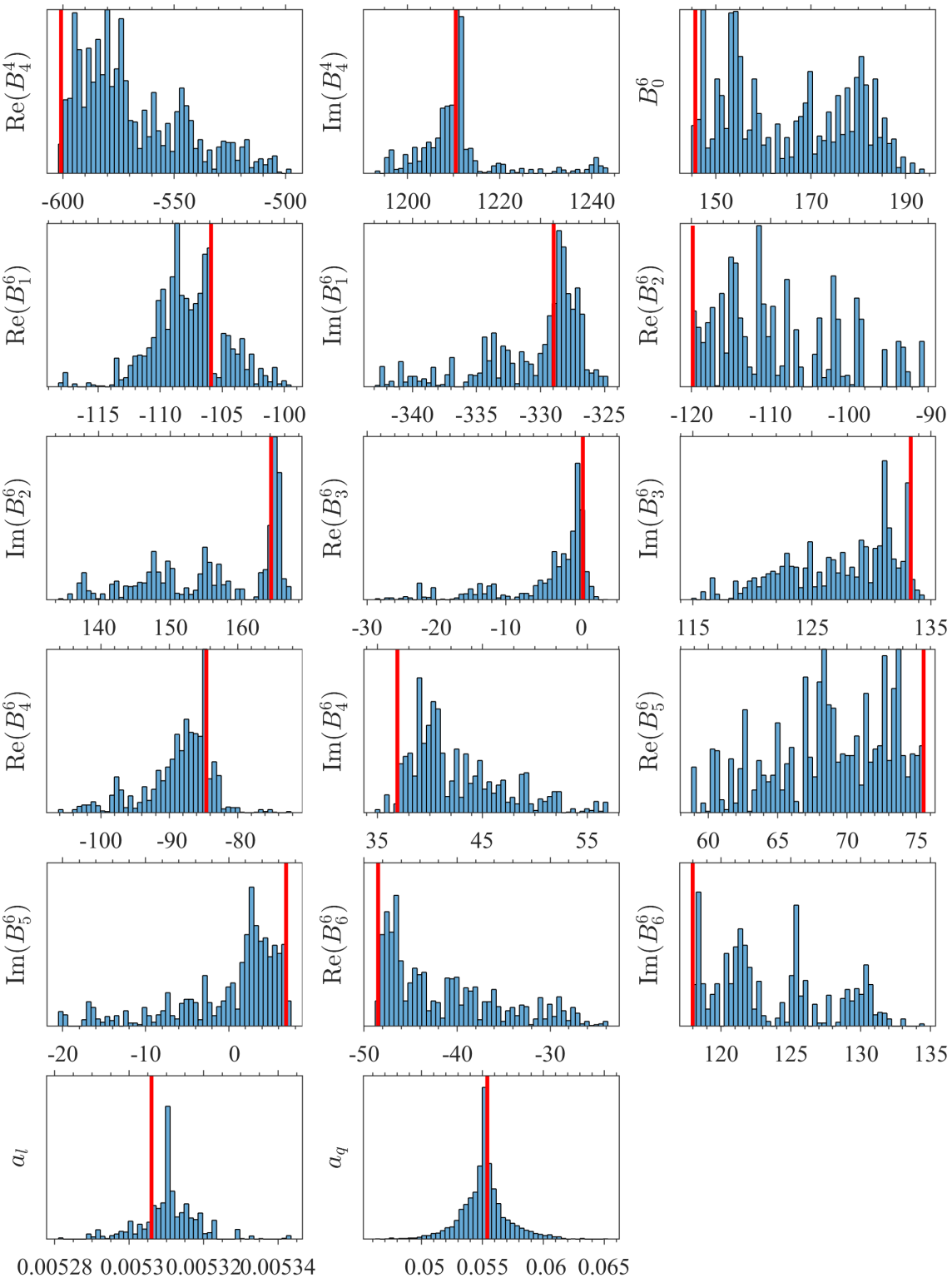

Figure 6.31: Variation of the free-ion, crystal-field and hyperfine parameters for site 1 in Er^{3+}:Y_2SiO_5 after the algorithm has been allowed to 'burn in'. The histograms represent approximations to the posterior probability distribution for the parameters. The red lines indicate the fitted value for each parameter. All parameters have units of cm^{-1}.

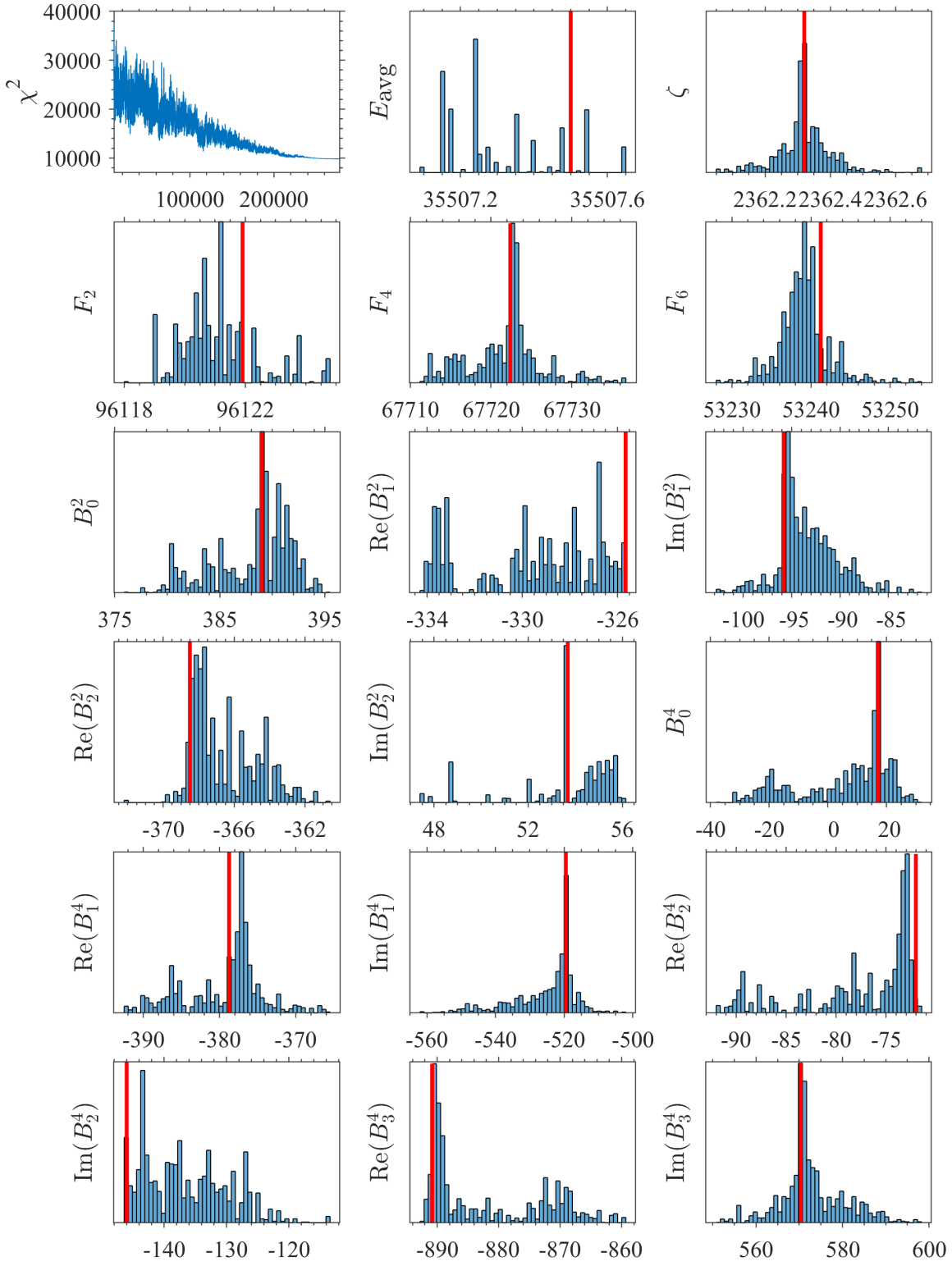

Figure 6.32: Variation of the free-ion, crystal-field and hyperfine parameters for site 2 in Er^{3+}:Y_2SiO_5 after the algorithm has been allowed to 'burn in'. The histograms represent approximations to the posterior probability distribution for the parameters. The red lines indicate the fitted value for each parameter. All parameters have units of cm^{-1}. Figure is continued over page.

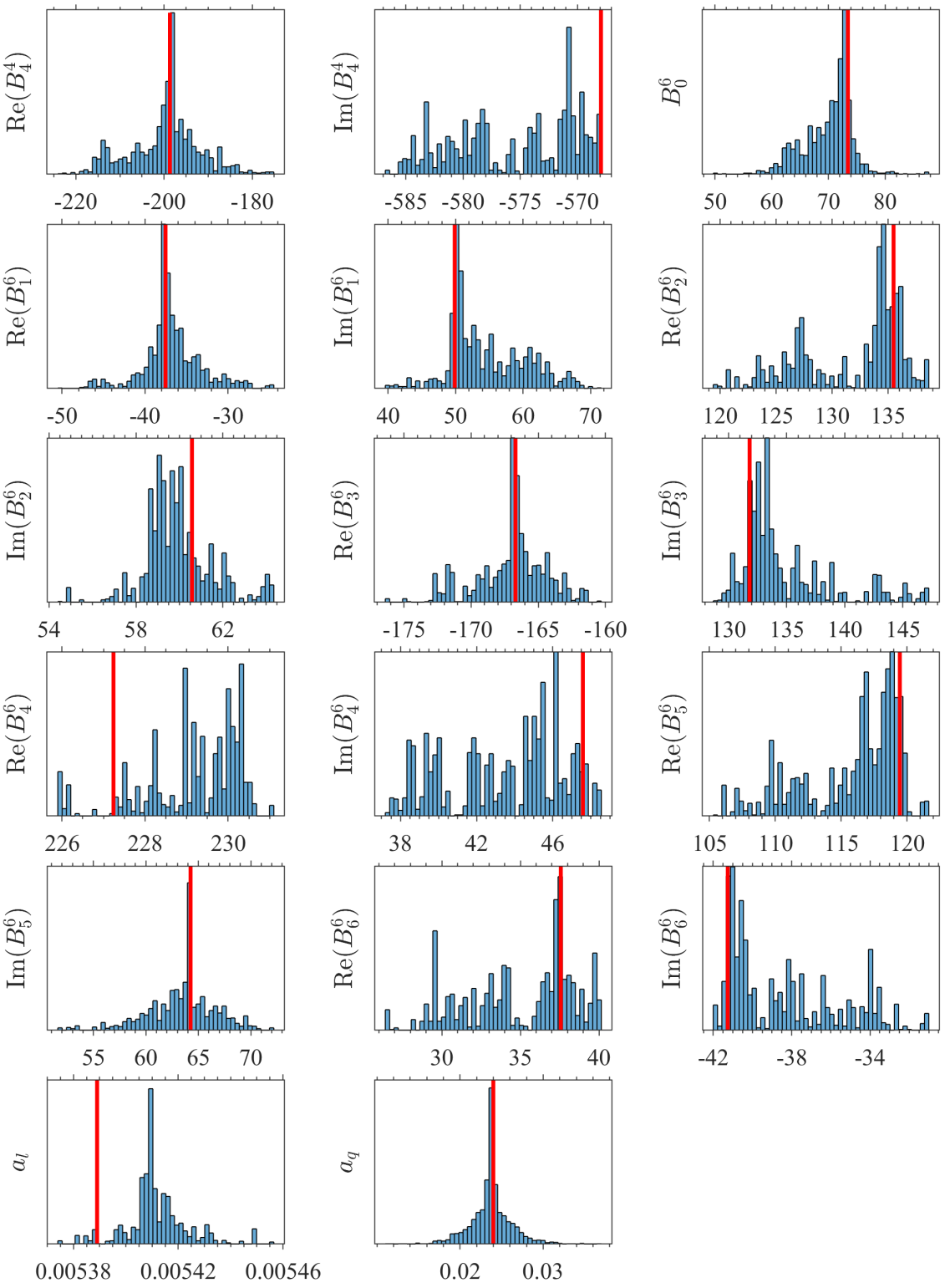

Figure 6.32: Variation of the free-ion, crystal-field and hyperfine parameters for site 2 of Er^{3+}:Y_2SiO_5 after the algorithm has been allowed to 'burn in'. The histograms represent approximations to the posterior probability distribution for the parameters. The red lines indicate the fitted value for each parameter. All parameters have units of cm^{-1}.

Of particular note is a large variation in the crystal-field parameters between those determined in this study and those determined by Horvath *et al.* [55] and Horvath [106], as depicted in Tables 6.4 and 6.5. Due to the large number of crystal-field parameters required to define the C_1 environment of Y_2SiO_5, it has proven difficult to find similarities between these parameter sets. In order to remedy this, the crystal-field potential due to each k rank tensor were calculated and are depicted in Figures 6.33 – 6.35 for site 1 and Figures 6.36 – 6.38 for site 2. The overall crystal-field potential would be given as the sum of the three k rank potentials. The crystal-field potentials calculated from the parameters determined in this study for site 1 have a similar orientation to the potentials calculated from the parameters calculated by Horvath [106], with the positions of the positive (red) and negative (cyan) regions in roughly the same location, while it deviates from the potentials calculated from the parameters calculated by Horvath *et al.* [55]. In the case of site 2, the crystal-field potentials calculated from the parameters determined in this study have a similar orientation to those determined by Horvath [106]. This is due to the choice of swapping the signs on the odd-q B_q^k parameters in the present study. For comparison, the potentials were also calculated from the unchanged parameters as seen in the bottom panels of Figures 6.36 – 6.38.

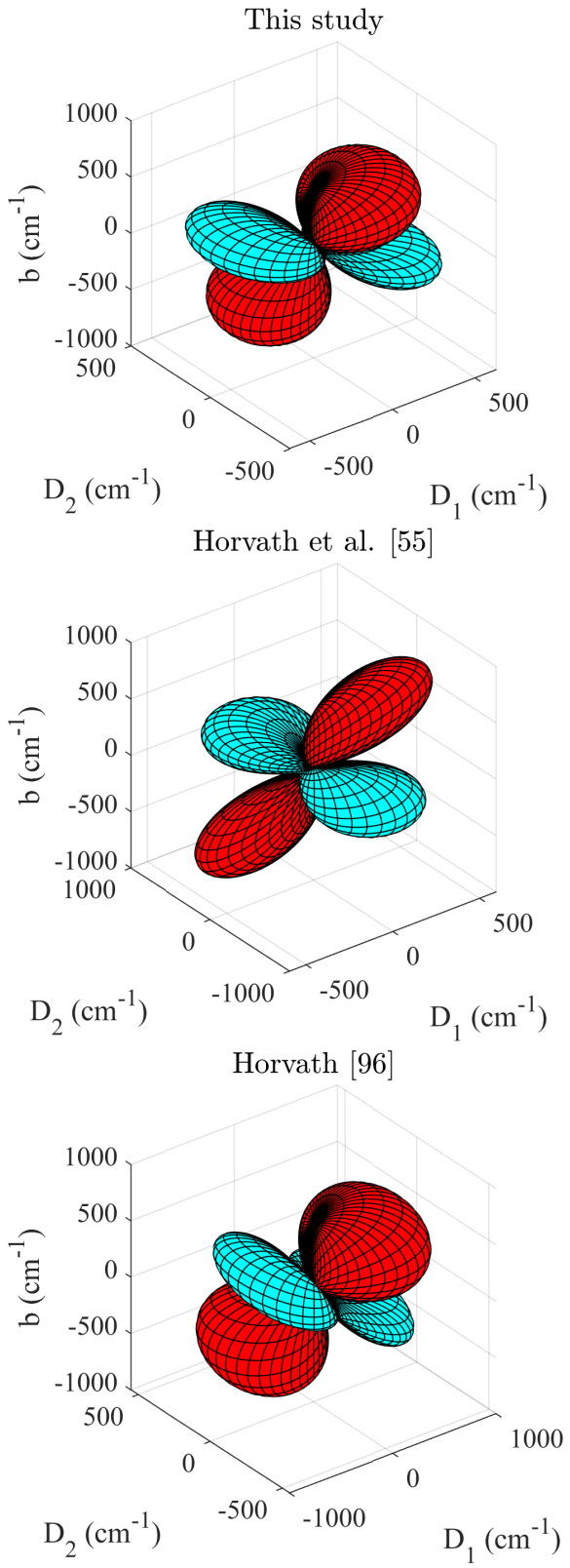

Figure 6.33: Visualisation of the 2nd rank crystal-field potential for site 1 in Er^{3+}:Y_2SiO_5. The potentials calculated from the parameters determined by Horvath *et al.* [55] and Horvath [106] are displayed for comparison. The distance from the origin represents the magnitude of the potential in a given direction, while the red depicts the regions where the potential is positive and the cyan depicts the regions where the potential is negative.

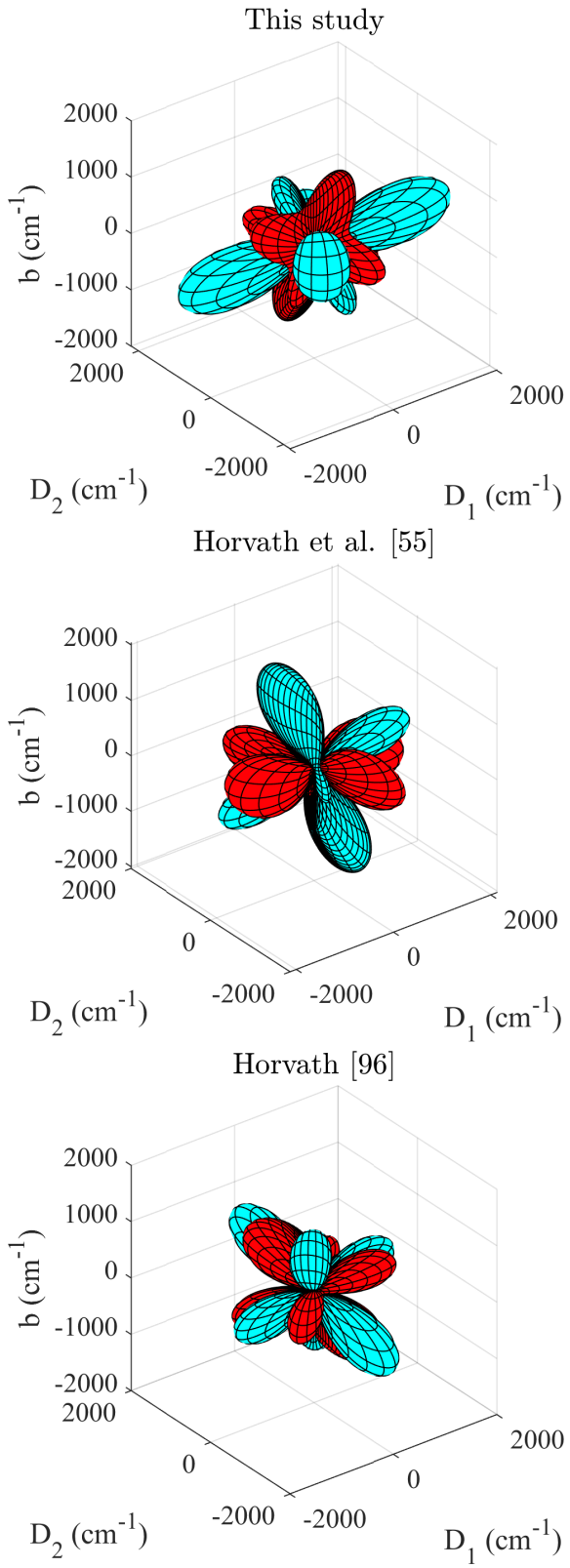

Figure 6.34: Visualisation of the 4$^{\text{th}}$ rank crystal-field potential for site 1 in Er^{3+}:Y_2SiO_5. The potentials calculated from the parameters determined by Horvath *et al.* [55] and Horvath [106] are displayed for comparison. The distance from the origin represents the magnitude of the potential in a given direction, while the red depicts the regions where the potential is positive and the cyan depicts the regions where the potential is negative.

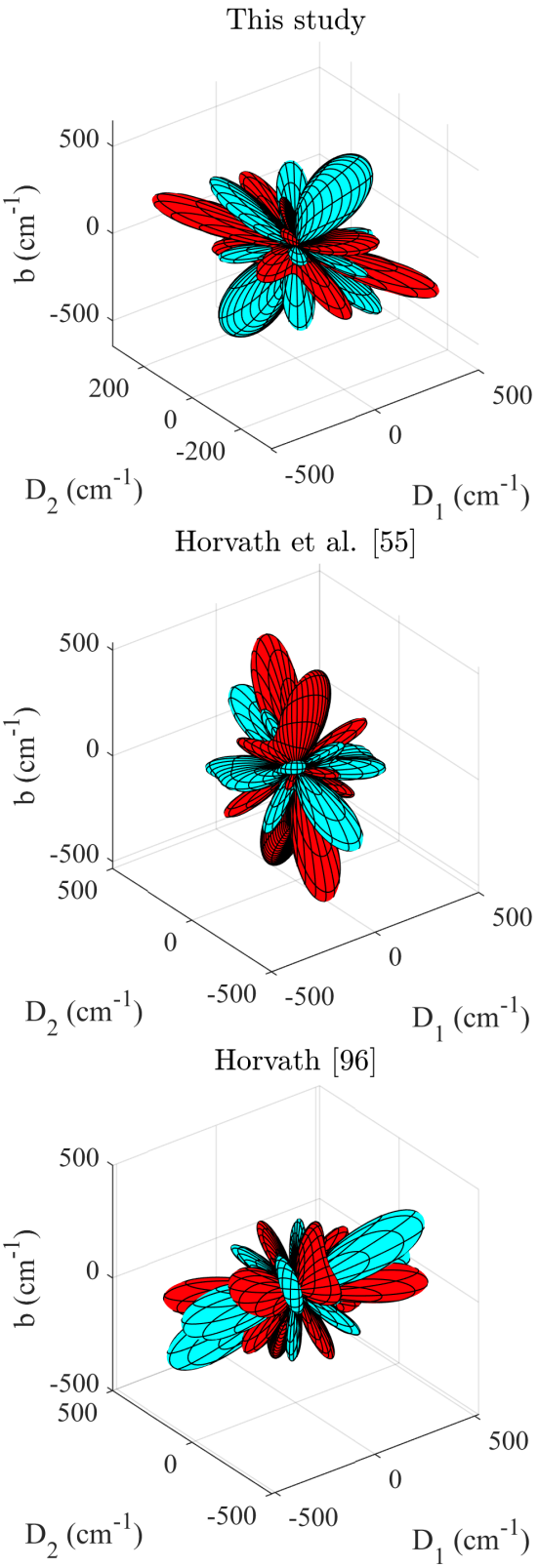

Figure 6.35: Visualisation of the 6th rank crystal-field potential for site 1 in Er^{3+}:Y_2SiO_5. The potentials calculated from the parameters determined by Horvath *et al.* [55] and Horvath [106] are displayed for comparison. The distance from the origin represents the magnitude of the potential in a given direction, while the red depicts the regions where the potential is positive and the cyan depicts the regions where the potential is negative.

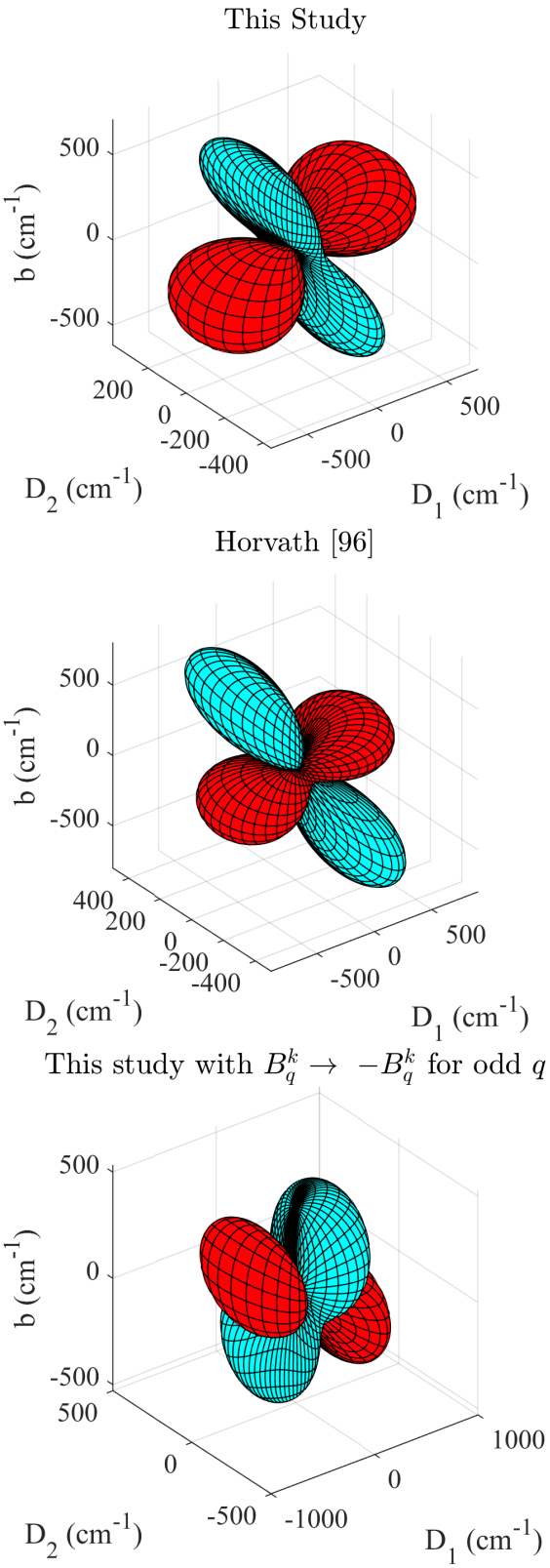

Figure 6.36: Visualisation of the 2nd rank crystal-field potential for site 2 in Er^{3+}:Y_2SiO_5. The potentials calculated from the parameters determined by Horvath [106] and the negative crystal-field parameters with odd-q from this study are displayed for comparison. The distance from the origin represents the magnitude of the potential in a given direction, while the red depicts the regions where the potential is positive and the cyan depicts the regions where the potential is negative.

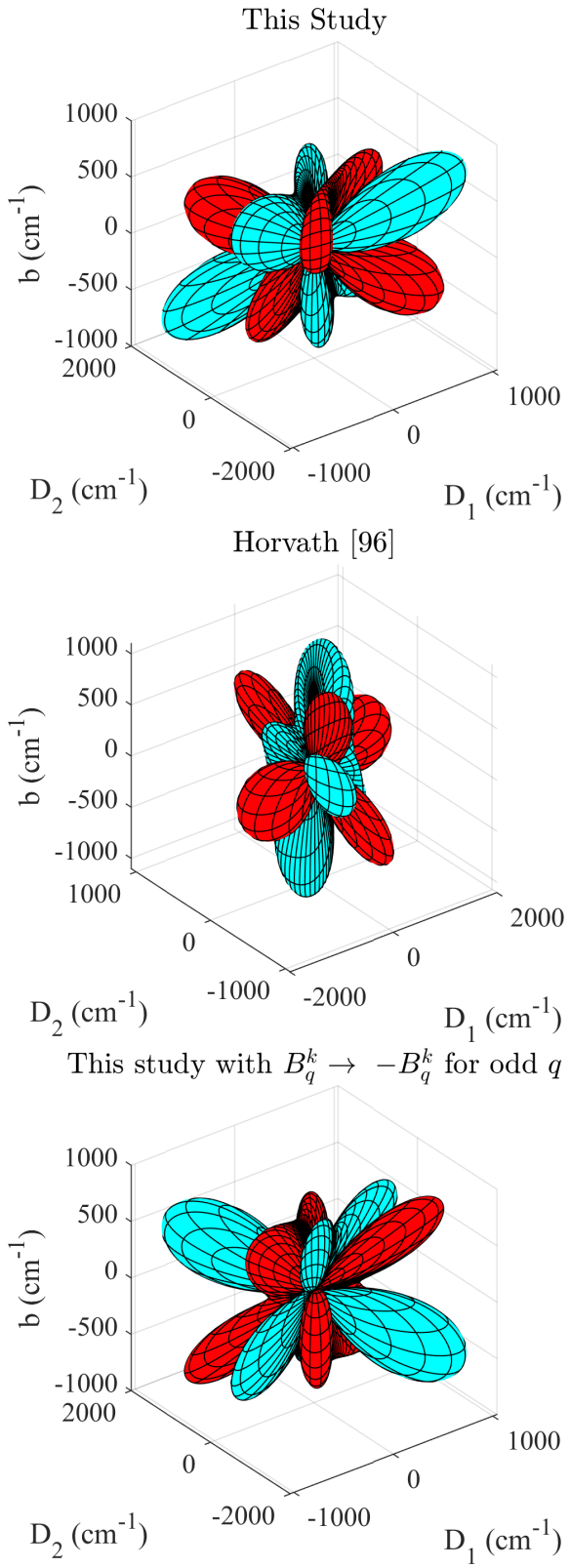

Figure 6.37: Visualisation of the 4th rank crystal-field potential for site 2 in Er^{3+}:Y_2SiO_5. The potentials calculated from the parameters determined by Horvath [106] and the negative crystal-field parameters with odd-q from this study are displayed for comparison. The distance from the origin represents the magnitude of the potential in a given direction, while the red depicts the regions where the potential is positive and the cyan depicts the regions where the potential is negative.

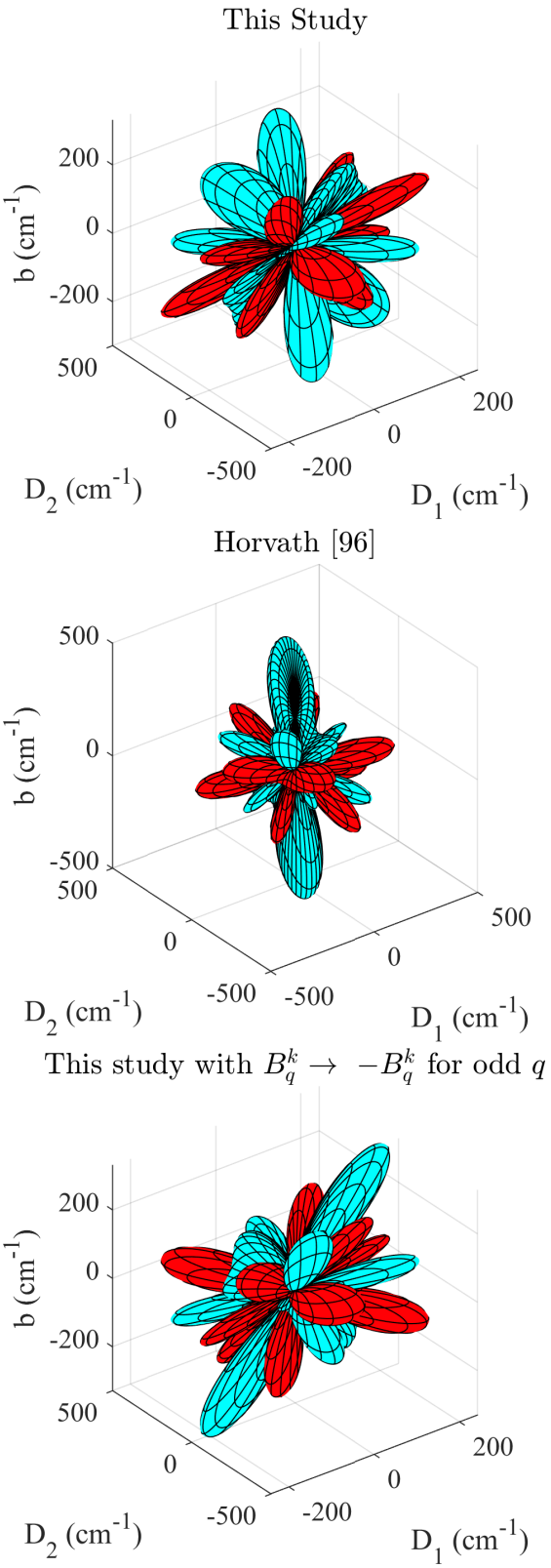

Figure 6.38: Visualisation of the 6$^{\text{th}}$ rank crystal-field potential for site 2 in Er^{3+}:Y_2SiO_5. The potentials calculated from the parameters determined by Horvath [106] and the negative crystal-field parameters with odd-q from this study are displayed for comparison. The distance from the origin represents the magnitude of the potential in a given direction, while the red depicts the regions where the potential is positive and the cyan depicts the regions where the potential is negative.

A further metric that can be used to compare the crystal-field parameters determined in this study and the crystal-field parameters determined by Horvath *et al.* [55] and Horvath [106] are the crystal-field strength parameters given by Equation (2.36). The crystal-field strength parameters for this study and studies performed by Horvath *et al.* were computed and are given in Table 6.7 [55, 106]. We see that the overall crystal-field strengths of this study for site 1 are consistent with those found in [55], but deviates from those found in [106]. For site 2 we see agreement between the crystal-field strengths found in this study and those found in [106].

Table 6.7: Crystal-field strength parameters for site 1 and site 2 in Er^{3+}:Y_2SiO_5. All values are in cm^{-1}. Parameters determined by Horvath *et al.* are also included for comparison [55, 106].

	Site 1			Site 2	
Parameter	This study	Horvath *et al.* [55]	Horvath [106]	This study	Horvath [106]
S^2	386.6	399.0	483.0	363.1	397.9
S^4	948.2	862.9	824.6	653.3	607.5
S^6	183.8	189.6	218.6	151.5	171.4

Despite the large variation between the crystal-field parameters determined in this study and the studies by Horvath *et al.* [55, 106], the overall shape and strength of the crystal-field are reasonably consistent between the three studies. The small deviations could be partially attributed to the different weighting between electronic, Zeeman and hyperfine data between the studies with Horvath *et al.* prioritising the magnetic-hyperfine structure of the $^4I_{15/2}Z_1$ ground and $^4I_{13/2}Y_1$ excited states, whereas this study focuses on the full electronic and magnetic structure of the $4f^{11}$ configuration of Er^{3+}:Y_2SiO_5. However this variation is further evidence that there exists multiple equally valid local minima rather than a true global minimum.

Tables 6.8 and 6.9 shows the spin Hamiltonian parameters of the $^4I_{15/2}Z_1$ and $^4I_{13/2}Y_1$ states of site 1 and site 2 respectively in Er^{3+}:Y_2SiO_5. The spin Hamiltonian parameters were estimated using our crystal-field model. The theoretically determined spin Hamiltonian parameters found by Horvath *et al.* [55, 106] in addition to the experimentally determined Spin Hamiltonian parameters determined by Chen *et al.* and Sun *et al.* [62, 110] are also included for comparison. Despite this study focusing on modelling the full electronic and magnetic of Er^{3+}:Y_2SiO_5 the model developed here also provides an excellent prediction of the hyperfine structure of the $^4I_{15/2}Z_1$ and $^4I_{13/2}Y_1$ states for both sites. We see that the g tensors determined in this study show very good agreement with the experimentally determined g tensors [62, 110]. In the case of the $^4I_{15/2}Z_1$ ground state for site 1, our g tensor provides closer agreement than the g tensor determined by Horvath *et al.* [55]. While the A tensors determine in this study also provides close agreement to those determined by Chen *et al.* and Horvath *et al.*, the Q tensors deviates a little. This is attributed to this study focusing on the electronic and magnetic structure of Er^{3+}:Y_2SiO_5, rather than the hyperfine structure and therefore struggles to model the small scale electric-quadrupole interaction.

Table 6.8: Spin Hamiltonian parameters for the $^4I_{15/2}Z_1$ and $^4I_{13/2}Y_1$ states for site 1 in Er^{3+}:Y_2SiO_5. All A and Q values are in MHz.

State	Study	g_{xx}	g_{yy}	g_{zz}	g_{xy}	g_{xz}	g_{yz}
$^4I_{15/2}Z_1$	This study	3.03	8.75	4.92	−3.00	−3.44	5.74
	Horvath *et al.* [55]	2.10	8.37	5.49	−3.43	−3.21	5.16
	Chen *et al.* [62]	2.90	8.90	5.12	−2.95	−3.56	5.57
	Sun *et al.* [110]	3.07	8.16	5.79	−3.14	−3.40	5.76
$^4I_{13/2}Y_1$	This study	1.63	3.66	8.29	−1.86	−2.98	5.11
	Horvath *et al.* [55]	2.04	4.44	7.94	−2.24	−3.40	5.15
	Sun *et al.* [110]	1.95	4.23	7.89	−2.21	−3.58	4.99
		A_{xx}	A_{yy}	A_{zz}	A_{xy}	A_{xz}	A_{yz}
$^4I_{15/2}Z_1$	This study	317.20	917.44	515.83	−314.96	−361.63	602.05
	Horvath *et al.* [55]	200.80	911.27	586.95	−344.23	−362.61	586.95
	Chen *et al.* [62]	274.29	827.50	706.15	−202.52	−350.82	635.15
$^4I_{13/2}Y_1$	This study	206.60	466.60	1061.93	−236.41	−380.64	653.32
	Horvath *et al.* [55]	271.96	583.12	1058.43	−293.37	−447.76	684.97
		Q_{xx}	Q_{yy}	Q_{zz}	Q_{xy}	Q_{xz}	Q_{yz}
$^4I_{15/2}Z_1$	This study	4.89	−4.23	−0.67	3.95	4.23	−5.39
	Horvath *et al.* [55]	9.32	−6.37	−2.95	1.92	2.26	−9.55
	Chen *et al.* [62]	10.40	−5.95	−4.44	−9.12	−9.96	−14.32
$^4I_{13/2}Y_1$	This study	5.90	0.42	−6.32	2.30	4.44	−5.31
	Horvath *et al.* [55]	6.84	0.30	−7.13	3.62	5.54	−7.13

Table 6.9: Spin Hamiltonian parameters for the $^4I_{15/2}Z_1$ and $^4I_{13/2}Y_1$ states for site 2 in Er^{3+}:Y_2SiO_5. All A and Q values are in MHz.

State	Study	g_{xx}	g_{yy}	g_{zz}	g_{xy}	g_{xz}	g_{yz}
$^4I_{15/2}Z_1$	This study	14.47	1.51	1.65	−1.89	2.37	0.02
	Chen *et al.* [62]	14.37	1.93	1.44	−1.77	2.40	−0.43
	Sun *et al.* [110]	14.65	1.97	0.90	−2.12	2.55	−0.55
$^4I_{13/2}Y_1$	This study	11.58	0.31	2.13	−0.69	4.44	−0.26
	Sun *et al.* [110]	12.03	0.21	1.77	−5.85	4.52	−0.30
		A_{xx}	A_{yy}	A_{zz}	A_{xy}	A_{xz}	A_{yz}
$^4I_{15/2}Z_1$	This study	1541.77	159.17	175.52	−200.91	253.34	1.61
	Chen *et al.* [62]	−1565.3	−15.3	127.8	219.0	−124.4	−0.7
$^4I_{13/2}Y_1$	This study	1504.47	40.73	276.53	−90.45	577.51	−34.26
		Q_{xx}	Q_{yy}	Q_{zz}	Q_{xy}	Q_{xz}	Q_{yz}
$^4I_{15/2}Z_1$	This study	−4.49	2.81	1.69	0.85	−1.45	−1.15
	Chen *et al.* [62]	−10.5	−19.5	30.0	−22.8	−3.1	−17.7
$^4I_{13/2}Y_1$	This study	−4.16	3.03	1.13	0.44	−2.73	−0.42

The crystal-field model presented in this study accurately reproduces the electronic, magnetic and hyperfine structure of Er^{3+}:Y_2SiO_5 that the model was fitted to. I will show that our crystal-field model is also able to predict the angular-dependence of the optical depth and high field hyperfine splittings, which was not utilised during the fitting process, and compare our predictions to values in the literature as an independent verification of our model [28, 166].

Figures 6.39 and 6.40 depicts the angular dependence of the optical depth for the $^4I_{15/2}Z_1 \longrightarrow {}^4I_{13/2}Y_1$ transition for sites 1 and 2 respectively. Also shown are values from in the literature [55, 106, 166]. Here the electric-field component of the light was aligned with the b axis, while the propagation vector, $\vec{k}$, was rotated in the D_1, D_2 plane (with $\theta = 0$ corresponding to $M \parallel D_2$, and $\theta = 90°$ corresponding to $M \parallel D_1$). I predict the maximum optical depth to be at 295.9° for site 1, while the experimentally determined maximum was found to be 298.6°. For site 2, I predict the maximum optical depth to be at 180.1°, compared to the experimentally determined maximum at 256.6° [166]. Our predictions agree very closely with those of Petit *et al.* for site 1 but was found to be out of phase for site 2. For site 1, [55] was found to be in phase with our predictions while [106] was found to be out of phase. For site 2, [106] was found to be in phase with our predictions. This highlights the necessity of including a large amount of directional data into the crystal-field fits, required in order to establish an orientation, with site 2 lacking hyperfine measurements of the $^4I_{13/2}Y_1$ state which was included for site 1.

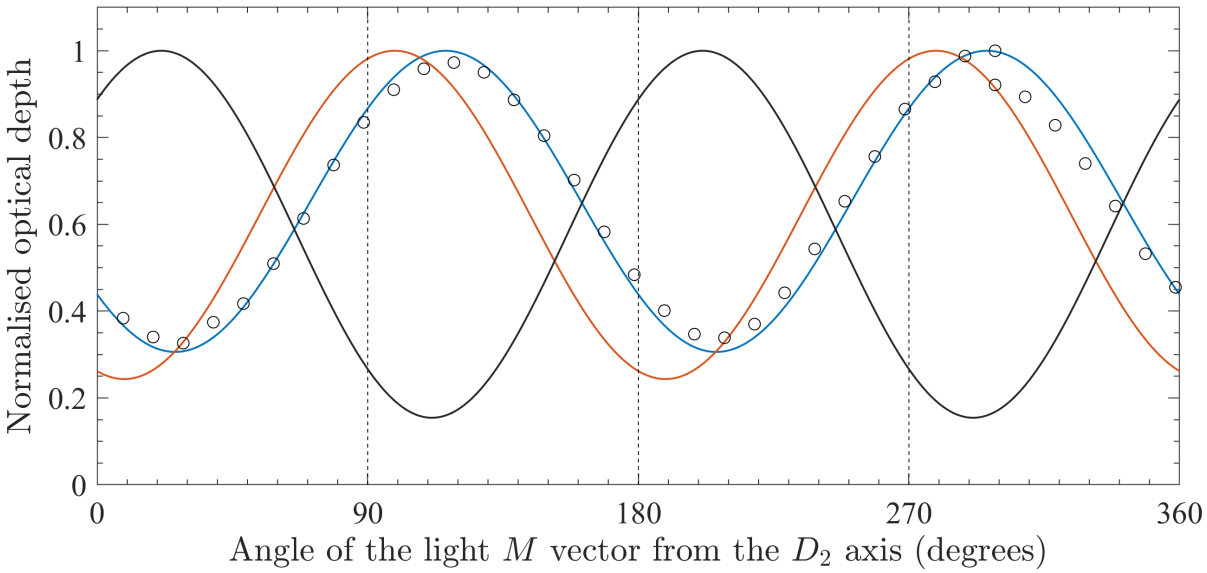

Figure 6.39: Angular dependence of the optical depth for the site 1 $Z_1 \rightarrow Y_1$ transition in Er^{3+}:Y_2SiO_5 with the magnetic field vector of the light, M, rotated in the D_1-D_2 plane. $\theta = 0$ corresponds to $M \parallel D_2$. The hollow circles are the experimentally determined optical depths [166], while the solid lines are theoretical predictions determined from the crystal-field models developed in this study (blue), by Horvath *et al.* (red), and Horvath (black) [55, 106]. The vertical lines were added to assist the reader.

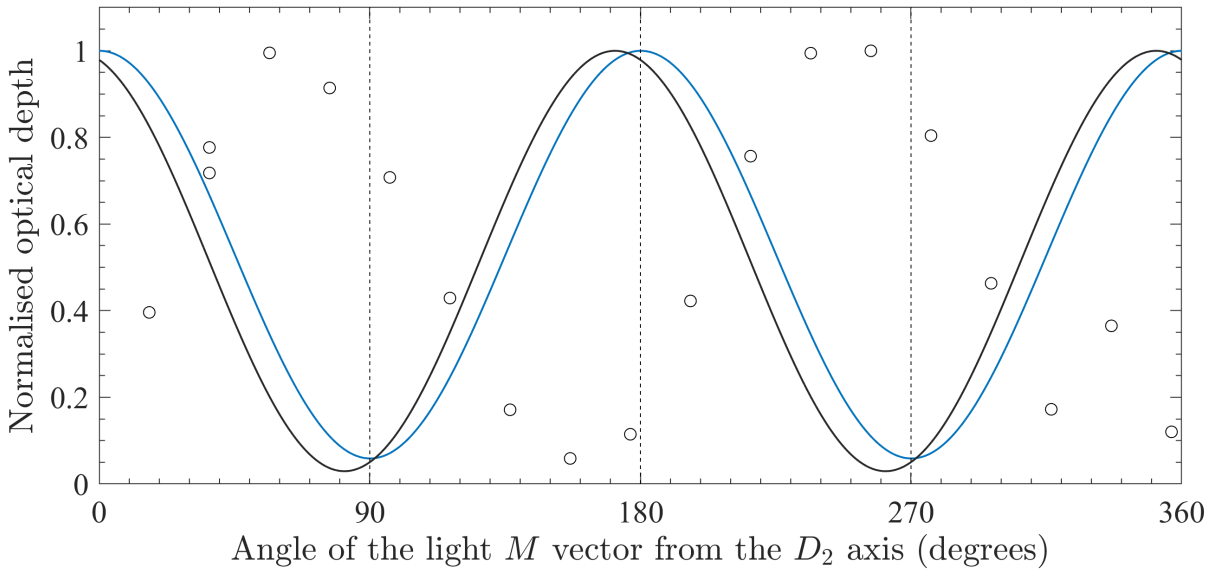

Figure 6.40: Angular dependence of the optical depth for the site 2 $Z_1 \rightarrow Y_1$ transition in Er^{3+}:Y_2SiO_5 with the magnetic field vector of the light, M, rotated in the D_1-D_2 plane. $\theta = 0$ corresponds to $M \parallel D_2$. The hollow circles are the experimentally determined optical depths [166], while the solid lines are theoretical predictions determined from the crystal-field models developed in this study (blue) and by Horvath (black) [106]. The vertical lines were added to assist the reader.

Table 6.10 shows the predicted and experimental hyperfine splittings of the ground $^4I_{15/2}Z_1$ and excited $^4I_{13/2}Y_1$ states at a magnetic field of 7 T applied along the D_1 axis for site 2 [28]. The theoretical hyperfine splittings, which were calculated from the crystal-field model determined in this study, agrees with the experimentally determined values to within 10 %. The small variations that do exist between the theoretical and experimental values are attributed to the lack of excited state hyperfine data for site 2 in Er^{3+}:Y_2SiO_5 that the model could be fitted to.

Table 6.10: Theoretical and experimental $^4I_{15/2}Z_1$ ground and $^4I_{13/2}Y_1$ excited states hyperfine splittings for site 2 with a magnetic field of 7 T applied along the D_1 axis [28]. The theoretical splittings were determined from our crystal-field model. All values are in MHz.

	$^4I_{15/2}Z_1$		$^4I_{13/2}Y_1$	
Transition	This study	Rančić *et al.*	This study	Rančić *et al.*
$1 \rightarrow 2$	897	995	928	994
$2 \rightarrow 3$	881	943	912	972
$3 \rightarrow 4$	865	898	895	953
$4 \rightarrow 5$	849	862	879	935
$5 \rightarrow 6$	833	831	863	918
$6 \rightarrow 7$	817	810	847	903
$7 \rightarrow 8$	801	796	831	889

6.5 Conclusion

In this chapter I aimed to further the crystal field analyses that have recently been undertaken by Horvath *et al.* [55, 106] by creating a comprehensive crystal-field model that predicts the full $4f^{11}$ electronic structure of both C_1 symmetry sites in Er^{3+}:Y_2SiO_5.

The first half of this chapter focuses on experimental work performed in order to provide sufficient data for the crystal-field fit. Through the use of temperature dependent spectroscopy, a total of 51 and 53 electronic states were assigned to site 1 and site 2 respectively across many multiplets up to the $^4G_{11/2}$ multiplet at ∼26 500 cm^{-1}. Additionally, Zeeman absorption spectroscopy was performed in order to determine g values up to the $^4F_{5/2}$ multiplet at ∼22 000 cm^{-1}, with a magnetic field applied parallel to the D_1, D_2 and b axes. A total of 68 g values (20 along the D_1 axis, 23 along the D_2 axis and 25 along the b axis) for site 1 and 70 g values (25 along the D_1 axis, 24 along the D_2 axis and 21 along the b axis) for site 2 were determined through this method.

The experimental work presented here, when combined with previous fluorescence, electron-paramagnetic resonance and Raman-heterodyne measurements from the literature [62, 110, 158], culminated in the creation of a crystal-field model that reproduces the electronic and magnetic of the full $4f^{11}$ configuration of Er^{3+}:Y_2SiO_5 while still accurately reproducing the hyperfine structure of the $^4I_{15/2}Z_1$ and $^4I_{13/2}Y_1$ states relevant to the 1.5 μm telecommunications transition. The crystal-field model presented here was also shown to accurately predict the polarisation and high field hyperfine structure of Er^{3+}:Y_2SiO_5, structure that was not fitted in order to create the model. Furthermore, the crystal-field parameters determined here can be scaled to other lanthanide ions in Y_2SiO_5 to assist in future crystal-field modelling that can predict ZEFOZ points before any extensive experimental investigation is required with possible quantum technologies applications.

Chapter 7

Transferability of parameters and predictions of the $4f^6$ configuration of Eu^{3+}:Y_2SiO_5

Parameterised crystal-field models for both Er^{3+}:Y_2SiO_5 and Sm^{3+}:Y_2SiO_5 was shown to be able to reproduce the electronic, magnetic and hyperfine structure used in the fitting process and predict structure that the models were not fitted to. In this chapter I will demonstrate the transferability of crystal-field parameters between ions. I show that crystal-field parameters obtained for Sm^{3+}:Y_2SiO_5 can be used to model the electronic and hyperfine structure of Eu^{3+}:Y_2SiO_5, by scaling the parameters to account for the change of electronic configuration from $4f^5$ to $4f^6$. Parameterising a crystal-field model for the non-Kramers system of Eu^{3+}:Y_2SiO_5 directly would be difficult as the system has no doublet states, making the magnetic response difficult to observe. This makes the transferability of parameters from neighbouring ions necessary. Eu^{3+}:Y_2SiO_5 was chosen due to its importance in QIP, with the longest coherence time to date [25], obtained though utilising the ZEFOZ technique, and the proximity of Eu^{3+} to Sm^{3+} in the lanthanide series.

7.1 Scaling crystal-field parameters

Trends have previously been established for ions in many host including, for example, the RE^{3+}:$Cs_2NaLnCl_6$ [43,63–66] and RE^{3+}:LaF_3 [49,67] systems, as discussed in Section 1.2. However, as both of these systems have higher symmetries than the C_1 symmetry of Y_2SiO_5, they require fewer crystal-field parameters to fully model the system. Due to the lack of data required to fit all 27 crystal-field parameters required for C_1 symmetry, I define three k-rank spherical tensor operators, which reduces the required parameter space to three crystal-field parameters. The ratios of each k-rank spherical tensor operators, $C^{(k)}$, each with an associated parameter, B^k, is defined to have the ratios found for Sm^{3+}:Y_2SiO_5 and are given in Equation (7.1). Fixing the ratios forces the crystal-field parameters to have the same orientation as Sm^{3+}:Y_2SiO_5.

$$C^{(k)} = \sum_{q=0}^{k} C_q^{(k)} \left(\frac{B_q^{(k)}(\mathrm{Sm})}{B_0^{(k)}(\mathrm{Sm})} \right) \tag{7.1}$$

Here $C_q^{(k)}$ are the spherical tensor operators described in Equation (2.25), while $B_q^k(\mathrm{Sm})$ are the crystal-field parameters found for Sm^{3+}:Y_2SiO_5, as given in Table 4.7.

To model the hyperfine structure of Eu^{3+}:Y_2SiO_5, the lattice contribution to the nuclear quadrupole interaction must be included, given by Equation (2.52). This would typically add five additional parameters, however, as they are proportional to the 2nd-rank crystal-field parameters, I define a 2nd-rank operator, with associated parameter, N^2, that has the same ratios as the above spherical tensor operators:

$$r_n^2(C_n)^{(2)} = \sum_{q=0}^{2} r_n^2(C_n)_q^{(2)} \left(\frac{B_q^{(k)}(\mathrm{Sm})}{B_0^{(k)}(\mathrm{Sm})} \right) \tag{7.2}$$

7.2 Predictions of the Eu^{3+}:Y_2SiO_5 hyperfine structure

Europium has two naturally occurring isotopes of near equal abundances, both with a nuclear spin of $I = \frac{5}{2}$. In this chapter I focus on the 151 isotope of europium, that has been used to obtain the six hour coherence time [25].

In order to predict the electronic structure of Eu^{3+}:Y_2SiO_5, five free-ion, three crystal-field and three hyperfine parameters were fitted to experimental data from the literature. The free-ion parameters that were allowed to vary were; the $4f^N$ barycenter, E_0, the three Slater parameters, F^k, and the spin-orbit parameter, ζ. The Slater parameters were constrained to the ratios determined by Carnall *et al.* [49], with $F^4/F^2 = 0.713$ and $F^6/F^2 = 0.512$. Other parameters were fixed to those found by Carnall *et al.* for Eu^{3+}:LaF_3 [49]. The k-rank crystal-field parameters, defined in Equation (7.1) were initially set to the values of the axial ($q = 0$) crystal-field parameters determined for Sm^{3+}:Y_2SiO_5, as given in Table 4.7. The magnetic-dipole, electric-quadrupole and the 2nd-rank lattice contribution to the electric-quadrupole parameter, defined in Equation (7.2), were also allowed to vary. The initial values for the hyperfine parameters were set to the values determined by Smith *et al.* for Eu^{3+}:Y_2O_3 [167]. The basin-hopping algorithm was used for the fitting process, with a total of 500 iterations. The matrix elements of the hyperfine levels were limited to the lowest 12 multiplets in order to enhance performance. Table 7.1 shows the weightings used for the various parameters sets during the fitting process. These values were chosen to optimise fitting to the hyperfine data.

The experimental data for site 1, which gives a total of 157 data points, are as follows:

- 24 electronic energy levels up to the $^7F_4$ multiplet at ∼3000 cm^{-1} determined by Könz *et al.* [58]. The $^7F_3W_7$ line could not be included due to a misprint while the assignments for the $^7F_5$ and $^7F_6$ multiplets were omitted as not all spectral lines could be observed by Könz *et al.* [58].
- 9 electronic energy levels belonging to the $^5D_0$ – $^5D_2$ multiplets, located at ∼20 000 cm^{-1}, as determined by Yano *et al.* [168].
- 4 data points from the zero-field hyperfine splittings for both the $^7F_0Z_1$ and $^5D_0A_1$ states, as determined by Cruzeiro *et al.* [169].
- 60 data points for the hyperfine splittings of the $^7F_0Z_1$ state, calculated from the **M** and **Q** tensors determined by Cruzeiro *et al.* [169]. The energy of each hyperfine state, besides the ground state (which was set as zero), was sampled at equally spaced intervals according to Equation (4.8), with $B_0 = 0.05$ T.
- 60 data points for the hyperfine splittings of the $^5D_0A_1$ state, calculated from the **M** and **Q** tensors determined by Cruzeiro *et al.* [169]. The energy of each hyperfine state besides the ground state (which was set as zero) was sampled at equally spaced intervals according to Equation (4.8), with $B_0 = 0.05$ T.

For site 2, a total of 91 data points was fitted to and are as follows:

- 18 electronic energy levels up to the $^7F_4$ multiplet at ∼3000 cm^{-1} determined by Könz *et al.* [58]. The assignments for the $^7F_3$, $^7F_5$ and $^7F_6$ multiplets were omitted as not all spectral lines could be observed by Könz *et al.* [58].
- 9 electronic energy levels belonging to the $^5D_0$ – $^5D_2$ multiplets, located at ∼20 000 cm^{-1}, as determined by Yano *et al.* [168].
- 4 data points from the zero-field hyperfine splittings for both the $^7F_0Z_1$ and $^5D_0A_1$ states, as determined by Ma *et al.* [170].
- 60 data points for the hyperfine splittings of the $^7F_0Z_1$ state, calculated from the **M** and **Q** tensors determined by Ma *et al.* [170]. The energy of each hyperfine state, besides the ground state (which was set as zero), was sampled at equally spaced intervals according to Equation (4.8), with $B_0 = 0.05$ T.

Table 7.1: Weightings used for different parameter sets during the fitting process for both sites in Eu^{3+}:Y_2SiO_5. These values were chosen to optimise fitting to the hyperfine data.

Data set	Weighting
Electronic levels	1
Zero-field hyperfine splittings	1×10^8
Data from the **M** and **Q** tensors	1×10^9

Theoretical and experimental electronic levels for both sites in Eu^{3+}:Y_2SiO_5 are given in Table 7.2. The experimentally determined values for the ^7F_J manifold are from [58] and the experimentally determined values for the ^5D_J manifold are from [168]. The standard deviations between theoretical and experimental electronic energy levels was found to be 30.3 cm^{-1} for site 1 and 33.5 cm^{-1} for site 2. There is some disagreement between the assignments made by Könz *et al.*, Yano *et al.* and those by Xue *et al.* on the energies of the electronic energy levels that may contribute to the large standard deviations [58, 168, 171]. Table 7.3 shows the parameters for both sites in Eu^{3+}:Y_2SiO_5.

Table 7.2: Theoretical and experimental electronic energy levels up to 22 000 cm^{-1} for both sites in Eu^{3+}:Y_2SiO_5. The theoretical electronic energies were calculated using the determined crystal-field Hamiltonian. All energies are in cm^{-1}.

		Site 1			Site 2		
Multiplet	State	Theory	Exp.	Diff.	Theory	Exp.	Diff.
$^7F_0$	Z_1	22	0	−22	7	0	−7
$^7F_1$	Y_1	270	201	−69	300	226	−74
	Y_2	431	420	−11	419	407	−12
	Y_3	477	485	8	452	493	41
$^7F_2$	X_1	860	860	0	934	904	−30
	X_2	901	880	−21	994	1002	8
	X_3	1057	964	−93	1042	1077	35
	X_4	1120	1086	−34	1141	1130	−11
	X_5	1268	1283	15	1185	1181	−4
$^7F_3$	W_1	1831	1848	17	1845	–	–
	W_2	1909	1934	25	1865	–	–
	W_3	1974	1987	13	1914	–	–
	W_4	2000	2012	12	1940	–	–
	W_5	2033	2050	17	1967	–	–
	W_6	2056	2118	62	1987	–	–
	W_7	2111	–	–	2008	–	–
$^7F_4$	V_1	2670	2676	6	2706	2695	−11
	V_2	2707	2732	25	2777	2737	−40
	V_3	2799	2808	9	2790	2804	14
	V_4	3006	2991	−15	2848	2855	7
	V_5	3058	3056	−2	2923	3015	92
	V_6	3120	3101	−19	2982	3025	43
	V_7	3169	3134	−35	3026	3045	19
	V_8	3182	3160	−22	3078	3090	12
	V_9	3237	3183	−54	3186	3127	−59

Continued over page.

		Site 1			Site 2		
Multiplet	State	Theory	Exp.	Diff.	Theory	Exp.	Diff.
$^7F_5$	U_1	3788	–	–	3799	–	–
	U_2	3803	–	–	3835	–	–
	U_3	3889	–	–	3887	–	–
	U_4	3923	–	–	3916	–	–
	U_5	3964	–	–	3950	–	–
	U_6	3971	–	–	3991	–	–
	U_7	4023	–	–	4014	–	–
	U_8	4108	–	–	4062	–	–
	U_9	4240	–	–	4179	–	–
	U_{10}	4269	–	–	4224	–	–
	U_{11}	4291	–	–	4290	–	–
$^7F_6$	T_1	4834	–	–	4885	–	–
	T_2	4860	–	–	4886	–	–
	T_3	5012	–	–	5062	–	–
	T_4	5023	–	–	5071	–	–
	T_5	5034	–	–	5075	–	–
	T_6	5054	–	–	5094	–	–
	T_7	5380	–	–	5171	–	–
	T_8	5390	–	–	5205	–	–
	T_9	5440	–	–	5232	–	–
	T_{10}	5498	–	–	5251	–	–
	T_{11}	5503	–	–	5284	–	–
	T_{12}	5579	–	–	5328	–	–
	T_{13}	5581	–	–	5337	–	–
$^5D_0$	A_1	17223	17240	17	17208	17235	27
$^5D_1$	B_1	18930	18951	21	18953	18955	2
	B_2	18979	18994	15	18986	18997	11
	B_3	19003	19021	18	18999	19016	17
$^5D_2$	C_1	21390	21384	−6	21432	21409	−23
	C_2	21400	21395	−5	21458	21424	−34
	C_3	21408	21414	6	21473	21445	−28
	C_4	21487	21519	32	21486	21494	8
	C_5	21505	21537	32	21496	21519	23

Table 7.3: Fitted values of the free-ion, crystal-field and hyperfine parameters for site 1 and site 2 in Eu^{3+}:Y_2SiO_5. All values are in cm^{-1}. The square brackets indicates the parameters that were held fixed during the fitting process, and were set to the values found for Eu^{3+}:LaF_3 [49].

Parameter	Site 1	Site 2
E_{avg}	63416.38	63655.16
F^2	82191.81	82591.91
F^4	58602.76	58888.03
F^6	42082.21	42287.06
ζ	1325.63	1336.89
α	[20.16]	[20.16]
β	[−566.9]	[−566.9]
γ	[1500]	[1500]
T^2	[300]	[300]
T^3	[40]	[40]
T^4	[60]	[60]
T^6	[−300]	[−300]
T^7	[370]	[370]
T^8	[320]	[320]
M^{tot}	[2.1]	[2.1]
P^{tot}	[360]	[360]
B^2	−357.10	202.22
B^4	2268.77	−556.83
B^6	45.83	606.25
a_l	0.0639	0.0453
a_Q	−0.0534	−0.0679
N^2	0.00638	−0.00524

Tables 7.4 and 7.5 show the reproduced zero-field hyperfine splittings of the $^7F_0Z_1$ and $^5D_0A_1$ states for site 1 and site 2. Values reproduced by our crystal-field Hamiltonian are compared to those determined from the spin Hamiltonian [169, 170]. We see that there is good agreement between the two Hamiltonians. For site 1, there is some disagreement in the literature on the ordering of the hyperfine levels since the experiments determine energy differences, rather than absolute energies [61,169,172]. Here, I follow the ordering given by Cruzeiro *et al.* [169].

Table 7.4: Zero-field hyperfine splittings of the $^7F_0Z_1$ and $^5D_0A_1$ states for site 1 in $^{151}Eu^{3+}$:Y_2SiO_5, predicted from our crystal-field model and compared to the predictions from the spin Hamiltonian [169]. The first level of each state was set to zero. All values are in MHz.

	$^7F_0Z_1$ state		$^5D_0A_1$ state	
Level	Crystal-field model	Spin Hamiltonian	Crystal-field model	Spin Hamiltonian
1	0	0	0	0
2	0	0	0	0
3	44.1	46.2	71.0	75.0
4	44.1	46.2	71.0	75.0
5	79.6	80.7	176.4	177.0
6	79.6	80.7	176.4	177.0

Table 7.5: Zero-field hyperfine splittings of the $^7F_0Z_1$ and $^5D_0A_1$ states for site 2 in $^{151}Eu^{3+}$:Y_2SiO_5, predicted from our crystal-field model and compared to the predictions from the spin Hamiltonian [170]. The spin Hamiltonian of the $^5D_0A_1$ state is currently unknown, however the zero-field splittings are known. The first level of each state was set to zero. All values are in MHz.

	$^7F_0Z_1$ state		$^5D_0A_1$ state	
Level	Crystal-field model	Spin Hamiltonian	Crystal-field model	Experimental
1	0	0	0	0
2	0	0	0	0
3	34.1	29.5	63.4	63.0
4	34.1	29.5	63.4	63.0
5	79.9	86.8	167.7	171.0
6	79.9	86.8	167.7	171.0

Figure 7.1 depicts the predicted magnetic dependence of the hyperfine levels of $^7F_0Z_1$ for site 1 (left) and site 2 (right). The predictions from the crystal-field Hamiltonians are given in blue while predictions from the spin Hamiltonians, determined by Cruzeiro *et al.* [169] for site 1 and Ma *et al.* [172] for site 2, are given in red. The magnetic field direction used is the ZEFOZ direction for site 1, utilised by Zhong *et al.* in order to obtain the 6 hour coherence time [25] and is in the $[-0.535, -0.634, 0.558]$ direction in the $[D_1, D_2, b]$ co-ordinate frame of the crystal. The same direction was used for site 2 as no studies have predicted ZEFOZ points for this site. There is excellent agreement between the predictions made by the crystal-field Hamiltonians and those made by the spin Hamiltonians for both sites, with the location of the known ZEFOZ point being predicted at ∼1.3 T in this direction for site 1 (marked on the figure). Note that the magnetic structure of the hyperfine states between the left panel of Figure 7.1 and that of Figure 1.1 are reversed due to the ambiguity in the ordering of these hyperfine states as discussed previously. Despite this, the transition energies and the location of the ZEFOZ point remains the same.

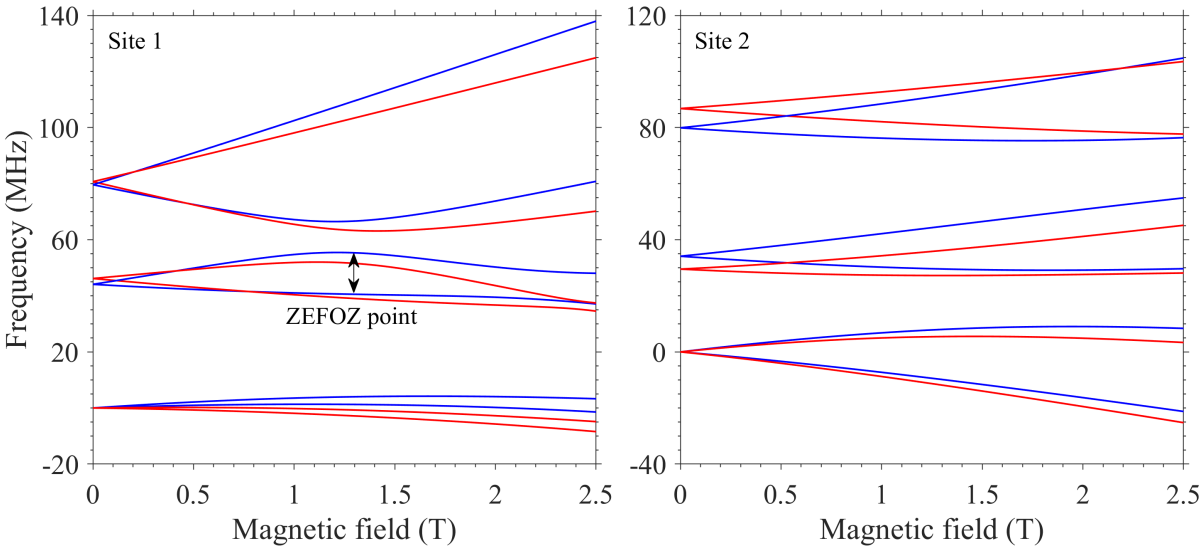

Figure 7.1: Simulated magnetic field dependence of the hyperfine structure belonging to the $^7F_0Z_1$ state for site 1 (left) and site 2 (right) in $^{151}Eu^{3+}$:Y_2SiO_5 with the magnetic field directed in a ZEFOZ direction of site 1. The blue lines are predictions from the crystal-field Hamiltonian, while the red lines are predictions using the spin Hamiltonians [169, 170].

7.3 Conclusion

This chapter focused on predicting the hyperfine structure of $^{151}Eu^{3+}$:Y_2SiO_5 using the crystal-field parameters developed for Sm^{3+}:Y_2SiO_5. Through restricting the crystal-field parameters to have the same orientation as Sm^{3+}:Y_2SiO_5, a crystal-field fit was performed to the available data for $^{151}Eu^{3+}$:Y_2SiO_5. The resulting crystal-field models were able to reproduce the zero-field hyperfine splittings, in addition to accurately predict the magnetic-field dependence on the hyperfine splittings for both sites. Additionally, the crystal-field model developed for site 1 was able to accurately predict the location of the known ZEFOZ point, which was utilised in obtaining the longest coherence time to date of six hours [86]. This demonstration of the transferability of parameters between ions may allow for the prediction of other ZEFOZ points within the electronic structure of lanthanide-doped Y_2SiO_5, which may be experimentally verified and investigated for use in QIP.

Chapter 8

Conclusions

The principle aim of this study was the development of crystal-field models for lanthanide ions doped into the low symmetry system of Y_2SiO_5, with the approach of including extensive directional data in the form of g values to the fits, in order to obtain a unique solution. I also demonstrated the transferability of crystal-field parameters in predicting the electronic structure of neighbouring lanthanide ions. Further development of this approach will allow predictions of possible ZEFOZ transitions for any lanthanide doped into Y_2SiO_5, with applications in QIP.

This work focused on the Sm^{3+}:Y_2SiO_5 and Er^{3+}:Y_2SiO_5 systems. Chapter 4 details the experimental work performed on Sm^{3+}:Y_2SiO_5, and the resulting crystal-field model. Multiple spectroscopic techniques, including Zeeman absorption, Raman heterodyne and fluorescence spectroscopy, were used to determine the electronic and magnetic structure of Sm^{3+}:Y_2SiO_5, up to the $^4G_{7/2}$ multiplet at $\sim$20 000 cm^{-1}. Additionally, the full g tensors of the $^6H_{5/2}Z_1$ and $^4G_{5/2}A_1$ states were determined. The experimental data was fitted to produce a crystal-field model for both sites that accurately reproduced the electronic and magnetic structure of Sm^{3+}:Y_2SiO_5.

Chapter 6 describes a similar approach for Er^{3+}:Y_2SiO_5. This system has been the subject of previous studies, with Horvath *et al.* creating crystal-field models for both sites [55, 106]. Here, I extend the work done by Horvath *et al.* to include a large amount of directional data in the form of g values along the three extinction axes of Y_2SiO_5, obtained through Zeeman spectroscopy. Additionally, significantly more electronic energy levels up to the $^4G_{11/2}$ multiplet at $\sim$26 500 cm^{-1} were obtained through temperature dependant spectroscopy. The electronic, magnetic and hyperfine structure was fitted to refine the crystal-field model for both sites in Er^{3+}:Y_2SiO_5. I showed that it was not only possible to reproduce the data fitted to, but was able to accurately predict polarisation and high-field hyperfine structure that was not included in the fit.

The models presented in this thesis are among the very few crystal-field models performed on a C_1 symmetry system, with other previously developed models only existing for Ce^{3+}:Y_2SiO_5, Nd^{3+}:Y_2SiO_5 and Yb^{3+}:Y_2SiO_5 [142–144].

In Chapter 7, the crystal-field parameters developed for Sm^{3+}:Y_2SiO_5 were scaled to fit to the available data for Eu^{3+}:Y_2SiO_5. The resulting crystal-field model was not only able to reproduce the zero-field hyperfine splittings, but was also able to accurately predict the magnetic-field dependence of the hyperfine structure. I have demonstrated the ability

to predict the ZEFOZ point that was utilised in order to obtain the longest observed coherence time to date of six hours [86]. The resulting crystal-field models will allow for the prediction of many more ZEFOZ points within the electronic-hyperfine structure of any lanthanide ion doped into Y_2SiO_5 which can then be experimentally determined, with the possibility of obtaining increasingly longer coherence times, which is required for applications in QIP.

While the electronic structure of Sm^{3+}:Y_2SiO_5 is determined by the interactions of the $4f$ electrons with the crystal lattice, at higher concentrations interactions between individual Sm^{3+} ions becomes important. Chapter 5 details the energy transfer mechanics of Sm^{3+}:Y_2SiO_5. Such studies are important with applications including the creation of efficient phosphors for WLED and solar cell technologies. With a Sm^{3+} concentration of 0.5 %, both intra- and inter-site energy transfer was observed through the use of site-selective fluorescence spectroscopy. Monte-carlo methods were used to model the temperature dependence of the temporal dynamics of the intra-site energy transfer, and was found to proceed using a dipole-dipole mechanism. The radiative fluorescence rates of the $^4G_{5/2}A_1$ state was found to be 360 s^{-1} for site 1 and 450 s^{-1} site 2 and were found to be insensitive to temperature. The site 1 energy transfer parameter was found to increase from 2.0×10^6 s^{-1} to 4.0×10^6 s^{-1} as the sample temperature is increased from 10 K - 300 K. The site 2 energy transfer parameter was found to increase from 1.3×10^5 s^{-1} to 4.0×10^5 s^{-1} over the same temperature range. Inter-site energy transfer can be observed for excitation of the $^4F_{3/2}$ multiplet of site 2 with the resultant fluorescence observed from the $^4G_{5/2}$ multiplet of site 1. While the process becomes very efficient as a function of temperature, the reverse process was found to remain very weak.

The insights gained into the structure and dynamics of lanthanide-doped Y_2SiO_5 is a crucial step in the development of more efficient quantum memories and phosphor materials. The crystal-field models presented here will allow for predictions of ZEFOZ points for many lanthanide doped Y_2SiO_5 systems, which can then be investigated in order to obtain increasingly longer coherence times, a requirement for quantum computing and communication devices. Additionally, future studies will be able to expand on this study by investigating the energy transfer mechanics as a function of Sm^{3+} concentration. As the energy transfer mechanics are highly dependant on the concentration of dopant ions, such studies will prove to be essential in the development of efficient phosphor materials from Sm^{3+}:Y_2SiO_5.

Publications

Published papers

- N. L. Jobbitt, S. J. Patchett, Y. Alizadeh, M. F. Reid, J.-P. R. Wells, S. P. Horvath, J. J. Longdell, A. Ferrier, P. Goldner, Transferability of crystal-field parameters for rare-earth ions in Y_2SiO_5 tested by Zeeman spectroscopy, Phys. Solid State 61 (5) (2019) 780-784. doi:10.1134/s1063783419050123.
- N. L. Jobbitt, J.-P. R. Wells, M. F. Reid, Energy transfer between Sm^{3+} ions in Y_2SiO_5 crystals, J. Lumin. 224 (2020) 117302. doi:10.1016/j.jlumin.2020.117302.
- N. L. Jobbitt, J.-P. R. Wells, M. F. Reid, J. J. Longdell, Raman heterodyne determination of the magnetic anisotropy for the ground and optically excited states of Y_2SiO_5 crystals doped with Sm^{3+}, Phys. Rev. B 103 (2021) 205114. doi:10.1103/PhysRevB.103.205114.
- N. L. Jobbitt, J.-P. R. Wells, M. F. Reid, S. P. Horvath, P. Goldner, A. Ferrier, Prediction of optical polarization and high-field hyperfine structure via a parametrized crystal-field model for low-symmetry centers in Er^{3+}-doped Y_2SiO_5, Phys. Rev. B 104 (2021) 155121. doi:10.1103/PhysRevB.104.155121.

Papers in preparation

- N. L. Jobbitt, J.-P. R. Wells, M. F. Reid, J. J. Longdell, Accounting for the electronic and magnetic structure of the magnetically insensitive Kramers system of Y_2SiO_5 doped with Sm^{3+} via a parameterized crystal-field model, In preparation for submission to J. Phys. B
- N. L. Jobbitt, J.-P. R. Wells, M. F. Reid, Predictions of ZEFOZ transitions in the technologically important system of Y_2SiO_5 doped with Eu^{3+}. In preparation for submission to Phys. Rev. Lett.

Conference talks and posters

- N. L. Jobbitt, J.-P. R. Wells, M. F. Reid, J. J. Longdell and P. Goldner. A novel approach to applying crystal-field analyses to the low symmetry system of samarium-doped yttrium orthosilicate. 12th Annual Dodd-Walls Centre Symposium, 2019. (Poster)
- N. L. Jobbitt, J.-P. R. Wells, M. F. Reid, J. J. Longdell and P. Goldner. A novel approach to applying crystal-field analyses to the low symmetry system of samarium-doped yttrium orthosilicate. New Zealand institute of physics conference, 2019. (Talk)
- N. L. Jobbitt, J.-P. R. Wells, M. F. Reid, J. J. Longdell The Intra- and Inter-Site Energy Transfer Dynamics of Sm^{3+}:Y_2SiO_5. 20th International Conference on Dynamical Processes in Excited States of Solids, 2019. (Poster)
- N. L. Jobbitt, J.-P. R. Wells, M. F. Reid and J. J. Longdell. Crystal-field Analyses and the Transferability of Parameters in Lanthanide-doped Y_2SiO_5. Dodd-Walls Centre Symposium, 2021. (Talk)

Bibliography

[1] M. A. Nielsen, Quantum Computation and Quantum Information, Cambridge University Press, 2010.

[2] D. Deutsch, R. Jozsa, Rapid solution of problems by quantum computation, Proc. R. Soc. Lond. A. 439 (1992) 553 – 558. doi:10.1098/rspa.1992.0167.

[3] E. Bernstein, U. Vazirani, Quantum complexity theory, SIAM J. Comput. 26 (5) (1997) 1411–1473. doi:10.1137/S0097539796300921.

[4] T. D. Ladd, F. Jelezko, R. Laflamme, Y. Nakamura, C. Monroe, J. L. O'Brien, Quantum computers, Nature 464 (2010) 45. doi:10.1038/nature08812.

[5] B. Wybourne, Optical spectroscopy of lanthanides: magnetic and hyperfine interactions, 1st Edition, CRC Press, 2007.

[6] R. W. Equall, Y. Sun, R. L. Cone, R. M. Macfarlane, Ultraslow optical dephasing in Eu^{3+}:Y_2SiO_5, Phys. Rev. Lett. 72 (1994) 2179–2182. doi:10.1103/PhysRevLett.72.2179.

[7] Y. Sun, C. Thiel, R. Cone, R. Equall, R. Hutcheson, Recent progress in developing new rare earth materials for hole burning and coherent transient applications, J. Lumin. 98 (1) (2002) 281 – 287. doi:10.1016/S0022-2313(02)00281-8.

[8] T. W. Mossberg, Time-domain frequency-selective optical data storage, Opt. Lett. 7 (2) (1982) 77–79. doi:10.1364/OL.7.000077.

[9] N. W. Carlson, L. J. Rothberg, A. G. Yodh, W. R. Babbitt, T. W. Mossberg, Storage and time reversal of light pulses using photon echoes, Opt. Lett. 8 (9) (1983) 483–485. doi:10.1364/OL.8.000483.

[10] H. Lin, T. Wang, G. A. Wilson, T. W. Mossberg, Experimental demonstration of swept-carrier time-domain optical memory, Opt. Lett. 20 (1) (1995) 91–93. doi:10.1364/OL.20.000091.

[11] H. Lin, T. Wang, G. A. Wilson, T. W. Mossberg, Heterodyne detection of swept-carrier frequency-selective optical memory signals, Opt. Lett. 20 (8) (1995) 928–930. doi:10.1364/OL.20.000928.

[12] X. A. Shen, R. Kachru, Experimental demonstration of impulse-equivalent time-domain optical memory, Opt. Lett. 21 (24) (1996) 2020–2022. doi:10.1364/OL.21.002020.

[13] Y. Li, A. Hoskins, F. Schlottau, K. H. Wagner, C. Embry, W. R. Babbitt, Ultrawideband coherent noise lidar range-doppler imaging and signal processing by use of

spatial-spectral holography in inhomogeneously broadened absorbers, Appl. Opt. 45 (25) (2006) 6409–6420. doi:10.1364/AO.45.006409.

[14] W. R. Babbitt, J. A. Bell, Coherent transient continuous optical processor, Appl. Opt. 33 (8) (1994) 1538–1548. doi:10.1364/AO.33.001538.

[15] J. Ruggiero, J.-L. Le Gouët, C. Simon, T. Chanelière, Why the two-pulse photon echo is not a good quantum memory protocol, Phys. Rev. A 79 (2009) 053851. doi:10.1103/PhysRevA.79.053851.

[16] N. Sangouard, C. Simon, J. c. v. Minář, M. Afzelius, T. Chanelière, N. Gisin, J.-L. Le Gouët, H. de Riedmatten, W. Tittel, Impossibility of faithfully storing single photons with the three-pulse photon echo, Phys. Rev. A 81 (2010) 062333. doi:10.1103/PhysRevA.81.062333.

[17] S. A. Moiseev, S. Kröll, Complete reconstruction of the quantum state of a single-photon wave packet absorbed by a doppler-broadened transition, Phys. Rev. Lett. 87 (2001) 173601. doi:10.1103/PhysRevLett.87.173601.

[18] M. Nilsson, S. Kröll, Solid state quantum memory using complete absorption and re-emission of photons by tailored and externally controlled inhomogeneous absorption profiles, Opt. Commun. 247 (4) (2005) 393–403. doi:10.1016/j.optcom.2004.11.077.

[19] B. Kraus, W. Tittel, N. Gisin, M. Nilsson, S. Kröll, J. I. Cirac, Quantum memory for nonstationary light fields based on controlled reversible inhomogeneous broadening, Phys. Rev. A 73 (2) (2006). doi:10.1103/physreva.73.020302.

[20] A. L. Alexander, J. J. Longdell, M. J. Sellars, N. B. Manson, Photon echoes produced by switching electric fields, Phys. Rev. Lett. 96 (2006) 043602. doi:10.1103/PhysRevLett.96.043602.

[21] M. P. Hedges, J. J. Longdell, Y. Li, M. J. Sellars, Efficient quantum memory for light, Nature 465 (2010) 1052–1056. doi:10.1038/nature09081.

[22] M. Afzelius, C. Simon, H. de Riedmatten, N. Gisin, Multimode quantum memory based on atomic frequency combs, Phys. Rev. A 79 (5) (2009). doi:10.1103/physreva.79.052329.

[23] H. de Riedmatten, M. Afzelius, M. U. Staudt, C. Simon, N. Gisin, A solid-state light–matter interface at the single-photon level, Nature 456 (2008) 773–777. doi:10.1038/nature07607.

[24] I. Usmani, M. Afzelius, H. de Riedmatten, N. Gisin, Mapping multiple photonic qubits into and out of one solid-state atomic ensemble, Nat. Commun. 1 (2010) 12. doi:10.1038/ncomms1010.

[25] M. Zhong, M. Hedges, R. Ahlefeldt, J. Bartholomew, S. Beavan, S. Wittig, J. Longdell, M. Sellars, Optically addressable nuclear spins in a solid with a six-hour coherence time, Nature 517 (2015) 177–80. doi:10.1038/nature14025.

[26] G. Heinze, C. Hubrich, T. Halfmann, Stopped light and image storage by electromagnetically induced transparency up to the regime of one minute, Phys. Rev. Lett. 111 (2013) 033601. doi:10.1103/PhysRevLett.111.033601.

[27] A. Arcangeli, R. M. Macfarlane, A. Ferrier, P. Goldner, Temperature dependence of nuclear spin coherence in $Eu^{3+} : Y_2SiO_5$, Phys. Rev. B 92 (2015) 224401. doi:10.1103/PhysRevB.92.224401.

[28] M. Rančić, M. P. Hedges, R. L. Ahlefeldt, M. J. Sellars, Coherence time of over a second in a telecom-compatible quantum memory storage material, Nat. Phys. 14 (1) (2017) 50–54. doi:10.1038/nphys4254.

[29] A. Ortu, A. Tiranov, S. Welinski, F. Fröwis, N. Gisin, A. Ferrier, P. Goldner, M. Afzelius, Simultaneous coherence enhancement of optical and microwave transitions in solid-state electronic spins, Nature Mater. 17 (2018) 671—-675. doi:10.1038/s41563-018-0138-x.

[30] S. Welinski, A. Tiranov, M. Businger, A. Ferrier, M. Afzelius, P. Goldner, Coherence time extension by large-scale optical spin polarization in a rare-earth doped crystal, Phys. Rev. X 10 (2020) 031060. doi:10.1103/PhysRevX.10.031060.

[31] J. V. Rakonjac, Y.-H. Chen, S. P. Horvath, J. J. Longdell, Long spin coherence times in the ground state and in an optically excited state of $^{167}Er^{3+}:Y_2SiO_5$ at zero magnetic field, Phys. Rev. B 101 (18) (2020). doi:10.1103/physrevb.101.184430.

[32] J. J. Longdell, M. J. Sellars, N. B. Manson, Hyperfine interaction in ground and excited states of praseodymium-doped yttrium orthosilicate, Phys. Rev. B 66 (2002) 035101. doi:10.1103/PhysRevB.66.035101.

[33] T. Zhong, J. M. Kindem, J. G. Bartholomew, J. Rochman, I. Craiciu, E. Miyazono, M. Bettinelli, E. Cavalli, V. Verma, S. W. Nam, F. Marsili, M. D. Shaw, A. D. Beyer, A. Faraon, Nanophotonic rare-earth quantum memory with optically controlled retrieval, Science 357 (6358) (2017) 1392–1395. doi:10.1126/science.aan5959.

[34] B. Lauritzen, J. c. v. Minář, H. de Riedmatten, M. Afzelius, N. Sangouard, C. Simon, N. Gisin, Telecommunication-wavelength solid-state memory at the single photon level, Phys. Rev. Lett. 104 (2010) 080502. doi:10.1103/PhysRevLett.104.080502.

[35] E. Fraval, M. J. Sellars, J. J. Longdell, Dynamic decoherence control of a solid-state nuclear-quadrupole qubit, Phys. Rev. Lett. 95 (2005) 030506. doi:10.1103/PhysRevLett.95.030506.

[36] A. M. Dibos, M. Raha, C. M. Phenicie, J. D. Thompson, Atomic source of single photons in the telecom band, Phys. Rev. Lett. 120 (2018) 243601. doi:10.1103/PhysRevLett.120.243601.

[37] S. Probst, H. Rotzinger, S. Wünsch, P. Jung, M. Jerger, M. Siegel, A. V. Ustinov, P. A. Bushev, Anisotropic rare-earth spin ensemble strongly coupled to a superconducting resonator, Phys. Rev. Lett. 110 (2013) 157001. doi:10.1103/PhysRevLett.110.157001.

[38] X. Fernandez-Gonzalvo, Y.-H. Chen, C. Yin, S. Rogge, J. J. Longdell, Coherent frequency up-conversion of microwaves to the optical telecommunications band in an Er:YSO crystal, Phys. Rev. A 92 (2015) 062313. doi:10.1103/PhysRevA.92.062313.

[39] J. J. Longdell, M. J. Sellars, Experimental demonstration of quantum-state tomography and qubit-qubit interactions for rare-earth-metal-ion-based solid-state qubits, Phys. Rev. A 69 (2004) 032307. doi:10.1103/PhysRevA.69.032307.

[40] L. Rippe, B. Julsgaard, A. Walther, Y. Ying, S. Kröll, Experimental quantum-state tomography of a solid-state qubit, Phys. Rev. A 77 (2008) 022307. doi:10.1103/PhysRevA.77.022307.

[41] N. Gisin, R. Thew, Quantum communication, Nat. Photonics 1 (3) (2007) 165–171. doi:10.1038/nphoton.2007.22.

[42] H. J. Kimble, The quantum internet, Nature 453 (7198) (2008) 1023–1030. doi:10.1038/nature07127.

[43] C.-K. Duan, P. A. Tanner, What use are crystal field parameters? a chemist's viewpoint, J. Phys. Chem. A 114 (19) (2010) 6055–6062. doi:10.1021/jp1015214.

[44] K. R. Ferguson, S. E. Beavan, J. J. Longdell, M. J. Sellars, Generation of light with multimode time-delayed entanglement using storage in a solid-state spin-wave quantum memory, Phys. Rev. Lett. 117 (2) (2016). doi:10.1103/physrevlett.117.020501.

[45] C. Laplane, P. Jobez, J. Etesse, N. Timoney, N. Gisin, M. Afzelius, Multiplexed on-demand storage of polarization qubits in a crystal, New Journal of Physics 18 (1) (2015) 013006. doi:10.1088/1367-2630/18/1/013006.

[46] H. Bethe, Termaufspaltung in kristallen, Annalen der Physik 395 (2) (1929) 133–208. doi:10.1002/andp.19293950202.

[47] B. R. Judd, J. A. White, Operator Techniques in Atomic Spectroscopy, Physics Today 17 (4) (1964) 72. doi:10.1063/1.3051549.

[48] G. H. Dieke, Spectra and energy levels of rare earth ions in crystals, Interscience, 1968.

[49] W. T. Carnall, G. L. Goodman, K. Rajnak, R. S. Rana, A systematic analysis of the spectra of the lanthanides doped into single crystal LaF_3, J. Chem. Phys. 90 (7) (1989) 3443–3457. doi:10.1063/1.455853.

[50] G. W. Burdick, J. B. Gruber, K. L. Nash, S. Chandra, D. K. Sardar, Analyses of $4f^{11}$ energy levels and transition intensities between stark levels of Er^{3+} in $Y_3Al_5O_{12}$, Spectrosc. Lett. 43 (5) (2010) 406–422. doi:10.1080/00387010.2010.487019.

[51] K. Gschneidner, L. Eyring, Handbook on the Physics and Chemistry of Rare Earths, 1st Edition, Vol. 23, North-Holland, Amsterdam, 1996.

[52] G. M. Williams, P. C. Becker, J. G. Conway, N. Edelstein, L. A. Boatner, M. M. Abraham, Intensities of electronic raman scattering between crystal-field levels of Ce^{3+} in $LuPO_4$: Nonresonant and near-resonant excitation, Phys. Rev. B 40 (1989) 4132–4142. doi:10.1103/PhysRevB.40.4132.

[53] J. Hölsä, R.-J. Lamminmäki, Analysis of the $4f^n$ energy-level structure of the RE^{3+} ions in REOCl, J. Lumin. 69 (5) (1996) 311–317. doi:10.1016/S0022-2313(96)00110-X.

[54] M. Mujaji, G. D. Jones, R. W. G. Syme, Polarization study and crystal-field analysis of the laser-selective excitation spectra of Ho^{3+} ions in CaF_2 and SrF_2 crystals, Phys. Rev. B 46 (1992) 14398–14410. doi:10.1103/PhysRevB.46.14398.

[55] S. Horvath, J. Rakonjac, Y.-H. Chen, J. Longdell, P. Goldner, J.-P. Wells, M. Reid, Extending phenomenological crystal-field methods to C_1 point-group symmetry: Characterization of the optically-excited hyperfine structure of $^{167}Er^{3+}$:Y_2SiO_5, Phys. Rev. Lett. 123 (5) (2019). doi:10.1103/physrevlett.123.057401.

[56] S. Horvath, M. Reid, J. Wells, M. Yamaga, High precision wavefunctions for hyperfine states of low symmetry materials suitable for quantum information processing, J. Lumin. 169 (2016) 773 – 776. doi:10.1016/j.jlumin.2015.02.045.

[57] M. Lovrić, P. Glasenapp, D. Suter, Spin hamiltonian characterization and refinement for Pr^{3+}:$YAlO_3$ and Pr^{3+}:Y_2SiO_5, Phys. Rev. B 85 (2012) 014429. doi:10.1103/PhysRevB.85.014429.

[58] F. Könz, Y. Sun, C. W. Thiel, R. L. Cone, R. W. Equall, R. L. Hutcheson, R. M. Macfarlane, Temperature and concentration dependence of optical dephasing, spectral-hole lifetime, and anisotropic absorption in Eu^{3+}: Y_2SiO_5, Phys. Rev. B 68 (2003) 085109. doi:10.1103/PhysRevB.68.085109.

[59] M. Lovrić, P. Glasenapp, D. Suter, B. Tumino, A. Ferrier, P. Goldner, M. Sabooni, L. Rippe, S. Kröll, Hyperfine characterization and spin coherence lifetime extension in Pr^{3+}:$La_2(WO_4)_3$, Phys. Rev. B 84 (2011) 104417. doi:10.1103/PhysRevB.84.104417.

[60] P. C. Hansen, M. J. M. Leask, B. M. Wanklyn, Y. Sun, R. L. Cone, M. M. Abraham, Spectral hole burning and optically detected nuclear quadrupole resonance in flux-grown stoichiometric europium vanadate crystals, Phys. Rev. B 56 (1997) 7918–7929. doi:10.1103/PhysRevB.56.7918.

[61] J. J. Longdell, A. L. Alexander, M. J. Sellars, Characterization of the hyperfine interaction in europium-doped yttrium orthosilicate and europium chloride hexahydrate, Phys. Rev. B 74 (2006) 195101. doi:10.1103/PhysRevB.74.195101.

[62] Y.-H. Chen, X. Fernandez-Gonzalvo, S. P. Horvath, J. V. Rakonjac, J. J. Longdell, Hyperfine interactions of Er^{3+} ions in Y_2SiO_5: Electron paramagnetic resonance in a tunable microwave cavity, Phys. Rev. B 97 (2018) 024419. doi:10.1103/PhysRevB.97.024419.

[63] C. A. Morrison, R. P. Leavitt, D. E. Wortman, Crystal-field analysis of triply ionized lanthanides in $Cs_2NaLnCl_6$, J. Chem. Phys. 73 (6) (1980) 2580–2598. doi:10.1063/1.440470.

[64] F. S. Richardson, M. F. Reid, J. J. Dallara, R. D. Smith, Energy levels of lanthanide ions in the cubic $Cs_2NaLnCl_6$ and Cs_2NaYCl_6:Ln^{3+} (doped) systems, J. Chem. Phys. 83 (8) (1985) 3813–3830. doi:10.1063/1.449092.

[65] M. F. Reid, F. S. Richardson, Free-ion, crystal-field, and spin-correlated crystal-field parameters for lanthanide ions in $Cs_2NaLnCl_6$ and Cs_2NaYCl_6:Ln^{3+} systems, J. Chem. Phys. 83 (8) (1985) 3831–3836. doi:10.1063/1.449093.

[66] P. Tanner, V. Ravi Kanth Kumar, C. Jayasankar, M. Reid, Analysis of spectral data and comparative energy level parametrizations for Ln^{3+} in cubic elpasolite crystals, J. Alloys Compd. 215 (1) (1994) 349–370. doi:10.1016/0925-8388(94)90865-6.

[67] P. Novák, J. Kuneš, K. Knížek, Crystal field of rare earth impurities in LaF_3, Opt. Mater. 37 (2014) 414–418. doi:10.1016/j.optmat.2014.07.001.

[68] H. M. Crosswhite, H. Crosswhite, Parametric model for f-shell configurations. I. the effective-operator hamiltonian, J. Opt. Soc. Am. B 1 (2) (1984) 246–254. doi:10.1364/JOSAB.1.000246.

[69] D. J. Newman, Theory of lanthanide crystal fields, Adv. Phys. 20 (84) (1971) 197–256. doi:10.1080/00018737100101241.

[70] D. J. Newman, B. Ng, The superposition model of crystal fields, Rep. Prog. Phys. 52 (6) (1989) 699–762. doi:10.1088/0034-4885/52/6/002.

[71] B. Z. Malkin, Crystal Field and Electron-Phonon Interaction in Rare-Earth Ionic Paramagnets, Elsevier, North Holland, Amsterdam, 1987, p. 13. doi:10.1016/B978-0-444-87051-3.50008-0.

[72] M. Brik, N. Avram, C. Avram, Advances of crystal field theory and exchange charge model, Magn. Reson. Solids 19 (01 2019). doi:10.26907/mrsej-19405.

[73] Y. Yeung, M. F. Reid, Crystal-field and superposition-model analyses of Pr^{3+}-LaF_3 in C_2 symmetry, J. Less Common Met. 148 (1) (1989) 213–217. doi:10.1016/0022-5088(89)90030-1.

[74] N. Magnani, G. Amoretti, A. Baraldi, R. Capelletti, Crystal-field and superposition model analysis of R^{3+}:BaY_2F_8 (R = Er, Dy, Nd), Eur. Phys. J. B 29 (2002) 79–84. doi:10.1140/epjb/e2002-00264-0.

[75] H. Li, X.-Y. Kuang, A.-J. Mao, Z.-H. Wang, Investigations of defect structure and EPR parameters for tetragonal Nd^{3+} centers in AWO_4 (A=Ca, Sr, Pb) crystals by superposition model analysis, Solid State Commun. 189 (2014) 47–51. doi:10.1016/j.ssc.2014.03.020.

[76] S. A. Klimin, D. S. Pytalev, M. N. Popova, B. Z. Malkin, M. V. Vanyunin, S. L. Korableva, High-resolution optical spectroscopy of Tm^{3+} ions in $LiYF_4$: Crystal-field energies, hyperfine and deformation splittings, and the isotopic structure, Phys. Rev. B 81 (2010) 045113. doi:10.1103/PhysRevB.81.045113.

[77] M. N. Popova, E. P. Chukalina, B. Z. Malkin, A. I. Iskhakova, E. Antic-Fidancev, P. Porcher, J. P. Chaminade, High-resolution infrared absorption spectra, crystal-field levels, and relaxation processes in $CsCdBr_3$:Pr^{3+}, Phys. Rev. B 63 (2001) 075103. doi:10.1103/PhysRevB.63.075103.

[78] V. Klekovkina, B. Malkin, Crystal field and magnetoelastic interactions in $Tb_2Ti_2O_7$, Opt. Spectrosc. 116 (06 2014). doi:10.1134/S0030400X14060137.

[79] R. Puche, P. Caro, Rare Earths, Editorial Complutense, 1998.

[80] T. Jansen, T. Jüstel, M. Kirm, H. Mägi, V. Nagirnyi, E. Tõldsepp, S. Vielhauer, N. Khaidukov, V. Makhov, Site selective, time and temperature dependent spec-

troscopy of Eu^{3+} doped apatites $(Mg, Ca, Sr)_2Y_8Si_6O_{26}$, J. Lumin. 186 (2017) 205 – 211. doi:10.1016/j.jlumin.2017.02.004.

[81] E. F. Schubert, J. K. Kim, Solid-state light sources getting smart, Science 308 (5726) (2005) 1274–1278. doi:10.1126/science.1108712.

[82] Q. Zhu, S. Ding, J. Xiahou, S. Li, X. Sun, J.-G. Li, A groundbreaking strategy for fabricating YAG:Ce^{3+} transparent ceramic films via sintering of LRH nanosheets on a sapphire substrate, Chem. Commun. 56 (2020) 12761–12764. doi:10.1039/D0CC05244B.

[83] J. Kang, L. Zhang, Y. Li, Y. Ma, B. Sun, Y. Liu, T. Zhou, F. A. Selim, C. Wong, H. Chen, Luminescence declining behaviors in YAG:Ce transparent ceramics for high power laser lighting, J. Mater. Chem. C 7 (2019) 14357–14365. doi:10.1039/C9TC04637B.

[84] S. W. Yoon, H. K. Park, K.-Y. Ko, J. Ahn, Y. R. Do, Various nanofabrication approaches towards two-dimensional photonic crystals for ceramic plate phosphor-capped white light-emitting diodes, J. Mater. Chem. C 2 (2014) 7513–7522. doi:10.1039/C4TC00945B.

[85] H. K. Park, S. W. Yoon, D. Y. Choi, Y. R. Do, Fabrication of wafer-scale TiO_2 nanobowl arrays via a scooping transfer of polystyrene nanospheres and atomic layer deposition for their application in photonic crystals, J. Mater. Chem. C 1 (2013) 1732–1738. doi:10.1039/C2TC00652A.

[86] Q. Zhou, L. Dolgov, A. M. Srivastava, L. Zhou, Z. Wang, J. Shi, M. D. Dramićanin, M. G. Brik, M. Wu, Mn^{2+} and Mn^{4+} red phosphors: synthesis, luminescence and applications in WLEDs. a review, J. Mater. Chem. C 6 (2018) 2652–2671. doi:10.1039/C8TC00251G.

[87] F. Zhang, S. Chen, J. F. Chen, H. L. Zhang, J. Li, X. J. Liu, S. W. Wang, Characterization and luminescence properties of AlON:Eu^{2+} phosphor for white-emitting-diode illumination, J. Appl. Phys. 111 (8) (2012) 083532. doi:10.1063/1.4705404.

[88] L. Dong, L. Zhang, W. Lü, B. Shao, S. Zhao, H. You, Preparation and photoluminescence of novel $La_8Ca_2(Si_4P_2O_{22}N_2)O_2$ oxynitride phosphors containing $Eu^{2+}/Ce^{3+}/Tb^{3+}$ ions, Dalton Trans. 48 (2019) 3028–3037. doi:10.1039/C8DT04810J.

[89] H.-D. Nguyen, R.-S. Liu, Narrow-band red-emitting Mn^{4+}-doped hexafluoride phosphors: synthesis, optoelectronic properties, and applications in white light-emitting diodes, J. Mater. Chem. C 4 (2016) 10759–10775. doi:10.1039/C6TC03292C.

[90] W. U. Khan, L. Zhou, Q. Liang, X. Li, J. Yan, N. U. Rahman, L. Dolgov, S. U. Khan, J. Shi, M. Wu, Luminescence enhancement and energy transfers of Ce^{3+} and Sm^{3+} in $CaSrSiO_4$ phosphor, J. Mater. Chem. C 6 (2018) 7612–7618. doi:10.1039/C8TC02143K.

[91] G. Ramakrishna, H. Nagabhushana, S. Prashantha, S. Sharma, B. Nagabhushana, Role of flux on morphology and luminescence properties of Sm^{3+} doped Y_2SiO_5 nanopowders for WLEDs, Spectrochim. Acta A 136 (2015) 356–365. doi:10.1016/j.saa.2014.09.041.

[92] S. Rühle, Tabulated values of the shockley–queisser limit for single junction solar cells, Sol. Energy 130 (2016) 139–147. doi:10.1016/j.solener.2016.02.015.

[93] B. T. Huy, B. Sengthong, P. Van Do, J. W. Chung, G. Ajith Kumar, V. X. Quang, V.-D. Dao, Y.-I. Lee, A bright yellow light from a Yb^{3+},Er^{3+}-co-doped Y_2SiO_5 upconversion luminescence material, RSC Adv. 6 (2016) 92454–92462. doi:10.1039/C6RA21768K.

[94] D. K. Yim, I.-S. Cho, S. Lee, C. H. Kwak, D. H. Kim, J.-K. Lee, K. S. Hong, Synthesis and characteristics of Tb-doped Y_2SiO_5 nanophosphors and luminescent layer for enhanced photovoltaic cell performance, J. Nanosci. Nanotechnol. 11 (10) (2011) 8748–8753. doi:10.1166/jnn.2011.3490.

[95] N. U. Rahman, W. U. Khan, S. Khan, X. Chen, J. Khan, J. Zhao, Z. Yang, M. Wu, Z. Chi, A promising europium-based down conversion material: organic–inorganic perovskite solar cells with high photovoltaic performance and UV-light stability, J. Mater. Chem. A 7 (2019) 6467–6474. doi:10.1039/C9TA00551J.

[96] M. J. Kang, E. G. Santoro, Y. S. Kang, Enhanced efficiency of functional smart window with solar wavelength conversion phosphor–photochromic hybrid film, ACS omega 3 (8) (2018) 9505–9512. doi:10.1021/acsomega.8b01091.

[97] T. Förster, Zwischenmolekulare energiewanderung und fluoreszenz, Annalen der Physik 437 (1-2) (1948) 55–75. doi:10.1002/andp.19484370105.

[98] D. L. Dexter, A theory of sensitized luminescence in solids, J. Chem. Phys. 21 (5) (1953) 836–850. doi:10.1063/1.1699044.

[99] H. M. Crosswhite, H. W. Moos, Optical Properties of Ions in Crystals, New York: Interscience, 1967.

[100] M. Inokuti, F. Hirayama, Influence of energy transfer by the exchange mechanism on donor luminescence, J. Chem. Phys. 43 (6) (1965) 1978 – 1989. doi:10.1063/1.1697063.

[101] S. O. Vasquez, C. D. Flint, A shell model for cross relaxation in elpasolite crystals: application to the $^3P_0$ and $^1G_4$ states of $Cs_2NaY_{1-x}Pr_xCl_6$, Chem. Phys. Lett 238 (4) (1995) 378–386. doi:10.1016/0009-2614(95)00398-N.

[102] T. Luxbacher, H. P. Fritzer, C. D. Flint, Cross relaxation from the $^4G_{5/2}$ state of Sm^{3+} in $Cs_2NaSm_xY_{1-x}Cl_6$ and $Cs_2NaSm_xGd_{1-x}Cl_6$: a comparison of multipole-multipole and anisotropic dielectric shell models, J. Phys.: Condens. Matt. 7 (49) (1995) 9683–9692. doi:10.1088/0953-8984/7/49/029.

[103] T. Luxbacher, H. P. Fritzer, C. D. Flint, Temperature dependence of luminescence decay from the $^4G_{5/2}$ state of Sm^{3+} in $Cs_2NaSm_xY_{1-x}Cl_6$ and $Cs_2NaSm_xEu_yY_{1-x-y}Cl_6$, J. Lumin. 71 (4) (1997) 313–319. doi:10.1016/S0022-2313(97)00097-5.

[104] J. Wijngaarden, S. Scheidelaar, T. Vlugt, M. Reid, A. Meijerink, Energy transfer mechanism for downconversion in the (Pr^{3+}, Yb^{3+}) couple, Phys. Rev. B 81 (2010) 155112. doi:10.1103/PhysRevB.81.155112.

[105] P. Vergeer, T. J. H. Vlugt, M. H. F. Kox, M. I. den Hertog, J. P. J. M. van der Eerden, A. Meijerink, Quantum cutting by cooperative energy transfer in $Yb_xY_{1-x}PO_4 : Tb^{3+}$, Phys. Rev. B 71 (2005) 014119. doi:10.1103/PhysRevB.71.014119.

[106] S. Horvath, High-resolution spectroscopy and novel crystal-field methods for rare-earth based quantum information processing, Ph.D. thesis, University of Canterbury (2016).

[107] B. Maksimov, V. Ilyukhin, Y. A. Kharitonov, N. Belov, Crystal structure of yttrium oxyorthosilicate $Y_2O_3 \cdot SiO_2 = Y_2SiO_5$, Kristallografiya 15 (926) (1970).

[108] C. Li, C. Wyon, R. Moncorge, Spectroscopic properties and fluorescence dynamics of Er^{3+}:Y_2SiO_5, IEEE J. Quantum Electron. 28 (4) (1992) 1209–1221. doi:10.1109/3.135248.

[109] R. D. Shannon, Revised effective ionic radii and systematic studies of interatomic distances in halides and chalcogenides, Acta Crystallographica Section A 32 (5) (1976) 751–767. doi:10.1107/S0567739476001551.

[110] Y. Sun, T. Böttger, C. Thiel, R. Cone, Magnetic g tensors for the $^4I_{15/2}$ and $^4I_{13/2}$ states of Er^{3+}:Y_2SiO_5, Phys. Rev. B 77 (2008). doi:10.1103/PhysRevB.77.085124.

[111] R. M. Macfarlane, Coherent transient and holeburning spectroscopy of rare earth ions in solids, edited by A. A. Kaplyanskii and R. M. Macfarlane (North-Holland, Amsterdam, 1987.

[112] G. H. Dieke, H. M. Crosswhite, The spectra of the doubly and triply ionized rare earths, Appl. Opt. 2 (7) (1963) 675–686. doi:10.1364/AO.2.000675.

[113] R. T. Wegh, A. Meijerink, R.-J. Lamminmäki, Jorma Hölsä, Extending Dieke's diagram, J. Lumin. 87-89 (2000) 1002–1004. doi:https://doi.org/10.1016/S0022-2313(99)00506-2.

[114] R. Withnall, J. Silver, 'Physics of Light Emission from Rare-Earth Doped Phosphors', Springer Berlin Heidelberg, 2012. doi:10.1007/978-3-540-79567-4_68.

[115] B. Wybourne, Spectroscopic properties of rare earths, Wiley-Interscience, New York, 1965.

[116] M. Weissbluth, Atoms and Molecules, Academic Press, 1978.

[117] G. Liu, Electronic Energy Level Structure, Springer Berlin Heidelberg, Berlin, Heidelberg, 2005, pp. 1–94. doi:10.1007/3-540-28209-2_1.

[118] A. R. Edmonds, Angular momentum in quantum mechanics, Princeton University Press, 1996.

[119] C. Nielson, G. F. Koster, Spectroscopic Coefficients for the p^n, d^n and f^n configurations, MIT press, 1963.

[120] Y. Y. Yeung, 'Superposition Model and its Applications', Springer Berlin Heidelberg, 2013.

[121] O. Guillot-Noël, Y. Le Du, F. Beaudoux, E. Antic-Fidancev, M. Reid, R. Marino, J. Lejay, A. Ferrier, P. Goldner, Calculation and analysis of hyperfine and quadrupole interactions in praseodymium-doped $La_2(WO_4)_3$, J. Lumin. 130 (9) (2010) 1557–1565. doi:https://doi.org/10.1016/j.jlumin.2009.12.023.

[122] S. Horvath, The pycf crystal-field theory package, https://bitbucket.org/sebastianhorvath/pycf.

[123] D. J. Wales, J. P. K. Doye, Global optimization by basin-hopping and the lowest energy structures of lennard-jones clusters containing up to 110 atoms, J. Phys. Chem. A 101 (28) (1997) 5111–5116. doi:10.1021/jp970984n.

[124] D. J. Wales, H. A. Scheraga, Global optimization of clusters, crystals, and biomolecules, Science 285 (5432) (1999) 1368–1372. doi:10.1126/science.285.5432.1368.

[125] N. Metropolis, A. W. Rosenbluth, M. N. Rosenbluth, A. H. Teller, E. Teller, Equation of state calculations by fast computing machines, J. Chem. Phys. 21 (6) (1953) 1087–1092. doi:10.1063/1.1699114.

[126] S. G. Johnson, The nlopt nonlinear-optimization package, http://ab-initio.mit.edu/nlopt.

[127] S. Kirkpatrick, C. D. Gelatt, M. P. Vecchi, Optimization by simulated annealing, Science 220 (4598) (1983) 671–680. doi:10.1126/science.220.4598.671.

[128] R. C. Aster, B. Borchers, C. H. Thurber, Parameter estimation and inverse problems, Vol. 90, Academic Press, 2011.

[129] A. Bukowski, Czochralski-grown silicon crystals for microelectronics, Acta Phys. Pol. A 124 (2013) 235–238. doi:10.12693/APhysPolA.124.235.

[130] C. Brandle, A. Valentino, G. Berkstresser, Czochralski growth of rare-earth orthosilicates (Ln2SiO5), J. Cryst. Growth 79 (1) (1986) 308 – 315. doi:10.1016/0022-0248(86)90454-9.

[131] B. Tumino, Growth and coherent spectroscopy of europium- and praseodymium-doped crystals for quantum memory applications, Ph.D. thesis, l'Université Pierre et Marie Curie (2013).

[132] J. Mlynek, N. C. Wong, R. G. DeVoe, E. S. Kintzer, R. G. Brewer, Raman heterodyne detection of nuclear magnetic resonance, Phys. Rev. Lett. 50 (1983) 993–996. doi:10.1103/PhysRevLett.50.993.

[133] N. C. Wong, E. S. Kintzer, J. Mlynek, R. G. DeVoe, R. G. Brewer, Raman heterodyne detection of nuclear magnetic resonance, Phys. Rev. B 28 (1983) 4993–5010. doi:10.1103/PhysRevB.28.4993.

[134] X. F. Gonzalvo, Coherent frequency conversion from microwave to optical fields in an erbium doped Y_2SiO_5 crystal: Towards the single photon regime, Ph.D. thesis, University of Otago (2017).

[135] J. V. Rakonjac, Hyperfine structure and coherent properties of erbium-167-doped yttrium orthosilicate, Master's thesis, University of Otago (2018).

[136] X. Fernandez-Gonzalvo, S. P. Horvath, Y.-H. Chen, J. J. Longdell, Cavity-enhanced raman heterodyne spectroscopy in Er^{3+} : Y_2SiO_5 for microwave to optical signal conversion, Phys. Rev. A 100 (2019) 033807. doi:10.1103/PhysRevA.100.033807.

[137] N. L. Jobbitt, S. J. Patchett, Y. Alizadeh, M. F. Reid, J.-P. R. Wells, S. P. Horvath, J. J. Longdell, A. Ferrier, P. Goldner, Transferability of crystal-field parameters for rare-earth ions in Y_2SiO_5 tested by Zeeman spectroscopy, Phys. Solid State 61 (5) (2019) 780–784. doi:10.1134/s1063783419050123.

[138] S. P. Horvath, J.-P. R. Wells, M. F. Reid, M. Yamaga, M. Honda, Electron paramagnetic resonance enhanced crystal field analysis for low point-group symmetry systems: C_{2v} sites in Sm^{3+}:CaF_2/SrF_2, J. Phys. Condens. Matter 31 (1) (2018) 015501. doi:10.1088/1361-648x/aaee5c.

[139] Y. Luo, L. Sun, J. Wang, Z. Tian, H. Nian, J. Wang, Tunable thermal properties in yttrium silicates switched by anharmonicity of low-frequency phonons, J. Eur. Ceram. Soc. 38 (4) (2018) 2043–2052. doi:10.1016/j.jeurceramsoc.2017.11.010.

[140] L. Zheng, G. Zhao, C. Yan, X. Xu, L. Su, Y. Dong, J. Xu, Raman spectroscopic investigation of pure and ytterbium-doped rare earth silicate crystals, J. Raman Spectrosc. 38 (11) (2007) 1421–1428. doi:10.1002/jrs.1789.

[141] J. A. Weil, J. R. Bolton, Electron Paramagnetic Resonance: Elementary Theory and Practical Applications, Wiley, 2007, Ch. 4, pp. 85–111.

[142] J. Wen, C.-K. Duan, L. Ning, Y. Huang, S. Zhan, J. Zhang, M. Yin, Spectroscopic distinctions between two types of Ce^{3+} ions in X2-Y_2SiO_5: A theoretical investigation, J. Phys. Chem. A 118 (27) (2014) 4988–4994, pMID: 24953347. doi:10.1021/jp5050207.

[143] A. A. Sukhanov, R. F. Likerov, R. M. Eremina, I. V. Yatsyk, T. P. Gavrilova, V. F. Tarasov, Y. D. Zavartsev, S. A. Kutovoi, Crystal environment of impurity Nd^{3+} ion in yttrium and scandium orthosilicate crystals, J. Magn. Reson. 295 (2018) 12–16. doi:https://doi.org/10.1016/j.jmr.2018.07.018.

[144] X. Zhou, H. Liu, Z. He, B. Chen, J. Wu, Investigation of the electronic structure and optical, EPR, and ODMR spectroscopic properties for $^{171}Yb^{3+}$-doped Y_2SiO_5 crystal: A combined theoretical approach, Inorg. Chem. 59 (18) (2020) 13144–13152, pMID: 32865403. doi:10.1021/acs.inorgchem.0c01430.

[145] M. Yamaga, H. Uno, S.-I. Tsuda, J.-P. R. Wells, T. P. J. Han, Resonant energy transfer and cross relaxation between Sm^{3+} ions in $LiYF_4$ crystals, J. Lumin. 132 (6) (2012) 1608 – 1617. doi:10.1016/j.jlumin.2012.01.028.

[146] W. U. Khan, L. Zhou, Q. Liang, X. Li, J. Yan, N. U. Rahman, L. Dolgov, S. U. Khan, J. Shi, M. Wu, Luminescence enhancement and energy transfers of Ce^{3+} and Sm^{3+} in $CaSrSiO_4$ phosphor, J. Mater. Chem. C 6 (2018) 7612–7618. doi:10.1039/C8TC02143K.

[147] P. V. Do, V. P. Tuyen, V. X. Quang, L. X. Hung, L. D. Thanh, T. Ngoc, N. V. Tam, B. T. Huy, Investigation of spectroscopy and the dual energy transfer mechanisms

of Sm^{3+}-doped telluroborate glasses, Opt. Mat. 55 (2016) 62 – 67. doi:10.1016/j.optmat.2016.03.023.

[148] J.-P. R. Wells, R. J. Reeves, Polarized laser selective excitation and Zeeman infrared absorption of Sm^{3+} centers in CaF_2 and SrF_2 crystals, Phys. Rev. B 61 (2000) 13593–13608. doi:10.1103/PhysRevB.61.13593.

[149] J.-P. R. Wells, G. D. Jones, R. J. Reeves, Energy transfer and laser spectroscopy of Eu^{3+} co-doped CaF_2:Sm^{3+}, J. Lumin. 72-74 (1997) 977–979. doi:10.1016/S0022-2313(96)00439-5.

[150] T. Kushida, Linewidths and thermal shifts of spectral lines in neodymium-doped yttrium aluminum garnet and calcium fluorophosphate, Phys. Rev. 185 (1969) 500–508. doi:10.1103/PhysRev.185.500.

[151] X. Chen, B. Di Bartolo, Phonon effects on sharp luminescence lines of Nd^{3+} in $Gd_3Sc_2Ga_3O_{12}$ garnet (GSGG), J. Lumin. 54 (5) (1993) 309 – 318. doi:10.1016/0022-2313(93)90090-A.

[152] D. K. Sardar, R. M. Yow, Optical characterization of inter-stark energy levels and effects of temperature on sharp emission lines of Nd^{3+} in $CaZn_2Y_2Ge_3O_{12}$, Opt. Mater. 10 (3) (1998) 191 – 199. doi:10.1016/S0925-3467(97)00172-9.

[153] R. J. Mears, L. Reekie, I. M. Jauncey, D. Payne, Low-noise erbium-doped fibre amplifier operating at 1.54μm, Electron. Lett. 23 (1987) 1026–1028(2). doi:10.1049/el:19870719.

[154] S. Probst, H. Rotzinger, A. V. Ustinov, P. A. Bushev, Microwave multimode memory with an erbium spin ensemble, Phys. Rev. B 92 (2015) 014421. doi:10.1103/PhysRevB.92.014421.

[155] E. Baldit, K. Bencheikh, P. Monnier, S. Briaudeau, J. A. Levenson, V. Crozatier, I. Lorgeré, F. Bretenaker, J. L. Le Gouët, O. Guillot-Noël, P. Goldner, Identification of Λ-like systems in Er^{3+} : Y_2SiO_5 and observation of electromagnetically induced transparency, Phys. Rev. B 81 (2010) 144303. doi:10.1103/PhysRevB.81.144303.

[156] O. Guillot-Noël, P. Goldner, Y. L. Du, E. Baldit, P. Monnier, K. Bencheikh, Hyperfine interaction of Er^{3+} ions in Y_2SiO_5: An electron paramagnetic resonance spectroscopy study, Phys. Rev. B 74 (2006) 214409. doi:10.1103/PhysRevB.74.214409.

[157] R. P. Budoyo, K. Kakuyanagi, H. Toida, Y. Matsuzaki, W. J. Munro, H. Yamaguchi, S. Saito, Electron paramagnetic resonance spectroscopy of Er^{3+} : Y_2SiO_5 using a josephson bifurcation amplifier: Observation of hyperfine and quadrupole structures, Phys. Rev. Mater. 2 (2018) 011403. doi:10.1103/PhysRevMaterials.2.011403.

[158] J. L. Doualan, C. Labbe, P. L. Boulanger, J. Margerie, R. Moncorge, H. Timonen, Energy levels of the laser active Er^{3+} ion in each of the two crystallographic sites of yttrium orthosilicate, J. Phys. Condens. Matter 7 (26) (1995) 5111–5126. doi:10.1088/0953-8984/7/26/017.

[159] T. Böttger, C. W. Thiel, R. L. Cone, Y. Sun, Effects of magnetic field orientation on optical decoherence in Er^{3+} : Y_2SiO_5, Phys. Rev. B 79 (2009) 115104. doi:10.1103/PhysRevB.79.115104.

[160] R. M. Macfarlane, T. L. Harris, Y. Sun, R. L. Cone, R. W. Equall, Measurement of photon echoes in Er^{3+}:Y_2SiO_5 at 1.5μm with a diode laser and an amplifier, Opt. Lett. 22 (12) (1997) 871–873. doi:10.1364/OL.22.000871.

[161] I. Kurkin, K. Chernov, Epr and spin-lattice relaxation of rare-earth activated centres in Y_2SiO_5 single crystals, Physica B+C 101 (2) (1980) 233–238. doi:10.1016/0378-4363(80)90107-2.

[162] T. Böttger, C. W. Thiel, Y. Sun, R. L. Cone, Optical decoherence and spectral diffusion at 1.5 μm in Er^{3+} : Y_2SiO_5 versus magnetic field, temperature, and Er^{3+} concentration, Phys. Rev. B 73 (2006) 075101. doi:10.1103/PhysRevB.73.075101.

[163] S. R. Hastings-Simon, B. Lauritzen, M. U. Staudt, J. L. M. van Mechelen, C. Simon, H. de Riedmatten, M. Afzelius, N. Gisin, Zeeman-level lifetimes in Er^{3+} : Y_2SiO_5, Phys. Rev. B 78 (2008) 085410. doi:10.1103/PhysRevB.78.085410.

[164] D. Hashimoto, K. Shimizu, Coherent raman beat analysis of the hyperfine sublevel coherence properties of $^{167}Er^{3+}$ ions doped in an Y_2SiO_5 crystal, J. Lumin. 171 (2016) 183–190. doi:10.1016/j.jlumin.2015.11.031.

[165] R. P. Budoyo, K. Kakuyanagi, H. Toida, Y. Matsuzaki, W. J. Munro, H. Yamaguchi, S. Saito, Phonon-bottlenecked spin relaxation of Er^{3+}:Y_2SiO_5 at sub-kelvin temperatures, Appl. Phys. Express 11 (4) (2018) 043002. doi:10.7567/apex.11.043002.

[166] Y. Petit, B. Boulanger, J. Debray, T. Chanelière, Demonstration of site-selective angular-resolved absorption spectroscopy of the $^4I_{15/2} \longrightarrow {}^4I_{13/2}$ erbium transition in the monoclinic crystal Y_2SiO_5, Opt. Mater. X 8 (2020) 100062. doi:10.1016/j.omx.2020.100062.

[167] K. M. Smith, M. F. Reid, R. L. Ahlefeldt, M. J. Sellars, Crystal-field calculation of nuclear electric quadrupole and shielding effects in europium doped crystals, Private communications (2021).

[168] R. Yano, M. Mitsunaga, N. Uesugi, Nonlinear laser spectroscopy of Eu^{3+}:Y_2SiO_5 and its application to time-domain optical memory, J. Opt. Soc. Am. B 9 (6) (1992) 992–997. doi:10.1364/JOSAB.9.000992.

[169] E. Z. Cruzeiro, J. Etesse, A. Tiranov, P.-A. Bourdel, F. Fröwis, P. Goldner, N. Gisin, M. Afzelius, Characterization of the hyperfine interaction of the excited $^5D_0$ state of Eu^{3+} : Y_2SiO_5, Phys. Rev. B 97 (2018) 094416. doi:10.1103/PhysRevB.97.094416.

[170] Y. Ma, Z.-Q. Zhou, C.-F. Li, G.-C. Guo, Hypefine interaction in the $^7F_0$ ground state of $^{151}Eu^{3+}$ and $^{153}Eu^{3+}$ doped in Y_2SiO_5 at two crystallographic sites, Private communications (2021).

[171] S.-L. Xue, Q. Wang, L.-B. Chen, Y.-Y. Zhao, F.-M. Li, S.-D. Zhang, H.-B. Wang, Z.-Q. Lin, Fluorescence properties of Eu^{3+}:Y_2SiO_5 single crystal, J. of Shanghai Univ. 5 (3) (2001) 191–195. doi:10.1007/s11741-996-0023-8.

[172] Y. Ma, Z.-Q. Zhou, C. Liu, Y.-J. Han, T.-S. Yang, T. Tu, Y.-X. Xiao, P.-J. Liang, P.-Y. Li, Y.-L. Hua, X. Liu, Z.-F. Li, J. Hu, X. Li, C.-F. Li, G.-C. Guo, A raman heterodyne study of the hyperfine interaction of the optically-excited state $^5D_0$ of Eu^{3+} : Y_2SiO_5, J. Lumin. 202 (2018) 32–37. doi:https://doi.org/10.1016/j.jlumin.2018.05.041.